The growth of galaxies and their gaseous haloes

Freeke van de Voort

The growth of galaxies and their gaseous haloes

P ROEFSCHRIFT

ter verkrijging van
de graad van Doctor aan de Universiteit Leiden,
op gezag van de Rector Magnificus prof. mr. P. F. van der Heijden,
volgens besluit van het College voor Promoties
te verdedigen op woensdag 28 maart 2012
klokke 16:15 uur

door
Frederieke van de Voort
geboren te Eindhoven
in 1983

Promotiecommissie

Promotor: Prof. dr. J. Schaye

Overige leden: Prof. dr. M. Franx
Prof. dr. K. H. Kuijken
Dr. J. Brinchmann
Dr. D. Kereš (University of California, San Diego, USA)

To Craig

TABLE OF CONTENTS

1
INTRODUCTION

Galaxy formation has undergone fast development in the past few decades, both theoretically and observationally. The number of observed galaxies is expanding rapidly and observations are pushing to lower masses and higher redshifts. Diffuse gas has been observed in absorption against bright background objects and in emission around galaxies. Simulations predict that the spatial distribution of the intergalactic medium, the cosmic web, has a profound impact on the evolution of galaxies. Gas accretion provides the fuel for star formation, which is inhibited by outflows powered by supernova explosions and active galactic nuclei (AGN). Star formation and feedback produce and distribute metals in the surrounding medium, which aids the process of galaxy formation. To understand the assembly of galaxies, we need to understand how they are fuelled.

1.1 Structure formation in the Universe

More than thirteen billion years ago the Universe was almost completely homogeneous. Tiny gas density fluctuations of the order 10^{-5} grew into everything we can see today. Structure on the largest scales is completely governed by gravity. The matter is concentrated in a 'cosmic web' of sheets and filaments that are determined by the original fluctuations and the cosmological parameters, principally $\Omega_{\rm m}$, Ω_Λ, h, σ_8, and n. The values of these parameters can be derived from accurate observations of the cosmic microwave background, the radiation emitted by recombining protons and electrons and redshifted by a factor of about 1100, and of the large-scale distribution of matter (e.g. Spergel et al., 2003; Komatsu et al., 2011).

The distribution of matter is not spherically symmetric, so the collapse will be different in different directions. First collapse happens in one dimension, forming sheets. When collapse happens in two dimenions, filaments form. In the end, collapse occurs in three dimension and haloes are formed. An illustration of the gas distribution in the present-day Universe is shown in Figure 1.1. Assuming spherical collapse, the internal density for collapsed haloes is $\rho_{\rm coll} \approx 18\pi^2\langle\rho_{\rm m}\rangle$ (Padmanabhan, 2002), where $\langle\rho_{\rm m}\rangle$ is the cosmic mean matter density:

$$\langle\rho_{\rm m}\rangle = \Omega_{\rm m}\rho_{\rm crit} = \Omega_{\rm m}(1+z)^3\rho_{\rm crit,0} = \Omega_{\rm m}(1+z)^3\frac{3H_0^2}{8\pi G}, \tag{1.1}$$

where H_0 is the $z = 0$ value of the Hubble parameter and G is the gravitational constant. The mass of this object then is $M_{\rm halo} = \frac{4}{3}\pi\rho_{\rm coll}R_{\rm vir}^3$, from which we can derive an expression for the virial radius:

$$R_{\rm vir} \approx \left(\frac{2GM_{\rm halo}}{H_0^2\Omega_{\rm m}18\pi^2}\right)^{1/3}\frac{1}{1+z} \tag{1.2}$$

or

$$R_{\rm vir} \approx 3.4 \cdot 10^2 \text{ kpc }\left(\frac{M}{10^{12}\,{\rm M_\odot}}\right)^{1/3}\left(\frac{\Omega_{\rm m}H_0^2}{1.3\times10^{-36}\,s^{-2}}\right)^{-1/3}\frac{1}{1+z}. \tag{1.3}$$

Galaxies form inside their much larger haloes in the highest density peaks and are dominated by baryons, because gas is able to cool, whereas dark matter can only lose energy due to gravitational interactions, e.g. dynamical friction. Galaxy properties therefore depend on other things than just gravity. The gas behaves like an ideal gas. Its pressure increases when its volume decreases or its temperature increases. It can move supersonically and it can therefore experience shocks, converting its kinetic energy into thermal energy.

While the collapse of dark matter halts as it reaches virial equilibrium in haloes, baryons can radiate away their binding energy, allowing them to collapse
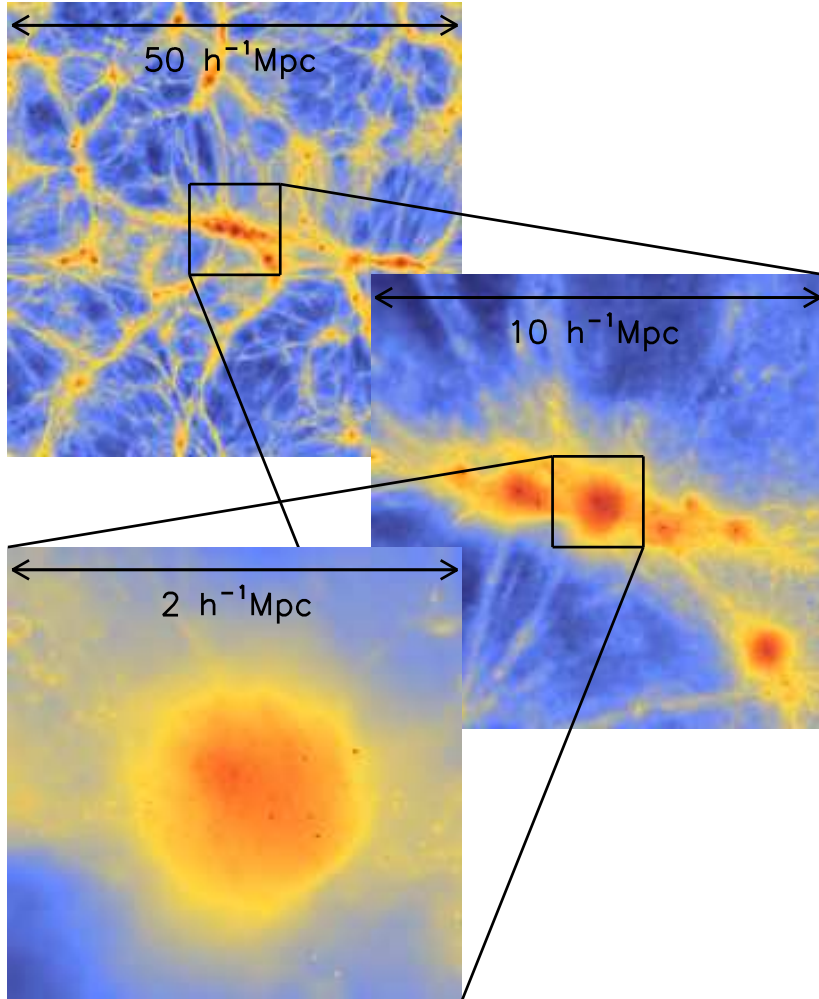
Figure 1.1: Zoom-in from 50 h^{-1}Mpc to 10 h^{-1}Mpc to 2 h^{-1}Mpc of the gas density in a 2 h^{-1}Mpc slice of the Universe at $z = 0$, centred on a massive halo ($M_{\text{halo}} = 10^{13.5}$ M$_\odot$), showing the filaments of the cosmic web and the haloes embedded within them. The colour bar is logarithmic, the same in all panels, and runs from the mean cosmic density (blue) to 10^4 times the mean density of the Universe (red). The simulation used is the reference simulation in a $(50\ h^{-1}\text{Mpc})^3$ volume from the OWLS project (Schaye et al., 2010).

further and fragment into smaller structures, such as stars and galaxies. The cooling time can be defined as the ratio of the thermal energy density of the gas and the cooling rate, which depends on the density, temperature, and metallicity of the gas, because it may be dominated by metal-line emission.

After virialization, a gas cloud can be in one of three regimes. If the characteristic cooling time exceeds the Hubble time-scale, the gas will not be able to radiate away the thermal energy that supports it and will therefore not collapse. If, on the other hand, the cooling time is smaller than the Hubble time, but larger than the dynamical time-scale, then the cloud can adjust its density and temperature quasi-statically. It will increase both its density and its temperature while maintaining hydrostatic equilibrium. Finally, if the cooling time is shorter than the dynamical time, the cloud will cool faster than it can collapse, lowering the Jeans mass and possibly leading to fragmentation. This is the regime in which galaxies are thought to form (Rees & Ostriker, 1977; Silk, 1977).

We can divide the gas in the Universe into a couple of different phases in temperature-density space. Their relative importance at $z = 4$, 2, and 0 is shown in Figure 1.2. Gas with densities up to $\sim 10^2$ times the cosmic average density represents the intergalactic medium (IGM). In the beginning, there was no structure and all gas had densities very close to the cosmic mean and therefore all gas started out in the IGM. At later times, a significant fraction of this gas resides in filamentary structures. The gas can be heated to temperatures above 10^5 K when kinetic energy, generated by gravitational infall or galactic winds, is converted into thermal energy. We refer to this tenuous, shock-heated gas as the warm-hot intergalactic medium (WHIM). The WHIM also includes denser halo gas. The intracluster medium is the very hot $T > 10^7$ K gas located in galaxy groups and clusters. Gas at overdensities $\rho / \langle \rho \rangle > 10^2$, but at much lower temperature ($T < 10^5$ K), resides mostly in the densest parts of filaments and low-mass haloes. Gas at very high densities $n_{\mathrm{H}} > 0.1$ cm^{-3} is located inside galaxies, in the interstellar medium (ISM).

Although the IGM completely dominates the mass budget at high redshift, by $z = 0$ the WHIM carries about the same amount of mass (Davé et al., 2001). The ICM is never very important, because the highest-mass objects are rare (e.g. Shull et al., 2011). The amount of gas in the ISM and in low-temperature halo gas peaks at $z = 3 - 2$ and declines thereafter (e.g. van de Voort et al., 2011b)

In the low-density IGM, the dominant cooling process is the expansion of the Universe. As the gas reaches higher densities, radiative cooling becomes more important. The cooling time t_{cool} is shorter at higher redshift, because the density, ρ, is higher and $t_{\mathrm{cool}} \propto \rho^{-1}$. The Hubble time t_{H} is also shorter, but with a weaker dependence, $t_{\mathrm{H}} \propto \rho^{1/2}$. Hence, galaxy formation will depend on redshift. The so-called cooling radius is the radius, from the halo centre, where t_{cool} equals t_{H}. If the cooling radius lies well inside the halo, which is the case for high-mass haloes, a quasi-static, hot atmosphere will form. Accretion onto the galaxy is then regulated by the cooling function. If, on the other hand, this
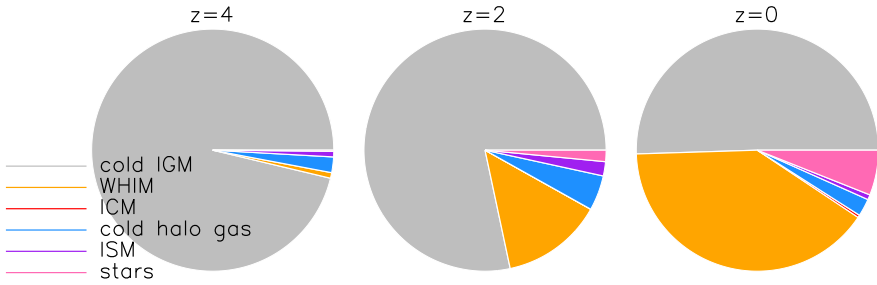
Figure 1.2: Distribution of baryonic matter amongst the different gas phases and stars. The cold IGM (grey) dominates, but becomes less important towards lower redshift. The WHIM (orange) becomes more important towards lower redshift. The ICM (red) is never very important. The amount of cold halo gas (blue) and ISM (purple) is largest at $z \approx 2$. The stellar mass keeps building up down to $z = 0$. The simulation used is the reference simulation in a $(50\ h^{-1}\mathrm{Mpc})^3$ volume from the OWLS project (Schaye et al., 2010).

radius is larger than the virial radius, then there will be no hot halo and the gas will not go through an accretion shock at the virial radius. The rapid cooling of gas in low-mass haloes was already shown by Rees & Ostriker (1977) and White & Rees (1978). The accretion rate onto the central galaxy then depends on the infall rate, but not on the cooling rate (White & Frenk, 1991).

Because haloes are not spherical, the cooling radius will not be the same for the entire halo. Gas can accrete onto a halo from the low-density IGM or along filaments of the cosmic web. The different gas densities will impact the temperature of the gas. As mentioned before, the gas needs to radiate away its energy to reach higher densities and thus to be able to enter a galaxy. Metal-line emission dominates the cooling function for metallicities $Z/Z_\odot \gtrsim 0.1$, which peaks at $T \approx 10^{5-5.5}$ K (Wiersma et al., 2009a). Gas at much higher temperatures will cool slowly. This gives rise to a bimodal temperature distribution for gas that accretes onto a massive halo (Kereš et al., 2005; Dekel & Birnboim, 2006).

Star formation in galaxies is fuelled by the accretion of gas from their haloes. Haloes replenish their gas reservoir by accreting from the IGM. When gas accretes onto a halo it can be shock-heated to the virial temperature of that halo and reach a quasi-static equilibrium supported by the pressure of the hot gas. We call this form of gas accretion 'hot-mode accretion' (Katz et al., 2003; Kereš et al., 2005). Because gas accreted onto high-mass haloes along filaments of the cosmic web or in clumps, or onto low-mass haloes, may not experience an accretion shock at the virial radius and will therefore remain cold until it accretes onto the central galaxy or is hit by an outflow, we refer to this mode of accretion as 'cold-mode accretion' (Katz et al., 2003; Kereš et al., 2005). Both modes can coexist. Especially at high redshift, cold streams penetrate the hot, virialized haloes of massive galaxies (Kereš et al., 2005; Dekel & Birnboim, 2006; Ocvirk

et al., 2008; Dekel et al., 2009a; Kereš et al., 2009a; van de Voort et al., 2011a; Powell et al., 2011).

After gas has become part of the multiphase ISM of a galaxy, stars can form out of it. Star formation in galaxies is observed to follow a close relation between the gas surface density and the star formation rate surface density (Kennicutt, 1998). The gas surface density can be related to the gas volume density and both are a function of the total thermal pressure (Schaye & Dalla Vecchia, 2008). The observed gas consumption time-scale, i.e. the gas mass divided by the star formation rate, is of the order of a Gyr.

In the absence of any feedback mechanism, gas accretion and star formation happen too efficiently and the amount of baryons in stars would greatly exceed the observed amount. Outflows are routinely detected in the form of blueshifted interstellar absorption lines in the spectra of star-forming galaxies (e.g. Steidel et al., 2010; Rubin et al., 2010; Rakic et al., 2011a), in X-ray emission and in hydrogen Balmer-α line emission (e.g. Lehnert et al., 1999; Cecil et al., 2001; Veilleux et al., 2005). Single supernova explosions can temporarily outshine their host galaxy. The material from the star that is expelled at high velocity, sweeps up material in front of it, thus evacuating a bubble of hot gas around the original star. When many supernovae occur in the same region, the bubbles can overlap and form superbubbles, which can lead to large-scale galactic outflows (e.g. Weaver et al., 1977; Mac Low & Ferrara, 1999).

Supermassive black holes are present in all massive galaxies (e.g. Kormendy & Richstone, 1995; Ferrarese & Merritt, 2000). Material accreting onto these black holes is thought to release some of its rest mass energy to power active galactic nuclei (AGN) (Salpeter, 1964). AGN are invoked as a mechanism powerful enough to quench star formation in the most massive galaxies by driving gas out at high velocities.

Stars produce heavy elements, which can be distributed in their surroundings by stellar winds and supernova explosions. These metals are ejected from the galaxy by galactic winds driven by supernovae or AGN and enrich the halo gas as well as part of the IGM (e.g. Wiersma et al., 2011). The enrichment enhances the cooling rate of the gas and previously ejected gas can be reaccreted by the same object or a different one (Oppenheimer et al., 2010). Because of large-scale outflows, the IGM, haloes, and galaxies are intimately connected and the cycle of baryons becomes complicated as outflows and inflows interact.

Even though there is plenty of observational evidence for galactic outflows, inflows are not commonly seen. It is, however, quite possible that the inflowing material has such small cross-sections that the signal is completely swamped by outflowing material (e.g. Faucher-Giguère & Kereš, 2011; Stewart et al., 2011a). Hot, hydrostatic halo gas is routinely studied using X-ray observations of galaxy groups and clusters and has perhaps even been detected around individual galaxies (e.g. Crain et al., 2010a,b; Anderson & Bregman, 2011). As of yet, there

is no direct evidence of cold-mode accretion, although there are some possible detections in emission (Rauch et al., 2011) and absorption (Ribaudo et al., 2011; Giavalisco et al., 2011).

Diffuse gas can be detected in absorption using a bright background source. UV and X-ray absorption line studies have revealed cold, neutral gas and the WHIM. Their interpretation is not easy, as there is only information along the line of sight and no information about the spatial extent of the absorbing cloud and often the location of the nearest galaxy is unknown. The neutral hydrogen column density distribution has been measured over ten orders of magnitude in $N_{\mathrm{H\,I}}$ (e.g. Tytler, 1987; Kim et al., 2002; Péroux et al., 2005; O'Meara et al., 2007; Prochaska & Wolfe, 2009; Noterdaeme et al., 2009; Prochaska et al., 2010). Low column density ($N_{\mathrm{H\,I}} < 10^{17.2}$ cm^2) material is known as the Lyman-α forest and originates mostly in the photo-ionized IGM (e.g. Bi et al., 1992; Cen et al., 1994; Hernquist et al., 1996; Theuns et al., 1998; Schaye, 2001a). Higher column density systems originate from gas in haloes and galaxies. By correlating the H I absorption in the spectra of background quasars with both the transverse and line of sight separations from foreground galaxies, Rakic et al. (2011b) have recently detected strong evidence for infall of cold gas on scales of $\sim 1.4 - 2.0$ proper Mpc at $z \approx 2.4$.

The gas emissivity in X-ray and UV scales with the square of the density. The signal is thus dominated by high-density regions. In this way, emission line studies complement the absorption line studies. They have the added advantage of providing a two-dimensional image, in addition to the third dimension provided by the redshift of the emission line, allowing us to study the three-dimensional spatial distribution. The interpretation of emitting gas would therefore be easier, but because the emission is very faint, detecting it is still a challenge.

How all processes occurring in galaxy formation interact is a field of active research. One can use numerical simulations as a tool to study this interplay and to predict the observational consequences.

1.2   Cosmological simulations

Because the time-scales involved in galaxy formation are generally very long compared to a human life time, numerical simulations are an excellent tool to study structure formation dynamically. Additionally it is possible to study a particular process by running two simulations, one with and one without it. The complex, non-linear behaviour of the density perturbations necessitates the use of supercomputers to perform the calculations. Numerical simulations have significantly improved our understanding of the large-scale structure in the Universe. Even though we know very little about the physical nature of dark matter and dark energy, the standard cosmological constant or vacuum-dominated cold dark matter (ΛCDM) model reproduces the observed large-scale structure and clustering of galaxies really well (Weinberg et al., 2004; Springel et al., 2005a).

Despite its many successes, this model is not sufficient to explain the properties of galaxies. Baryonic processes, that are not all well understood, are essential ingredients. Through feedback they can even impact the dark matter distribution, a process that one should take into account when doing precision cosmology (van Daalen et al., 2011; Semboloni et al., 2011).

Most cosmological simulations, i.e. simulations of structure formation in a representative part of the universe, use particles to discretize the mass, because of the superior spatial resolution to grid-based codes. The spatial resolution is automatically higher in denser regions, where galaxies form. Little time is spent on calculations in low density regions, where properties do not change rapidly anyway. Another advantage of particle-based simulations is that there is no preferred spatial direction and the resolution is increased continuously from low- to high-density regions. An advantage that is particularly important for this thesis is that we can trace the mass back in time to investigate its history.

The advantage of grid-based codes is that they are superior in resolving discontinuities, such as shocks. Turbulence and instabilities are also more easily resolved. An added advantage is that one can choose a different property than density as a refinement criterion and achieve high resolution in any region of interest.

The expansion of the universe is dealt with by using comoving coordinates. In physical space every volume element expands by an equal amount, set by the cosmological parameters. To deal with the thermodynamic property of baryons, smoothed particle hydrodynamics (SPH) can be used, in which some properties of particles, e.g. density and metallicity, are smoothed over space by a spline kernel function. Unfortunately, in SPH simulations shocks are not resolved as true discontinuities, but they are smeared out over a few smoothing lengths, leading to in-shock cooling (Hutchings & Thomas, 2000). This problem can be avoided by using a sufficiently high resolution (Creasey et al., 2011).

Although cosmological simulations can provide sufficiently accurate calculations for diffuse gas, once the gas reaches high densities, that are characteristic of the ISM, the multiphase medium cannot be resolved. The formation of individual stars from molecular clouds is not (yet) possible in cosmological simulations. The effect that stars have, through e.g. ionizing photons, metal production, stellar winds, and supernova explosions, has to be modelled with subgrid prescriptions. Subgrid models are also needed for radiative cooling, because it happens on the atomic level, and for accretion onto black holes, because the scale of the accretion disc is not resolved.

The goal of developing subgrid models is that, even though the small-scale physics is dealt with in an approximate, global sense, its effect is the same on scales that are resolved. Unfortunately it is not always clear what the large-scale effect should be and there is a lot of (unwanted) freedom in the subgrid modelling. The OverWhelmingly Large Simulations (Schaye et al., 2010, OWLS) project contains a suite of more than fifty cosmological, hydrodynamical sim-

ulations. There is a reference model and all other simulations are variations on this model, in the sense that only one parameter or one model was varied at a time. Even though there are certainly uncertainties associated with these simulations, their importance can be quantified by comparing simulations with different resolution and different subgrid physics. In this thesis we use a subset of the OWLS runs and will focus on the properties of gas accretion and their consequences, the effect of feedback, and the observational signature of diffuse gas outside galaxies.

1.3 This thesis

Numerical studies of the nature of gas accretion have revealed a bimodality, at least for massive haloes. The temperature of gas accretion onto haloes is either $\lesssim 10^5$ K or close to the virial temperature of the halo (Kereš et al., 2005; Dekel & Birnboim, 2006; Ocvirk et al., 2008; Dekel et al., 2009a; Kereš et al., 2009a; van de Voort et al., 2011a; Powell et al., 2011). Even though dividing accreting gas into two modes does not change the problem simulations have with reproducing observations, it can shed light on the physical mechanism behind it. In this thesis the following open questions will be addressed:

1. What are the properties of accreting gas? How do the properties of gas accretion onto haloes affect the accretion onto galaxies and subsequently the star formation rates of the galaxies?

2. What is the impact of realistic outflows on the inflowing gas? Is star formation quenched by ejecting gas from the ISM or by preventing it from accreting? Which processes set the global star formation rate?

3. Has cold-mode accretion already been observed as H I absorption systems? If so, in what kind of objects is it found? Is the cold-mode gas accreting for the first time or reaccreting?

4. Can we observe halo gas in emission in the near future? If so, which metal lines would be most promising and what do they tell us about the physical state of the gas?

A brief summary of the contents of this thesis is given below.

Chapter 2: Gas accretion onto galaxies and haloes
We found that gas accretion is mostly smooth, with mergers only becoming important for groups and clusters. Without supernova or AGN feedback the gas accretion rate onto haloes scales like the dark matter accretion rate. The same is not true for gas accretion onto galaxies, because the gas has to cool before it can enter the ISM of the galaxy. Including feedback from supernovae or AGN reduces the halo accretion rate by factors of a few and galaxy accretion rates by up to an order of magnitude, because outflowing gas prevents the inflowing

gas from accreting. Galactic winds increase the halo mass at which the central galaxies grow most efficiently by about two orders of magnitude to $M_{\text{halo}} \approx 10^{12} \, \text{M}_\odot$.

Gas accretion is bimodal, with maximum past temperatures either of the order of the virial temperature or $\lesssim 10^5$ K. We define cold-mode (hot-mode) accretion as gas that is accreted and whose temperature did not exceed (did exceed) $10^{5.5}$ K before it accreted onto a galaxy. The fraction of the gas accreted onto haloes in the hot mode is insensitive to feedback and metal-line cooling. It increases with decreasing redshift, but is mostly determined by the halo mass. In contrast, for accretion onto galaxies, the cold mode is always significant and the relative contributions of the two accretion modes are more sensitive to feedback and metal-line cooling. (This work has been completed and published, van de Voort et al. 2011a.)

Chapter 3: The drop in the cosmic SFR below redshift 2

Given that hot- and cold-mode accretion vary with redshift and halo mass, we determine their roles in shaping the global star formation rate density. Including feedback processes is essential to match observations of the global star formation rate density, because it reduces the star formation rate in low- and high-mass galaxies. The cosmic star formation rate is observed to drop sharply after $z = 2$. We find that the drop in the star formation rate follows a corresponding decline in the global cold-mode accretion rate density onto haloes, but with a delay of the order of the gas consumption time-scale in the interstellar medium.

In contrast to cold-mode accretion, which peaks at $z \approx 3$, the hot mode continues to increase to $z \approx 1$ and remains roughly constant thereafter. By $z = 0$, the hot mode strongly dominates the global accretion rate onto haloes, but most of the hot halo gas never accretes onto galaxies. AGN feedback plays a crucial role by preferentially preventing the gas that entered haloes in the hot mode from accreting onto their central galaxies. Consequently, in the absence of AGN feedback, gas accreted in the hot mode would become the dominant source of fuel for star formation and the drop-off in the cosmic star formation rate would be much less steep. (This work has been completed and published, van de Voort et al. 2011b.)

Chapter 4: Gas properties in and around haloes

We study the properties of gas inside and around galaxy haloes as a function of radius and halo mass. The properties of cold- and hot-mode gas are clearly distinguishable in the outer parts of massive haloes. The cold-mode gas is mostly confined to clumpy filaments that are in pressure equilibrium with the diffuse, hot-mode gas. Besides being colder and denser, cold-mode gas typically has a much lower metallicity and is much more likely to be infalling. However, the spread in the properties of the gas is large. Due to a strong cooling flow near the central galaxy, the properties of gas accreted through the cold and hot modes in

the inner halo are indistinguishable. Stronger feedback results in larger outflow velocities and pushes hot-mode gas to larger radii. The differences between cold- and hot-mode gas resemble those between inflowing and outflowing gas, although they are somewhat smaller. The gas properties evolve as expected from virial arguments, which can also account for the dependence of many gas properties on halo mass. (This work has been completed and submitted, van de Voort & Schaye 2012.)

Chapter 5: Cold flows as H I absorption systems

We use the OWLS reference simulation that has been post-processed with radiative transfer to study the contribution of cold flows to the observed $z = 3$ column density distribution of neutral hydrogen, which our simulation reproduces. We have found that nearly all of the H I absorption arises in gas that has remained colder than $10^{5.5}$ K, at least while it was extragalactic. In addition, the majority of the H I is rapidly falling towards a nearby galaxy, with non-negligible contributions from outflowing and static gas. Above a column density of $N_{\mathrm{H I}} = 10^{17}$ cm^{-2}, most of the absorbers reside inside haloes, but the interstellar medium only dominates for $N_{\mathrm{H I}} > 10^{21}$ cm^{-2}. Haloes with total mass below 10^{10} M$_\odot$ dominate the absorption for $10^{17} < N_{\mathrm{H I}} < 10^{21}$ cm^{-2}, but the average halo mass increases sharply for higher column densities.

Systems with $N_{\mathrm{H I}} > 10^{17}$ cm^{-2} are closely related to star formation: most of their H I either will become part of the interstellar medium before $z = 2$ or has been ejected from a galaxy at $z > 3$. Cold accretion flows are critical for the success of our simulation in reproducing the observed rate of incidence of damped Lyman-α and particularly that of Lyman limit systems. We therefore conclude that cold accretion flows exist and have already been detected in the form of high column density H I absorbers. (This work has been completed and is in press, van de Voort et al. 2012.)

Chapter 6: Metal-line emission from galaxy haloes

The gas outside of galaxies is diffuse and therefore faint. With current and upcoming instruments we may be able to detect the halo gas in emission, even if only in a statistical sense. We calculate the expected metal-line emission as a function of radius from the central galaxy and compare it to the capabilities of current and future facilities. We found that detecting metal-line emission in the UV from halo gas at high redshift will be a challenge for upcoming instruments. When stacking galaxies to reduce the noise, it is in principle possible to observe C III, C IV, O VI, Si III, and Si IV out to $10 - 20$ per cent of the virial radius in haloes larger than 10^{11} M$_\odot$. These lines are somewhat brighter in haloes at low redshift, but future UV missions should aim to achieve a flux limit of 10^{-19} ergs s^{-1}cm^2 arcsec^2. At low redshift, proposed X-ray telescopes can detect O VIII emission out to the virial radius of groups and clusters. C VI, N VII, and O VII can also be detected to smaller radii, $0.1 - 0.5$R$_{\mathrm{vir}}$. Actually observing this gas would enable us to confirm or revise what we have learned from simula-

tions. (This work is in an advanced stage of preparation and will be submitted soon.)

1.4   Outlook

Research will never truly be finished, because there will always be new questions that arise. Significant progress will be made in the near future in the study of galaxy formation, both observationally and theoretically. As observations improve, simulations will have to improve as well. Higher spatial resolution and time resolution will lead to improvements, especially when it goes hand in hand with the development of more advanced subgrid models.

Although we can quantify the uncertainties with the suite of simulations used for this thesis, many of the observed properties of galaxies are not reproduced by a single simulation. The Evolution and Assembly of GaLaxies and their Environments (EAGLE) project will be the largest SPH simulation down to $z = 0$ as of yet, with a resolution high enough to resolve the Jeans scale up to the star formation threshold and a volume large enough to contain a significant amount of massive haloes. The strategy is to tune the feedback parameters to match the observed stellar mass function and the stellar mass-halo mass relation. This will result in a large sample of relatively realistic, well-resolved massive galaxies and will therefore be well-suited for comparing to observations.

Radiative transfer is usually not taken into account in cosmological simulations. Instead, all the gas is assumed to be optically thin and is exposed to the same ionizing UV background radiation. In reality, inhomogeneous ionizing radiation from local sources and self-shielding of the gas can change the temperature and density of gas in haloes and in the IGM, so it should be included. Recent progress in radiative transfer modelling will make this feasible.

Numerical simulations help us investigate what is happening outside of galaxies, but we need to observe the material to confirm our ideas. Future instruments that have been designed for the detection of UV and X-ray emission will certainly aid our understanding. In particular, next year MUSE, an integral field spectrograph, will be installed on the VLT, which is expected to detect many sources, in emission and absorption (Bacon et al., 2010). Additionally, proposed X-ray missions would be ideal for detecting metal-line emission from the WHIM in the centres and outskirts of massive haloes and studying the gas properties (e.g. den Herder et al., 2011).

Lyman-α radiation is an important tool for observing the distant Universe, because it is much brighter than metal-line emission. Its interpretation is still a challenge, because the Lyman-α line is a resonant line and photons scatter many times before escaping, which strongly affects the line profile. Lyman-α radiative transfer simulations will allow us to disentangle radiative transfer effects from the kinematics of the gas in a statistically meaningful sample and help to interpret observations.

2

THE RATES AND MODES OF GAS ACCRETION ONTO GALAXIES AND THEIR GASEOUS HALOES

We study the rate at which gas accretes onto galaxies and haloes and investigate whether the accreted gas was shocked to high temperatures before reaching a galaxy. For this purpose we use a suite of large cosmological, hydrodynamical simulations from the OWLS project, which uses a modified version of the smoothed particle hydrodynamics code GADGET-3. We improve on previous work by considering a wider range of halo masses and redshifts, by distinguishing accretion onto haloes and galaxies, by including important feedback processes, and by comparing simulations with different physics.

Gas accretion is mostly smooth, with mergers only becoming important for groups and clusters. The specific rate of gas accretion onto haloes is, like that for dark matter, only weakly dependent on halo mass. For halo masses $M_{\mathrm{halo}} \gg 10^{11}$ M$_\odot$ it is relatively insensitive to feedback processes. In contrast, accretion rates onto galaxies are determined by radiative cooling and by outflows driven by supernovae and active galactic nuclei. Galactic winds increase the halo mass at which the central galaxies grow the fastest by about two orders of magnitude to $M_{\mathrm{halo}} \sim 10^{12}$ M$_\odot$.

Gas accretion is bimodal, with maximum past temperatures either of order the virial temperature or $\lesssim 10^5$ K. The fraction of gas accreted onto haloes in the hot mode is insensitive to feedback and metal-line cooling. It increases with decreasing redshift, but is mostly determined by halo mass, increasing gradually from less than 10% for $\sim 10^{11}$ M$_\odot$ to greater than 90% at $\sim 10^{13}$ M$_\odot$. In contrast, for accretion onto galaxies the cold mode is always significant and the relative contributions of the two accretion modes are more sensitive to feedback and metal-line cooling. On average, the majority of stars present in any mass halo at any redshift were formed from gas accreted in the cold mode, although the hot mode contributes typically over 10% for $M_{\mathrm{halo}} \gtrsim 10^{11}$ M$_\odot$.

Thus, while gas accretion onto haloes can be robustly predicted, the rate

of accretion onto galaxies is sensitive to uncertain feedback processes. Nevertheless, it is clear that galaxies, but not necessarily their gaseous haloes, are predominantly fed by gas that did not experience an accretion shock when it entered the host halo.

Freeke van de Voort, Joop Schaye, C. M. Booth,
Marcel R. Haas, and Claudio Dalla Vecchia

2.1   Introduction

In the standard cosmological constant or vacuum dominated cold dark matter (ΛCDM) model mass assembles hierarchically, with the smallest structures forming first. While the collapse of dark matter halts as it reaches virial equilibrium in haloes, baryons can radiate away their binding energy, allowing them to collapse further and fragment into smaller structures, such as stars and galaxies. These galaxies then grow through mergers and gas accretion.

After virialization, a gas cloud can be in one of three regimes. If the characteristic cooling time exceeds the Hubble time-scale, the gas will not be able to radiate away the thermal energy that supports it and will therefore not collapse. If, on the other hand, the cooling time is smaller than the Hubble time, but larger than the dynamical time-scale, then the cloud can adjust its density and temperature quasi-statically. It will increase both its density and temperature while maintaining hydrostatic equilibrium. Finally, if the cooling time is shorter than the dynamical time, the cloud will cool faster than it can collapse, lowering the Jeans mass and possibly leading to fragmentation. This is the regime in which galaxies are thought to form (Silk, 1977; Rees & Ostriker, 1977). In reality the situation must, however, be more complicated as the density, and thus the cooling and dynamical times, will vary with radius.

Gas falling towards a galaxy gains kinetic energy until it reaches the hydrostatic halo. If the infall velocity is supersonic, it will experience a shock and heat to the virial temperature of the halo. According to the simplest picture of spherical collapse, all gas in a dark matter halo is heated to the virial temperature of that halo, reaching a quasi-static equilibrium supported by the pressure of the hot gas. Gas can subsequently cool radiatively and settle into a rotationally supported disc, where it can form stars (e.g. Fall & Efstathiou, 1980). We call this form of gas accretion *'hot accretion'* (Katz et al., 2003; Kereš et al., 2005).

Within some radius, the so-called cooling radius, the cooling time of the gas will, however, be shorter than the age of the Universe. If the cooling radius lies well inside the halo, which is the case for high-mass haloes, a quasi-static, hot atmosphere will form. Accretion onto the galaxy is then regulated by the cooling function. If, on the other hand, this radius is larger than the virial radius, then there will be no hot halo and the gas will not go through an accretion shock at the virial radius. Because gas accreted in this manner may never have been heated to the virial temperature, we refer to this mode of accretion as *'cold accretion'* (Katz et al., 2003; Kereš et al., 2005). The rapid cooling of gas in low-mass haloes was already shown by Rees & Ostriker (1977) and White & Rees (1978). The accretion rate onto the central galaxy then depends on the infall rate, but not on the cooling rate (White & Frenk, 1991). Simulations confirmed the existence of gas inside haloes which was never heated to the virial temperature of the halo (Katz & Gunn, 1991; Kay et al., 2000; Fardal et al., 2001; Katz et al., 2003).

The cooling time t_{cool} is shorter at higher redshift, because the density, ρ, is higher and $t_{\text{cool}} \propto \rho^{-1}$. The Hubble time t_{H} is also shorter, but with a weaker

dependence, $t_H \propto \rho^{-1/2}$. Hence, the mode of gas accretion onto galaxies will depend on redshift, with cold accretion more prevalent at higher redshifts for a fixed virial temperature. The mode of gas accretion will also depend on halo mass. Higher-mass haloes have higher virial temperatures and thus, at least for $T \gtrsim 10^6$ K, longer cooling times. Hence, hot accretion will dominate for the most massive haloes. The dominant form of accretion will thus depend on both the mass of the halo and on the accretion redshift (Katz et al., 2003; Birnboim & Dekel, 2003; Kereš et al., 2005; Ocvirk et al., 2008; Kereš et al., 2009a; Brooks et al., 2009; Crain et al., 2010a).

Although both analytic and semi-analytic studies of galaxy formation usually assume spherical symmetry (e.g. Binney, 1977; White & Frenk, 1991; Birnboim & Dekel, 2003), numerical simulations show different geometries. As the matter in the Universe collapses, it forms a network of sheets and filaments, the so-called 'cosmic web'. Galaxies form in the densest regions, the most massive galaxies where filaments intersect. These structures can have an important effect on gas accretion. If a galaxy is being fed along filaments, the average density of the accreting gas will be higher. The cooling time will thus be smaller and it will be easier to radiate away the gravitational binding energy. Filaments may therefore feed galaxies preferentially through cold accretion. Both modes can coexist. Especially at high redshift, cold streams penetrate the hot virialized haloes of massive galaxies (Kereš et al., 2005; Dekel & Birnboim, 2006; Ocvirk et al., 2008; Kereš et al., 2009a; Dekel et al., 2009a).

Galaxy colours and morphologies are observed to be roughly bimodal. They can be divided into two main classes: blue, star forming spirals and red, passive ellipticals (e.g. Kauffmann et al., 2003; Baldry et al., 2004). The latter tend to be more massive and to reside in clusters. It has been suggested by Dekel & Birnboim (2006) that this observed bimodality is caused by the two different mechanisms for gas accretion. If, for example, feedback from active galactic nuclei (AGN) were to prevent the hot gas from cooling, massive galaxies with little cold accretion would have very low star formation rates. If, on the other hand, cold accretion flows were less susceptible to such feedback, then low-mass haloes could host discs of cold gas, which could form stars efficiently. However, this cannot be the whole story, because suppressing star formation from gas accreted in the hot mode is not nearly sufficient to reproduce the observations (Kereš et al., 2009b).

In this work we use a large number of cosmological, hydrodynamical simulations from the OverWhelmingly Large Simulations project (OWLS; Schaye et al., 2010) to investigate accretion rates, the separation of hot and cold modes, and their dependence on halo mass and redshift. Our work extends earlier work in several ways. By combining simulations with different box sizes, each of which uses at least as many particles as previous simulations, we are able to cover a large dynamic range in halo masses and a large range of redshifts. While earlier work used only a single physical model, our use of a range of models allows us to study the role of metal-line cooling, supernova (SN) feedback, and AGN

feedback. Some of these processes had been ignored by earlier studies. For example, Kereš et al. (2005, 2009a,b) ignored metal-line cooling and SN feedback. Using a semi-analytic model, Benson & Bower (2010) emphasized the importance of including the effect of feedback. Brooks et al. (2009) did not include metal-line cooling, but did include SN feedback. Ocvirk et al. (2008) included both metal-line cooling and weak SN feedback, but could only study the high-redshift behaviour as their simulation was stopped at $z \approx 1.5$. AGN feedback was not included by any previous study, although Khalatyan et al. (2008) did show the existence of cold accretion in a simulation of a single group of galaxies with AGN feedback. In contrast to previous work, we distinguish between accretion onto haloes and accretion onto galaxies (i.e. the interstellar medium, or ISM). We find that while hot mode accretion dominates the growth of high-mass haloes, cold mode accretion is still most important for the growth of the galaxies in these haloes. The different physical models give similar results for accretion onto haloes, implying that the results are insensitive to feedback processes, but the inclusion of such processes is important for accretion onto galaxies.

This paper is organized as follows. The simulations are described in Section 2.2, including all the model variations. In Section 2.3 we describe some properties of the gas in the temperature-density plane for our fiducial simulation. The ways in which haloes are identified and gas accretion is determined is discussed in Section 2.4. The accretion rates for all simulations can be found in Section 2.5, for accretion onto haloes as well as for accretion onto galaxies. In Section 2.6 we compare hot and cold accretion onto haloes for the different simulations and we do the same for accretion onto galaxies in Section 2.7. Finally, we compare our results with previous work in Section 2.8 and summarize our conclusions in Section 2.9.

2.2   Simulations

To investigate the temperature distribution of accreted gas, we use a modified version of GADGET-3 (last described in Springel, 2005b), a smoothed particle hydrodynamics (SPH) code that uses the entropy formulation of SPH (Springel & Hernquist, 2002), which conserves both energy and entropy where appropriate. This work is part of the OWLS (Schaye et al., 2010) project, which consists of a large number of cosmological simulations, with varying (subgrid) physics. We first summarize the subgrid prescriptions for the reference simulation. The other simulations are described in Section 2.2.1. As the simulations are fully described in Schaye et al. (2010), we will only summarize their main properties here.

The cosmological simulations described here assume a ΛCDM cosmology with parameters as determined from the Wilkinson microwave anisotropy probe year 3 (WMAP3) results, $\Omega_m = 1 - \Omega_\Lambda = 0.238$, $\Omega_b = 0.0418$, $h = 0.73$, $\sigma_8 = 0.74$, $n = 0.951$. These values are consistent[1] with the WMAP year 7

---

[1]The only significant discrepancy is in σ_8, which is 8% lower than the value favoured by the

Table 2.1: Simulation parameters: simulation identifier, comoving box size (L_{box}), number of dark matter particles (N, the number of baryonic particles is equal to the number of dark matter particles), mass of dark matter particles (m_{DM}), initial mass of gas particles (m_{gas}), final simulation redshift, number of resolved haloes (containing more than 250 dark matter particles) at $z = 2$ ($N_{halo}(z = 2)$), and number of resolved haloes (containing more than 250 dark matter particles) at $z = 0$ ($N_{halo}(z = 0)$).

simulation	L_{box} (h^{-1}Mpc)	N	m_{DM} ($M_\odot$)	m_{gas} ($M_\odot$)	z_{final}	$N_{halo}(z = 2)$	$N_{halo}(z = 0)$
L100N512	100	512^3	5.56×10^8	1.19×10^8	0	10913	18463
L100N256	100	256^3	4.45×10^9	9.84×10^9	0	838	2849
L050N512	50	512^3	6.95×10^7	1.48×10^7	0	12648	15884
L025N512	25	512^3	8.68×10^6	1.85×10^6	2	12768	-
L025N256	25	256^3	6.95×10^7	1.48×10^7	2	1653	-
L025N128	25	128^3	5.56×10^8	1.19×10^8	0	159	338

data (Komatsu et al., 2011).

A cubic volume with periodic boundary conditions is defined, within which the mass is distributed over N^3 dark matter and as many gas particles. The box size (i.e. the length of a side of the simulation volume) of the simulations used in this work is 25, 50, or 100 h^{-1}Mpc, with $N = 512$, unless stated otherwise. The (initial) particle masses for baryons and dark matter are $1.2 \times 10^8 (\frac{L_{\text{box}}}{100\ h^{-1}\text{Mpc}})^3 (\frac{N}{512})^{-3}$ M$_\odot$ and $5.6 \times 10^8 (\frac{L_{\text{box}}}{100\ h^{-1}\text{Mpc}})^3 (\frac{N}{512})^{-3}$ M$_\odot$, respectively, and are listed in Table 2.1, as are the number of resolved haloes at $z = 2$ and $z = 0$. We use the notation L***N###, where *** indicates the box size and ### the number of particles per dimension. The gravitational softening length is 7.8 $(\frac{L_{\text{box}}}{100\ h^{-1}\text{Mpc}})(\frac{N}{512})^{-1}$ h^{-1}kpc comoving, i.e. 1/25 of the mean dark matter particle separation, but we imposed a maximum of 2 $(\frac{L_{\text{box}}}{100\ h^{-1}\text{Mpc}})(\frac{N}{512})^{-1}$ h^{-1}kpc proper.

The primordial abundances are $X = 0.752$ and $Y = 0.248$, where X and Y are the mass fractions of hydrogen and helium, respectively. The abundances of eleven elements (hydrogen, helium, carbon, nitrogen, oxygen, neon, magnesium, silicon, sulphur, calcium, and iron) released by massive stars (type II SNe and stellar winds) and intermediate mass stars (type Ia SNe and asymptotic giant branch stars) are followed as described in Wiersma et al. (2009b). We assume the stellar initial mass function (IMF) of Chabrier (2003), ranging from 0.1 to 100 M$_\odot$. As described in Wiersma et al. (2009a), radiative cooling and heating are computed element-by-element in the presence of the cosmic microwave background radiation and the Haardt & Madau (2001) model for the UV/X-ray background from galaxies and quasars.

Star formation is modelled according to the recipe of Schaye & Dalla Vecchia (2008). The Jeans mass cannot be resolved in the cold ISM, which could lead to artificial fragmentation (e.g. Bate & Burkert, 1997). Therefore a polytropic equation of state $P_{\text{tot}} \propto \rho_{\text{gas}}^{4/3}$ is implemented for densities exceeding $n_{\text{H}} = 0.1$ cm^{-3}, where P_{tot} is the total pressure and ρ_{gas} the density of the gas. It keeps the Jeans mass fixed with respect to the gas density, as well as the ratio of the Jeans length and the SPH smoothing kernel. Gas particles with proper densities $n_{\text{H}} \geq 0.1$ cm^{-3} and temperatures $T \leq 10^5$ K are moved onto this equation of state and can be converted into star particles. The star formation rate (SFR) per unit mass depends on the gas pressure and is set to reproduce the observed Kennicutt-Schmidt law (Kennicutt, 1998).

Feedback from star formation is implemented using the prescription of Dalla Vecchia & Schaye (2008). About 40 percent of the energy released by type II SNe is injected locally in kinetic form. The rest of the energy is assumed to be lost radiatively. Each gas particle within the SPH smoothing kernel of the newly formed star particle has a probability of being kicked. For the reference model, the mass loading parameter $\eta = 2$, meaning that on average the total mass of the particles being kicked is twice the mass of the star particle formed. Because

---

WMAP 7-year data.

Table 2.2: Simulation parameters: simulation identifier, cooling including metals (Z cool), wind velocity (v_{wind}), wind mass loading (η), and AGN feedback included (AGN). Differences from the reference model are indicated in bold face. The last column gives the box size and particle number, from Table 2.1, used with these simulation parameters (L_{box} and N).

simulation	Z cool	v_{wind} (km/s)	η	AGN	L_{box} and N
REF	yes	600	2	no	all listed in Table 2.1
NOSN	yes	**0**	**0**	no	*L100N512* at $z = 2$
NOSN_NOZCOOL	**no**	**0**	**0**	no	*L100N512, L025N512*
NOZCOOL	**no**	600	2	no	*L100N512, L025N512*
WML4	yes	600	**4**	no	*L100N512, L025N512*
WML1V848	yes	**848**	**1**	no	*L100N512, L025N512*
DBLIMF-CONTSFV1618	yes	**600 & 1618**	2	no	*L100N512, L025N512*
WDENS	yes	**density dependent**		no	*L100N512, L025N512*
AGN	yes	600	2	**yes**	*L100N512, L025N512*

the winds sweep up surrounding material, the effective mass loading can be higher. The initial wind velocity is 600 km/s for the reference model, which is consistent with observations of starburst galaxies, both locally (Veilleux et al., 2005) and at high redshift (Shapley et al., 2003). Schaye et al. (2010) showed that these parameter values yield a peak, global star formation rate density that agrees with observations.

The simulation data is saved at discrete output redshifts with interval $\Delta z = 0.125$ at $0 \leq z \leq 0.5$, $\Delta z = 0.25$ at $0.5 < z \leq 4$, and $\Delta z = 0.5$ at $4 < z \leq 9$. This is the time resolution used for determining accretion rates.

2.2.1 Model variations

To see whether or not our results are sensitive to specific physical processes or subgrid prescriptions, we have performed a suite of simulations in which many of the simulation parameters are varied. These are listed in Table 2.2.

The importance of metal-line cooling can be demonstrated by comparing the reference simulation (*REF*) to a simulation in which primordial abundances are assumed when calculating the cooling rates (*NOZCOOL*). Similarly, the effect of including SN feedback can be studied by comparing a simulation without SN feedback (*NOSN*) to the reference model. Because the metals cannot be expelled without feedback, they pile up, causing efficient cooling and star formation. To limit the cooling rates, we performed a simulation in which both cooling by metals and feedback from SNe were ignored (*NOSN_NOZCOOL*). Simulation *NOSN_L025N512* was stopped just below $z = 4$ and the $z = 0.125$ snapshot is missing for *NOSN_L100N512*. We therefore cannot always show results for this simulation.

In massive haloes the pressure of the ISM is too high for winds with velocities of 600 km/s to blow the gas out of the galaxy (Dalla Vecchia & Schaye, 2008). Keeping the wind energy per unit stellar mass constant, we increased the wind velocity by $\sqrt{2}$ to $v_{\mathrm{wind}} = 848$ km/s, while halving the mass loading to $\eta = 1$ (*WML1V848*). To enable the winds to eject gas from haloes with even higher masses, the velocity and mass loading can be scaled with the local sound speed, while keeping the energy injected per unit stellar mass constant (*WDENS*).

To investigate the dependence on SN energy given to the ISM, we ran a simulation using almost all of the energy available from SNe. The wind mass loading $\eta = 4$, a factor of two higher than in the reference simulation. The wind velocity is the same, $v_{\mathrm{wind}} = 600$ km/s (*WML4*).

There is some evidence that the IMF is top-heavy in extreme environments, like starburst galaxies (e.g. Padoan et al., 1997; Klessen et al., 2007; Dabring-hausen et al., 2009). We have performed a simulation in which the IMF is top-heavy for stars formed at high pressures, $P_{\mathrm{tot}}/k_{\mathrm{B}} > 1.7 \times 10^5$ cm^{-3}K, where k_{B} is Boltzmann's constant, and therefore in high-mass haloes. The critical pressure was chosen such that $\sim$10% of the stars are formed with a top-heavy IMF. It results in more SNe per solar mass of stars formed and therefore stronger

winds. More energy is therefore put into the winds blown by these star particles, $v_{\mathrm{wind}} = 1618$ km/s and $\eta = 2$ (*DBLIMFCONTSFV1618*).

Finally, we have included AGN feedback (*AGN*). Black holes inject 1.5% of the rest-mass energy of the accreted gas into the surrounding matter in the form of heat. The model is described and tested in Booth & Schaye (2009), who also demonstrate that it reproduces the observed mass density in black holes and the observed scaling relations between black hole mass and both central stellar velocity dispersion and stellar mass. McCarthy et al. (2010) have shown that our model AGN reproduces the observed stellar mass fractions, SFRs, stellar age distributions and thermodynamic properties of galaxy groups.

2.2.2   Maximum past temperature

The Lagrangian nature of the simulation is exploited by tracing each fluid element back in time, which is particularly convenient for this project, in which we are studying the temperature history of accreted gas. During the simulations the maximum temperature, T_{max}, and the redshift at which it was reached, z_{max}, were stored in separate variables. The variables were updated for each SPH particle at every time step for which the temperature was higher than the previous maximum temperature. The artificial temperature the particles obtain when they are on the equation of state (i.e. when they are part of the unresolved multiphase ISM) was ignored in this process. This may cause us to underestimate the maximum past temperature of gas that experienced an accretion shock at higher densities. Ignoring such shocks is, however, consistent with our aims, as we are interested in the maximum temperature reached *before* the gas entered the galaxy.

Shock heating could be missed if the particle heats and cools rapidly in a single time step. In SPH simulations, a shock is smeared out over a few smoothing lengths, leading to in-shock cooling (Hutchings & Thomas, 2000). We find the average value for the infall velocity to be $\sim 5 \times 10^2 \left(\frac{M}{10^{13}\ M_\odot}\right)^{1/3} (1+z)^{1/2}$ km/s. On average the SPH smoothing length at halo accretion is $\sim 10^2$ kpc (comoving) for all *L100N512* simulations and at all redshifts. The particle will take $10^8 \left(\frac{M}{10^{13}\ M_\odot}\right)^{-1/3} (1+z)^{-3/2}$ years to traverse this distance. A shock will therefore take at least a few times 10^8 years. In reality the accretion shock will proceed almost instantaneously, minimizing radiative losses. In the simulations described here gas cools at each time step, so also while it is being shocked. The finite spatial resolution can thus result in lower maximum temperatures than the actual post-shock temperatures. If this effect were important, increasing the resolution would increase the hot fraction, i.e. the fraction of the gas that is accreted in the hot mode, because the accretion shocks would be less broadened. The opposite is the case, as we will show in Figure 2.9.

Even with infinite time resolution, the post-shock temperatures may, however, not be well defined. Electrons and protons will temporarily have different
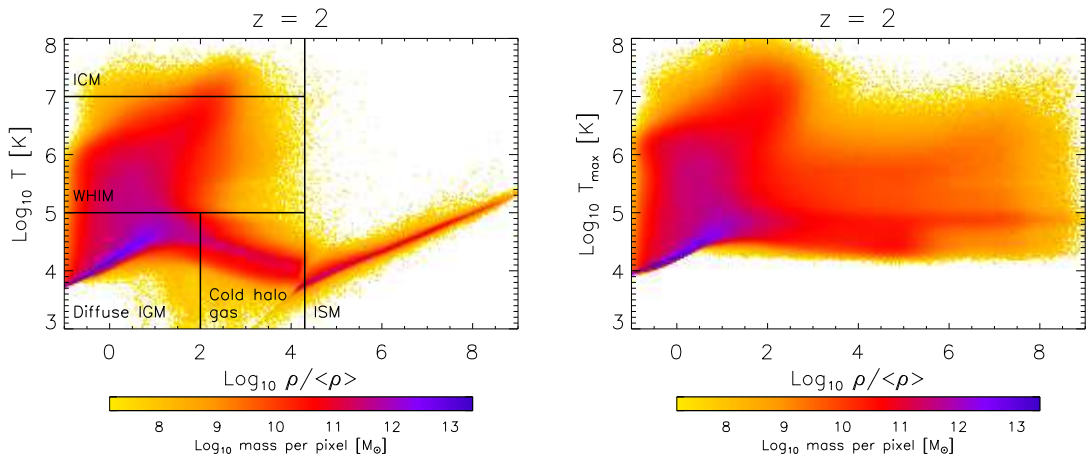
Figure 2.1: Current temperature (left) and maximum past temperature (right) against current overdensity for gas particles at $z = 2$ in the reference simulation in a 50 h^{-1}Mpc box. The logarithm of the total gas mass in a pixel is used for colour coding. The black lines separate the different phases of the gas. Gas with $T \gtrsim 10^5$ K has been shock heated. The $T - \rho$ relation for cold, low-density gas ($T \lesssim 10^5$ K and $\rho \lesssim 10\langle\rho\rangle$) is set by heating by the UV background and adiabatic cooling. At $\rho/\langle\rho\rangle > 10^{1.5}$ radiative cooling dominates over cooling by the expansion of the Universe. Gas with $n_{\rm H} > 0.1$ cm^{-3} ($\rho/\langle\rho\rangle > 10^{4.3}$ at $z = 2$) is assumed to be part of the unresolved, multiphase ISM and is put on an effective equation of state. The 'temperature' of this gas merely reflects the pressure of the multiphase ISM and is therefore not used to update $T_{\rm max}$. The scatter in the equation of state is caused by adiabatic cooling of inactive particles in between time steps. Gas that is condensing onto haloes or inside haloes has $T_{\rm max} \gtrsim 10^{4.5}$ K, which reflects the peak in the T-ρ relation (at $\rho/\langle\rho\rangle > 10^{1.5}$, $T \sim 10^{4.5}$ K) visible in the left panel.

temperatures in the post-shock gas, because they differ in mass, an effect that we have not included. It will take a short while before they equilibrate through collisions or plasma effects. Another effect, which is also not included in our simulations, is that shocks may be preceded by radiation from the shock, which may affect the temperature evolution.

2.3   The temperature-density distribution

The left-hand panel of Figure 2.1 shows the mass-weighted distribution of gas in the temperature-density plane at $z = 2$ for simulation *REF_L050N512*. Gas with densities up to $\sim 10^2$ times the cosmic average density represents the diffuse intergalactic medium (IGM). A significant fraction of this gas resides in filamentary structures. It can be heated to temperatures above 10^5 K when kinetic energy, generated by gravitational infall or galactic winds, is converted into thermal energy. We refer to this tenuous, shock-heated gas as the warm-hot intergalactic medium (WHIM). The intracluster medium (ICM) is the very hot $T \gtrsim 10^7$ K gas located in galaxy groups and clusters. Gas at overdensities $\rho/\langle\rho\rangle \gtrsim 10^2$, but much lower temperatures ($T \sim 10^4$ K) resides mostly in filaments and low-mass haloes.

   Most of the gas is located in the purple region, with $\rho/\langle\rho\rangle < 10$. The temperature of this gas is determined by the combination of photoheating by the UV background and adiabatic cooling by the expansion of the Universe. Although the slope of this temperature-density relation is close to adiabatic, it is actually determined by the temperature dependence of the recombination rate (Hui & Gnedin, 1997).

   The turnover density, above which the typical gas temperatures decrease, occurs when radiative cooling starts to dominate over adiabatic cooling. The overdensity at which this happens depends on redshift. At $z = 2$ it occurs at $\rho/\langle\rho\rangle \approx 10^{1.5}$. The distribution of the WHIM (broad red region, with $T > 10^5$ K) is set in part by the cooling function, to which especially heavier atoms, like oxygen, contribute. In particular, the lack of dense gas ($\rho/\langle\rho\rangle \gtrsim 10^3$) with 10^5 K $\lesssim T \lesssim 10^7$ K is due to radiative cooling.

   Gas with proper hydrogen number density $n_H > 0.1$ cm^{-3}, corresponding at this redshift to overdensity $\rho/\langle\rho\rangle > 10^{4.3}$, represents the ISM. This high-density gas is put on an equation of state if its temperature was below 10^5 K when it crossed the density threshold, because the cold and warm phases of this dense medium are not resolved by the simulations. Therefore, the temperature merely reflects the imposed effective pressure and the density should be interpreted as the mean density of the unresolved multi-phase ISM. The spread in the temperature-density relation on the equation of state is caused by the adiabatic extrapolation of inactive particles between time steps. In addition, the relation is broadened by differences in the mean molecular weight, μ, of the gas, which depends on the density, temperature and elemental abundances of the gas.

   The right-hand panel of Figure 2.1 shows the maximum past temperature

reached at $z \geq 2$, as a function of the $z = 2$ baryonic overdensity. All dense gas has reached temperatures of $\gtrsim 10^{4.5}$ K at some point. Dense ($\rho/\langle\rho\rangle > 10^{1.5}$) gas cannot have T_{max} much below $10^{4.5}$ K, because of photoheating[2]. The maximum past temperature tends to remain constant once the gas has reached densities $\gtrsim 10^2 \langle\rho\rangle$, resulting in the horizontal trend in the figure. There is no dense $\rho/\langle\rho\rangle \sim 10^4$ gas at the highest maximum temperatures (above 10^7 K), because the cooling time of gas that is heated to this temperature at lower densities ($\rho/\langle\rho\rangle \sim 10^{2-3}$) is longer than a Hubble time, preventing it from cooling and reaching higher densities.

The maximum past temperature reached for dense gas depends on whether the gas has been heated to the virial temperature of its halo and on whether it has been shock-heated by galactic winds.

2.4 Defining gas accretion

To see how haloes accrete gas, we first need to find and select the haloes. This can be done in several different ways and we will discuss three of them. Although we choose to use the one based on the gravitational binding energy, our results are insensitive to the halo definition we use. Finally, we link haloes in two subsequent snapshots in order to determine which gas has entered the haloes.

2.4.1 Identifying haloes and galaxies

The first step towards finding gravitationally bound structures is to identify dark matter haloes. These can for example be found using a Friends-of-Friends (FoF) algorithm. If the separation between two dark matter particles is less than 20% of the average separation (the linking length $b = 0.2$), they are placed in the same group. Because the particles all have the same mass, a fixed value of b will correspond to a fixed overdensity at the boundary of the group of $\rho/\langle\rho\rangle \approx 60$ (e.g. Frenk et al., 1988). Assuming a radial density profile $\rho(r) \propto r^{-2}$, corresponding to a flat rotation curve, such a group has an average overdensity of $\langle\rho_{halo}\rangle/\langle\rho\rangle \approx 180$ (e.g. Lacey & Cole, 1994), close to the value for a virialized object predicted by the top-hat spherical collapse model (e.g. Padmanabhan, 2002). The minimum number of dark matter particles in a FoF group is set to 25. Many of the smallest groups will not be gravitationally bound. Baryonic particles are placed in a group if their nearest dark matter neighbour is part of the group.

Problems arise because unbound particles can be attached to a group, physically distinct groups can be linked by a small (random) particle bridge, and because substructure within a FoF halo is not identified. We use SUBFIND (Springel et al., 2001; Dolag et al., 2009) on the FoF output to find the gravitationally bound particles and to identify subhaloes. The properties of gas that is being accreted are expected to depend on the properties of the parent (or main) halo in which

---

[2]Exceptions are gas that reached high densities before reionization, which happens at $z = 9$ in our simulations, and gas with very high metallicities.

the subhaloes are embedded. We therefore only look at accretion onto these main haloes and exclude gas accretion by satellites.

Another way of defining haloes is to use a spherical overdensity criterion. The radius R_{vir}, centred on the most bound particle of a FoF halo, is found within which the average density agrees with the prediction of the top-hat spherical collapse model in a ΛCDM cosmology (Bryan & Norman, 1998). All the particles within R_{vir} are then included in the halo.

We chose to use only main haloes identified by SUBFIND, but we have checked that our results do not change significantly when using FoF groups or spherical overdensities instead.

Except for Figures 2.2, 2.9, and 2.15, we include only main haloes containing more than 250 dark matter particles in our analysis of halo accretion. This corresponds to a minimum total halo mass of $M_{\mathrm{halo}} \approx 10^{11.2}$ M$_\odot$ in the 100 h^{-1}Mpc box, $10^{10.3}$ M$_\odot$ in the 50 h^{-1}Mpc box, and $10^{9.4}$ M$_\odot$ in the 25 h^{-1}Mpc box. For these limits our mass functions agree very well with the Sheth & Tormen (1999) fit.

For each resolved halo, we identify the ISM of the central galaxy with the star forming (i.e. $n_{\mathrm{H}} > 0.1$ cm^{-3}) gas particles in the main halo which are inside 15% of the virial radius (Sales et al., 2010). We use 15% of the virial radius to exclude small star forming substructures in the outer halo, which are not identified by SUBFIND. Gas accretion onto satellite galaxies is excluded.

Because the galaxy is much smaller than its parent halo, it is not as well resolved. When investigating accretion onto galaxies (as opposed to haloes), we therefore impose a 1000 dark matter particle limit, corresponding to a minimum total halo mass of $M_{\mathrm{halo}} \approx 10^{11.8}$ M$_\odot$ in the 100 h^{-1}Mpc box, $10^{10.9}$ M$_\odot$ in the 50 h^{-1}Mpc box, and $10^{10.0}$ M$_\odot$ in the 25 h^{-1}Mpc box. The exceptions are Figure 2.2 and 2.15, which show accretion rates and hot fractions down to 1 dex below this limit. See Section 2.5 for more discussion on convergence.

2.4.2 Selecting gas particles accreted onto haloes

We select gas particles accreted onto haloes as follows. For each halo at $z = z_2$ (which we will also refer to as 'the descendant') we identify its progenitor at the previous output redshift $z_1 > z_2$. We determine which halo contains most of the descendant's 25 most bound dark matter particles and refer to this halo as 'the progenitor'. If the fraction of the descendant's 25 most bound particles that was not in any halo at z_1 is greater than the fraction that was part of the progenitor, then we discard the halo from our analysis, which rarely happens above our resolution threshold. If two or more haloes contain the same number of those 25 particles, we select the one that contains the dark matter particle that is most bound to the descendant.

We identify those particles that are in the descendant, but not in its progenitor as having been accreted at $z_2 \leq z < z_1$. The accreted particles have to be gaseous at z_1, i.e. before they were accreted, but can be either gaseous or stellar at redshift

z_2. The accreted gas can have densities exceeding the star formation threshold, in which case it cannot obtain a higher maximum past temperature. Gas can be accreted multiple times.

To distinguish mergers from smooth accretion, we exclude accreted particles that reside in (sub)haloes above some maximum mass at redshift z_1. We would like to have a criterion that is not directly dependent on resolution, so that the same objects are included in runs with different particle numbers if the simulations are converged with respect to resolution. We therefore set this maximum allowed halo mass to 10% of the descendant's (main halo) mass. Thus, smooth accretion excludes mergers with a mass ratio greater than 1:10. We experimented with different thresholds and the results are insensitive to this choice.

2.4.3 Selecting gas particles accreted onto galaxies

We consider particles that are part of the ISM or stellar at z_2, and that were gaseous but not part of the ISM at z_1, to have been accreted onto a galaxy at $z_2 \leq z < z_1$. Gas can be accreted multiple times. Accretion onto the ISM and accretion onto a galaxy are the same in this study and these terms are used interchangeably.

In this way, accretion through galaxy mergers is automatically excluded, because the gas that is part of the ISM of another galaxy at z_1 is excluded. We can allow for mergers by identifying those particles that are in the galaxy at z_2, but were not in the progenitor galaxy at z_1.

2.5 Total gas accretion rates

For brevity, accretion between, for example, $z = 2.25$ and $z = 2$ will be referred to as accretion just before $z = 2$.

The average total gas accretion rate of a halo depends on its mass. Figure 2.2 shows the average specific accretion rates $\Omega_{\mathrm{m}} \dot{M}_{\mathrm{gas}} / \Omega_{\mathrm{b}} M_{\mathrm{halo}}$, where Ω_{m} and Ω_{b} are the matter and baryon density parameters, respectively, as a function of halo mass for $z = 2$ (top panel) and $z = 0$ (bottom panel) for haloes containing at least 100 dark matter particles for various simulations using the reference model. Thick curves show the specific accretion rates onto haloes. We have divided the gas accretion rate by the total halo mass and baryon fraction $\Omega_{\mathrm{b}} / \Omega_{\mathrm{m}}$, so that the normalization gives an estimate of the time it would take a halo to grow to its current mass with the current accretion rate.

The thin curves in Figure 2.2 show specific smooth accretion rates onto galaxies against halo mass. While the inverse of the specific halo accretion rate equals the time it takes to grow the halo at its current accretion rate, the same is not true for the specific galaxy accretion rate, because we divide by the halo mass rather than by the galaxy mass. This definition allows us, however, to directly compare the two accretion rates.
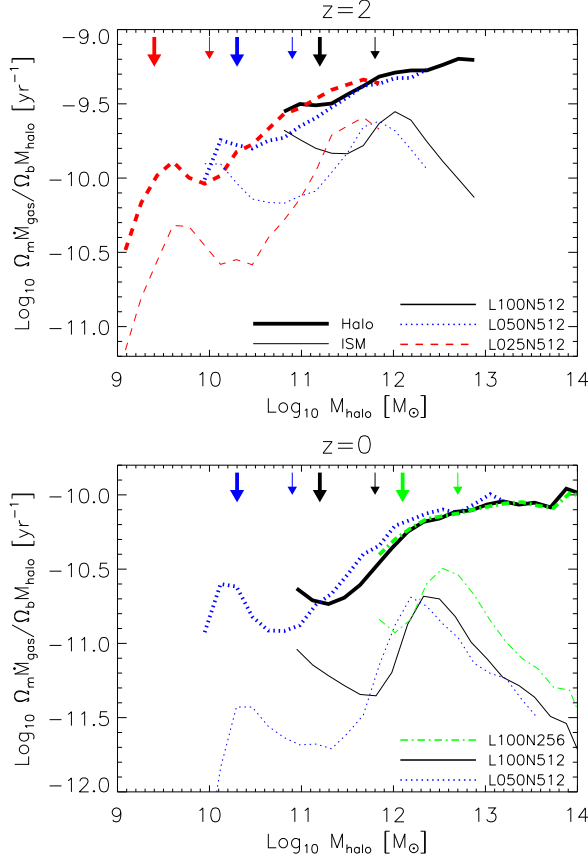
Figure 2.2: Specific gas smooth accretion rates onto *haloes* (higher, thick curves) and central *galaxies* (lower, thin curves) against total halo mass at $z = 2$ (top panel) and $z = 0$ (bottom panel). The normalization for halo accretion gives an estimate of the time it would take a halo to grow to its current mass at the current accretion rate. The same is not true for galaxy accretion, since we use the same normalization as for halo accretion. Both panels show simulations spanning a factor 64 in mass resolution. Each mass bin contains at least 10 haloes. Big (small) arrows correspond to the adopted resolution limit for accretion onto haloes (galaxies) for *L025N512* (red), *L050N512* (blue), *L100N512* (black) and *L100N256* (green). The specific halo accretion rate is converged and increases slightly with halo mass. The specific galaxy accretion rate is not fully converged at $z = 2$, but the convergence is better at $z = 0$. The galaxy accretion rate increases with halo mass for $M_{halo} < 10^{12}$ $M_{\odot}$ and decreases with halo mass for higher halo masses. It is much smaller than the halo accretion rate.

Comparing the three thick curves in each panel, we see that the specific halo accretion rate is converged with the numerical resolution. It increases with halo mass, especially at low halo masses. The specific galaxy accretion rate (thin curves) is not fully converged at $z = 2$, but the convergence improves at $z = 0$ (compare the two highest resolutions, dotted and solid curve, at the high mass end). Below $M_{halo} < 10^{12}$ M$_\odot$ the specific galaxy accretion rate increases more steeply with halo mass than the specific halo accretion rate. Above this halo mass, the specific galaxy accretion rate decreases steeply, whereas the rate keeps increasing for haloes. The accretion rate onto galaxies is always much lower than the halo accretion rate and this difference is larger at $z = 0$. Hence, only a small fraction of the gas accreted onto haloes ends up in galaxies and the efficiency of galaxy formation is highest in haloes with $M_{halo} \approx 10^{12}$ M$_\odot$.

The dynamic range covered by these simulations is very large, because we use different box sizes. The resolution increases with decreasing box size. We have performed box size convergence tests (at fixed resolution), but do not show them as the convergence with box size is excellent for all halo masses. Increasing the resolution shows that the halo accretion rates are not fully converged around the 100 particle resolution threshold adopted in Figure 2.2. In this regime, halo mergers cannot always be identified. In the rest of this paper, we therefore set the minimum halo mass for accretion onto haloes to correspond to 250 dark matter particles, as indicated by the big arrows.

The galaxy accretion rates diverge at the low-mass end. This is expected, because haloes with 100 dark matter particles will have very few star forming gas particles and because 15% of the virial radius is close to the spatial resolution limit. We will therefore only include the haloes where 15% of the virial radius is larger than 5 times the softening length and therefore consisting of at least 1000 dark matter particles, as indicated by the small arrows. The galaxy accretion rates at the high-mass end are not completely converged at $z = 2$. The accretion rate decreases by up to a factor of two if the mass resolution is increased by a factor of 64. With increasing resolution, more gas reaches higher densities. If this gas becomes star forming before accreting onto the central galaxy, it is not included in the smooth accretion rate. If we instead include galaxy mergers (not shown), which increases the accretion rate for high-mass galaxies slightly, then the results are in fact fully converged for the 50 and 25 h^{-1}Mpc box.

The bottom panel shows that the convergence is better at $z = 0$.

Although the results of these convergence tests are encouraging, we caution the reader that we cannot exclude the possibility that higher resolution simulations would show larger differences. For example, Dalla Vecchia & Schaye (2008) found that higher resolution is required to obtained converged predictions for the galactic winds. On the other hand, it is not clear the resolution requirements inferred by Dalla Vecchia & Schaye (2008) carry over to the present simulations, because they used idealized, isolated disc galaxies that started with thinner stellar disks than are formed in our simulations and their gas disks were initially embedded in a vacuum.
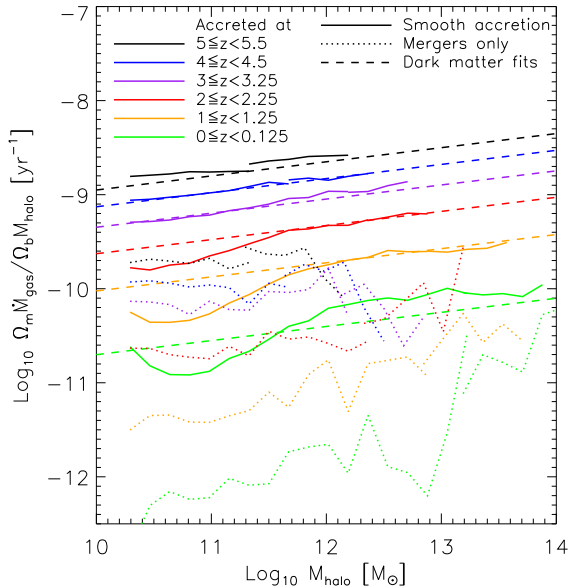
2.5.1 Accretion onto haloes

Figure 2.3: Specific gas accretion rates onto haloes for redshifts $z = 5$ (black, top curve) to $z = 0$ (green, bottom curve) against the total halo mass at the redshift of accretion for the simulation *REF_L050N512*. We added the highest mass bins from *REF_L100N512* to extend the dynamic range. The solid curves are for smooth accretion, whereas the dotted curves show the specific accretion rate due to mergers with mass ratios greater than 1:10. Each mass bin contains at least 10 haloes. Dashed lines show fits to dark matter accretion rates (Dekel et al., 2009b; Neistein et al., 2006). The specific smooth accretion rate decreases with redshift and increases only mildly with halo mass. Except for clusters ($M_{\mathrm{halo}} \geq 10^{14} M_{\odot}$) at $z = 0$, halo growth is dominated by smooth accretion.

Figure 2.3 shows the average specific gas accretion rate onto haloes as a function of halo mass for $z = 5$ (black, top curve) to $z = 0$ (green, bottom curve) for run *L050N512*. We also show the high-mass bins from *L100N512*, which are not sampled by *L050N512*, because of its smaller volume. The solid curves show the rates for smooth accretion, the dotted curves for mergers with mass ratios greater than 1:10. The specific smooth accretion rate decreases with decreasing redshift and increases slowly with halo mass. The accretion rate, as opposed to the *specific* accretion rate, is thus roughly proportional to the halo mass.

Our accretion rates are generally in quantitative agreement with other simulations (Ocvirk et al., 2008; Kereš et al., 2005). They also agree well with a fit to an analytic prediction for dark matter accretion rates based on the extended

Press-Schechter formalism given by Dekel et al. (2009b) and derived by Neistein et al. (2006). This fit is shown by the dashed lines. For low-mass haloes ($M_{\text{halo}} \leq 10^{12}$ M$_\odot$) at $0 \leq z \leq 2$ the accretion rate is lower than predicted. This suppression is due to SN winds, as we will discuss below. Without SN feedback, the gas accretion rates follow the dark matter accretion rates also for low-mass haloes at low redshift.

The specific gas accretion rate through mergers is much lower than the specific smooth accretion rate, except for high-mass haloes ($M_{\text{halo}} \gtrsim 10^{14}$ M$_\odot$) at $z = 0$. The dominance of smooth accretion is consistent with recent work on *dark matter* accretion, which has shown that mergers with mass ratios greater than 1:10 contribute less than 20-30% to the total halo accretion and at least 10-40% of the accretion is genuinely diffuse (Fakhouri & Ma, 2010; Angulo & White, 2010; Genel et al., 2010; Wang et al., 2011).

The power of the OWLS project lies in the fact that many simulations have been performed with different prescriptions for physical processes such as cooling and feedback. They have been described in Section 2.2. Figure 2.4 shows how the different physical processes affect the specific halo accretion rates at $z = 2$ (black curves) and at $z = 0$ (red curves). At $z = 2$, we include results from both the *L025N512* and *L100N512* versions of each model in order to extend the range of halo masses. These simulations have different box sizes and differ by a factor of 64 in mass resolution. For some models the run with lower resolution and larger box size, which is used for the high halo masses, is not fully converged, resulting in discontinuities. Only the *L100N512* simulations were run down to $z = 0$.

The first thing to notice is the fact that the halo smooth accretion rates are very similar for all models. For the simulations with strong winds (*DBLIMF-CONTSFV1618*) or AGN feedback (*AGN*) the rates are smaller than those for the reference model by up to 0.3-0.4 dex. The other models differ even less, except for the run without SN feedback (*NOSN_NOZCOOL*) which predicts 0.6 dex higher accretion rates at the lowest halo masses. The differences are similar at the two redshifts.

The left panel of Figure 2.4 shows the effect of excluding metal-line cooling and SN feedback. The simulations without SN feedback (*NOSN*, which is only available for *L100N512* at $z = 2$, and *NOSN_NOZCOOL*) have nearly completely flat specific accretion curves. As is the case for dark matter accretion rates, there is only a small increase with halo mass (see Figure 2.3). Including SN feedback with $v_{\text{wind}} = 600$ km/s (*REF* and *NOZCOOL*) reduces the accretion rates for low-mass haloes by up to 0.6 dex (at $M_{\text{halo}} = 10^{10}$ M$_\odot$). It is possible that the true accretion rates are the same, but some gas is pushed out of the halo before a snapshot is made and is therefore not counted as having accreted. A more likely possibility is, however, that galactic winds prevented the gas around low-mass haloes from accreting. Hence, more gas remains available for accretion onto massive galaxies which explains why those have somewhat higher accretion rates if SN feedback is included. Excluding metal-line cooling has no effect on
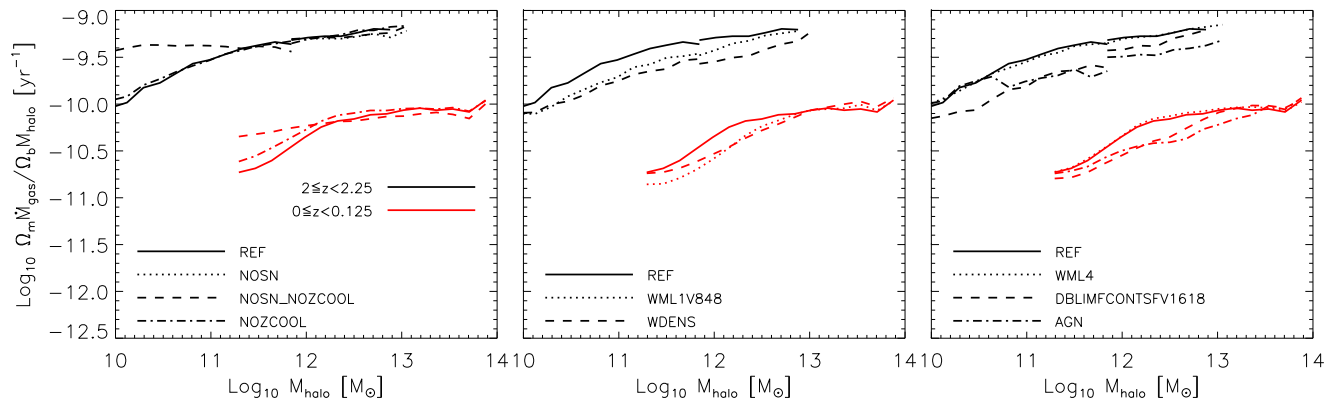
Figure 2.4: Specific gas smooth accretion rates onto *haloes* against total halo mass at $z = 2$ (top, black curves) and at $z = 0$ (bottom, red curves) for different simulations. The normalization gives an estimate of the time it would take a halo to grow to its current mass at the current accretion rate. The curves at low (high) halo masses are for simulations in a 25 (100) h^{-1}Mpc box using 2×512^3 particles. The solid curves use a simulation with the reference parameters (*REF*) and are repeated in all panels. The different simulations are described in Section 2.2.1. Each mass bin contains at least 10 haloes. Each halo contains at least 1000 dark matter particles for the $z = 2$ curves. This is higher than our resolution limit for accretion onto haloes, but it removes the overlap between simulations of different resolution. Each halo at $z = 0$ contains at least 250 dark matter particles. *Left panel:* Turning off feedback from SNe results in up to 0.6 dex higher accretion rates, for low-mass haloes. *Middle panel:* Increasing the wind velocity causes the specific accretion rate to decrease by up to 0.2 dex, over the mass range where the feedback is efficient. *Right panel:* Efficient feedback from a top-heavy IMF or from AGN even reduces the accretion rates for the highest halo masses, although the differences between these models are still small, at most 0.3 dex.
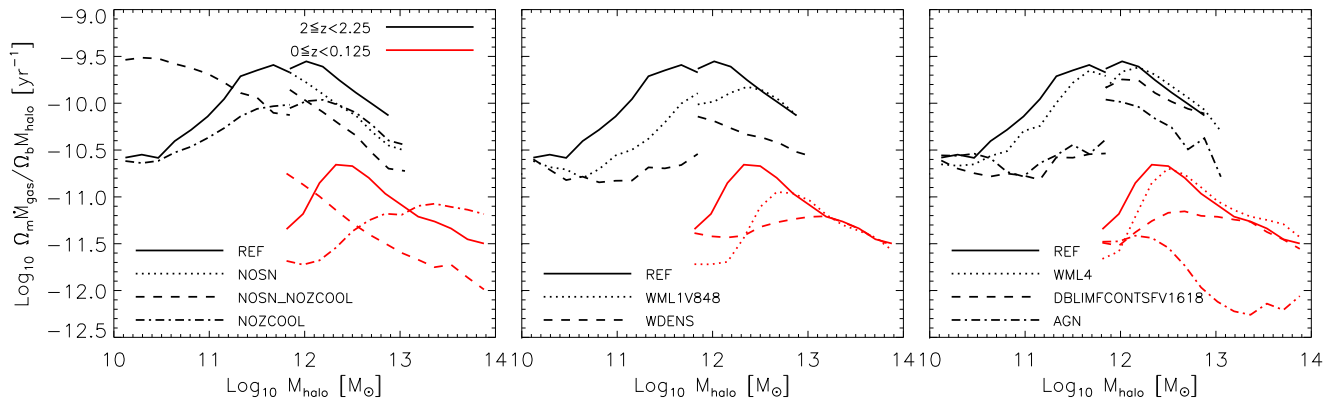
Figure 2.5: Specific gas smooth accretion rates onto *galaxies* against halo mass for different simulations. The curves at low (high) halo masses are derived from simulations in a 25 (100) h^{-1}Mpc box using 2×512^3 particles. The line styles, colours, and normalization are identical to those used in Figure 2.4. The normalization does *not* give an estimate for the time it would take the galaxy to grow, because we divide by the halo mass, not the galaxy mass. Each mass bin contains at least 10 haloes. In the absence of SN feedback the specific accretion rate onto galaxies declines with halo mass, indicating that gas accretes less efficiently onto galaxies in higher-mass haloes. Leaving out metal-line cooling decreases the accretion rate most strongly for $M_{\rm halo} \sim 10^{12}$ $M_\odot$. Efficient SN feedback reduces the accretion rates substantially for galaxies in low-mass haloes, resulting in a peak in the specific gas accretion rate at $M_{\rm halo} \sim 10^{12}$ $M_\odot$. The effects of feedback and metal-line cooling are much stronger for accretion onto galaxies than for accretion onto haloes and can result in differences of an order of magnitude.

the halo accretion rates. This indicates that halo accretion rates are not set by cooling.

SN feedback models with higher wind velocities, but using the same amount of energy per unit stellar mass, plotted in the middle panel of Figure 2.4, give lower accretion rates over the range of masses for which the winds are able to eject gas. Higher wind velocities keep the feedback efficient up to higher halo masses (Dalla Vecchia & Schaye, 2008; Schaye et al., 2010, Haas et al. in preparation).

The right panel shows the results for models that use more energy for feedback than the reference model. A top-heavy IMF in starbursts (*DBLIMFCON-TSFV1618*) reduces the accretion rates by up to 0.3 dex. AGN feedback (*AGN*) reduces the accretion rates by up to 0.4 dex for $M_{\mathrm{halo}} \gtrsim 10^{11}$ M$_\odot$.

In summary, metal-line cooling does not significantly change the halo accretion rates, but very efficient feedback from stars and/or AGN can suppress the accretion rates by factors of a few.

2.5.2 Accretion onto galaxies

The three lower, thin curves in the top and bottom panels of Figure 2.2 show specific smooth accretion rates onto galaxies (i.e. the ISM) against total halo mass at $z = 2$ and 0, respectively. The specific accretion rate peaks at $M_{\mathrm{halo}} \approx 10^{12}$ M$_\odot$. At $z = 0$ the peak occurs at slightly higher halo masses. For both redshifts the peak falls at $T_{\mathrm{vir}} \sim 10^6$ K, close to the bump in the cooling curve due to iron (Wiersma et al., 2009a). At higher halo masses, and thus higher virial temperatures, cooling times become long, preventing shocked gas from condensing onto galaxies. At lower halo masses, feedback prevents gas from entering the ISM. For $M_{\mathrm{halo}} \approx 10^{12}$ M$_\odot$ the galaxy accretion rate is about a factor of two lower than the halo accretion rate, but the difference is much larger for other halo masses.

Figure 2.5 shows the same as Figure 2.4, but for accretion onto galaxies. For models *WDENS*, *DBLIMFCONTSFV1618*, and *AGN* the convergence is poor for the low-resolution runs, as can be seen from the discontinuities. Because the feedback in these models depends on the gas density, they are sensitive to the resolution (Schaye et al., 2010). Note, however, that the difference in mass resolution is enormous, a factor of 64, and that the high-resolution model may thus be much closer to convergence than the comparison suggests. Nevertheless, we caution the reader that the accretion rates may be different for higher resolution simulations.

The variations in the feedback prescriptions result in similar differences as for accretion onto haloes, although they are generally much larger. Excluding metal-line cooling gives slightly different results than halo accretion.

For $M_{\mathrm{halo}} \lesssim 10^{13}$ M$_\odot$ less gas reaches the star formation threshold (i.e. accretes onto galaxies) without metal-line cooling (*NOZCOOL*), particularly for $M_{\mathrm{halo}} \sim 10^{12}$ M$_\odot$ at $z = 2$ and $M_{\mathrm{halo}} \sim 10^{12.4}$ M$_\odot$ at $z = 0$. The reduction is less
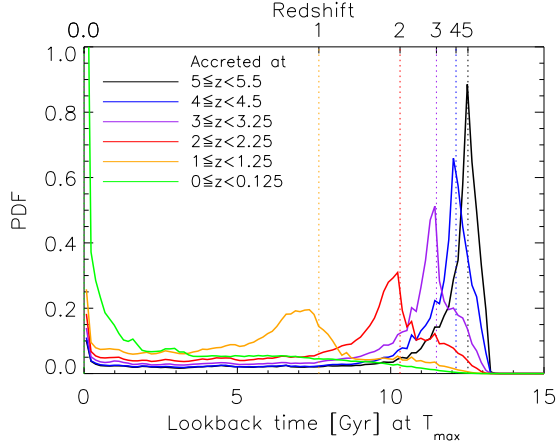
Figure 2.6: PDF of the lookback time at which the maximum past temperature (evaluated at $z = 0$) was reached for gas accreted just before $z = 5, 4, 3, 2, 1$, and 0 in black, blue, purple, red, orange, and green, respectively, combining *REF_L050N512* and *REF_L100N512*. The top *x*-axis indicates the corresponding redshift. The maximum temperature reached by a gas particle is associated with the accretion event, as evidenced by the fact that the PDFs peak at the accretion redshift.

than 0.4 dex at $z = 2$, but a full order of magnitude at $z = 0$. For $M_{halo} \gtrsim 10^{13}$ M$_\odot$ more gas accretes onto galaxies at $z = 0$ if metal-line cooling is excluded. Because there is less cooling, less gas accretes onto low-mass galaxies and at high redshift. Therefore, there is more gas left to accrete onto high mass galaxies at low redshift.

For simulations without SN feedback the specific galaxy accretion rate peaks at $M_{halo} \sim 10^{10}$ M$_\odot$, which is two orders of magnitude lower than when SN feedback is included. Without SN feedback, the galaxy accretion rates are a bit *lower* for high halo masses. This could be because much of the gas that accreted onto a halo at higher redshift has in that case already been accreted onto the galaxy's progenitors. Alternatively, the galaxy accretion rates could be higher in the presence of SN feedback due to the increased importance of recycling. If winds are able to blow gas out of the galaxy, but not out of the halo, as may be the case for high-mass haloes, then the same gas elements may be accreted onto the galaxy more than once (Oppenheimer et al., 2010). For $M_{halo} \lesssim 10^{11}$ M$_\odot$ at $z = 2$ and $M_{halo} \lesssim 10^{12}$ M$_\odot$ at $z = 0$, on the other hand, the accretion rates are higher, because more gas accretes onto the halo and because there is no feedback to stop halo gas from accreting onto the galaxy.

Galaxy accretion rates are thus much more sensitive to metal-line cooling and to SN and AGN feedback than halo accretion rates. The difference between models can be as large as 1 dex. Feedback processes determine the halo mass for which galaxy formation is most efficient.

2.6   Hot and cold accretion onto haloes

Figure 2.6 demonstrates that most of the gas reaches its maximum temperature around the time it is accreted onto a halo. Here the probability density function (PDF) of the lookback time at which the gas reaches its maximum temperature, evaluated at $z = 0$, is shown for baryonic particles that were accreted as gas particles onto haloes at different redshifts. The vertical dotted lines show the times at which the gas was accreted onto a halo. The fact that the PDFs peak around the accretion redshifts shows that the maximum temperature is usually related to the accretion event.

Some of the gas reaches its maximum temperature significantly later than the redshift at which it was accreted. When two galaxies merge, gas can shock to higher temperatures. Gas can also be affected by winds resulting from SN feedback. Because we are primarily interested in gas accretion, we will from now on evaluate the maximum past temperature of the gas at the first available output redshift after accretion.

Gas can be accreted cold onto haloes with well developed virial shocks if its density is sufficiently high, as can for example be the case in filaments. To illustrate this we show in the left two columns of Figure 2.7 the gas overdensity and the temperature in a cubic region of $1\ h^{-1}$ Mpc (comoving) centred on three example haloes at $z = 2$ taken from the full sample of 12768 haloes in the high-resolution reference simulation (*REF_L025N512*). The haloes have total masses $M_{\mathrm{halo}} \approx 10^{12.5}$, 10^{12}, and $10^{11.5}$ M$_\odot$ (from top to bottom), corresponding to comoving virial radii of 379, 264, and 170 h^{-1}kpc, respectively, shown as white circles in the temperature plots. Their virial temperatures are $T_{\mathrm{vir}} \approx 10^{6.3}$, $10^{6.0}$, and $10^{5.7}$ K, respectively. The colour scales are the same for all three haloes. We can immediately see that the average temperature increases with halo mass. Hot gas, heated either by accretion shocks or SN feedback, extends to several virial radii. Without SN feedback, the hot gas would trace the virial radius more accurately for the two lowest mass haloes, as can be seen for the 10^{12} M$_\odot$ halo in Figure 2.13.

Most of the gas around the $10^{12.5}$ M$_\odot$ halo has been heated to temperatures above 10^6 K and the halo will get most of its gas through hot accretion. Cold streams do penetrate the virial radius, but they seem to break up as they get close to the centre. Even so, a number of small, dense clumps do survive and remain relatively cold. Such cold clumps originating from filamentary gas were also studied by Sommer-Larsen (2006) and Kereš & Hernquist (2009).

The 10^{12} M$_\odot$ halo is located at the intersection of three filaments. The gas in the filaments is denser and colder than in the surrounding medium. The cold streams become narrower as they get closer to the centre. They are compressed by the high pressure, shock-heated gas around them (Kereš et al., 2009a). Cold streams bring gas directly and efficiently to the inner halo.

The $10^{11.5}$ M$_\odot$ halo is embedded in a single filament. It has the lowest virial temperature, so the hot gas is much colder than in the highest mass halo. Cold
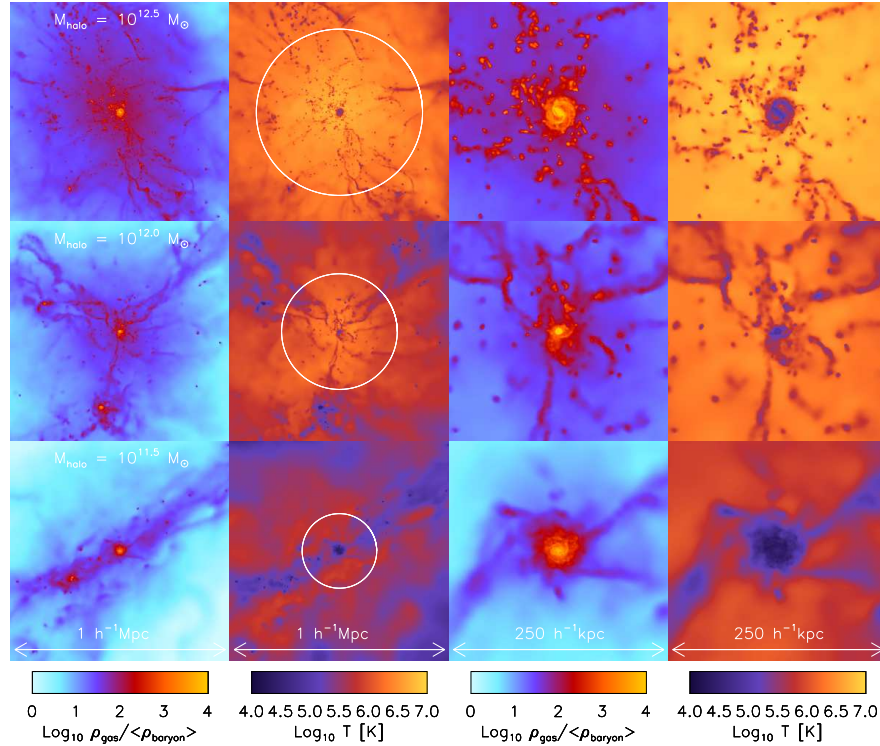
Figure 2.7: Gas overdensity (first and third columns) and temperature (second and fourth columns) in a cubic region of 1 h^{-1} comoving Mpc (first and second columns) and 250 h^{-1} comoving kpc (third and fourth columns) centred on haloes of $M_{\mathrm{halo}} \approx 10^{12.5}$, 10^{12}, and $10^{11.5}$ M$_\odot$ (from top to bottom) at $z = 2$ for simulation *REF_L025N512*. The white circles indicate the virial radii of the haloes, as computed using the overdensity criterion from Bryan & Norman (1998). Cold, dense streams bring gas to the centre. The temperature of the hot gas increases with halo mass. Hot accretion dominates for high-mass haloes, cold accretion for low-mass haloes. The galaxies in the centres of these haloes are discs, surrounded by cold gas. This cold gas is in clumps ($M_{\mathrm{halo}} \approx 10^{12.5}$), disrupted streams ($M_{\mathrm{halo}} \approx 10^{12}$), or smooth streams ($M_{\mathrm{halo}} \approx 10^{11.5}$).

streams are most prominent and broadest in this halo. This halo will get most of its gas through cold accretion.

The right two columns of Figure 2.7 shows zooms of the central 250 h^{-1} kpc (comoving). The $10^{12.5}$ $M_\odot$ halo contains a large number of cold clumps. The galaxies in the 10^{12} and $10^{11.5}$ $M_\odot$ haloes are being fed by cold, dense streams. All of these galaxies have formed discs. The galaxy in the $10^{12.5}$ $M_\odot$ halo has clear spiral arms and a bar-like structure. The galaxy in the 10^{12} $M_\odot$ halo has a very small disc with cold gas around it, which looks more disturbed. The galaxy in the $10^{11.5}$ $M_\odot$ halo is fairly large with a lot of cold material accreting onto it.

The maximum temperature reached by shock-heated gas is expected to scale with the virial temperature of the halo. However, we do not expect the ratio of T_{max} and T_{vir} to be exactly unity, because of departures from spherical symmetry, adiabatic compression after virialization, and the factor of a few difference between different definitions of T_{vir}.

Dividing T_{max} by T_{vir} would take out the redshift and halo mass dependence of the virial temperature. We calculate the virial temperature as follows

$$T_{\mathrm{vir}} = \left(\frac{G^2 H_0^2 \Omega_{\mathrm{m}} 18\pi^2}{54} \right)^{1/3} \frac{\mu m_{\mathrm{H}}}{k_B} M_{\mathrm{halo}}^{2/3} (1+z),$$

$$\approx 3.0 \times 10^5 \text{ K } \left(\frac{\mu}{0.59} \right) \left(\frac{M_{\mathrm{halo}}}{10^{12} \text{ M}_\odot} \right)^{2/3} (1+z), \qquad (2.1)$$

where G is the gravitational constant, H_0 the Hubble constant, μ the mean molecular weight, m_{H} the mass of a hydrogen atom, and k_{B} Boltzmann's constant[3].

2.6.1 Dependence on halo mass

Figure 2.8 illustrates the dependence of the maximum past temperature on halo mass. Shown are scatter plots of the maximum past temperature reached by gas accreting onto haloes just before $z = 2$ (top panel) and $z = 0$ (bottom panel) against the mass of the halo at these redshifts. The logarithm of the accreted gas mass per $(h^{-1}\mathrm{Mpc})^3$ in a pixel is used for colour coding. The virial temperature is indicated by the black line.

A clear bimodality is visible for accretion at $z = 2$, with a minimum at $T_{\mathrm{max}} \approx 10^{5.5}$ K, indicated by the dotted line. This minimum coincides with a maximum at $T \approx 10^{5-5.5}$ K in the cooling function (e.g. Wiersma et al., 2009a). For gas accreted in the hot mode, which includes most of the gas accreting onto high-mass haloes, the maximum past temperature is within a factor ≈ 3 of the virial temperature and displays the same dependence on mass. The temperature of the gas accreted in the cold mode is independent of halo mass.

At $z = 0$, the lowest T_{max} values are higher than at $z = 2$. This shift occurs because the density, and hence the cooling rate, increases with redshift. At fixed

---

[3]This definition is a factor 2/3 lower than the virial temperature used by some other authors (e.g. Barkana & Loeb, 2001).
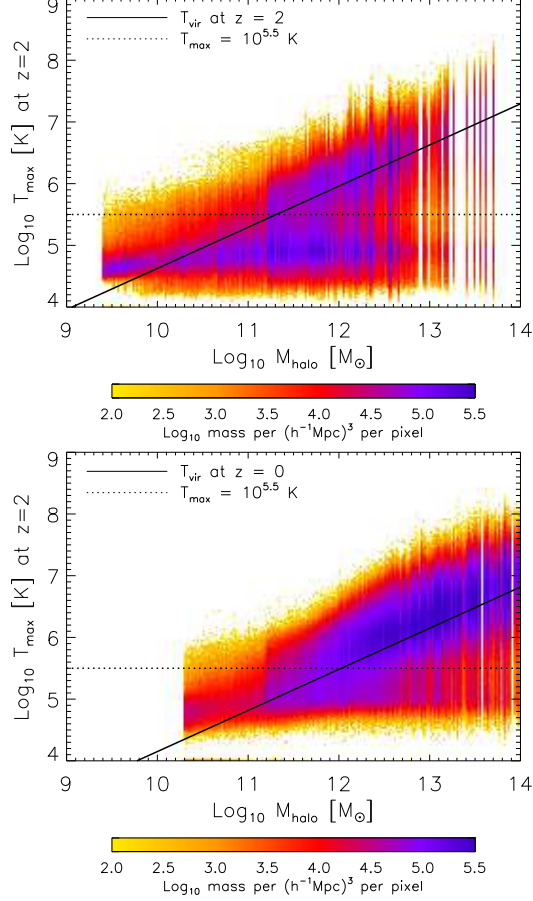
Figure 2.8: Maximum past temperature at $z = 2$ (top panel) and $z = 0$ (bottom panel) against total halo mass of the gas smoothly accreted onto haloes for models *REF_L025N512* and *REF_L100N512* (top panel) and *REF_L050N512* and *REF_L100N512* (bottom panel). The logarithm of the total gas mass per $(h^{-1}\mathrm{Mpc})^3$ in a pixel is used for colour coding. The solid line indicates the virial temperature of the halo. The dotted line shows $T_{\max} = 10^{5.5}$ K, where there is a minimum in the mass per pixel at $z = 2$. The temperature of gas that is accreted hot scales with the virial temperature. For low-mass haloes, the temperatures of hot and cold accreted gas are comparable. Hot mode accretion is more important for higher halo masses and lower redshifts.

halo mass, the highest T_{max} values are lower at $z = 0$, because the virial temperature of a halo at fixed mass decreases with decreasing redshift, as can be seen from Equation 2.1. For haloes with virial temperatures $T_{vir} \lesssim 10^5$ K it becomes impossible to tell from this plot whether or not the gas has gone through a virial shock because the virial temperature is similar to the maximum past temperature reached by gas accreting in the cold mode. This makes it difficult to separate hot and cold accretion for low-mass haloes at low redshift. As we will show below, separating hot and cold accretion using a fixed value of T_{max}/T_{vir} is more difficult than using a fixed value of T_{max}, because the minimum in the distribution is less pronounced and because it evolves (Kereš et al., 2005). In most of this paper, we will therefore use a fixed maximum temperature threshold of $T_{max} = 10^{5.5}$ K.

The relative importance of hot accretion increases with halo mass (e.g. Ocvirk et al., 2008). The top panel of Figure 2.9 shows the fraction of gas smoothly accreting onto haloes in the hot mode, just before $z = 2$ for simulations *REF_L100-N512*, *REF_L050N512*, and *REF_L025N512*. The bottom panel shows this for accretion just before $z = 0$ for simulations *REF_L100N256*, *REF_L100N512*, and *REF_L050N512*. A particle accreted just before $z = 2$ is considered to have been accreted hot if $T_{max}(z = 2) \geq 10^{5.5}$ K. The error bars show the 1σ halo to halo scatter.

We have checked, but do not show, that the results are fully converged with box size for fixed resolution. In each panel the three simulations span a factor 64 in mass resolution. The hot fraction decreases slightly with increasing resolution, but the differences are very small. This slight decrease could arise because higher density regions inside clumps and filaments are better sampled with increasing resolution, leading to higher cooling rates in cold gas.

Hot mode accretion becomes indeed more important for higher mass systems. This is expected because only sufficiently massive haloes are capable of providing pressure support for a stable virial shock (e.g. Birnboim & Dekel, 2003). The median hot fraction (not shown) behaves similarly to the mean, although it is smaller for low-mass haloes.

There is no sharp transition from cold to hot accretion. At $z = 2$, the hot mode accretion increases from 20% to 80% when halo mass increases from 10^{11} to 10^{13} $M_\odot$. The properties of galaxies are therefore not expected to change suddenly at a particular halo mass as has been assumed in some semi-analytic models (e.g. Cattaneo et al., 2008; Croton & Farrar, 2008).

In Figure 2.10 we compare this result to that obtained when we define hot mode accretion using a maximum temperature threshold that depends on the virial temperature. Using $T_{max} = T_{vir}$ shows that, even for the most massive haloes, only about 40% of the gas reaches a temperature higher than T_{vir} at $z = 2$. At $z = 0$ about 70% of the gas accreting onto massive haloes reaches T_{vir}. Because gas going through a virial shock may only heat to a factor of a few below T_{vir}, this definition does not discriminate well between hot and cold accretion. If we decrease the critical T_{max}/T_{vir}, then the hot fraction gets close to
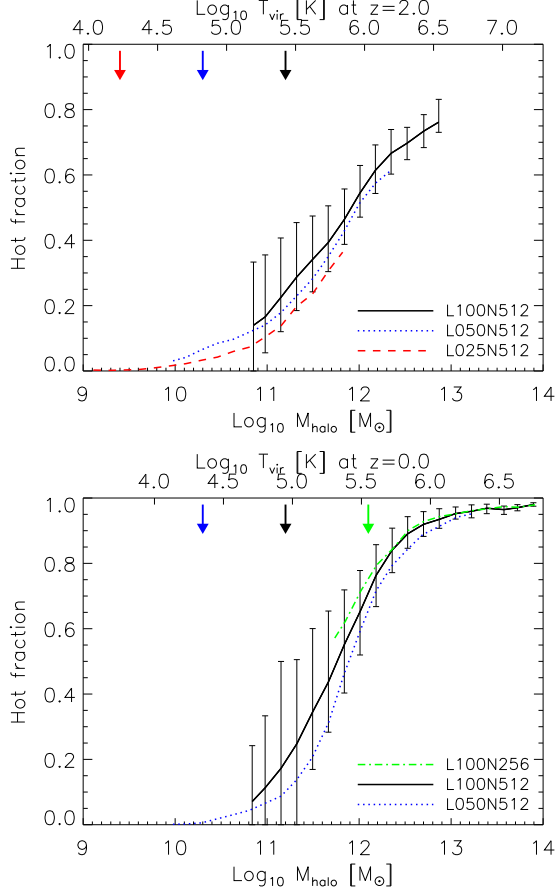
Figure 2.9: Average fraction of the gas, smoothly accreted onto haloes between $z = 2.25$ and $z = 2$ (top panel) or between $z = 0.125$ and $z = 0$ (bottom panel), that has maximum past temperature $T_{max} \geq 10^{5.5}$ K. The different curves are from simulations of the same reference model but spanning a factor of 64 in mass resolution for each panel. The error bars show the 1σ halo to halo scatter for simulation *REF_L100N512*. Each mass bin contains at least 10 haloes. Arrows correspond to the adopted resolution limit for accretion onto haloes. Cold mode accretion dominates for $M_{halo} < 10^{12}$ $M_\odot$, but the transition is very gradual.
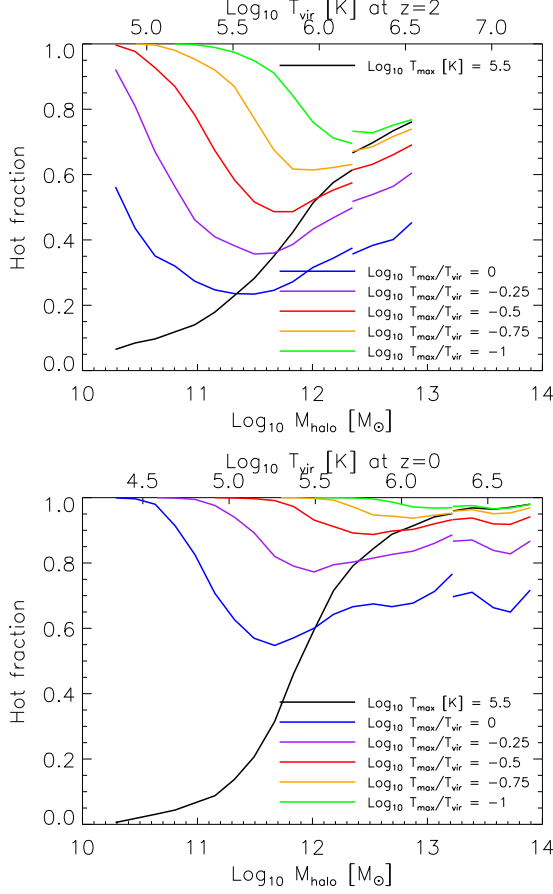
Figure 2.10: The average fraction of the gas, accreted onto haloes just before $z = 2$ (top panel) or $z = 0$ (bottom panel), that has maximum past temperature above a certain temperature threshold. The results are for simulation *REF_L050N512* with the highest mass haloes from *REF_L100N512*. The thresholds for the blue, purple, red, orange, and green curves (bottom to top) are $T_{max}/T_{vir} = 1$, $10^{-0.25}$, $10^{-0.5}$, $10^{-0.75}$, and 0.1, respectively. The black curve shows the average fraction with $T_{max} \geq 10^{5.5}$ K and is identical to the black curve in Figure 2.9. Each mass bin contains at least 10 haloes. The hot fraction depends strongly on the choice we make for the threshold, particularly for lower-mass haloes.

our previously determined value for the high-mass haloes. For low-mass haloes, however, this results in a sharp upturn of f_{hot} as it must approach unity if the threshold maximum temperature falls much below 10^5 K.

The hot fraction therefore depends very much on the definition of the temperature threshold. Depending on the definition, gas accreted cold may in fact have experienced a virial shock. For haloes with $T_{vir} \gg 10^5$ K, however, we can safely separate hot and cold accretion and trust the result that a larger fraction of the gas goes through a virial shock for higher-mass haloes.

In the rest of this paper, we will define hot mode accretion using a fixed maximum past temperature threshold of $T_{max} = 10^{5.5}$ K.

2.6.2 Smooth accretion versus mergers

So far we have only looked at 'smooth' accretion, i.e. we excluded mergers with a mass ratio greater than 1:10. We could have chosen not to exclude mergers, because the gas reservoir of a halo can also grow through mergers. Even though mergers with ratios greater than 1:10 contribute only $\sim 10\%$ of the total gas accretion for $M_{halo} < 10^{14}$ M$_\odot$ (see Figure 2.3), it is interesting to investigate the differences for hot and cold accretion.

Figure 2.11 compares the hot fraction of smooth accretion (solid curves) and all accretion (dotted curves), which takes into account both smooth accretion and mergers. The differences are negligibly small. Indeed, the hot fraction for gas accreted in mergers (not shown) is nearly the same as that for gas accreted smoothly.

2.6.3 Dependence on redshift

The fraction of gas that is accreted onto haloes in the hot mode also depends on redshift, as can be seen from Figure 2.11 where the hot fraction is plotted against halo mass for different redshifts. For a given halo mass, the hot fraction increases with time between $z = 5$ and $z = 1$. Below $z = 1$ the rate of evolution slows down, presumably because structure formation slows down, and the sign of the evolution may reverse for low-mass haloes due to the decrease of T_{vir} with time.

At high redshift the proper density of the Universe is higher and the cooling time is therefore shorter ($t_{cool} \propto \rho^{-1} \propto (1+z)^{-3}$). The Hubble time is also shorter, but its dependence on redshift is weaker ($t_H \propto H^{-1} \propto (\Omega_m(1+z)^3 + \Omega_\Lambda)^{-1/2}$, so $t_H \propto (1+z)^{-3/2}$ at high redshift and t_H is independent of redshift at low redshift). The dynamical time at fixed overdensity has the same redshift dependence as t_H. Hence, cooling is more efficient at higher redshifts (e.g. Birnboim & Dekel, 2003) and the hot fraction will thus be lower for a fixed virial temperature. For a fixed halo mass, the evolution in the hot fraction is smaller, because T_{vir} is higher at higher redshifts. The environment can also play a role. At high redshift ($z > 2$), 10^{12} M$_\odot$ haloes are rare and they tend to reside in highly overdense regions at the intersections of the filaments that make up the cosmic
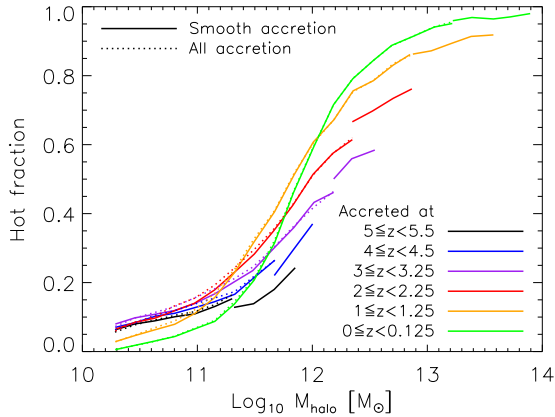
Figure 2.11: Hot fraction for accretion onto haloes just before $z = 5$, 4, 3, 2, 1, and 0 against halo mass at the same redshift. The curves at low halo masses are obtained from simulation *REF_L050N512*. At the high-mass end we have added curves for simulation *REF_L100N512* to extend the dynamic range. Gas is considered to have been accreted hot if it has $T_{max} \geq 10^{5.5}$. The dotted curves show the hot fraction including both smooth accretion and mergers. Each mass bin contains at least 10 haloes. For a fixed halo mass, hot accretion tends to be more important at lower redshift.

web. Haloes of the same mass are, however, more common at low redshift and form in single filaments, with more average densities. Hence, cold streams may be able to feed massive haloes at high redshift, whereas this may not be possible at low redshift (Kereš et al., 2005; Dekel & Birnboim, 2006).

The specific accretion rate of gas onto haloes increases mildly with halo mass for $0 < z < 5$, see Figure 2.3. Splitting this into hot and cold specific accretion rates reveals a steep increase with halo mass for hot accretion, as shown in Figure 2.12. The specific cold accretion rate decreases with halo mass for $M_{halo} \gtrsim 10^{12} \, M_\odot$.

From observations we know that the specific star formation rate, i.e. the SFR divided by the stellar mass, declines with both time and stellar mass (e.g. Brinchmann et al., 2004; Bauer et al., 2005; Feulner et al., 2005; Chen et al., 2009). The decline in the specific SFR may be related to the decline in the specific cold accretion rate. However, the decline is much stronger in the observations and present for the entire stellar mass range probed.

2.6.4 Effects of physical processes

As discussed in Section 2.5, feedback from SNe and AGN decreases the halo accretion rate, while metal-line cooling has very little effect. In this Section we will discuss the influence of cooling and feedback on the hot and cold accretion fractions at $z = 2$ and $z = 0$.
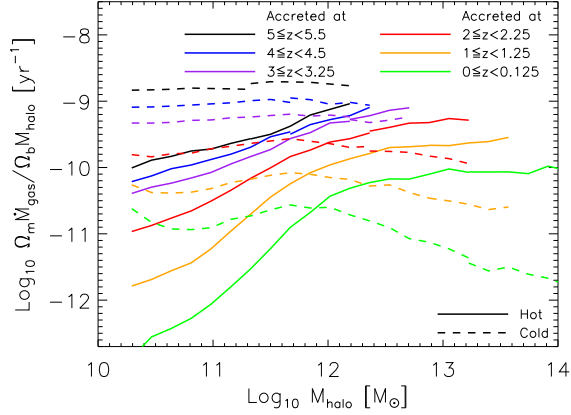
Figure 2.12: Specific smooth accretion rates of gas onto haloes against total halo mass just before redshifts $z = 5$ (black, top curve) to $z = 0$ (green, bottom curve) for the simulation *REF_L050N512*, with the highest mass bins from *REF_L100N512*. The solid and dashed curves are the rates for hot ($T_{max} \geq 10^{5.5}$ K) and cold ($T_{max} < 10^{5.5}$ K) accretion, respectively. Each mass bin contains at least 10 haloes. The specific hot accretion rate increases with halo mass, whereas the specific cold accretion rate decreases for $M_{halo} > 10^{12}$ M$_\odot$.

To investigate the influence of galactic winds driven by SN feedback, we ran simulations with no SN feedback at all and with more effective galactic wind models, that can eject gas from more massive haloes. In other simulations, cooling rates are computed assuming primordial abundances. We have also included AGN feedback in one simulation.

To illustrate the effect these different processes have on an individual halo, Figure 2.13 shows the same 10^{12} M$_\odot$ halo as was shown in the middle panel of Figure 2.7 for five different simulations. From top to bottom are shown: no SN feedback and no metal-line cooling (*NOSN_NOZCOOL*); no metal-line cooling (*NOZCOOL*); reference SN feedback (*REF*); density dependent SN feedback (*WDENS*); reference SN feedback and AGN feedback (*AGN*). The colour coding shows gas overdensity in the left panels and temperature in the right panels. The stronger the feedback (top row: weakest feedback, bottom row: strongest feedback) the more fragmented the streams become. All models predict the presence of cold, dense gas throughout much of the halo. The diffuse halo gas is heated to higher temperatures in simulations with strong SN or AGN feedback than in the reference simulation. The radius out to which gas is heated increases for strong feedback models.

Figure 2.14 shows how the fraction of the gas that accretes smoothly onto haloes just before $z = 2$ (top panels) and $z = 0$ (bottom panels) in the hot mode, i.e. with $T_{max} \geq 10^{5.5}$ K, depends on the physical processes that are modelled. Even though the hot fractions are not completely converged at the low-mass end
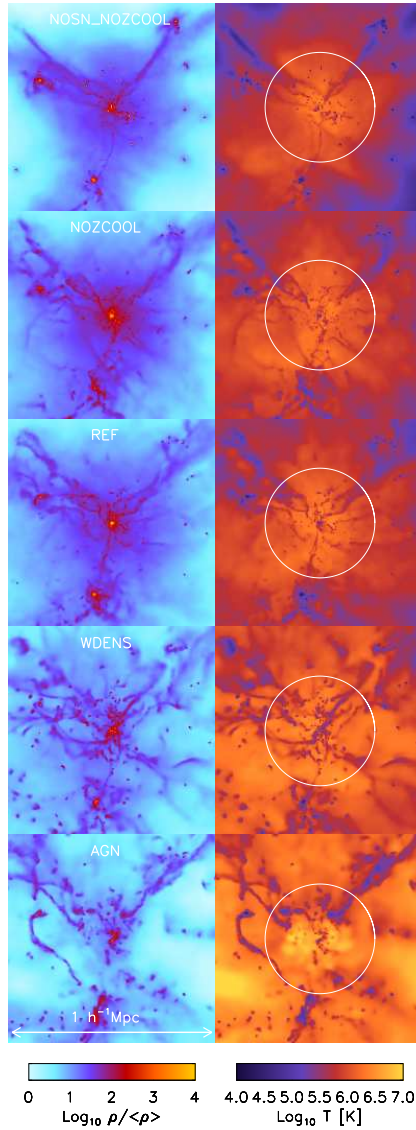
Figure 2.13: Gas overdensity (left) and temperature (right) in a $1\ h^{-1}$ comoving Mpc box centred on a halo of $10^{12}\ \mathrm{M}_\odot$ at $z = 2$. We show the same halo as was shown in the middle panel of Figure 2.7, but now for five different models. The white circles indicate the virial radius of the halo. From top to bottom: no SN feedback and no metal-line cooling (*NOSN_NOZCOOL*), no metal-line cooling (*NOZCOOL*), reference SN feedback (*REF*), density dependent SN feedback (*WDENS*), reference SN feedback, and AGN feedback (*AGN*). These simulations used 2×512^3 particles in a $25\ h^{-1}$Mpc box. The structure of the cold streams changes, but they exist in all simulations. The hot gas extends to larger radii and has a higher temperature if feedback is more efficient. The structure inside the halo is clearly different in different simulations, but cold gas is always present outside the disc.
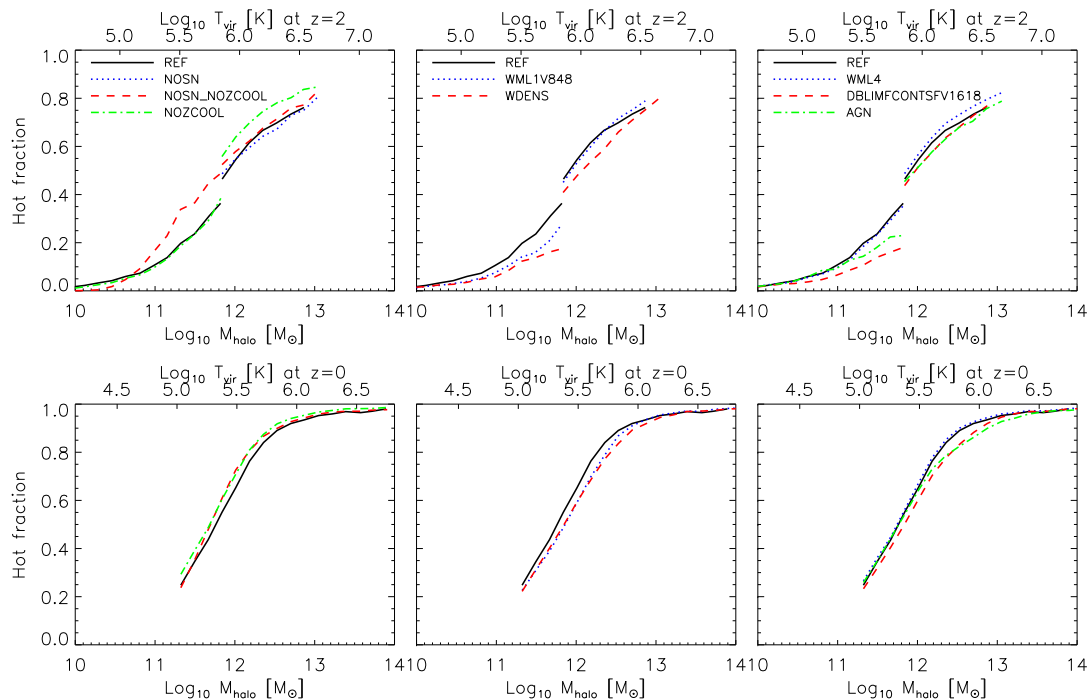
Figure 2.14: The average fraction of the gas that accreted smoothly onto haloes just before $z = 2$ (top panels) and $z = 0$ (bottom panels), that reached maximum past temperatures above $10^{5.5}$ K (by $z = 2$ and $z = 0$, respectively) is plotted as a function of total halo mass. The line styles are identical to those used in Figure 2.4. The curves at the high-mass end are from simulations *L100N512*. At $z = 2$ the curves at the low-mass end are from simulations *L025N512*, resulting in a factor 64 higher mass resolution. Each mass bin contains at least 10 haloes. At $z = 2$, each halo contains at least 1000 dark matter particles. This is higher than our resolution limit for accretion onto haloes, but it removes the overlap between simulations of different resolution. The differences between the simulations are small. Efficient feedback generally reduces the hot fraction, indicating that hot gas is more vulnerable to feedback than cold gas.

for some of the *L100N512* runs, the trend with halo mass and the effect of the variations in the simulations are robust. The haloes above $M_{\mathrm{halo}} \approx 10^{12}$ M$_\odot$ in the *L025N512* runs (not plotted) show an increase in the hot fraction as steep as the *L100N512* runs. Before discussing the differences between the models, we stress that these differences are small. The fraction of the gas that accretes onto a halo of a given mass and at a given redshift in the hot mode can thus be robustly estimated. It is insensitive to uncertainties in the baryonic physics, such as radiative cooling and feedback from star formation and AGN.

We first focus on the left panels, which compare simulations with and without metal-line cooling and with and without SN feedback. For high-mass haloes the fraction of gas accreting in the hot mode is a little bit higher without metal-line cooling, because the gas will reach higher temperatures if the cooling rates are lower. The effect is, however, small.

The hot fraction depends only slightly on the specific feedback model used if the energy per unit stellar mass is kept fixed, as can be seen from the middle panels of Figure 2.14. The hot fraction is a bit lower for the model with the most effective feedback (*WDENS*).

The right panels show that AGN feedback decreases the hot fraction, though the effect is not large and limited to high-mass ($\gg 10^{11}$ M$_\odot$) haloes. More effective stellar feedback as a result of a top-heavy IMF in starbursts (*DBLIMF-CONTSFV1618*) reduces the hot fraction more for low-mass $\lesssim 10^{12}$ M$_\odot$ haloes. These results suggest that the hot accretion mode is slightly more affected by feedback than the cold mode. Because the hot gas is less dense than the cold gas and because it spans a greater fraction of the sky as seen by the galaxy, it is more likely to be affected by feedback. It has been argued by several authors that AGN feedback would therefore couple mostly to the hot gas (Kereš et al., 2005; Dekel & Birnboim, 2006). Our results show that this effect is small, although we will show below that it is important for accretion onto galaxies residing in high-mass haloes at low redshift. The main conclusion is that the fraction of the gas that accretes onto haloes in the hot mode is insensitive to feedback from SNe and AGN.

2.7   Hot and cold accretion onto galaxies

A significant fraction of the gas that accretes onto haloes may remain in the hot, low-density halo. This gas never cools and it will not get into the inner galaxy and contribute to the SFR. This diffuse gas may be easily pushed out of the halo by galactic winds. It is therefore of interest to look not only at the gas that accretes onto haloes, but also at the gas that actually accretes onto galaxies. After all, it is only the gas that is accreted onto galaxies that is available for star formation.

Gas is by definition cold when it accretes onto a galaxy, because it must cool below $T = 10^5$ K to be able to join the ISM. However, by using T_{max} we are probing the entire temperature history of the gas and not just the temperature at

the time of accretion. Gas accreting onto a galaxy in the hot mode has been hot in the past (usually when it accreted onto the halo), but was able to cool down and reach the central galaxy. Gas accreting onto a galaxy in the cold mode has never been hot in the past.

In Figure 2.15 we show the hot fraction for accretion onto haloes (dotted curve), accretion onto the ISM (solid curve), and for stars formed (dashed curve) just before $z = 2$ (top panel) and just before $z = 0$ (bottom panel) for the $50\ h^{-1}$Mpc reference simulation. To illustrate the convergence, we also show the hot fraction for accretion onto the ISM for simulations with different resolutions. We show all results down to halo masses corresponding to 100 dark matter particles, i.e. 1 dex below our resolution limit.

For high-mass haloes ($M_{\mathrm{halo}} \gtrsim 10^{12}\ \mathrm{M}_\odot$) hot mode accretion is less important for accretion onto the ISM, and therefore for star formation, than for accretion onto haloes. For $T_{\mathrm{vir}} \gtrsim 10^6$ K the hot fraction remains approximately constant with mass, even though the hot fraction for halo accretion becomes larger. The lower hot fractions arise because the temperature of the hot gas increases with the virial temperature and for these temperatures hotter gas has a longer cooling time (e.g. Wiersma et al., 2009a), making it less likely to enter the galaxy. In reality, cold, dense clouds may be disrupted more easily than in SPH simulations, which could push the hot fraction up (Agertz et al., 2007).

On the other hand, for low-mass haloes ($T_{\mathrm{vir}} \lesssim 10^{5.5}$ K) the hot fraction for accretion onto galaxies is higher than for accretion onto haloes. The virial temperature of these haloes is so low that the maximum temperature will only be above $10^{5.5}$ K if the gas was heated by SN feedback. This can happen after the gas has accreted onto the halo, but before the gas joins the ISM, explaining the higher hot fraction for accretion onto galaxies. Indeed, Oppenheimer et al. (2010) have shown that the re-accretion of gas that has been ejected by galactic winds can be important. The hot fraction for low-mass haloes is lower in simulations without feedback, confirming our interpretation (see Figure 2.17).

As expected, for recently formed stars the hot fraction is comparable to that for gas that recently accreted onto the ISM, although it is a bit lower. It is slightly lower because of the time delay between accretion and star formation. The gas from which the stars were formed was typically accreted at higher redshift and onto lower-mass haloes, which corresponds to lower hot fractions.

Our lowest resolution simulations underestimate the hot fraction somewhat at their low-mass ends, but this regime is excluded by our adopted resolution limit, as indicated by the arrows. However, for $z = 0$ the results are also not fully converged at the high-mass end ($M_{\mathrm{halo}} > 10^{12}\ \mathrm{M}_\odot$). For high-mass haloes the hot fraction decreases with increasing resolution, as we also saw for accretion onto haloes (see Figure 2.9), although the effect is much larger for accretion onto galaxies. This is likely because higher densities can be reached with higher resolution. Cold mode accretion may thus be somewhat more important for fuelling massive galaxies than our simulations suggest.

The evolution of the hot fraction of gas accreted onto the ISM is shown in
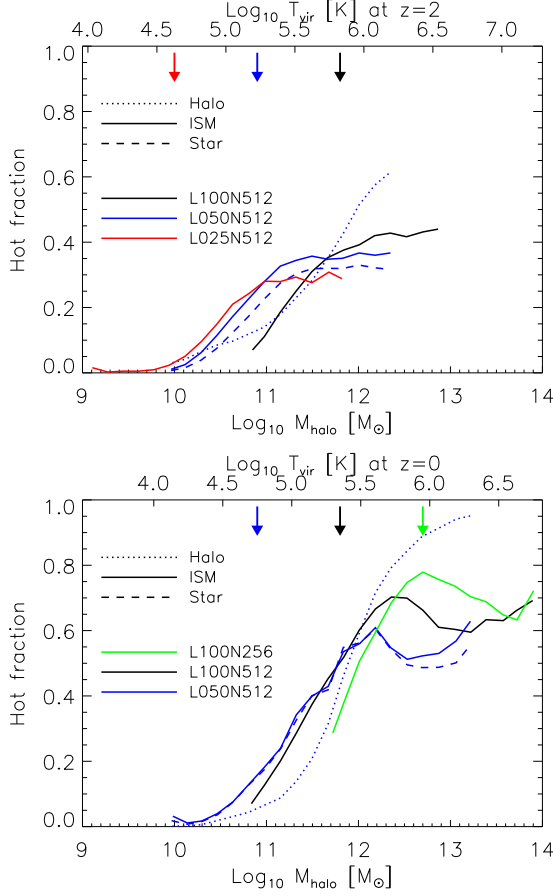
Figure 2.15: The dotted curve shows the average fraction of gas smoothly accreted onto haloes at $z = 2$ (top panel) and $z = 0$ (bottom panel), that has maximum past temperatures above $T_{max} = 10^{5.5}$ K. The solid curves show the average fraction of the gas smoothly accreted onto the ISM with maximum past temperatures above $T_{max} = 10^{5.5}$ K. The dashed curves show the fraction of the stars formed in the same redshift intervals from gas with maximum past temperatures above $T_{max} = 10^{5.5}$ K. These reference simulations span a factor of 64 in mass resolution in each panel. Each mass bin contains at least 10 haloes. Arrows correspond to the adopted resolution limit for accretion onto galaxies. For high-mass haloes, the hot fractions for accretion onto haloes and galaxies diverge. The hot fraction for recently formed stars follows the same trend as for accretion onto the ISM.

Figure 2.16: Hot fraction against halo mass for accretion onto the ISM just before $z = 5$, 4, 3, 2, 1, and 0 shown from bottom to top by the curves in black, blue, 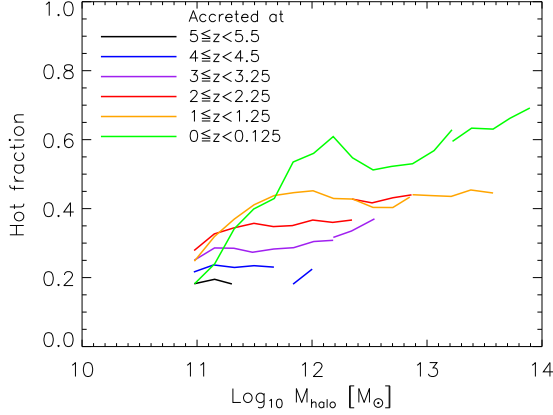purple, orange, red, and green, respectively. The curves at low halo masses are obtained from model *REF_L050N512*. At the high-mass end we have added curves for *REF_L100N512* to extend the dynamic range. Each mass bin contains at least 10 haloes. The hot fraction increases with redshift, except for haloes with virial temperatures which fall below $10^{5.5}$ K, the value we use to separate hot and cold accretion ($M_{\rm halo} \lesssim 10^{11.5}$ M$_\odot$ and $z \lesssim 1$). The hot fraction varies less strongly with halo mass than for accretion onto haloes.

Figure 2.16 from $z = 5$ (bottom, black curve) to $z = 0$ (top, green curve) as a function of halo mass. The trend with redshift is the same as for accretion onto haloes (see Figure 2.11). The hot fraction increases with decreasing redshift for all halo masses, except when the virial temperatures fall below $10^{5.5}$ K, the value we use to separate the hot and cold accretion modes, which happens for $M_{\rm halo} \lesssim 10^{11.5}$ M$_\odot$ at $z \lesssim 1$. The hot fraction for accretion onto galaxies increases less steeply with halo mass than for accretion onto haloes. This is due to the fact that the cooling time of the hot gas increases for higher-mass haloes, making it less likely that hot gas reaches the central galaxy.

For haloes with $T_{\rm vir} \gtrsim 10^6$ K, the hot fraction of gas that reaches the ISM is much lower than the hot fraction of all the gas that accretes onto the halo. At high redshift ($z \gtrsim 4$) cold accretion is the dominant mode for feeding galaxies. At lower redshift ($z \lesssim 2$) hot and cold accretion are comparable. Except for high-mass haloes at low redshift ($M_{\rm halo} > 10^{13}$ M$_\odot$ at $z = 0$), hot mode accretion is less important for feeding the central galaxy than cold mode accretion. It is always less important for the growth of galaxies than it is for the growth of haloes, though it is never negligible. We found the hot fraction of recently formed stars to be slightly lower, because it takes some time to convert the gas into stars. Cold mode accretion is most important for the total build-up of stellar mass in galaxies.

We have not included galaxy mergers. Including mergers preferentially brings in gas accreted in the cold mode, because that gas was already part of the ISM. This reduces the hot fraction slightly for high-mass haloes at low redshift. Cold mode accretion is therefore also the main mode for galaxy growth in this case.

2.7.1   Effects of physical processes

We showed the effect of feedback, metal-line cooling, and cosmology on galaxy accretion rates in Section 2.5. Feedback reduces these rates, while including metal-line cooling increases them. In this Section we discuss their consequences for the relative importance of hot and cold accretion.

Figure 2.17 shows the hot fraction of the gas that reaches the ISM between $z = 2.25$ and $z = 2$ as a function of halo mass for the same simulations as were shown for accretion onto haloes in Figure 2.14. Even though the hot fractions are not completely converged for the *L100N512* runs, the trend with halo mass and the effect of the variations in the physics are robust. As was the case for accretion onto haloes, the trends are the same for all simulations, although the differences between models are larger for accretion onto the ISM than for accretion onto haloes. At $z = 2$, the hot mode is less important for accretion onto the ISM, and therefore less important for star formation, than the cold mode. For the halo mass range shown at $z = 0$ ($\gtrsim 10^{12}$ M$_\odot$), the hot mode is slightly more important than the cold mode.

We can observe the difference between simulations with and without metal-line cooling and with and without SN feedback in the left panels. The simulation without metal-line cooling (*NOZCOOL*) has a slightly smaller hot fraction than the simulation with metal-line cooling (*REF*) at $z = 2$ and for $M_{\mathrm{halo}} \lesssim 10^{12.5}$ M$_\odot$ at $z = 0$. Because the cooling times are longer in the absence of metal-line cooling, less hot gas is able to reach the high densities that define the ISM. For accretion onto haloes we found the opposite effect (see Figure 2.14), because the lower cooling rate increases the maximum temperature reached by gas accreted onto haloes and hence increases the corresponding hot fraction. For high mass haloes ($M_{\mathrm{halo}} \gtrsim 10^{13}$ M$_\odot$) at $z = 0$, the hot fraction is much higher in the absence of metal-line cooling. In Figure 2.5 we have seen that metal-line cooling strongly increases the accretion rates onto galaxies in lower mass galaxies. Thus, without metal-line cooling, less hot gas accretes onto low-mass haloes, leaving more hot gas to accrete onto their higher mass descendants.

We can compare the simulation without metal-line cooling (*NOZCOOL*) to the one without SN feedback and without metal-line cooling (*NOSN_NOZCOOL*). In the simulations with feedback a higher fraction of the gas accreted onto the ISM has been hot, presumably because some of the gas accreted cold onto haloes was heated by outflows before it joined the ISM (for the last time). At the high-mass end at $z = 0$ the differences between the curves parallels those in the specific accretion rates (Figure 2.5). This suggests that here SN feedback increases the hot fraction because it prevents the accretion of hot gas onto lower mass
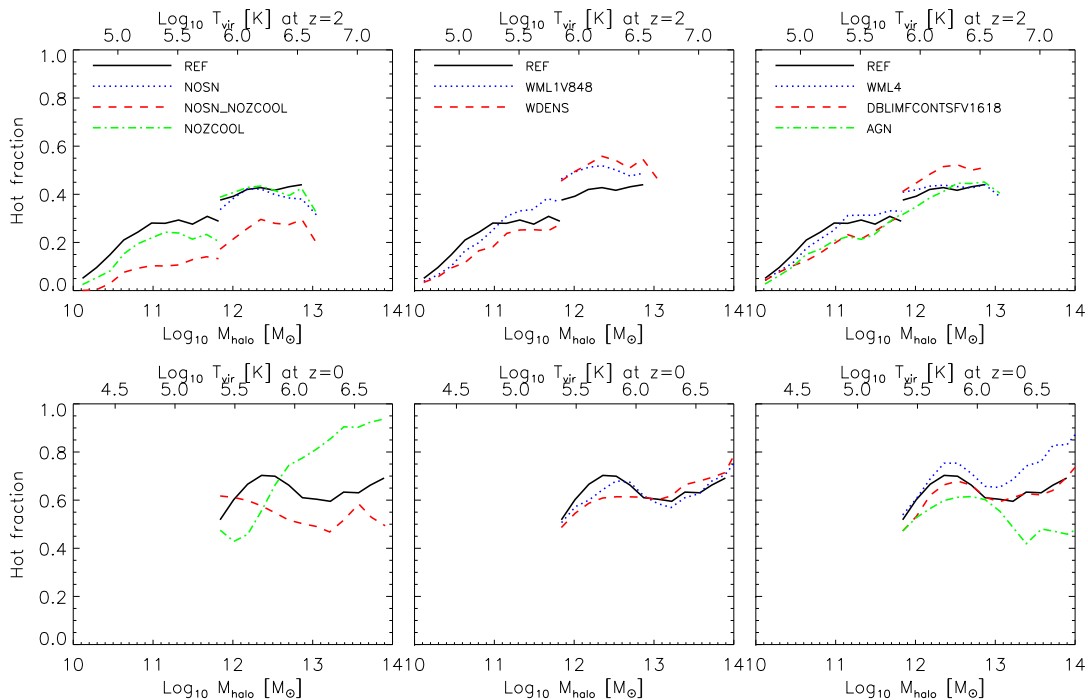
Figure 2.17: The average fraction of the gas accreting onto the ISM at $z = 2$ (top panels) and $z = 0$ (bottom panels), that has maximum past temperatures $T_{max} \geq 10^{5.5}$ K. The line styles are identical to those used in Figure 2.14. The curves at the low and high-mass ends are from simulations *L025N512* and *L100N512*, respectively, which differ by a factor 64 in mass resolution. Each mass bin contains at least 10 haloes. Differences in results from different simulations are mostly small, except for $M_{halo} > 10^{13}$ M$_\odot$ at $z = 0$ if metal-line cooling is ignored or AGN feedback is added.

progenitors, leaving more gas available to cool in high-mass galaxies, where the SN feedback is inefficient. The effect of SN feedback on the hot fraction at $z = 2$ is much smaller if metal-line cooling is included (*NOSN*). This may indicate that the increase in the cooling rates due to the metals carried by the winds compensates for the extra shock heating.

The middle panels show the result for simulations with different values for the SN feedback parameters, but the same amount of SN energy per unit stellar mass formed. The hot fractions are similar, though slightly higher if the feedback model is more efficient (*WML1V848* for $M_{\rm halo} > 10^{11}$ M$_\odot$ and *WDENS* for $M_{\rm halo} > 10^{12}$ M$_\odot$ at $z = 2$).

Results for simulations with a prescription for SN feedback that use more energy and for a model including AGN feedback are shown in the right panels. Perhaps surprisingly, at $z = 2$ the simulation including AGN feedback (*AGN*) gives results similar to the reference simulation. The accretion rate onto the galaxy is suppressed by up to 1 dex, as can be seen in Figure 2.5, but the hot fraction is almost the same. At $z = 0$ the hot fraction is somewhat lower, though still above 40%.

In Figure 2.14 we showed that the hot fraction for the gas accreting onto haloes does not change much if we vary the prescriptions for feedback and radiative cooling. To first order, the same conclusion is true for the gas that accretes onto the ISM and thus becomes star forming, although the differences are larger. At $z = 2$ the hot fraction decreases significantly if both SN feedback and metal-line cooling are turned off. For high-mass galaxies ($M_{\rm halo} > 10^{13}$ M$_\odot$) at $z = 0$ the importance of the hot mode increases substantially if metal-line cooling is excluded and decreases significantly if AGN feedback is added. The specific implementation of the SN feedback does not have a large effect on the fraction of the gas accreting onto galaxies that has a maximum past temperature $T_{\rm max} \geq 10^{5.5}$ K.

2.8   Comparison with previous work

We can compare our results to the pioneering work of Kereš et al. (2005, 2009a), and Ocvirk et al. (2008). All these studies used 250,000 K as the critical temperature to separate hot and cold accretion. We used $10^{5.5} = 316,228$ K, but our results would have been very similar if we had used 250,000 K.

Ocvirk et al. (2008) use an adaptive mesh refinement (AMR) code and include metal enrichment and cooling, but only weak SN feedback and no AGN feedback. They use only a single simulation, whose resolution is similar to our *L025N512* runs. Their simulation was only run to $z \approx 1.5$, so we can only compare to our high-redshift results. Their box size of 50 h^{-1}Mpc is too small to sample haloes with mass $\gtrsim 10^{13}$ M$_\odot$. As their simulation is not Lagrangian, they cannot trace the gas back in time, and were forced to separate the cold and hot modes based on current temperatures.

For $z = 2 - 3$ they predict that the hot fraction for accretion onto haloes reaches 0.5 at $M_{halo} \sim 10^{11.5}$ $M_\odot$, whereas we find $M_{halo} \sim 10^{12}$ $M_\odot$. For higher redshifts we predict somewhat higher hot fractions. We predict a gradual increase in the transition mass with redshift, but see no sign of the sudden change between $z = 3$ and 4 that they found.

For accretion onto galaxies, which they measure at 0.2 virial radii, Ocvirk et al. (2008) also do not predict a sudden change with redshift. As the gas at this radius is not necessarily star forming and has not necessarily cooled down to $T \leq 10^5$ K, it is not possible to make a completely fair comparison. They find no change with redshift, whereas we find strong evolution. The hot fraction increases up to their highest halo mass, reaching values close to unity for $10^{12.5}$ $M_\odot$. In our simulations, however, the hot fraction for accretion onto galaxies is approximately constant and never exceeds 0.4 at $z \geq 2$. As we are using the SPH technique, it is possible that our simulations suffer from in-shock cooling, which would lead to an underestimate of the hot fraction. However, we find that the hot fraction in fact decreases with increasing resolution, the opposite of what we would expect if this were an important effect. Perhaps the difference is due to the fact that we do not update the maximum past temperature once the gas has become star forming. If the accretion shock onto the galaxy happens after that time, we would underestimate the maximum temperature. This is, however, consistent with our aims, as we are interested in the maximum temperature reached *before* the gas entered the galaxy.

Kereš et al. (2005, 2009a) use SPH codes. They ignore metal-line cooling and do not include feedback from SNe or AGN. The resolution of their main simulation is comparable to our *L100N512* runs, but their simulation volume is more than eight times smaller. Their mass resolution is nearly two orders of magnitudes worse than for our *L025N512* runs. They identify galaxies using a different group finder, SKID, which links bound stars and dense, cold gas ($\rho / \langle \rho_{baryon} \rangle > 1000$ and $T < 30,000$ K). These groups are considered to be galaxies. In contrast to our work, they include accretion onto both central galaxies and satellites, which could also lead to somewhat different results. Accretion onto haloes was not investigated.

Contrary to our results and those of Kereš et al. (2009a), Kereš et al. (2005) find that the hot fraction continues to increase with halo mass and that there is no significant evolution. However, using the same method, Kereš et al. (2009a) find much lower hot fractions than Kereš et al. (2005). They find that this difference is mostly due to the fact that they switched to the entropy conserving formulation of SPH of Springel & Hernquist (2002), which prevents overcooling due to artificial phase mixing and which we have used as well. We will therefore only compare with Kereš et al. (2009a) (and only for accretion onto galaxies).

At high redshift ($z = 4$) we find similar results for the hot fractions as Kereš et al. (2009a), although ours are slightly higher, which is due to the fact that we include SN feedback. At $z \leq 2$ they find that the hot fraction first increases, reaches a maximum around $M_{halo} = 10^{12}$ $M_\odot$, after which it decreases. We

find that the hot fraction varies less strongly with halo mass and that it remains approximately constant at the high mass end.

Our results are also in qualitative agreement with Brooks et al. (2009), who used SPH simulations (without metal-line cooling and AGN feedback) of a few individual galaxies with $M_{\text{halo}} \lesssim 10^{12}$ M$_\odot$. A detailed comparison is difficult as their sample is too small to obtain statistics and because they used a more complicated criterion to separate the different accretion modes.

2.9 Conclusions

Before summarizing and discussing our findings, we list our main conclusions:

- To first order, the rate of gas accretion onto haloes follows that of dark matter. Except for low-mass haloes ($M_{\text{halo}} \ll 10^{11}$ M$_\odot$), feedback changes these rates only slightly.

- Except for groups and clusters, gas accretes mostly smoothly (i.e. not through mergers with mass ratios greater than 1:10).

- The rate at which gas accretes onto galaxies is set by radiative cooling, which is sensitive to the abundance of heavy elements, and by feedback from SNe and AGN. Galactic winds driven by star formation increase the halo mass at which the central galaxies grow the fastest by about two orders of magnitude to $M_{\text{halo}} \sim 10^{12}$ M$_\odot$.

- The signs of the effects of feedback and metal-line cooling on gas accretion can change with halo mass.

- Gas accretion is bimodal, with maximum past temperatures either of order the virial temperature or $\lesssim 10^5$ K. Both modes can be present in a single halo, the cold mode being most prominent in filaments.

- The fraction of gas accreted in the hot mode (i.e. maximum past temperature $T_{\text{max}} \geq 10^{5.5}$ K), increases with halo mass and with decreasing redshift.

- For accretion onto haloes, the relative importance of the hot and cold modes is is robust to changes in the feedback prescriptions. Cold and hot accretion dominate for $M_{\text{halo}} \ll 10^{12}$ M$_\odot$ and $M_{\text{halo}} \gg 10^{12}$ M$_\odot$, respectively.

- For accretion onto galaxies the cold mode is always significant and the relative importance of the two accretion modes is much more sensitive to feedback and cooling than is the case for halo accretion.

- On average, most of the stars present in any mass halo at any redshift were formed from gas accreted in the cold mode, although the hot mode contributes typically over 10% for $M_{\text{halo}} \gtrsim 10^{11}$ M$_\odot$ (see Figure 2.18 below).

While the rate at which dark matter accretes onto haloes can be reliably calculated, the situation is rather more complicated for gas. Gas may be heated through accretion shocks, but can also radiate away its thermal energy. This cooling rate is, however, strongly affected by contamination with metals blown out of galaxies. Such galactic winds driven by star formation or accreting supermassive black holes may also directly halt or reverse the accretion, which may in turn cause gas elements to be recycled multiple times.

Pressing questions include: What fraction of the gas accreting onto haloes experiences a shock near the virial radius? How does this fraction vary with halo mass and redshift? What fraction of the gas that falls into a dark matter halo accretes onto a galaxy and how does this vary with mass and redshift? How do processes like metal-line cooling and feedback from star formation and AGN affect gas accretion? We addressed these questions by analysing a large number of cosmological, hydrodynamical simulations from the OWLS project (Schaye et al., 2010). By repeating the simulations many times with varying parameters, we investigated what physical processes drive the accretion of gas onto galaxies and haloes. For each physical model we combined at least two 2×512^3 particle simulations in order to cover a dynamic range of about 4 orders of magnitude in halo mass ($M_{\mathrm{halo}} \sim 10^{10} - 10^{14}$ M$_\odot$). Schaye et al. (2010) have shown that the simulation with AGN feedback is able to reproduce the steep slope of the observed star formation rate density at $z < 2$. This is a significant improvement over previous simulations. In a future paper we will discuss the contributions of hot and cold accretion to the cosmic star formation history.

Except for $M_{\mathrm{halo}} \gg 10^{13}$ M$_\odot$ at low redshift, mergers with mass ratios exceeding 1:10 contribute $\lesssim 10\%$ of the total accretion onto haloes. The growth of haloes is thus dominated by smooth accretion. The specific rate of smooth gas accretion onto haloes is close to that for dark matter accretion, particularly at higher redshifts. It decreases with time and increases with halo mass. The increase with halo mass is, however, gradual and the gradient decreases with increasing halo mass. To first order, the halo accretion rate scales linearly with the halo mass.

The rate of accretion onto haloes is relatively insensitive to the inclusion of metal-line cooling. Efficient feedback can reduce the halo accretion rates by factors of a few. In particular, for $z = 2$ we find that SN feedback reduces the halo accretion rate of low-mass haloes ($M_{\mathrm{halo}} \sim 10^{10}$ M$_\odot$) by a factor of about four, but is typically not efficient for $M_{\mathrm{halo}} \gtrsim 10^{13}$ M$_\odot$.

As is the case for accretion onto haloes, accretion onto galaxies is mostly smooth. Clumpy accretion, which in this case we defined as accretion of material that already had densities $n_{\mathrm{H}} \geq 0.1$ cm^{-3} at the previous snapshot, becomes of comparable importance as smooth accretion only for $M_{\mathrm{halo}} \gtrsim 10^{13}$ M$_\odot$.

While the specific accretion rate onto haloes increases slowly with halo mass over the full range spanned by our simulations, the specific accretion rate onto galaxies increases rapidly for $M_{\mathrm{halo}} \ll 10^{12}$ M$_\odot$ and drops quickly for $M_{\mathrm{halo}} \gg 10^{12}$ M$_\odot$. The halo mass at which the specific accretion rate onto galaxies peaks

is sensitive to feedback from SNe and AGN. Without SN feedback, the specific accretion rate peaks at $M_{halo} \sim 10^{10}$ M$_\odot$, where it exceeds the rate predicted by runs that do include SN feedback by an order of magnitude. For higher mass haloes ($M_{halo} \gg 10^{11}$ M$_\odot$), on the other hand, SN feedback tends to increase the specific accretion rates by about a factor of two, either because of the increased importance of recycling (i.e. the same gas can be re-accreted after it has been ejected, see Oppenheimer et al. 2010) or because without SN feedback the accreted gas would already have been consumed in lower mass progenitor galaxies. AGN feedback can strongly reduce the accretion rates onto galaxies. This sensitivity to feedback is in contrast to accretion onto haloes. In the absence of metal-line cooling, the peak in the specific accretion rate is less pronounced. Hence, cooling and feedback set the efficiency of galaxy formation by controlling what fraction of the gas that accretes onto haloes is able to accrete onto galaxies.

The rate of accretion onto galaxies is smaller than the accretion rate onto haloes. The difference between the two rates increases with time and is minimal for $M_{halo} \sim 10^{12}$ M$_\odot$. For this mass the difference increases from a factor of two at $z = 2$ to a factor of four at $z = 0$.

Tracing back in time, most gas particles that reside in haloes at $z = 0$ reached their maximum temperature around, or shortly after, the time they were first accreted onto a halo. In the presence of a photo-ionising background, essentially all gas accreting smoothly onto haloes has been heated to $\gtrsim 10^5$ K. For haloes with virial temperatures $\gg 10^5$ K the probability distribution for the maximum past temperature reached by gas accreted onto haloes is bimodal. The low temperature peak at $\sim 10^5$ K represents gas that accreted predominantly through large-scale filaments (but still smoothly). The higher densities in the filaments enable efficient cooling which in turn prevents the establishment of a stable accretion shock (e.g. Kereš et al., 2005; Dekel & Birnboim, 2006). The high-temperature peak coincides with the virial temperature of the halo and is reached through an accretion shock near the virial radius.

We separated these two modes of smooth gas accretion according to the maximum past temperature of the gas, which we updated for each particle at each time step, and referred to them as cold ($T_{max} < 10^{5.5}$ K) and hot ($T_{max} \geq 10^{5.5}$ K) accretion, respectively. For high-mass haloes (virial temperatures $\gtrsim 10^6$ K), the hot fraction, i.e. the fraction of gas that is accreted in the hot mode, reflects the fraction of the accreted gas that has experienced an accretion shock near the virial radius. We emphasized, however, that for gas accreted onto haloes with virial temperatures $\lesssim 10^{5.5}$ K ($M_{halo} \lesssim 10^{11.5}$ M$_\odot$ at $z = 2$ and $M_{halo} \lesssim 10^{12}$ M$_\odot$ at $z = 0$) gas accreted in the cold mode (according to our definition) may also have gone through a virial shock.

The fraction of the gas that is accreted onto haloes and galaxies of a given mass in the cold mode typically increases with redshift. This is because radiative cooling is more efficient at high redshift, where the gas densities are higher (and the cooling time is more sensitive to the density than the dynamical and Hubble times).

For accretion onto haloes, the relative importance of the two modes is mostly determined by the halo mass. At $z = 0$ the hot fraction increases from less than 0.1 at $M_{halo} \sim 10^{11}$ M$_\odot$ to more than 0.9 at $M_{halo} \sim 10^{13}$ M$_\odot$. For all redshifts for which we have sufficient statistics ($z < 5$), the hot fraction reaches 0.5 for $M_{halo} \sim 10^{12}$ M$_\odot$, in reasonable agreement with the predictions of Birnboim & Dekel (2003) and Dekel & Birnboim (2006) for metal enriched gas at the virial radius and with previous simulations (Kereš et al., 2005; Ocvirk et al., 2008; Kereš et al., 2009a). Contrary to accretion onto haloes, the hot fraction for gas accreted onto galaxies is only weakly dependent on halo mass. In particular, the hot fraction for accretion onto galaxies is nearly constant for $M_{halo} \gtrsim 10^{12}$ M$_\odot$ and remains below 0.5, except at $z \approx 0$.

For accretion onto haloes, the relative importance of the cold and hot modes is mostly insensitive to the inclusion of metal-line cooling or feedback from SNe and AGN. For accretion onto galaxies the effects are stronger, though generally still weak. The main exceptions are galaxies in high-mass haloes $M_{halo} > 10^{13}$ M$_\odot$ at low redshift. For these systems the hot mode becomes much more important in the absence of metal-line cooling (because less gas has cooled onto their progenitors) and substantially less important if AGN feedback is considered (because it efficiently removes hot gas).

As expected, the hot fraction for the gas that is converted into stars is very similar to that of the gas that accretes onto galaxies. As illustrated in Figure 2.18, where we show the fraction of the total stellar mass formed from gas which has reached $T_{max} \geq 10^{5.5}$ K in its past. For the full range of redshifts and halo masses probed by our simulations, the majority of stars are formed from gas accreted in the cold mode.

Both the comparison of our different models and the comparison with Ocvirk et al. (2008) suggest that the conclusions regarding accretion onto haloes are robust, at least for $z < 4$. The gas accretion rate is similar to that of the dark matter and dominated by smooth accretion. The hot mode changes from being negligible at $M_{halo} \lesssim 10^{11}$ M$_\odot$ to strongly dominant at $M_{halo} \gtrsim 10^{13}$ M$_\odot$. Contrary to accretion onto haloes, the mode and particularly the rate of gas accretion onto galaxies, and hence the provision of fuel for star formation, is affected by uncertain processes such as metal-line cooling and especially feedback from star formation and AGN. This is reflected in the large differences in the predictions by different groups. It seems clear, however, that the hot mode is much less important for the growth of galaxies than it is for the growth of haloes.

We conclude that the rate and manner in which gas accretes onto haloes is an important ingredient of models for the formation and evolution of galaxies and that this process can be understood using simple physics. However, halo accretion gives by itself little insight into the rate and mode through which gas accretes onto galaxies. To understand galaxy formation, it is crucial to consider feedback processes, such as metal enrichment and outflows driven by SNe and AGN.
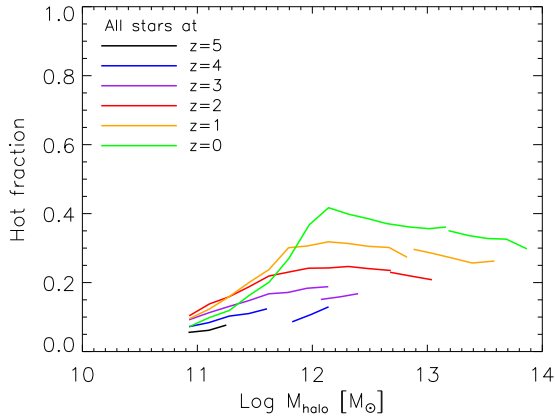
Figure 2.18: Fraction of the stellar mass at the indicated redshifts, that formed from gas that had earlier reached temperatures exceeding $T_{max} \geq 10^{5.5}$ K, as a function of the host halo mass at the corresponding redshifts for the simulation *REF_L050N512*. We added the highest mass bins from *REF_L100N512* to extend the dynamic range. Each mass bin contains at least 10 haloes. At any time and for any halo mass, hot mode accretion contributed less than 40% to the total stellar mass.

Acknowledgements

3

The drop in the cosmic star formation rate below redshift 2 is caused by a change in the mode of gas accretion and by active galactic nucleus feedback

The cosmic star formation rate is observed to drop sharply after redshift $z = 2$. We use a large, cosmological, smoothed particle hydrodynamics simulation to investigate how this decline is related to the evolution of gas accretion and to outflows driven by active galactic nuclei (AGN). We find that the drop in the star formation rate follows a corresponding decline in the global cold-mode accretion rate density onto haloes, but with a delay of order the gas consumption time scale in the interstellar medium. Here we define cold-mode (hot-mode) accretion as gas that is accreted and whose temperature has never exceeded (did exceed) $10^{5.5}$ K. In contrast to cold-mode accretion, which peaks at $z \approx 3$, the hot mode continues to increase to $z \approx 1$ and remains roughly constant thereafter. By the present time, the hot mode strongly dominates the global accretion rate onto haloes. Star formation does not track hot-mode halo accretion because most of the hot halo gas never accretes onto galaxies. AGN feedback plays a crucial role by preferentially preventing gas that entered haloes in the hot mode from accreting onto their central galaxies. Consequently, in the absence of AGN feedback, gas accreted in the hot mode would become the dominant source of fuel for star formation and the drop off in the cosmic star formation rate would be much less steep.

Freeke van de Voort, Joop Schaye, C. M. Booth, and Claudio Dalla Vecchia

3.1   Introduction

The cosmic star formation rate (SFR) is observed to peak between redshifts $z \approx 3$ and $z \approx 2$ after which it decreases by an order of magnitude (e.g. Hopkins & Beacom, 2006). Its evolution is thought to be determined by the combination of the formation and growth of (dark matter) haloes, which depends on cosmology, and the distribution of SFRs in haloes as a function of halo mass and redshift. The latter depends on processes such as gas accretion, stellar mass loss, radiative cooling, (re-)ionization, and feedback from star formation and active galactic nuclei (AGN) (e.g. Schaye et al., 2010).

The observed rates of star formation in galaxies can only be sustained for long periods of time if the galaxies are being fed continuously (e.g. Bauermeister et al., 2010). This feeding happens through the accretion of gas from the inter-galactic medium. In the simplest picture of spherical collapse, it is assumed that all gas accreting onto a halo is shock-heated to the virial temperature of the halo, reaching a quasi-static equilibrium supported by the pressure of the hot gas. If the cooling time of the halo gas is sufficiently short, then it may subsequently enter the central galaxy. Whether or not the halo gas can accrete onto the galaxy therefore depends on both the temperature and the density of the gas (Rees & Ostriker, 1977). However, if the cooling time of gas that has gone through a (hypothetical) accretion shock at the virial radius is short compared with the age of the Universe, then there can be no hydrostatic halo and hence also no virial shock. This will be the case for low-mass haloes (Rees & Ostriker, 1977; White & Rees, 1978). The accretion rate onto the central galaxy then depends on the infall rate, but not on the cooling rate (White & Frenk, 1991). Indeed, Birnboim & Dekel (2003) showed that a virial shock is absent for low-mass haloes in a spherically symmetric simulation.

However, cosmological simulations show significant deviations from spherical symmetry. Galaxies form inside the filaments that make up the cosmic web and these filaments contribute significantly to, or even dominate, the gas supply of galaxies (Dekel et al., 2009a). Because the density inside filaments is higher than that of the ambient gas, the cooling time of the gas is much shorter and the gas can accrete cold onto haloes of higher masses than predicted by spherically symmetric models (e.g. Kereš et al., 2005; Dekel & Birnboim, 2006). This cold gas can reach the high densities of the interstellar medium (ISM) much more efficiently than the tenuous, hot gas in the halo. It is this 'cold mode' of accretion that predominantly feeds the galaxy and powers star formation (Kereš et al., 2009a; Brooks et al., 2009; van de Voort et al., 2011a, hereafter V11).

The fraction of the accreted gas that is accreted cold, i.e. the fraction of the gas that did not pass through a virial shock, depends on both halo mass and redshift (Kereš et al. 2005; Dekel & Birnboim 2006; Ocvirk et al. 2008; Kereš et al. 2009a; Brooks et al. 2009; V11). In V11 we used simulations to show that the rate at which gas accretes onto central galaxies is generally much lower than the rate at which gas accretes onto their host haloes. Furthermore, we found that while

halo accretion rates are determined by the depth of the gravitational potentials, galaxy accretion rates are also sensitive to processes such as metal-line cooling and feedback from star formation and AGN.

Here we use a large cosmological hydrodynamical simulation that includes radiative cooling (computed element by element and thus including metal lines), star formation, stellar mass loss, and outflows driven by both supernovae and AGN, to determine how hot and cold accretion influence the global star formation history (SFH). We calculate global accretion rate densities, both for hot- and cold-mode accretion, and for accretion onto haloes as well as accretion onto galaxies. We will compare the evolution of these different global accretion rates to the resulting global SFH and learn how they all link together. We will show that the sharp drop in the global SFH after $z \approx 2$ reflects the corresponding sharp drop in the rate of cold-mode accretion onto haloes. Motivated by semi-analytic models and simulations that have shown AGN feedback to be crucial for the suppression of star formation in high-mass haloes (e.g. Springel et al., 2005; Bower et al., 2006; Croton et al., 2006; Lagos et al., 2008; Booth & Schaye, 2009; McCarthy et al., 2010), we use an identical simulation, except for the omission of feedback from AGN, to investigate the effect of AGN feedback on the global accretion rates. We will show that the hot accretion mode is more strongly suppressed by AGN feedback than the cold mode. Without AGN feedback, low-redshift star formation would not be predominantly fuelled by the cold accretion mode and the drop in the cosmic SFR would be much less strong.

The outline of this paper is as follows. In Section 3.2 we briefly describe the simulations from which we derive our results and discuss our method for selecting recently accreted gas. In Section 3.3 we compare global accretion rates to the cosmic SFR and show which haloes contribute most to the global accretion rates and the cosmic SFH. In Section 3.4 we investigate the effect of AGN feedback on the hot and cold accretion rate densities. Finally, we summarize and discuss our results in Section 3.5.

3.2   Simulations

We use a modified version of GADGET-3 (last described in Springel, 2005b), a smoothed particle hydrodynamics (SPH) code that uses the entropy formulation of SPH (Springel & Hernquist, 2002), which conserves both energy and entropy where appropriate. This work is part of the OverWhelmingly Large Simulations (OWLS) project (Schaye et al., 2010), which consists of a large number of cosmological simulations with varying (subgrid) physics. Here we make use of the so-called 'AGN' and 'reference' models, which are identical except that only model AGN includes supermassive black holes and AGN feedback. The AGN simulation will be our fiducial model, but we will compare it with the OWLS reference model in Section 3.4. As the simulations are fully described in Schaye

et al. (2010), we will only summarize their main properties here.

The simulations described here assume a ΛCDM cosmology with parameters $\Omega_m = 1 - \Omega_\Lambda = 0.238$, $\Omega_b = 0.0418$, $h = 0.73$, $\sigma_8 = 0.74$, $n = 0.951$. These values are consistent[1] with the WMAP 7-year data (Komatsu et al., 2011).

A cubic volume with periodic boundary conditions is defined, within which the mass is distributed over N^3 dark matter and as many gas particles. The box size (i.e. the length of a side of the simulation volume) of the simulations used in this work is 100 h^{-1} comoving Mpc, with $N = 512$. The (initial) particle masses for baryons and dark matter are 1.2×10^8 $M_\odot$ and 5.6×10^8 $M_\odot$, respectively. The gravitational softening length is 7.8 h^{-1}comoving kpc, i.e. 1/25 of the mean dark matter particle separation, but we imposed a maximum of 2 h^{-1}proper kpc, which is reached at $z = 2.91$.

The abundances of eleven elements released by massive stars and intermediate mass stars are followed as described in Wiersma et al. (2009b). We assume the stellar initial mass function (IMF) of Chabrier (2003), ranging from 0.1 to 100 $M_\odot$. As described in Wiersma et al. (2009a), radiative cooling and heating are computed element by element in the presence of the cosmic microwave background radiation and the Haardt & Madau (2001) model for the UV/X-ray background from galaxies and quasars.

Star formation is modelled according to the recipe of Schaye & Dalla Vecchia (2008). A polytropic equation of state $P_{tot} \propto \rho_{gas}^{4/3}$ is imposed for densities exceeding $n_H = 0.1$ cm^{-3}, where P_{tot} is the total pressure and ρ_{gas} the density of the gas. Gas particles with proper densities $n_H \geq 0.1$ cm^{-3} and temperatures $T \leq 10^5$ K are moved onto this equation of state and can be converted into star particles. The star formation rate (SFR) per unit mass depends on the gas pressure and is set to reproduce the observed Kennicutt-Schmidt law (Kennicutt, 1998).

Feedback from star formation is implemented using the prescription of Dalla Vecchia & Schaye (2008). About 40 per cent of the energy released by type II SNe is injected locally in kinetic form. The rest of the energy is assumed to be lost radiatively. The initial wind velocity is 600 km s^{-1}.

Our fiducial simulation includes AGN feedback. The model, which is a modified version of the model introduced by Springel et al. (2005), is fully described and tested in Booth & Schaye (2009). In short, a seed mass black hole is placed in every resolved halo. These black holes grow by accretion of gas, which results in the injection of energy in the surrounding medium, and by mergers.

The accretion rate onto the black hole equals the so-called Bondi-Hoyle accretion rate (Bondi & Hoyle, 1944) if the gas density is low ($n_H < 10^{-1}$ cm^{-3}). However, in dense, star-forming gas, where the accretion rate would be severely underestimated because the simulations do not include a cold, interstellar gas phase and because the Jeans scales are unresolved, the accretion rate is mul-

---

[1]The only significant discrepancy is in σ_8, which is 8 per cent, or 2.3σ, lower than the value favoured by the WMAP 7-year data.

tiplied by an efficiency parameter, α, given by $\alpha = (n_H/n_H^*)^\beta$, where $n_H^* = 0.1$ cm^{-3} is the threshold density for star formation and $\beta = 2$. Note, however, that our results are insensitive to the choice for β as long as it is chosen to be large (see Booth & Schaye 2009). A fraction of 1.5 per cent of the rest-mass energy of the accreted gas is injected into the surrounding medium in the form of heat, by increasing the temperature of at least one neighbouring gas particle by at least 10^8 K. The minimum temperature increase ensures that the feedback is effective, because the radiative cooling time of the heated gas is sufficiently long, and results in fast outflows. When AGN feedback is included, the SFR is reduced for haloes with $M_{halo} \gtrsim 10^{12}$ M$_\odot$ (Booth & Schaye, 2009). The AGN simulation reproduces the observed mass density in black holes at $z = 0$ and the black hole scaling relations (Booth & Schaye, 2009) and their evolution (Booth & Schaye, 2010) as well as the observed optical and X-ray properties, stellar mass fractions, SFRs, stellar age distributions and the thermodynamic profiles of groups of galaxies (McCarthy et al., 2010).

The Lagrangian nature of the simulation is exploited by tracing each fluid element back in time, which is particularly convenient for this work, as it allows us to study the temperature history of accreted gas. During the simulations the maximum past temperature, T_{max}, was stored in a separate variable. The variable was updated for each SPH particle at every time step for which the temperature exceeded the previous maximum temperature. The artificial temperature the particles obtain when they are on the equation of state (i.e. when they are part of the unresolved multiphase ISM) was ignored in this process. This may cause us to underestimate the maximum past temperature of gas that experienced an accretion shock at higher densities. Ignoring such shocks is, however, consistent with our aims, as we are interested in the maximum temperature reached *before* the gas entered the galaxy.

Resolution tests are not included in this paper. However, Schaye et al. (2010) have shown that the box size and resolution of the reference simulation used in this paper suffice to obtain nearly converged results for the cosmic SFH at $z < 3$, which changes by much less than a factor of 2 when changing the resolution by a factor of 8. At higher redshifts the global SFR density is, however, underestimated as a result of the finite resolution. Because AGN feedback moves the peak star formation activity to lower-mass haloes, the convergence of the AGN simulation may be slightly worse. V11 tested the convergence of accretion rates and the fraction of the accretion due to the hot mode as a function of halo mass. They found that increasing the resolution gives slightly higher cold accretion fractions, which would only strengthen the conclusions of this work. For quantities averaged over the entire simulation volume, we have to keep in mind that the minimum halo mass that is included depends on the resolution. The global fraction of gas accreted in the cold mode may therefore also depend on the resolution, because the cold fraction increases with decreasing halo mass. Increasing the resolution would allow us to include lower-mass haloes, thus increasing the global cold accretion fraction. Again, this would only strengthen

our conclusions.

3.2.1 Accretion and mergers

In this section we summarize our method for determining the gas accretion rates onto haloes and galaxies and the amount of star formation within haloes. Our method is described in more detail in V11. We use SUBFIND (Dolag et al., 2009) to identify gravitationally bound haloes and subhaloes. In this work we only investigate accretion onto haloes that are not embedded inside larger haloes. In other words, we do not consider subhaloes. The simulations are saved at discrete output redshifts, called snapshots. The redshift intervals between snapshots are $\Delta z = 0.25$ for $0 < z \leq 4$, and $\Delta z = 0.5$ for $4 < z \leq 6$. This is the time resolution for determining accretion rates. For all haloes, called descendants, with more than 100 dark matter particles (i.e. with $M_{\text{halo}} \gtrsim 10^{10.8}$ $M_{\odot}$), we find the progenitor at the previous output redshift. We do this by finding the group containing most of the 25 most bound dark matter particles of the descendant. Haloes without a well-defined progenitor are discarded from our analysis. All gas entering a halo, both from accretion and from mergers, contributes to its growth. We therefore identify all the gas and recently formed star particles that are in the descendant, but not in its progenitor.

To participate in star formation, gas has to enter not only the halo, but also the ISM of the galaxy. For the same haloes as we have selected above, we identify all particles entering the ISM (i.e. moving onto the equation of state) of the descendant galaxy between the two consecutive output redshifts. Galaxy mergers are therefore automatically included. To make sure we are not looking at accretion onto substructures within the main halo, we only consider accretion taking place within the inner 15 per cent of the virial radius. This corresponds to the growth of the central galaxy.

Finally, we identify all the stars formed in the same haloes and redshift bins to calculate the corresponding SFRs. Again, unresolved haloes and satellites are excluded.

We decided to include gas contributed by mergers, as well as smoother accretion flows, because both are mechanisms by which haloes and galaxies grow and both can provide fuel for star formation. We note, however, that the contribution from mergers is much smaller than that from smooth accretion. Mergers with mass ratios greater than 1:10 account for only $\lesssim 10$ per cent of the total halo growth, except in groups and clusters at low redshift (see V11).

The simulations used for this study do not resolve haloes below $M_{\text{halo}} = 10^{10.8}$ $M_{\odot}$. We are therefore missing contributions to the global accretion rates and SFR from lower mass haloes. Because we use a fixed maximum past temperature threshold of $10^{5.5}$ K to distinguish hot from cold accretion (see below), small haloes with virial temperatures below this threshold will by definition accrete almost all gas in the cold mode. The mass regime that we investigate here

is therefore the most interesting regime, where changes in accretion mode are expected to occur (Dekel & Birnboim, 2006).

3.3   Global accretion and star formation

Schaye et al. (2010) showed that without feedback from supernovae and AGN, the SFR density is overpredicted by a large factor at $z \lesssim 2$. By including supernova feedback they could lower the SFR density, but if the predicted SFR density matched the observed peak at $z \approx 2$, then it overpredicted the SFR density at $z = 0$. The drop in the global SFR below $z = 2$ is much closer to the observed slope if AGN feedback is included, but in that case the SFR density may be slightly too low (Schaye et al., 2010). This discrepancy could be solved by decreasing the efficiency of feedback from star formation, which had been set to reproduce the observed peak in the SFH using models without AGN feedback. It is, however, not clear how seriously we should take the discrepancy, since the AGN simulation does reproduce the observed masses and ages of the central galaxies of groups (McCarthy et al., 2010). This would suggest that the problem may be solved by increasing σ_8 from 0.74 to the currently favoured value of 0.81, which would have a relatively strong effect on global star formation rates (see Schaye et al., 2010) while leaving the evolution of haloes of a given mass nearly unchanged. Because, for the purposes of this work, the AGN simulation is the most realistic run from the OWLS suite, we will adopt it as our fiducial model. In Section 3.4 we will discuss how its predictions differ from those of a simulation without AGN feedback.

The temperature of accreting gas has been found to follow a bimodal distribution (e.g. Kereš et al. 2005; V11). Therefore, two modes of accretion are considered: the hot and the cold mode. The cooling function peaks at about $T = 10^{5-5.5}$ K (e.g. Wiersma et al., 2009a), so there is little gas around this temperature. We therefore define hot (cold) accretion as accreted gas with maximum past temperatures above (below) $10^{5.5}$ K. Much of the gas that is shock-heated to much higher temperatures is expected to stay hot for a long time, whilst gas that is heated to lower temperatures can more easily cool and condense onto the galaxy.

When considering accretion onto galaxies, it is important to note that the terms 'hot' and 'cold' refer to the maximum past temperature rather than the current temperature. In fact, gas that has been shock-heated to temperatures in excess of $10^{5.5}$ K *must* cool down before it can accrete onto a galaxy, as we identify this type of accretion as gas joining the ISM, which in our simulations means that the gas density crosses the threshold of $n_{\mathrm{H}} = 0.1$ cm^{-3} while the temperature $T \leq 10^5$ K. Thus, although gas that, according to our terminology (which is consistent with that used in the literature), is accreted hot onto galaxies has been hot in the past, it is cold at the time of accretion. In V11 we showed that the maximum past temperature is usually reached around the time the gas
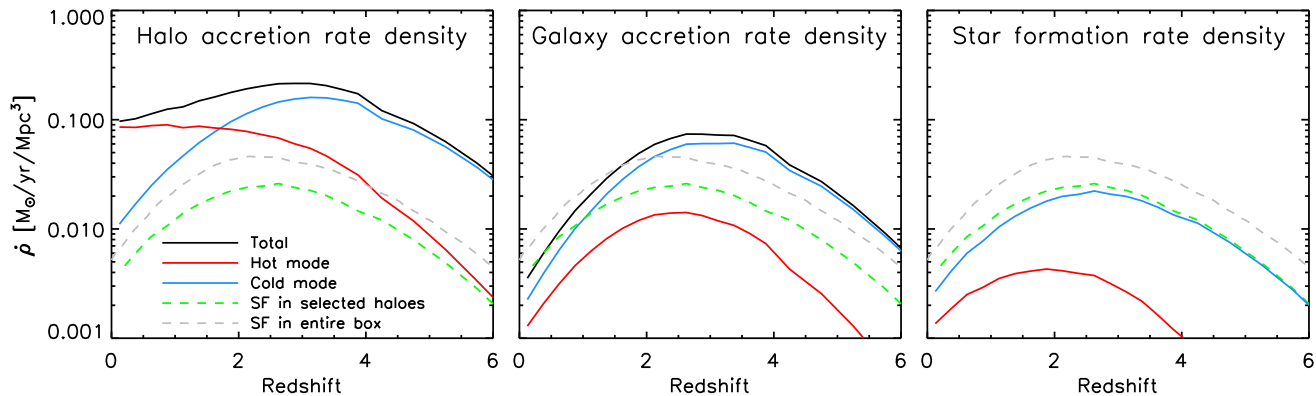
Figure 3.1: Evolution of global accretion rate and SFR densities in resolved haloes with well-defined progenitors. The left, middle, and right panels show global accretion rate densities onto haloes, onto central galaxies, and global SFR densities, respectively. Red and blue curves show accretion rate densities (left and middle panels) and SFR densities (right panel) resulting from hot- and cold-mode accretion, respectively. In all panels, the black curve is the sum of the red and blue curves, the green curve shows the global SFR density in the selected haloes, and the grey curve shows the global SFR density in the entire simulation box. The small 'step' visible at $z \approx 4$ is caused by the sudden increase in the time resolution for determining accretion, i.e. Δz between snapshots decreases by a factor of two at $z = 4$. Galaxies accrete most of their gas in the cold mode and this mode is responsible for an even larger fraction of the star formation. Because of outflows driven by supernovae and AGN, the SFR density is generally lower than the galaxy accretion rate density. The global SFR declines more rapidly than either the total and hot-mode accretion rate densities. This decline must therefore be caused by the drop in global cold-mode accretion rate, though with a delay.

accreted onto the halo.

The global accretion rate density onto *haloes*, i.e. the gas mass accreting onto resolved haloes per year and per comoving Mpc^3, is shown in the left panel of Figure 3.1 by the solid, black curve. The solid, red and blue curves show global accretion rates for hot- and cold-mode accretion, respectively. These global accretion rate densities are averaged over the time interval between two snapshots. The SFR density in the haloes we consider is shown by the green curve. The SFH in the entire box is shown by the dashed, grey curve. It is higher than the dashed, green curve, because the latter excludes star formation in subhaloes and unresolved haloes (i.e. $M_{\text{halo}} < 10^{10.8}$ M$_\odot$).

The global accretion rate onto resolved main haloes (solid, black curve) peaks at $z \approx 3$. It is fairly constant, varying only by about a factor of two from $z \approx 4$ down to $z \approx 0$. The average accretion rate onto haloes of a given mass decreases more strongly towards lower redshift (V11). However, the number of haloes at a fixed mass increases and higher mass haloes form with decreasing redshift. The combination of these effects results in an almost constant global accretion rate density. We note, however, that the normalization and shape are not fully converged with respect to resolution: higher resolution simulations may find higher total and cold accretion rate densities. Increasing the resolution would allow us to include haloes with lower masses, which would boost the cold accretion rate density by up to a factor of $\sim 2-3$. The total accretion rate density would therefore increase at $z \gtrsim 2$, where cold accretion dominates. The global accretion rate is an order of magnitude higher than the global SFR in the same haloes (green, dashed curve), indicating that most of the gas that accretes onto haloes never forms stars.

The global growth of haloes is dominated by cold accretion for $z > 2$, but by $z = 0$ the contribution of the hot mode exceeds that of the cold mode by an order of magnitude. The cold accretion rate density peaks around $z = 3$ and falls rapidly thereafter, while the hot accretion rate density increases down to $z \approx 2$ and flattens off at lower redshifts. The global SFR peaks around $z = 2$ and declines by an order of magnitude to $z = 0$. An order of magnitude drop is also visible for the global cold accretion rate from $z = 3$ to $z = 0$. Neither the total nor the hot accretion rate histories can explain the drop in the cosmic SFH, which must therefore be driven by the drop in the cold accretion rate.

The middle panel of Figure 3.1 shows the global accretion rates onto central *galaxies*. The green and grey curves are identical to the ones shown in the left panel. The black, red, and blue curves describe the total, hot, and cold accretion rate densities, respectively. The total accretion rate shows the amount of gas that joins the ISM. The gas can, however, be removed from the ISM by supernova and AGN feedback, as well as by dynamical processes. This is why the overall normalization of the SFR is generally lower than the ISM accretion rate. The global SFR peaks later than the global galaxy accretion rate ($z \approx 2$ versus $z \approx 3$, which corresponds to a difference of ~ 1 Gyr in the age of the Universe). This delay probably results from the time it takes to convert interstellar gas into stars.

The long gas consumption time scale implied by the assumed, Kennicutt star formation law (~ 1 Gyr for typical densities) allows the existence of reservoirs of accreted gas. The SFR can therefore temporarily be higher than the galaxy accretion rate, as happens for $z < 0.5$ (compare the dashed, green curve with the solid, black curve, which include the same sample of resolved haloes). Gas returned to the ISM by stellar mass loss, a process that is included in our simulations and that becomes important for $z < 1$ (Schaye et al., 2010; Leitner & Kravtsov, 2010), also increases the SFR relative to the accretion rate.

As we did in the left panel of Figure 3.1 for accretion onto haloes, we split the global accretion rate onto galaxies into separate contributions from the hot and cold modes. The global hot accretion rate peaks around $z = 2$, as does the SFR density. The hot accretion rate is, however, not nearly enough to account for all the star formation in these galaxies, falling short by at least a factor of 2 at all redshifts. At $z > 3$, the global cold accretion rate is an order of magnitude higher than the global hot accretion rate. This difference decreases to ~ 0.25 dex by $z = 0$. At all redshifts, it is mostly cold accretion that allows for the growth of *galaxies*, even though hot accretion dominates the growth of *haloes* below $z \approx 2$.

Comparing the middle panel to the left panel, we notice that the global cold accretion rate onto galaxies is a factor of $\sim 3 - 4$ lower than the cold accretion rate onto haloes. Not all cold gas that accretes onto haloes makes it into the central galaxy to form stars (see also V11). The shapes of the blue curves are, however, similar, indicating that the fraction of the gas accreting cold onto the halo that proceeds to accrete onto the galaxy is roughly constant with time.

The situation is very different for global hot accretion rates (red curves). Hot accretion onto the ISM has already peaked at $z \approx 2.5$, while hot accretion onto haloes continues to increase down to $z = 0$. This can be explained by noting that as the Universe evolves, gas is heated to higher temperatures, because haloes become more massive. In addition, the average density of the Universe goes down. The lower densities and higher temperatures gives rise to longer cooling times. Moreover, winds from supernovae and AGN eject low-entropy gas at high redshift, raising the entropy of the gas in haloes at low redshift (Crain et al., 2010a; McCarthy et al., 2011). Hence, as time goes on, more of the halo gas is unable to cool and reach the central galaxy. While the gravitational potential is the most important factor for the growth of haloes, for the growth of galaxies, the cooling function and feedback processes also come into play.

The right panel of Figure 3.1, which shows the global SFR densities due to hot and cold accretion, confirms that the main fuel for star formation is gas accreted in the cold mode. The difference becomes smaller towards lower redshift. However, even at $z = 0$ hot mode gas contributes 0.3 dex less than cold mode gas.

To investigate which haloes contribute most to the global accretion rates and SFHs, we show the same quantities as in Figure 3.1 for three different halo mass bins in Figure 3.2. From top to bottom, the mass ranges are $10^{11} \leq M_{halo} < 10^{12}$ $M_{\odot}$, $10^{12} \leq M_{halo} < 10^{13}$ $M_{\odot}$, and $M_{halo} \geq 10^{13}$ $M_{\odot}$, which contain 21813,

Figure 3.2: Evolution of global accretion rate densities onto haloes (left column), galaxies (middle column), and global SFR densities (right column) for different halo mass bins. From top to bottom only haloes have been included with: $10^{11} \leq M_{\mathrm{halo}} < 10^{12}$ M$_\odot$, $10^{12} \leq M_{\mathrm{halo}} < 10^{13}$ M$_\odot$, and $M_{\mathrm{halo}} \geq 10^{13}$ M$_\odot$. The curves show the same quantities as in Figure 3.1. Above $z \approx 3.5$ the highest mass bin contains no haloes. At all redshifts most of the cold halo accretion, galaxy accretion, and star formation happens in low-mass haloes (i.e. $M_{\mathrm{halo}} < 10^{12}$ M$_\odot$). At $z \gtrsim 2$ low-mass haloes also dominate the global hot halo accretion rates. At $z \lesssim 1$ the total halo accretion rate is dominated by high-mass haloes, but nearly all of the gas is accreted hot and unable to accrete onto galaxies.

2804, and 285 haloes at $z = 0$. The shape of the total halo accretion rate density in the lowest mass range is in agreement with that found by Bouché et al. (2010) based on an extended Press-Schechter formalism and a fit to dark matter accretion rates in N-body simulations.

For $z > 2$ the global accretion rate densities onto haloes (left column), galaxies (middle column), and the global star formation rate density (right column) are all dominated by haloes with $M_{\mathrm{halo}} < 10^{12}$ $M_\odot$ (top row). At that time, higher-mass haloes are still too rare to contribute significantly. Below $z \approx 2$ haloes with $M_{\mathrm{halo}} = 10^{12-13}$ $M_\odot$ (middle row) begin to contribute significantly and for accretion onto haloes, but not for accretion onto galaxies or star formation, their contribution is overtaken by $M_{\mathrm{halo}} = 10^{13-14}$ $M_\odot$ haloes (bottom row) around $z = 1$.

Observe that the global halo accretion rate density starts to decline at $z \approx 3$ and $z \approx 2$ for the low and middle halo mass bins, respectively, and that it keeps increasing down to $z = 0$ for $M_{\mathrm{halo}} \geq 10^{13}$ $M_\odot$. The global cold accretion rate density decreases with time for $z < 3$, $z < 2.5$, and $z < 1$ for the low, middle, and high halo mass bins, respectively.

Both the galaxy accretion rate density and the SFR density are dominated by $M_{\mathrm{halo}} < 10^{12}$ $M_\odot$ haloes at all redshifts. Towards lower redshifts, high-mass haloes account for larger fractions of the total galaxy accretion rate density and SFR density, though they never dominate. High-mass haloes do dominate the halo accretion rate at low redshift, but nearly all of the gas is accreted hot and only a very small fraction of this gas is subsequently able to cool down onto galaxies.

3.4 Effect of AGN feedback

It is interesting to see what the influence of AGN feedback is on our results. Because AGN feedback is more important in higher-mass haloes, for which hot-mode accretion is more important, we expect it to have a larger effect on the hot-mode accretion rate density. Moreover, it has been hypothesized (e.g. Kereš et al., 2005; Dekel & Birnboim, 2006) that hot, dilute gas may be more vulnerable to AGN feedback than cold streams and may therefore be preferentially prevented from accreting onto galaxies. Indeed, Theuns et al. (2002) had already demonstrated that supernova-driven outflows follow the path of least resistance, leaving the cold filaments that produce HI absorption intact.

McCarthy et al. (2011) have shown that feedback from AGN at high redshift increases the entropy of the halo gas at low redshift. The hot gas will therefore be even hotter and less dense at low redshift than it would be in the absence of AGN feedback, making it more susceptible to being heated or entrained in an outflow, and thus to being prevented from accreting.

We compare our fiducial simulation, which includes AGN feedback, to the OWLS 'reference model' which is identical to our fiducial run except that it does

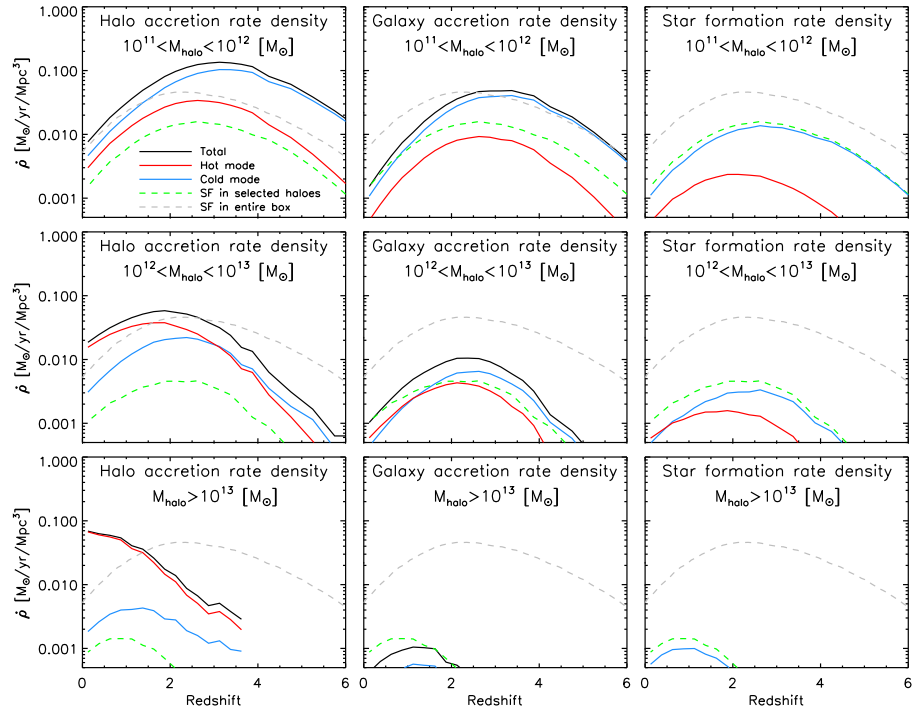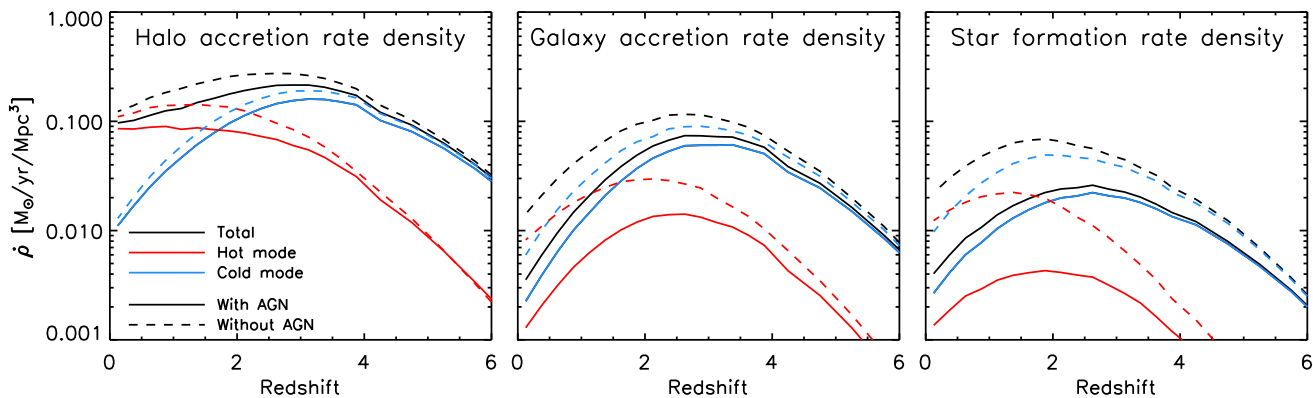**Figure 3.3:** Evolution of global accretion rate densities onto haloes (left column), galaxies (middle column), and global SFR densities for simulations with (solid curves, same as in Figure 3.1) and without (dashed curves) AGN feedback. The black, red, and blue curves show the global accretion and SFR densities from all, hot-mode, and cold-mode accretion, respectively. AGN feedback suppresses halo accretion only slightly, but the effect on galaxy accretion and star formation is large, up to an order of magnitude. AGN feedback preferentially suppresses *hot*-mode galaxy accretion and star formation from gas accreted in the *hot* mode.

not include black holes and AGN feedback. This allows us to assess the effect of AGN feedback on the global hot and cold accretion rates. Figure 3.3 shows the same solid curves as were shown in Figure 3.1. They indicate the total, hot, and cold accretion rate densities onto haloes (left panel) and onto galaxies (middle panel) and the star formation rate density resulting from all, hot, and cold accretion (right panel). The dashed curves show the same global accretion rates and SFHs for the simulation without AGN feedback. For accretion onto galaxies and for star formation the differences are striking. When AGN feedback is excluded, late-time star formation is no longer predominantly fuelled by gas accreted in the cold mode.

As expected, all accretion rate densities are reduced by the inclusion of AGN feedback. The effect on halo accretion is, however, small, as was also shown by V11. The hot and cold halo accretion rate densities are reduced by at most 0.2 and 0.1 dex, respectively. This reduction implies that AGN feedback also affects some gas outside of haloes. Even though the effect is small, AGN feedback reduces hot halo accretion more than cold halo accretion.

The differential effect of AGN feedback on hot and cold accretion is much more pronounced for accretion onto galaxies than for accretion onto haloes and it increases towards lower redshift. At very high redshift ($z = 9$), Powell et al. (2011) have shown that outflows (driven by supernova feedback) do not affect the galaxy inflow rates. Our results indicate that this may change towards lower redshifts, when densities are much lower. While AGN feedback reduces cold accretion rate densities by up to 0.4 dex (at $z = 0$), the hot accretion rate densities decrease by up to 0.8 dex (also at $z = 0$). The SFR densities are reduced by up to 0.6 dex for star formation powered by cold-mode accretion, but by 1 dex for hot-mode accretion. The reduction due to AGN feedback is thus ~ 0.4 dex greater for the hot mode than for the cold mode, both for galaxy accretion and for star formation. The larger reduction indicates that AGN feedback preferentially, but not exclusively, prevents hot mode gas from accreting onto galaxies and participating in star formation.

Hence, the inclusion of AGN feedback strongly boosts the size of the drop in the cosmic SFR at late times. This preferential suppression of hot accretion is the result of two effects, namely of the differential effect at a fixed halo mass, indicating that hot-mode gas is more vulnerable to feedback than cold-mode gas, and of the fact that AGN feedback is effective only in massive haloes (with $M_{halo} \gtrsim 10^{12}$), for which hot accretion is important. The latter is the dominant effect.

3.5   Conclusions

We have investigated the evolution of the global gas accretion rate densities onto haloes and onto their central galaxies and we have done so for both the hot and cold accretion modes. In addition, we studied the contributions from gas

accreted through the cold and hot modes to the cosmic star formation history. We made use of a 100 Mpc/h, 2×512^3 particle SPH simulation from the OWLS project that includes radiative cooling (computed element by element and thus including metal lines), star formation, stellar mass loss, supernova feedback, and AGN feedback. We isolated the effect of AGN feedback by comparing to a second simulation that did not include AGN, but which was otherwise identical. The hot and cold accretion modes were separated by using a fixed maximum past temperature threshold of $T_{\max} = 10^{5.5}$ K.

The global gas accretion rate density onto haloes is much higher than that onto galaxies and both rates exceed the cosmic SFR density. This confirms the finding of V11 that most of the gas accreting onto haloes does not result in star formation. This is the case for both accretion modes, but the differences are larger for the hot mode.

The global SFR declines after $z \approx 2$, whereas the global hot-mode accretion rate onto haloes shows no such trend. From this, we conclude that the global SFR follows the drop in the global cold-mode accretion rate onto haloes, which sets in at $z \approx 3$, but with a delay of order the gas consumption time scale in the ISM. Star formation tracks cold-mode accretion rather than hot-mode accretion because cold streams can reach the central galaxy, where star formation takes place, much more easily than gas that is shock-heated to high temperatures near the virial radius. Much of the hot gas cannot cool within a Hubble time and therefore cannot accrete onto the central galaxy. In addition, we demonstrated that it is very important that hot gas is more susceptible to removal by outflows driven by feedback from AGN. Without AGN feedback, gas accreted in the hot mode contributes significantly to the cosmic SFR below $z = 1$ and the drop in the SFR below $z = 2$ would be much smaller.

For the hot mode the difference between the accretion rates onto haloes and onto galaxies is larger at lower redshifts. While the hot accretion mode dominates the growth of haloes by an order of magnitude at $z \approx 0$, it is still less important than cold accretion for the growth of the central galaxies. At $z > 2$, cold accretion even dominates the global accretion rate onto haloes.

We demonstrated that AGN feedback suppresses accretion onto galaxies and that it does so much more efficiently for the hot mode than for the cold mode. This happens because AGN feedback only becomes more efficient than feedback from star formation in high-mass haloes, which are dominated by hot accretion, and because hot-mode gas is more dilute and therefore more vulnerable to feedback. In addition, as demonstrated by McCarthy et al. (2011), by ejecting low-entropy halo gas at high redshift ($z \gtrsim 2$), AGN feedback results in an increase of the entropy, and thus a reduction of the cooling rates, of hot halo gas at low redshift.

While Kereš et al. (2009a) did not investigate accretion onto haloes, they did also find that cold accretion is most important for the growth of galaxies, with hot accretion becoming increasingly important towards lower redshifts (see also Kereš et al. 2005; Ocvirk et al. 2008; Brooks et al. 2009; V11). However, their

simulation included neither winds from supernovae nor feedback from AGN. AGN feedback was in fact ignored by all previous cosmological simulations investigating gas accretion except for Khalatyan et al. (2008), who simulated a single object, and except for V11. Our results suggest that the neglect of this important process leads to a strong overestimate of the global accretion rate and SFR densities and of the importance of the hot accretion mode for galaxy accretion and star formation.

In summary, the rapid decline in the cosmic SFR density below $z = 2$ is driven by the corresponding drop in the cold accretion rate density onto haloes. The total accretion rate onto haloes falls off much less rapidly because the hot mode becomes increasingly important. AGN feedback, which acts preferentially on gas accreted in the hot mode, prevents the hot halo gas from accreting onto galaxies and forming stars and is therefore a crucial factor in the steep decline of the cosmic SFR density.

Acknowledgements

4

Properties of gas in and around galaxy haloes

We study the properties of gas inside and around galaxy haloes as a function of radius and halo mass, focusing mostly on $z = 2$, but also showing some results for $z = 0$. For this purpose, we use a suite of large cosmological, hydrodynamical simulations from the OverWhelmingly Large Simulations project. The properties of cold- and hot-mode gas, which we separate depending on whether the temperature has been higher than $10^{5.5}$ K while it was extragalactic, are clearly distinguishable in the outer parts of massive haloes (virial temperatures $\gg 10^5$ K). The differences between cold- and hot-mode gas resemble those between inflowing and outflowing gas. The cold-mode gas is mostly confined to clumpy filaments that are approximately in pressure equilibrium with the diffuse, hot-mode gas. Besides being colder and denser, cold-mode gas typically has a much lower metallicity and is much more likely to be infalling. However, the spread in the properties of the gas is large, even for a given mode and a fixed radius and halo mass, which makes it impossible to make strong statements about individual gas clouds. Metal-line cooling causes a strong cooling flow near the central galaxy, which makes it hard to distinguish gas accreted through the cold and hot modes in the inner halo. Stronger feedback results in larger outflow velocities and pushes hot-mode gas to larger radii. The gas properties evolve as expected from virial arguments, which can also account for the dependence of many gas properties on halo mass. We argue that cold streams penetrating hot haloes are observable as high-column density H I Lyman-α absorption systems in sightlines near massive foreground galaxies.

Freeke van de Voort & Joop Schaye
Monthly Notices of the Royal Astronomical Society
Submitted (2012), arXiv:1111.5039

4.1   Introduction

The gaseous haloes around galaxies grow by accreting gas from their surroundings, the intergalactic medium, which is the main reservoir for baryons. The galaxies themselves grow by accreting gas from their haloes, from which they can form stars. Some of the gas is, however, returned to the circumgalactic medium by galactic winds driven by supernovae (SNe) or active galactic nuclei (AGN) and by dynamical processes such as tidal or ram pressure forces. Such interactions between the different gas phases are essential for galaxy formation and evolution.

The physical state of the gas in and around haloes will determine how fast galaxies grow. Quantifying and understanding the properties of the gas is therefore vital for theories of galaxy formation. It is also crucial for making predictions and for the interpretation of observations as the physical state of the gas determines how much light is absorbed and emitted.

Theoretical and computational studies of the accretion of gas onto galaxies have revealed the existence of two distinct modes. In the first mode the inflowing gas experiences an accretion shock as it collides with the hot, hydrostatic halo near the virial radius. At that point it is shock-heated to temperatures similar to the virial value and typically remains part of the hot halo for longer than a dynamical time. If it reaches a sufficiently high density, it can cool radiatively and settle into a disc (e.g. Rees & Ostriker, 1977; White & Rees, 1978; Fall & Efstathiou, 1980). This mode is referred to as 'hot-mode accretion' (Katz et al., 2003; Kereš et al., 2005). If, on the other hand, the cooling time of the gas is short compared to the dynamical time, which is the case for haloes of sufficiently low mass, a hot halo is unable to form and the accreting gas will not go through a shock near the virial radius. The accretion rate then depends on the infall rate instead of on the cooling rate (White & Frenk, 1991; Birnboim & Dekel, 2003; Dekel & Birnboim, 2006). Additionally, simulations have shown that much of the gas enters the halo along dense filaments or in clumps, which gives rise to short cooling times, even in the presence of a hot, hydrostatic halo. This denser gas does not go through an accretion shock near the virial radius and will therefore remain cold until it accretes onto the central galaxy or is hit by an outflow (e.g. Kereš et al., 2005; Dekel et al., 2009a; van de Voort et al., 2011a). We refer to this mode as 'cold-mode accretion' (Katz et al., 2003; Kereš et al., 2005).

Hot- and cold-mode accretion play very different roles in the formation of galaxies and their gaseous haloes (Kereš et al., 2005; Ocvirk et al., 2008; Kereš et al., 2009a,b; Brooks et al., 2009; Dekel et al., 2009a; Crain et al., 2010a; van de Voort et al., 2011a,b; Powell et al., 2011; Faucher-Giguère et al., 2011). It has been shown that cold-mode accretion is more important at high redshift, when the density of the Universe is higher. Hot-mode accretion dominates the fuelling of the gaseous haloes of high-mass systems (halo mass $> 10^{12} \, M_\odot$; e.g. Ocvirk et al., 2008; van de Voort et al., 2011a). The importance of hot-mode accretion is much reduced when considering accretion onto galaxies (as opposed to haloes)

(Kereš et al., 2009a; van de Voort et al., 2011a). At $z \geq 1$ all galaxies accrete more than half of their material in the cold mode, although the contribution of hot-mode accretion is not negligible for high-mass haloes. Cold-mode accretion provides most of the fuel for star formation and shapes the cosmic star formation rate density (van de Voort et al., 2011b).

van de Voort et al. (2011a,b) investigated the roles of feedback mechanisms on the gas accretion. They found that while the inclusion of metal-line cooling has no effect on the accretion onto haloes, it does increase the accretion rate onto galaxies, because it decreases the cooling time of the hot halo gas. Feedback from SNe and AGN can reduce the accretion rates onto haloes by factors of a few, but accretion onto galaxies is suppressed by up to an order of magnitude. The inclusion of AGN feedback is particularly important for suppressing hot-mode accretion onto galaxies, because it is mainly effective in high-mass haloes and because diffuse gas is more susceptible to outflows.

Hot, hydrostatic halo gas is routinely studied using X-ray observations of galaxy groups and clusters and has perhaps even been detected around individual galaxies (e.g. Crain et al., 2010a,b; Anderson & Bregman, 2011). As of yet, there is no direct observational evidence for cold-mode accretion, even though there are claims of individual detections in H I absorption based on the low metallicity and proximity to a galaxy of the absorption system (Ribaudo et al., 2011; Giavalisco et al., 2011). Cosmological simulations can reproduce the observed H I column density distribution (Altay et al., 2011). They show that cold-mode accretion is responsible for much of the observed high column density H I absorption at $z \sim 3$. In particular, most of the detected Lyman limit and low column density damped Lyman-α absorption may arise in cold accretion streams (Fumagalli et al., 2011a; van de Voort et al., 2012).

It has also been claimed that the diffuse Lyman-α emission detected around some high-redshift galaxies is powered by cold accretion (e.g. Fardal et al., 2001; Dijkstra & Loeb, 2009; Goerdt et al., 2010; Rosdahl & Blaizot, 2011), but both simulations and observations indicate that the emission is more likely scattered light from central H II regions (e.g. Furlanetto et al., 2005; Faucher-Giguère et al., 2010; Steidel et al., 2010; Hayes et al., 2011; Rauch et al., 2011).

The temperature is, however, not the only difference between the two accretion modes. In this paper we use the suite of cosmological hydrodynamical simulations from the OverWhelmingly Large Simulations project (OWLS; Schaye et al., 2010) to investigate other physical properties, such as the gas density, pressure, entropy, metallicity, radial peculiar velocity, and accretion rate of the gas in the two modes. We will study the dependence of gas properties on radius for haloes of total mass $\sim 10^{12}$ M$_\odot$ and the dependence on halo mass of the properties of gas just inside the virial radius. Besides contrasting the hot and cold accretion modes, we will also distinguish between inflowing and outflowing gas. While most of our results will be presented for $z = 2$, when both hot- and cold-mode accretion are important for haloes of mass $\sim 10^{12}$ M$_\odot$, we will also present some results for $z = 0$, which are therefore directly relevant for ob-

servations of gas around the Milky Way. We will make use of the different OWLS runs to investigate how the results vary with the efficiency of the feedback and the cooling.

This paper is organized as follows. The simulations are described in Section 4.2, including the model variations, the way in which haloes are identified, and our method for distinguishing gas accreting in the hot and cold modes. In Sections 4.3 and 4.4 we study the radial profiles and the dependence on halo mass, respectively. In Section 4.5 we discuss the difference in physical properties between inflowing and outflowing gas. We assess the effect of metal-line cooling and feedback from SNe and AGN on the gas properties in Section 4.6. In Section 4.7 we study the properties of gas around Milky Way-sized galaxies at $z = 0$. Finally, we discuss and summarize our conclusions in Section 4.8.

4.2   Simulations

To investigate the gas properties in and around haloes, we make use of simulations taken from the OWLS project (Schaye et al., 2010), which consists of a large number of cosmological simulations, with varying (subgrid) physics. Here, we make use of a subset of these simulations. We first summarize the reference simulation, from which we derive our main results. The other simulations are described in Section 4.2.1. For a full description of the simulations, we refer the reader to Schaye et al. (2010). Here, we will only summarize their main properties.

We use a modified version of GADGET-3 (last described in Springel, 2005b), a smoothed particle hydrodynamics (SPH) code that uses the entropy formulation of SPH (Springel & Hernquist, 2002), which conserves both energy and entropy where appropriate.

All the cosmological simulations used in this work assume a ΛCDM cosmology with parameters derived from the WMAP year 3 data, $\Omega_m = 1 - \Omega_\Lambda = 0.238$, $\Omega_b = 0.0418$, $h = 0.73$, $\sigma_8 = 0.74$, $n = 0.951$ (Spergel et al., 2007). These values are consistent[1] with the WMAP year 7 data (Komatsu et al., 2011). The primordial abundances are $X = 0.752$ and $Y = 0.248$, where X and Y are the mass fractions of hydrogen and helium, respectively.

A cubic volume with periodic boundary conditions is defined, within which the mass is distributed over N^3 dark matter and as many gas particles. The box size (i.e. the length of a side of the simulation volume) of the simulations used in this work are 25, 50, and 100 h^{-1}Mpc, with $N = 512$. The (initial) particle masses for baryons and dark matter are $1.5 \times 10^7 (\frac{L_{box}}{50\ h^{-1}\text{Mpc}})^3$ M$_\odot$ and $7.0 \times 10^7 (\frac{L_{box}}{50\ h^{-1}\text{Mpc}})^3$ M$_\odot$, respectively, and are listed in Table 4.1. We use the notation $L{*}{*}{*}N\#\#\#$, where ${*}{*}{*}$ indicates the box size in comoving Mpc/h and

---

[1]The most significant discrepancy is in σ_8, which is 8 per cent, or 2.3σ, lower than the value favoured by the WMAP 7-year data.

Table 4.1: Simulation parameters: simulation identifier, comoving box size (L_{box}), number of dark matter particles (N, the number of baryonic particles is equal to the number of dark matter particles), mass of dark matter particles (m_{DM}), initial mass of gas particles ($m_{gas}^{initial}$), number of haloes with $10^{11.5}$ M$_\odot$ < M_{halo} < $10^{12.5}$ M$_\odot$, and number of haloes with more than 100 dark matter particles.

simulation	L_{box} (h^{-1}Mpc)	N	m_{DM} (M$_\odot$)	$m_{gas}^{initial}$ (M$_\odot$)	number of haloes with $10^{11.5}$ M$_\odot$ < M_{halo} < $10^{12.5}$ M$_\odot$	number of resolved haloes at $z = 2$
L100N512	100	512^3	5.56×10^8	1.19×10^8	4407 ($z = 2$)	32167
L050N512	50	512^3	6.95×10^7	1.48×10^7	518 ($z = 2$); 1033 ($z = 0$)	32663
L025N512	25	512^3	8.68×10^6	1.85×10^6	59 ($z = 2$)	25813

the number of particles per dimension. The gravitational softening length is initially 3.9 $(\frac{L_{\text{box}}}{50\ h^{-1}\text{Mpc}})$ h^{-1} comoving kpc, i.e. 1/25 of the mean dark matter particle separation, but we imposed a maximum of 1 $(\frac{L_{\text{box}}}{50\ h^{-1}\text{Mpc}})$ h^{-1}kpc proper. We use simulation *REF_L050N512* for our main results. The *L025N512* simulations are used for images, for comparisons between simulations with different subgrid physics, and for resolution tests. The *L100N512* run is only used for the convergence tests shown in the Appendix.

The abundances of eleven elements (hydrogen, helium, carbon, nitrogen, oxygen, neon, magnesium, silicon, sulphur, calcium, and iron) released by massive stars (type II SNe and stellar winds) and intermediate mass stars (type Ia SNe and asymptotic giant branch stars) are followed as described in Wiersma et al. (2009b). We assume the stellar initial mass function (IMF) of Chabrier (2003), ranging from 0.1 to 100 $M_\odot$. As described in Wiersma et al. (2009a), radiative cooling and heating are computed element-by-element in the presence of the cosmic microwave background radiation and the Haardt & Madau (2001) model for the UV/X-ray background from galaxies and quasars. The gas is assumed to be optically thin and in (photo)ionization equilibrium.

Star formation is modelled according to the recipe of Schaye & Dalla Vecchia (2008). The Jeans mass cannot be resolved in the cold, interstellar medium (ISM), which could lead to artificial fragmentation (e.g. Bate & Burkert, 1997). Therefore, a polytropic equation of state $P_{\text{tot}} \propto \rho_{\text{gas}}^{4/3}$ is implemented for densities exceeding $n_H = 0.1$ cm^{-3}, where P_{tot} is the total pressure and ρ_{gas} the density of the gas. This equation of state makes the Jeans mass, as well as the ratio of the Jeans length and the SPH smoothing kernel, independent of the density. Gas particles whose proper density exceeds $n_H \geq 0.1$ cm^{-3} while they have temperatures $T \leq 10^5$ K are moved on to this equation of state and can be converted into star particles. The star formation rate per unit mass depends on the gas pressure and is set to reproduce the observed Kennicutt-Schmidt law (Kennicutt, 1998).

Feedback from star formation is implemented using the prescription of Dalla Vecchia & Schaye (2008). About 40 per cent of the energy released by type II SNe is injected locally in kinetic form. The rest of the energy is assumed to be lost radiatively. Each gas particle within the SPH smoothing kernel of the newly formed star particle has a probability of being kicked. For the reference model, the mass loading parameter $\eta = 2$, meaning that, on average, the total mass of the particles being kicked is twice the mass of the star particle formed. Because the winds sweep up surrounding material, the effective mass loading can be much higher. The initial wind velocity is 600 km s^{-1} for the reference model. Schaye et al. (2010) showed that these parameter values yield a peak global star formation rate density that agrees with observations.

Table 4.2: Simulation parameters: simulation identifier, cooling including metals (Z cool), initial wind velocity (v_{wind}), initial wind mass loading (η), AGN feedback included (AGN). Differences from the reference model are indicated in bold face.

simulation	Z cool	v_{wind} (km s^{-1})	η	AGN
REF	yes	600	2	no
NOSN_NOZCOOL	**no**	**0**	**0**	no
NOZCOOL	**no**	600	2	no
WDENS	yes	**density dependent**		no
AGN	yes	600	2	**yes**

4.2.1 Variations

To investigate the effect of feedback and metal-line cooling, we have performed a suite of simulations in which the subgrid prescriptions are varied. These are listed in Table 4.2.

The importance of metal-line cooling can be demonstated by comparing the reference simulation (*REF*) to a simulation in which primordial abundances are assumed when calculating the cooling rates (*NOZCOOL*). We also performed a simulation in which both cooling by metals and feedback from SNe were omitted (*NOSN_NOZCOOL*). To study the effect of SN feedback, this simulation can be compared to (*NOZCOOL*).

In massive haloes the pressure of the ISM is too high for winds with velocities of 600 km s^{-1} to blow the gas out of the galaxy (Dalla Vecchia & Schaye, 2008). To make the winds effective at higher halo masses, the velocity can be scaled with the local sound speed, while adjusting the mass loading so as to keep the energy injected per unit stellar mass constant at ≈ 40 per cent (*WDENS*).

Finally, we have included AGN feedback (*AGN*). Black holes grow via mergers and gas accretion and inject 1.5 per cent of the rest-mass energy of the accreted gas into the surrounding matter in the form of heat. The model is based on the one introduced by Springel et al. (2005) and is described and tested in Booth & Schaye (2009), who also demonstrate that the simulation reproduces the observed mass density in black holes and the observed scaling relations between black hole mass and central stellar velocity dispersion and between black hole mass and stellar mass. McCarthy et al. (2010) have shown that model *AGN* reproduces the observed stellar mass fractions, star formation rates, and stellar age distributions in galaxy groups, as well as the thermodynamic properties of the intragroup medium.

4.2.2 Identifying haloes

The first step towards finding gravitationally bound structures is to identify dark matter haloes. These can be found using a Friends-of-Friends (FoF) algorithm. If the separation between two dark matter particles is less than 20 per cent of the average separation (the linking length $b = 0.2$), they are placed in the same group. Baryonic particles are linked to a FoF halo if their nearest dark matter neighbour is in that halo. We then use SUBFIND (Dolag et al., 2009) to find the most bound particle of a FoF halo, which serves as the halo centre. In this work we use a spherical overdensity criterion, considering all the particles in the simulation. We compute the virial radius, R_{vir}, within which the average density agrees with the prediction of the top-hat spherical collapse model in a ΛCDM cosmology (Bryan & Norman, 1998). At $z = 2$ this corresponds to a density of $\rho = 169\langle\rho\rangle$.

We include only haloes containing more than 100 dark matter particles in our analysis, corresponding to a minimum dark matter halo mass of $M_{\mathrm{halo}} = 10^{10.7}$, $10^{9.8}$, and $10^{8.9}$ $M_\odot$ in the 100, 50, and 25 h^{-1}Mpc box, respectively. For these limits our mass functions agree very well with the Sheth & Tormen (1999) fit. Table 4.1 lists, for each simulation of the reference model, the number of haloes with mass $10^{11.5}$ $M_\odot < M_{\mathrm{halo}} < 10^{12.5}$ $M_\odot$ and the number of haloes with more than 100 dark matter particles.

4.2.3 Hot- and cold-mode gas

During the simulations the maximum past temperature, T_{max}, was stored in a separate variable. The variable was updated for each SPH particle at every time step for which the temperature was higher than the previous maximum past temperature. The artificial temperature the particles obtain when they are on the equation of state (i.e. when they are part of the unresolved multiphase ISM) was ignored in this process. This may cause us to underestimate the maximum past temperature of gas that experienced an accretion shock at densities $n_{\mathrm{H}} > 0.1$ cm^{-3}. Ignoring such shocks is, however, consistent with our aims, as we are interested in the maximum temperature reached *before* the gas entered the galaxy. Note, however, that the maximum past temperature of some particles may reflect shocks in outflowing rather than accreting gas.

Another reason why T_{max} may underestimate the true maximum past temperature, is that in SPH simulations a shock is smeared out over a few smoothing lengths, leading to in-shock cooling (Hutchings & Thomas, 2000). If the cooling time is of the order of, or smaller than, the time step, then the maximum temperature will be underestimated. Creasey et al. (2011) have shown that a particle mass of 10^6 $M_\odot$ is sufficient to avoid numerical overcooling of accretion shocks onto haloes, like in our high-resolution simulations (*L025N512*). The Appendix shows that our lower-resolution simulations give very similar results.

Even with infinite resolution, the post-shock temperatures may, however, not

be well defined. Because electrons and protons have different masses, they will have different temperatures in the post-shock gas and it may take some time before they equilibrate through collisions or plasma effects. We have ignored this complication. Another effect, which was also not included in our simulation, is that shocks may be preceded by the radiation from the shock, which may affect the temperature evolution. Disregarding these issues, van de Voort et al. (2011a) showed that the distribution of T_{max} is bimodal and that a cut at $T_{max} = 10^{5.5}$ K naturally divides the gas into cold- and hot-mode accretion and that it produces similar results as studies based on adaptive mesh refinement simulations (Ocvirk et al., 2008). This T_{max} threshold was chosen because the cooling function peaks at $10^{5-5.5}$ K (e.g. Wiersma et al., 2009a), which results in a minimum in the temperature distribution. Additionally, the UV background can only heat gas to about 10^5 K, which is therefore characteristic for cold-mode accretion. In this work we use the same $T_{max} = 10^{5.5}$ K threshold to separate the cold and hot modes.

4.3 Physical properties: dependence on radius

The gas in the Universe is distributed in a cosmic web of sheets, filaments, and haloes. The filaments also affect the structure of the haloes that reside inside them or at their intersections. At high redshift, cold, narrow streams penetrate hot haloes and feed galaxies efficiently (e.g. Kereš et al., 2005; Dekel & Birnboim, 2006; Agertz et al., 2009; Ceverino et al., 2010; van de Voort et al., 2011a). The middle row of Figure 4.1 shows the overdensity in several haloes with different masses, ranging from $M_{halo} = 10^{12.5}$ (left panel) to $10^{10.5}$ M$_\odot$ (right panel), taken from the high-resolution reference simulation (*REF_L025N512*) at $z = 2$. Each image is four virial radii on a side, so the physical scale decreases with decreasing halo mass, as indicated in the middle panels. To illustrate the morphologies of gas that was accreted in the different modes, we show the density of the cold- and hot-mode gas separately in the top and bottom panels, respectively. The spatial distribution is clearly different. Whereas the cold-mode gas shows clear filaments and many clumps, the hot-mode gas is much more spherically symmetric and smooth, particularly for the higher halo masses. The filaments become broader, relative to the size of the halo, for lower mass haloes. In high-mass haloes, the streams look disturbed and some fragment into small, dense clumps, whereas they are broad and smooth in low-mass haloes. Cold-mode accretion is clearly possible in haloes that are massive enough to have well-developed virial shocks if the density of the accreting gas is high, which is the case when the gas accretes along filaments or in clumps.

   Figure 4.2 shows several physical quantities for the gas in a cubic $1\ h^{-1}$ comoving Mpc region, which is about four times the virial radius, centred on the 10^{12} M$_\odot$ halo from Figure 4.1. These properties are (from the top-left to the bottom-right): gas overdensity, temperature, maximum past temperature, pres-
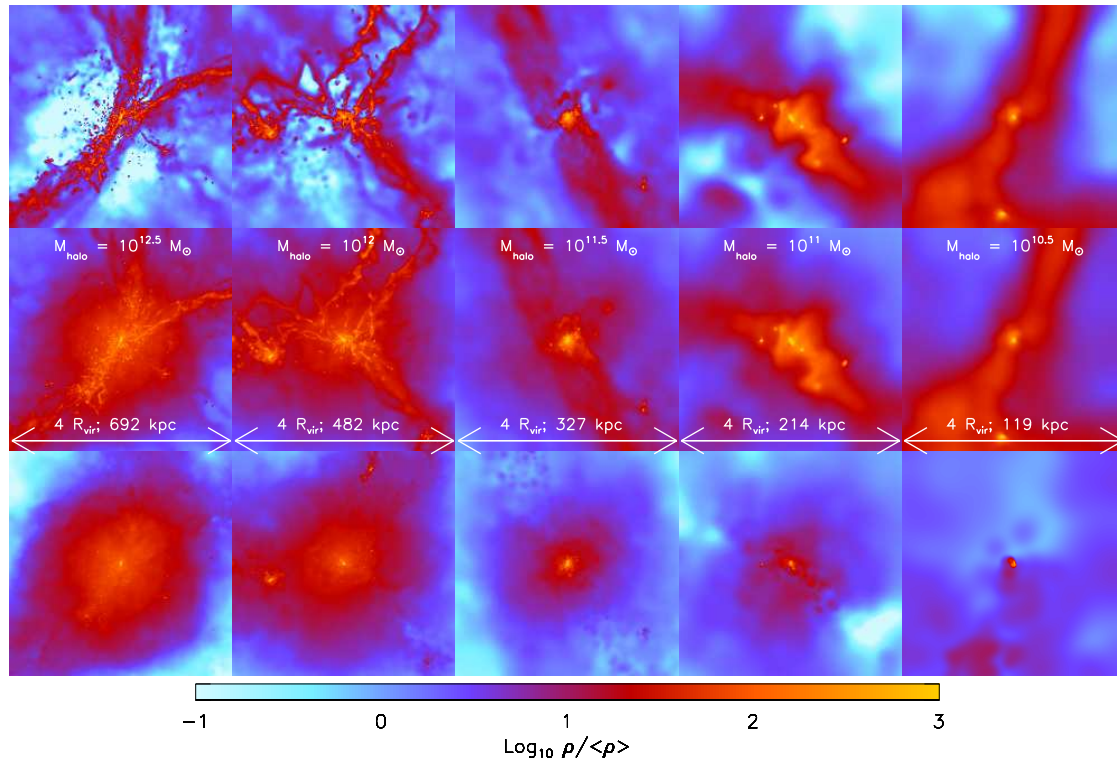
Figure 4.1: Gas overdensity at $z = 2$ in and around haloes with, from left to right, $M_{halo} = 10^{12.5}$, 10^{12}, $10^{11.5}$, 10^{11}, and $10^{10.5}$ M$_\odot$ taken from the simulation *REF_L025N512*. All images show projections of the gas density in cubes of 4 virial radii on a side. The proper sizes of the images are indicated in the panels of the middle row. In the middle column all gas was included. In the top (bottom) row we have only included cold- (hot-)mode gas, i.e. gas with $T_{max} < 10^{5.5}$ K ($T_{max} \geq 10^{5.5}$ K). The filaments, streams, and dense clumps consist of gas that has never been heated to temperatures greater than $10^{5.5}$ K.
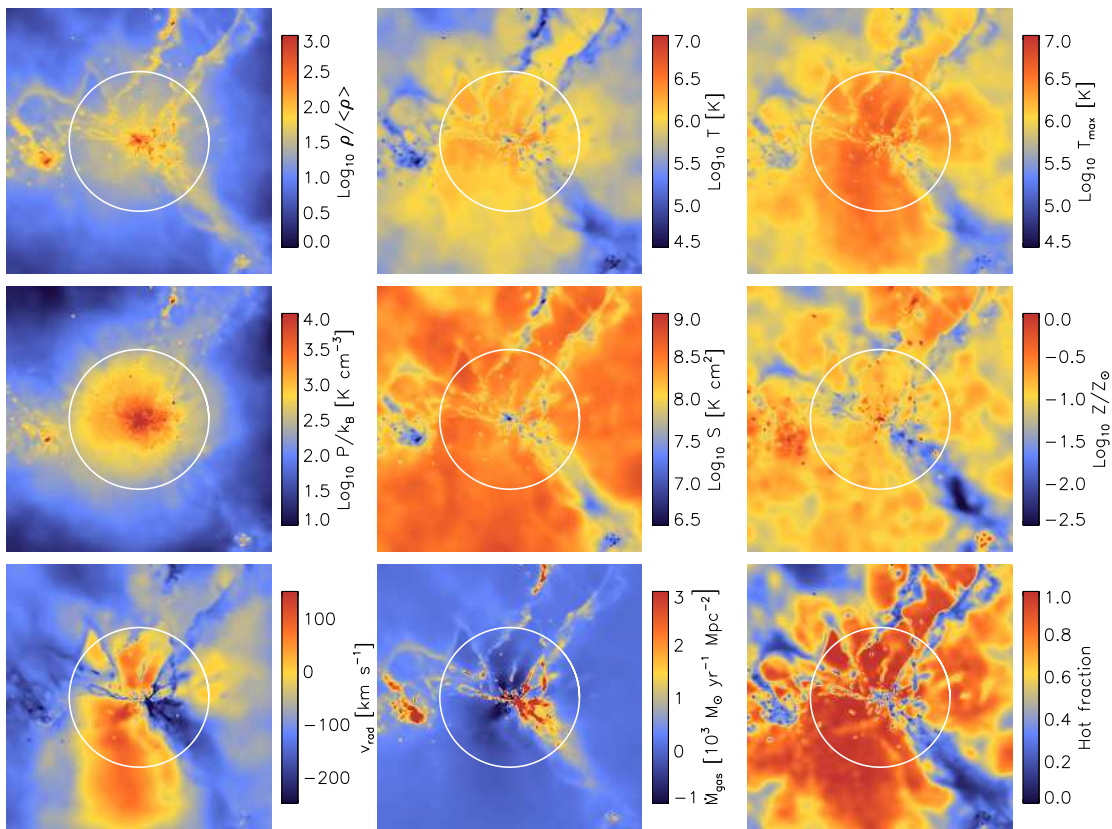
Figure 4.2: From the top-left to the bottom-right: gas overdensity, temperature, maximum past temperature, pressure, entropy, metallicity, radial peculiar velocity, radial mass flux (in solar mass per year per proper Mpc^2), and hot fraction in a cubic 1 h^{-1} comoving Mpc region centred on a halo of $M_{\rm halo} \approx 10^{12}$ M$_\odot$ at $z = 2$ taken from the *REF_L025N512* simulation. The white circles indicate the virial radius.

sure, entropy, metallicity, radial peculiar velocity, radial mass flux, and finally the "hot fraction" which we define as the mass fraction of the gas that was accreted in the hot mode (i.e. that has $T_{max} \geq 10^{5.5}$ K). The properties are mass-weighted and projected along the line of sight. The virial radius is 264 h^{-1} comoving kpc and is indicated by the white circles.

In Figure 4.3 we show the same quantities as in Figure 4.2 as a function of radius for the haloes with $10^{11.5}$ M$_\odot$ < M_{halo} < $10^{12.5}$ M$_\odot$ at $z = 2$ in simulation *REF_L050N512*. The black curves show the median values for all gas, except for the last two panels which show the mean values. The red (blue) curves show the median or mean values for hot- (cold-)mode gas, i.e. gas with maximum past temperatures above (below) $10^{5.5}$ K. The shaded regions show values within the 16th and 84th percentiles. Hot-mode gas at radii larger than $2R_{vir}$ is dominated by gas associated with other haloes and/or large-scale filaments.

All the results we show are weighted by mass. In other words, we stacked all 518 haloes in the selected mass range using R/R_{vir} as the radial coordinate. The black curves in Figure 4.3 (except for the last two panels) then show the values of the corresponding property (e.g. the gas overdensity in the top-left panel) that divide the total mass in each radial bin in half, i.e. half the mass lies above the curve. We have done the same analysis for volume-weighted quantities by computing, as a function of radius, the values of each property that divides the total volume, i.e. the sum of m_{gas}/ρ, in half but we do not show the results. The volume is completely dominated by hot-mode gas out to twice the virial radius, reaching 50 per cent at $3R_{vir}$. Even though the volume-weighted hot fraction is very different, the properties of the gas and the differences between the properties of hot- and cold-mode gas are similar if we weigh by volume rather than mass.

We find that the median density of cold-mode gas is higher, by up to 1 dex, than that of hot-mode gas and that its current temperature is lower, by up to 2 dex, at least beyond $0.2R_{vir}$. The hot-mode maximum past temperature is on average about an order of magnitude higher than the cold-mode maximum past temperature. The median pressure of the hot-mode gas only exceeds that of the cold mode by a factor of a few, but for the entropy the difference reaches 2.5 dex. For $R \gtrsim R_{vir}$ the gas metallicity in the cold mode is lower and has a much larger spread (four times larger at R_{vir}) than in the hot mode. Cold-mode gas is flowing in at much higher velocities, by up to 150 km s^{-1}, and dominates the accretion rate at all radii. Below, we will discuss these gas properties individually and in more detail.

4.3.1 Density

The halo shown in Figure 4.2 is being fed by dense, clumpy filaments as well as by cooling diffuse gas. The filaments are overdense for their radius, both inside and outside the halo. The top-left panel of Figure 4.3 shows that the overdensity of both hot- and cold-mode gas increases with decreasing radius, from ~ 10 at
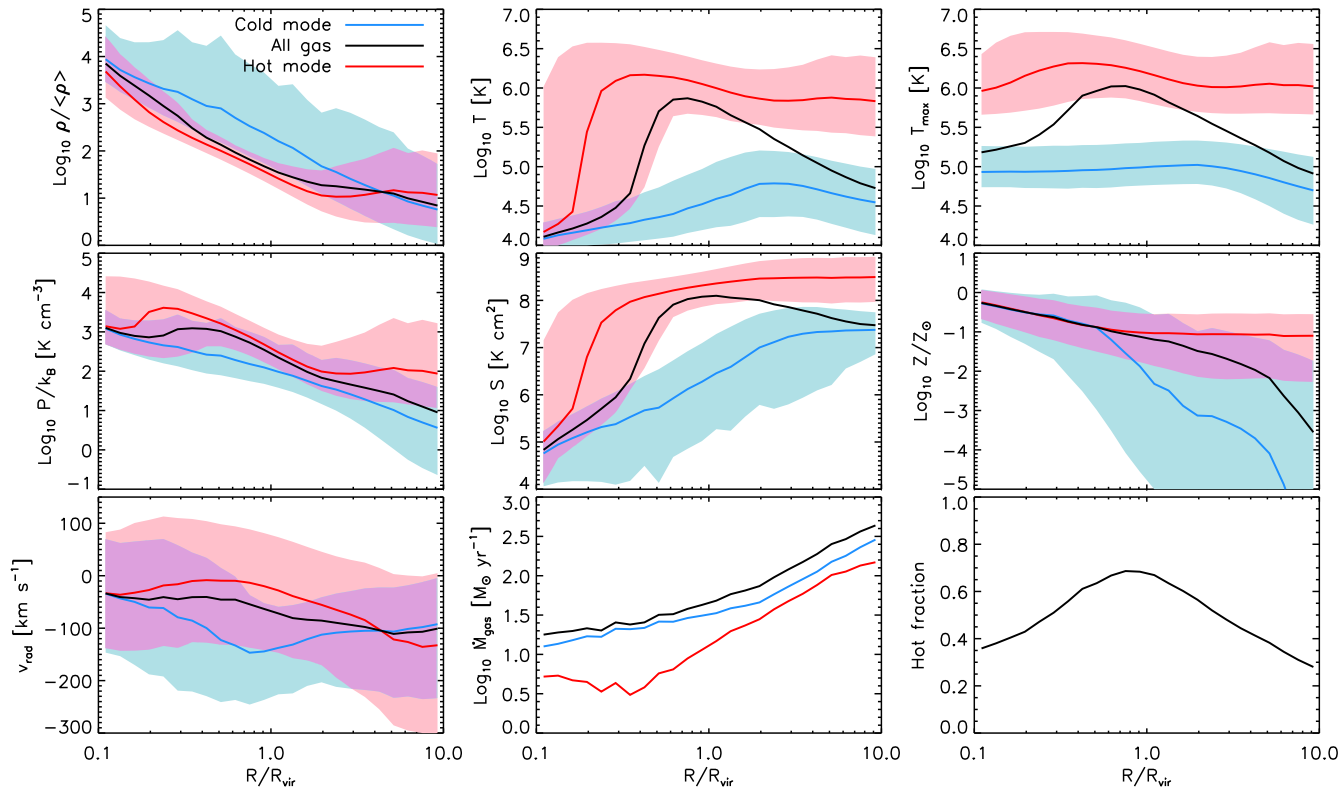
Figure 4.3: Properties of gas in haloes with $10^{11.5}$ M$_\odot$ < M_{halo} < $10^{12.5}$ M$_\odot$ at $z = 2$ as a function of radius for all (black curves), hot-mode (red curves), and cold-mode (blue curves) gas. Results are shown for the simulation *REF_L050N512*. Shaded regions show values within the 16th and 84th percentiles, i.e., the $\pm 1\sigma$ scatter around the median. From the top-left to the bottom-right, the different panels show the mass-weighted median gas overdensity, temperature, maximum past temperature, pressure, entropy, metallicity, radial peculiar velocity, the mean accretion rate, and the mean mass fraction of hot-mode gas, respectively.

$10R_{\rm vir}$ to $\sim 10^2$ at $R_{\rm vir}$ and to 10^4 at $0.1R_{\rm vir}$. The median density of cold-mode gas is higher by up to an order of magnitude than that of hot-mode gas for all radii $0.1R_{\rm vir} < R < 4R_{\rm vir}$. The cold-mode gas densities exhibit a significant scatter of about 2 dex, as opposed to about 0.4 dex for hot-mode gas at $R_{\rm vir}$, which implies that the cold-mode gas is much clumpier. Beyond $4R_{\rm vir}$ the median hot-mode density becomes higher than for the cold mode, because there the hot-mode gas is associated with different haloes and/or large-scale filaments, which are also responsible for heating the gas.

4.3.2   Temperature

Hot gas, heated either by accretion shocks or by SN feedback, extends far beyond the virial radius (top-middle of Figure 4.2). Most of the volume is filled with hot gas. The location of cold gas overlaps with that of dense gas, so the temperature and density are anti-correlated. This anti-correlation is a result of the fact that the cooling time deceases with the gas density.

For $R \gtrsim 0.2R_{\rm vir}$ the temperatures of the hot- and cold-mode gas do not vary strongly with radius (top middle panel of Figure 4.3). Note that this panel shows the *current* temperature and not the maximum *past* temperature. Gas accreted in the hot mode has a temperature $\sim 10^6$ K at $R > 0.2R_{\rm vir}$, which is similar to the virial temperature. The median temperature of the hot-mode gas increases slightly from $\approx 2R_{\rm vir}$ to $\approx 0.2R_{\rm vir}$ because the hot gas is compressed as it falls in. Within $0.5R_{\rm vir}$ the scatter increases and around $0.2R_{\rm vir}$ the median temperature drops sharply to $\sim 10^4$ K. The dramatic decrease in the temperature of the hot-mode gas is a manifestation of the strong cooling flow that results when the gas has become sufficiently dense to radiate away its thermal energy within a dynamical time. The median temperature of cold-mode gas peaks at slightly below 10^5 K around $2R_{\rm vir}$ and decreases to $\sim 10^4$ K at $0.1\ R_{\rm vir}$. The peak in the temperature of the cold-mode gas is determined by the interplay between photo-heating by the UV background and radiative cooling. The temperature difference between the two accretion modes reaches a maximum of about 2 dex at $0.3R_{\rm vir}$ and vanishes around $0.1R_{\rm vir}$.

4.3.3   Maximum past temperature

The maximum past temperature (top-right panel of Figure 4.2) is by definition at least as high as the current temperature, but its spatial distribution correlates well with that of the current temperature. As shown by Figure 4.3, the difference between maximum past temperature and current temperature is small at $R \gtrsim R_{\rm vir}$, but increases towards smaller radii and becomes 1 dex for cold-mode gas and 2 dex for hot-mode gas at $0.1R_{\rm vir}$.

While the temperature of the cold-mode gas decreases with decreasing radius, its maximum past temperature stays constant at $T_{\rm max} \approx 10^5$ K. This value of $T_{\rm max}$ is reached around $2R_{\rm vir}$ as a result of heating by the UV background.

Both the current and the maximum past temperature of the hot-mode gas increase with decreasing radius for $R > 0.3R_{\rm vir}$. The fact that $T_{\rm max}$ decreases below $0.3R_{\rm vir}$ shows that it is, on average, the colder part of the hot-mode gas that can reach these inner radii. If it were a random subset of all the hot-mode gas, then $T_{\rm max}$ would have stayed constant.

4.3.4 Pressure

As required by hydrostatic equilibrium, the gas pressure generally increases with decreasing radius (middle-left panels of Figures 4.2 and 4.3). However, the median pressure profile (Figure 4.3) does show a dip around $0.2 - 0.3R_{\rm vir}$ that reflects the sharp drop in the temperature profiles. Here catastrophic cooling leads to a strong cooling flow and thus a breakdown of hydrostatic equilibrium.

Comparing the pressure map with those of the density and temperature, the most striking difference is that the filaments become nearly invisible inside the virial radius, whereas they stood out in the density and temperature maps. However, beyond the virial radius the filaments do have a higher pressure than the diffuse gas. This suggests that pressure equilibrium is quickly established after the gas accretes onto the haloes.

Figure 4.3 shows that the difference between the pressures of the hot- and cold-mode gas increases beyond $2R_{\rm vir}$. This is because at these large radii the hot-mode gas is associated with other haloes and/or large-scale filaments, while the cold-mode gas is intergalactic, so we do not expect them to be in pressure equilibrium. Moving inwards from the virial radius, the median pressure difference increases until it reaches about an order of magnitude at $0.3R_{\rm vir}$. At smaller radii the pressures become nearly the same because the hot-mode gas cools down to the same temperature as the cold-mode gas.

Although it takes some time to reach pressure equilibrium if the hot gas is suddenly heated, we expect the hot and cold gas to be approximately in equilibrium inside the halo, because a phase with a higher pressure will expand, lowering its pressure, and compressing the phase with the lower pressure, until equilibrium is reached. While the pressure distributions do overlap, there is still a significant difference between the two. This difference decreases somewhat with increasing resolution, because the cold gas reaches higher densities and thus higher pressures, as is shown in the Appendix. From the example pressure map (Figure 4.2) we can see that the filaments inside the halo are in fact approximately in pressure equilibrium with the diffuse gas around them. At first sight this seems at odds with the fact that the median pressure profiles are different. However, the pressure map also reveals an asymmetry in the pressure inside the halo, with the gas to the left of the centre having a higher pressure than the gas to the right of the centre. Because there is also more hot-mode gas to the left, this leads to a pressure difference between the two modes when averaged over spherical shells, even though the two phases are locally in equilibrium. The asymmetry arises because the hot-mode gas is a space-filling gas and the flow

has to converge towards the centre of the halo, which increases its pressure. The cold-mode gas is not space filling and therefore does not need to compress as much.

4.3.5 Entropy

We define the entropy as

$$S \equiv \frac{P(\mu m_{\mathrm{H}})^{5/3}}{k_{\mathrm{B}}\rho^{5/3}},$$
(4.1)

where μ is the mean molecular weight, m_{H} is the mass of a hydrogen atom, and k_{B} is Boltzmann's constant. Note that the entropy remains invariant for adiabatic processes. In the central panel of Figure 4.2 we clearly see that the filaments have much lower entropies than the diffuse gas around them. This is expected for cold, dense gas.

For $R > R_{\mathrm{vir}}$ the median entropy of hot-mode gas is always higher than that of cold-mode gas (Figure 4.3). While the entropy of the cold-mode gas decreases smoothly and strongly towards the centre of the halo, the entropy of the hot-mode gas decreases only slightly down to $0.2R_{\mathrm{vir}}$ after which it drops steeply. Cold-mode gas cools gradually, but hot-mode gas cannot cool until it reaches high enough densities, which results in a strong cooling flow.

4.3.6 Metallicity

The middle-right panels of Figures 4.2 and 4.3 show that the cold-mode streams have much lower metallicities than the diffuse, hot-mode gas, at least for $R \gtrsim R_{\mathrm{vir}}$. The cold-mode gas also has a much larger spread in metallicity, four orders of magnitude at R_{vir}, as opposed to only one order of magnitude for hot-mode gas.

The gas in the filaments tends to have a lower metallicity, because most of it has never been close to a star-forming region, nor has it been affected by galactic winds, which tend to avoid the filaments (Theuns et al., 2002). The radial velocity image in the bottom-left panel of Figure 4.2 confirms that the winds take the path of least resistance. The cold mode also includes dense clumps, which show a wide range of metallicities. If the density is high enough for embedded star formation to occur, then this can quickly enrich the entire clump. The enhanced metallicity will increase its cooling rate, making it even more likely to accrete in the cold mode (recall that our definition of the maximum past temperature ignores shocks in the ISM). On the other hand, clumps that have not formed stars remain metal-poor. The metallicity spread is thus caused by a combination of being shielded from winds driven by the central galaxy and exposure to internal star formation.

At R_{vir} the median metallicity of the gas is subsolar, $Z \sim 10^{-1} \, Z_{\odot}$ for hot-mode gas and $Z \sim 10^{-2} \, Z_{\odot}$ for cold-mode gas. However, we caution the reader

that the median cold-mode metallicity is not converged with numerical resolution (see the Appendix) and could in fact be much lower. The metallicity increases towards the centre of the halo and this increase is steeper for cold-mode gas. The metallicity difference between the two modes disappears at $R \approx 0.5R_{\rm vir}$, but we find this radius to move inwards with increasing resolution (see the Appendix). Close to the centre the hot gas cools down and ongoing star formation in the disc enriches all the gas. The scatter in the metallicity decreases, especially for cold-mode gas, to ~ 0.7 dex.

As discussed in detail by Wiersma et al. (2009b), there is no unique definition of metallicity in SPH. The metallicity that we assign to each particle is the ratio of the metal mass density and the total gas density at the position of the particle. These "SPH-smoothed abundances" were also used during the simulation for the calculation of the cooling rates. Instead of using SPH-smoothed metallicities, we could, however, also have chosen to compute the metallicity as the ratio of the metal mass and the total gas mass of each particle. Using these so-called particle metallicities would sharpen the metallicity gradients at the interfaces of different gas phases. Indeed, we find that using particle metallicities decreases the median metallicity of the metal-poor cold mode. For the hot mode the median particle metallicity is also lower than the median smoothed metallicity, but it increases with resolution, whereas the cold-mode particle metallicities decrease with resolution.

While high-metallicity gas may belong to either mode, gas with metallicity $\lesssim$ 10^{-3} $Z_\odot$ is highly likely to be part of a cold flow. This conclusion is strengthened when we increase the resolution of the simulation or when we use particle rather than SPH-smoothed metallicities. Thus, a very low metallicity appears to be a robust way of identifying cold-mode gas.

4.3.7   Radial velocity

The radial peculiar velocity is calculated with respect to the halo centre after subtracting the peculiar velocity of the halo. The peculiar velocity of the halo is calculated by taking the mass-weighted average velocity of all the gas particles within 10 per cent of virial radius. Note that the Hubble flow is not included in the radial velocities shown. It is unimportant inside haloes, but is about a factor of two larger than the peculiar velocity at $10R_{\rm vir}$.

The bottom-left panel of Figure 4.2 shows that gas outside the haloes is, in general, moving towards the halo (i.e. it has a negative radial velocity). Within the virial radius, however, more than half of the projected area is covered by outflowing gas. These outflows are not only caused by SN feedback. In fact, simulations without feedback also show significant outflows (see Figures 4.7 and 4.8). A comparison with the pressure map shows that the outflows occur in the regions where the pressure is relatively high for its radius (by $0.1 - 0.4$ dex, see Figures 4.5 and 4.6). The inflowing gas is associated with the dense, cold streams, but the regions of infall are broader than the cold filaments. Some of

the hot-mode gas is also flowing in along with the cold-mode gas. These fast streams can penetrate the halo and feed the central disc. At the same time, some of the high temperature gas will expand, causing mild outflows in high pressure regions and these outflows are strengthened by SN-driven winds.

The hot-mode gas is falling in more slowly than the cold-mode gas or is even outflowing (bottom-left panel of Figure 4.3). This is expected, because the gas converts its kinetic energy into thermal energy when it goes through an accretion shock and because a significant fraction of the hot-mode gas may have been affected by feedback. For hot-mode gas the median radial velocity is closest to zero between $0.3R_{vir} < R < 1R_{vir}$. Most of it is inflowing at smaller radii, where the gas temperature drops dramatically, and also at larger radii.

The cold-mode gas appears to accelerate to -150 km s^{-1} towards R_{vir} (i.e. radial velocities becoming more negative) and to decelerate to -30 km s^{-1} from R_{vir} towards the disc. We stress, however, that the behaviour of individual gas elements is likely to differ significantly from the median profiles. Individual, cold gas parcels will likely accelerate until they go through an accretion shock or are hit by an outflow, at which point the radial velocity may suddenly vanish or change sign. If this is more likely to happen at smaller radii, then the median profiles will show a smoothly decelerating inflow. Finally, observe that while there is almost no outflowing cold-mode gas around the virial radius, close to the central galaxy ($R \lesssim 0.3R_{vir}$) a significant fraction is outflowing.

4.3.8 Accretion rate

The appropriate definition of the accretion rate in an expanding Universe depends on the question of interest. Here we are interested in the mass growth of haloes in a comoving frame, where the haloes are defined using a criterion that would keep halo masses constant in time if there were no peculiar velocities. An example of such a halo definition is the spherical overdensity criterion, which we use here, because the virial radius is in that case defined as the radius within which the mean internal density is a fixed multiple of some fixed comoving density.

The net amount of gas mass that is accreted per unit time through a spherical shell S with comoving radius $x = R/a$, where a is the expansion factor, is then given by the surface integral

$$\dot{M}_{gas}(x) \quad = \quad -\int_S a^3 \rho \dot{x} \frac{dS}{a^2} \tag{4.2}$$

$$= \quad -\int_S \rho v_{rad} dS, \tag{4.3}$$

where $a^3\rho$ and dS/a^2 are a comoving density and a comoving area, respectively, and the radial peculiar velocity is $v_{rad} \equiv a\dot{x}$. We evaluate this integral as follows,

$$\dot{M}_{gas}(R) = -\sum_{R \leq r_i < R+dR} \frac{m_{gas,i} v_{rad,i}}{V_{shell}} A_{shell}, \tag{4.4}$$

where

$$V_{\text{shell}} = \frac{4\pi}{3}((R + dR)^3 - R^3),$$ (4.5)

$$A_{\text{shell}} = 4\pi(R + \frac{1}{2}dR)^2,$$ (4.6)

r_i is the radius of particle i, and dR is the bin size. Note that a negative accretion rate corresponds to net outflow.

The mass flux map shown in the bottom-middle panel of Figure 4.2 is computed per unit area for each pixel as $\Sigma_i m_{\text{gas},i} v_{\text{rad},i}/V_{\text{pix}}$, where V_{pix} is the proper volume of the pixel. The absolute mass flux is highest in the dense filaments and in the other galaxies outside R_{vir}, because they contain a lot of mass and have high inflow velocities.

The gas accretion rate $\dot{M}_{\text{gas}}(R/R_{\text{vir}})$ computed using equation (4.4) is shown as the black curve in the bottom-middle panel of Figure 4.3. The accretion rate is averaged over all haloes in the mass bin we are considering here ($10^{11.5}\ \text{M}_\odot < M_{\text{halo}} < 10^{12.5}\ \text{M}_\odot$). Similarly, the red and blue curves are computed by including only hot- and cold-mode particles, respectively. The accretion rate is positive at all radii, indicating net accretion for both modes. The inflow rate is higher for the cold mode even though the hot-mode gas dominates the mass budget around the virial radius (see Section 4.3.9). The hot-mode gas accretion rate is a combination of the density and the radial velocity of the hot-mode gas, as well as the amount of mass in the hot mode. Gas belonging to the cold mode at $R > R_{\text{vir}}$ may later become part of the hot mode after it has reached $R < R_{\text{vir}}$.

The extended halo is not in a steady state, because the accretion rate varies with radius. Moving inwards from $10R_{\text{vir}}$ to R_{vir}, the net rate of infall drops by about an order of magnitude. This implies that the (extended) halo is growing: the flux of mass that enters a shell from larger radii exceeds the flux of mass that leaves the same shell in the direction of the halo centre. This sharp drop in the accretion rate with decreasing radius is in part due to the fact that some of the gas at $R > R_{\text{vir}}$ is falling towards other haloes that trace the same large-scale structure.

Within the virial radius the rate of infall of all gas and of cold-mode gas continues to drop with decreasing radius, but the gradient becomes much less steep ($d \ln \dot{M}/d \ln R \approx 0.4$), indicating that the cold streams are efficient in transporting mass to the central galaxy. For the hot mode the accretion rate only flattens at $R \lesssim 0.4R_{\text{vir}}$ around the onset of catastrophic cooling. Hence, once the hot-mode gas reaches small enough radii, its density becomes sufficiently high for cooling to become efficient, and the hot-mode accretion becomes efficient too. However, even at $0.1R_{\text{vir}}$ its accretion rate is still much lower than that of cold-mode gas.

4.3.9   Hot fraction

Even though the average hot fraction, i.e. the mean fraction of the gas mass that has a maximum past temperature greater than $10^{5.5}$ K, of the halo in the image

is close to 0.5, few of the pixels actually have this value. For most pixels f_{hot} is either close to one or zero (bottom-right panel of Figure 4.2), confirming the bimodal nature of the accretion.

The bottom-right panel of Figure 4.3 shows that the hot fraction peaks around the virial radius, where it is about 70 per cent. Although the hot fraction decreases beyond the virial radius, it is still 30 per cent around $10R_{\text{vir}}$. The hot-mode gas at very large radii is associated with other haloes and/or large-scale filaments. Within the halo the hot fraction decreases from 70 per cent at R_{vir} to 35 per cent at $0.1R_{\text{vir}}$. While hot-mode accretion dominates the growth of haloes, most of the hot-mode gas does not reach the centre. Cold-mode accretion thus dominates the growth of galaxies.

4.4 Dependence on halo mass

In Figure 4.4 we plot the same properties as in Figure 4.3 as a function of halo mass for gas at radii $0.8R_{\text{vir}} < R < R_{\text{vir}}$, where differences between hot- and cold-mode gas are large. Grey, dashed lines show analytic estimates and are discussed below. The dotted, grey line in the top-left panel indicates the star formation threshold, i.e. $n_{\text{H}} = 0.1 \text{ cm}^{-3}$. The differences between the density and temperature of the hot- and cold-mode gas increase with the mass of the halo. The average temperature, maximum past temperature, pressure, entropy, metallicity, absolute radial peculiar velocity, absolute accretion rate, and the hot fraction all increase with halo mass.

We can compare the gas overdensity at the virial radius to the density that we would expect if baryons were to trace the dark matter, ρ_{vir}. We assume an NFW profile (Navarro et al., 1996), take the mean internal density, $\Delta\langle\rho\rangle$, from spherical collapse calculations (Bryan & Norman, 1998) and the halo mass-concentration relation from Duffy et al. (2008) and calculate the mean overdensity at R_{vir}. This is plotted as the dashed, grey line in the top-left panel of Figure 4.4. It varies very weakly with halo mass, because the concentration depends on halo mass, but this is invisible on the scale of the plot. For all halo masses the median density is indeed close to this analytic estimate. While the same is true for the hot-mode gas, for high-mass haloes ($M_{\text{halo}} \gtrsim 10^{12} \text{ M}_\odot$) the median density of cold-mode gas is significantly higher than the estimated density and the difference reaches two orders of magnitude for $M_{\text{halo}} \sim 10^{13} \text{ M}_\odot$. A significant fraction of the cold-mode gas in these most massive haloes is star forming and hence part of the ISM of satellite galaxies. The fact that cold-mode gas becomes denser and thus clumpier with halo mass could have important consequences for the formation of clumpy galaxies at high redshift (Dekel et al., 2009b; Agertz et al., 2009; Ceverino et al., 2010).

The blue curve in the top-middle panel shows that the median temperature of the cold-mode gas at R_{vir} decreases slightly with halo mass, from 40,000 K to 15,000 K. This reflects the increase in the median density of cold-mode gas with
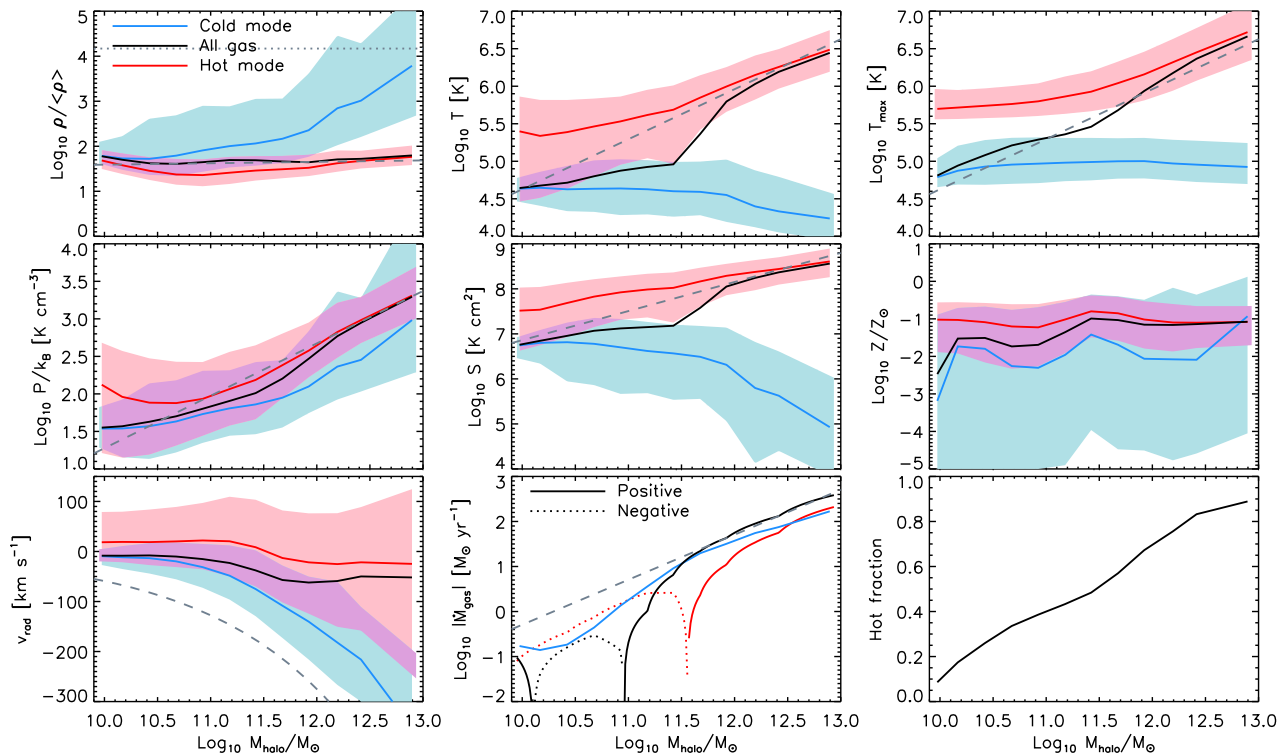
Figure 4.4: Properties of gas at $0.8R_{\rm vir} < R < R_{\rm vir}$ at $z = 2$ as a function of halo mass for all (black curves), hot-mode (red curves), and cold-mode (blue curves) gas. Results are shown for the simulation *REF_L050N512*. Shaded regions show values within the 16th and 84th percentiles, i.e., the $\pm1\sigma$ scatter around the median. From the top-left to the bottom-right, the different panels show the mass-weighted median gas overdensity, temperature, maximum past temperature, pressure, entropy, metallicity, radial peculiar velocity, the mean accretion rate, and the mean mass fraction of hot-mode gas, respectively. The horizontal, dotted line in the first panel indicates the threshold for star formation ($n_{\rm H} = 0.1$ cm^{-3}). The dashed, grey curves show analytic estimates from virial arguments.

halo mass, which results in shorter cooling times. The median temperature of the hot-mode gas increases with halo mass and is approximately equal to the virial temperature for $M_{\mathrm{halo}} \gtrsim 10^{11.5}$ M$_\odot$. The virial temperature is plotted as the dashed, grey line and is given by

$$T_{\mathrm{vir}} = \left(\frac{G^2 H_0^2 \Omega_{\mathrm{m}} \Delta}{54} \right)^{1/3} \frac{\mu m_{\mathrm{H}}}{k_B} M_{\mathrm{halo}}^{2/3} (1+z), \tag{4.7}$$

$$\approx 9.1 \times 10^5 \text{ K} \left(\frac{M_{\mathrm{halo}}}{10^{12} \text{ M}_\odot} \right)^{2/3} \left(\frac{1+z}{3} \right), \tag{4.8}$$

where G is the gravitational constant, H_0 the Hubble constant and μ is assumed to be equal to 0.59.

While much of the gas accreted onto low-mass haloes in the hot mode has a temperature smaller than $10^{5.5}$ K and has therefore already cooled down substantially[2], there is very little overlap in the current temperatures of gas accreted in the two modes for haloes with $T_{\mathrm{vir}} \gtrsim 10^6$ K. Because the cooling rates decrease with temperature for $T > 10^{5.5}$ K (e.g. Wiersma et al., 2009a), most of the hot-mode gas in haloes with higher temperatures stays hot. For the same reason, the median temperature of all gas rises sharply at $M \approx 10^{11.5}$ M$_\odot$ ($T_{\mathrm{vir}} \approx 10^{5.5}$ K) and is roughly equal to T_{vir} for $M_{\mathrm{halo}} > 10^{12}$ M$_\odot$.

The top-right panel shows that the median maximum past temperature of gas at the virial radius is close to the virial temperature, which is again shown as the grey dashed curve, for the full range of halo masses shown. Some of the gas does, however, have a maximum past temperatures that differs strongly from the virial temperature. The largest difference is found for cold-mode gas in high-mass haloes. Because of its high density, its cooling time is short and the gas does not shock to the virial temperature. The maximum past temperature of gas accreted in the cold mode is close to 10^5 K for all halo masses. For $M_{\mathrm{halo}} < 10^{10.5}$ M$_\odot$ this temperature is higher than the virial temperature. The gas in low-mass haloes has not been heated to its maximum temperature by a virial shock, but by the UV background radiation or by shocks from galactic winds. Heating by the UV background is the dominant process, because simulations without supernova feedback show the same result (see Figure 4.8). The maximum past temperature of hot-mode gas follows the virial temperature closely for high-mass haloes. For $T_{\mathrm{vir}} < 10^{5.5}$ K ($M_{\mathrm{halo}} \lesssim 10^{11.5}$ M$_\odot$) the maximum past temperature of the hot-mode gas remains approximately constant, at around $10^{5.7}$ K, because of our definition of hot-mode gas ($T_{\mathrm{max}} \geq 10^{5.5}$ K).

The pressure of the gas increases roughly as $M_{\mathrm{halo}}^{2/3}$ (middle-left panel). We can estimate the pressure at the virial radius from the virial temperature and the density at the virial radius.

$$\frac{P_{\mathrm{vir}}}{k_{\mathrm{B}}} = \frac{T_{\mathrm{vir}} \rho_{\mathrm{vir}}}{\mu m_{\mathrm{H}}}, \tag{4.9}$$

---

[2]Note that for haloes with $T_{\mathrm{vir}} \lesssim 10^{5.5}$ K the median hot-mode temperature is affected by the requirement $T_{\mathrm{max}} > 10^{5.5}$ K (our definition of hot-mode gas).

where μ is assumed to be equal to 0.59. This pressure is shown by the dashed, grey line. The actual pressure is very close to this simple estimate. It scales with mass as the virial temperature because the density at the virial radius is nearly independent of the mass. For all halo masses the median pressure of the gas accreted in the hot-mode is about a factor of two higher than the median pressure of the cold-mode gas.

The central panel shows that the entropy difference between hot- and cold-mode gas increases with halo mass, because the entropy of hot-mode gas increases with halo mass, whereas the cold-mode entropy decreases. The hot-mode gas follows the slope of the relation expected from virial arguments,

$$S_{\mathrm{vir}} = \frac{P_{\mathrm{vir}}(\mu m_{\mathrm{H}})^{5/3}}{k_{\mathrm{B}}\rho_{\mathrm{vir}}^{5/3}}, \tag{4.10}$$

where μ is assumed to be equal to 0.59. S_{vir} is shown as the dashed, grey line.

The middle-right panel shows that the median gas metallicity at the virial radius increases from $\sim 10^{-2}\,Z_{\odot}$ for $M_{\mathrm{halo}} \sim 10^{10}\,\mathrm{M}_{\odot}$ to $\sim 10^{-1}\,Z_{\odot}$ for $10^{13}\,\mathrm{M}_{\odot}$. This increase reflects the increased fraction of hot-mode gas (see the bottom-right panel) and an increase in the median metallicity of the cold-mode gas, which is probably due to the fact that a greater fraction of the gas resides in the ISM of satellite galaxies for more massive haloes (see the top-left panel). The scatter in the metallicity of the cold-mode gas is always very large. The hot-mode gas has a median metallicity $\sim 10^{-1}\,Z_{\odot}$ for all halo masses, which is similar to the predicted metallicity of the warm-hot intergalactic medium (Wiersma et al., 2011).

The black curve in the bottom-left panel shows that for all halo masses more mass is falling into the halo than is flowing out. The radial velocity distributions are, however, very broad. A substantial fraction of the hot-mode gas, more than half for $M_{\mathrm{halo}} < 10^{11.5}\,\mathrm{M}_{\odot}$, is outflowing at R_{vir}. Cold-mode gas is predominantly inflowing for all masses, but the fraction of outflowing gas becomes significant for $M_{\mathrm{halo}} < 10^{11.5}\,\mathrm{M}_{\odot}$.

As expected, the gas at the virial radius falls in faster for higher-mass haloes and the absolute velocities are larger for cold-mode gas. We can compare the radial peculiar velocity to the escape velocity,

$$v_{\mathrm{esc}} = \sqrt{\frac{2GM_{\mathrm{halo}}}{R_{\mathrm{vir}}}}, \tag{4.11}$$

$$\approx 275\ \mathrm{km\,s}^{-1}\left(\frac{M_{\mathrm{halo}}}{10^{12}\,\mathrm{M}_{\odot}}\right)^{1/3}\left(\frac{1+z}{3}\right)^{1/2}, \tag{4.12}$$

where we used

$$R_{\mathrm{vir}} = \left(\frac{2GM}{H_0^2 \Omega_{\mathrm{m}} \Delta} \right)^{1/3} \frac{1}{1+z}, \tag{4.13}$$

$$\approx 114 \,\mathrm{kpc} \left(\frac{M_{\mathrm{halo}}}{10^{12} \, \mathrm{M}_\odot} \right)^{1/3} \left(\frac{1+z}{3} \right)^{-1}. \tag{4.14}$$

We show $-v_{\mathrm{esc}}$ by the dashed, grey curve. We only expect the gas to have a velocity close to this estimate if it fell in freely from very large distances and if the Hubble expansion, which damps peculiar velocities, were unimportant. However, we do expect the scaling with mass to be more generally applicable. For the cold mode the trend with halo mass is indeed well reproduced by the escape velocity.

On average, for halo masses above $10^{11} \, \mathrm{M}_\odot$, the net accretion rate is positive, which means that more mass is flowing in than is flowing out (bottom-middle panel). Therefore, unsurprisingly, the haloes are growing. For haloes with $10^{10} \, \mathrm{M}_\odot < M_{\mathrm{halo}} < 10^{11} \, \mathrm{M}_\odot$ the mean accretion rate is negative (indicating net outflow), but small ($\sim 0.1 \, \mathrm{M}_\odot \, \mathrm{yr}^{-1}$). The mean accretion rate of cold-mode gas is positive for all halo masses, but for hot-mode gas there is net outflow for $M_{\mathrm{halo}} < 10^{11.5} \, \mathrm{M}_\odot$. Although these haloes are losing gas that is currently hot-mode, their hot-mode gas reservoir may still be increasing if cold-mode gas is converted into hot-mode gas. For higher-mass haloes, the hot-mode accretion rate is also positive and it increases approximately linearly with halo mass. This is the regime where the implemented supernova feedback is not strong enough to blow gas out of the halo. This transition mass is increased by more than an order of magnitude when more effective supernova feedback or AGN feedback is included (not shown). For $M_{\mathrm{halo}} > 10^{12.5} \, \mathrm{M}_\odot$ the hot-mode inflow rate is slightly stronger than the cold-mode inflow rate.

The grey, dashed curve indicates the accretion rate a halo with a baryon fraction $\Omega_{\mathrm{b}}/\Omega_{\mathrm{m}}$ would need to have to grow to its current baryonic mass in a time equal to the age of the Universe at $z = 2$,

$$\dot{M} = \frac{\Omega_{\mathrm{b}} M_{\mathrm{halo}}}{\Omega_{\mathrm{m}} t_{\mathrm{Universe}}}. \tag{4.15}$$

Comparing this analytic estimate with the actual mean accretion rate, we see that they are equal for $M_{\mathrm{halo}} > 10^{11.5} \, \mathrm{M}_\odot$, indicating that these haloes are in a regime of efficient growth. For lower-mass haloes, the infall rates are much lower, indicating that the growth of these haloes has halted, or that their baryon fractions are much smaller than $\Omega_{\mathrm{b}}/\Omega_{\mathrm{m}}$.

The bottom-right panel of Figure 4.4 shows that, at the virial radius, hot-mode gas dominates the gas mass for high-mass haloes. The hot fraction at R_{vir} increases from 10 per cent in haloes of $\sim 10^{10} \, \mathrm{M}_\odot$ to 90 per cent for $M_{\mathrm{halo}} \sim 10^{13} \, \mathrm{M}_\odot$. Note that for haloes with $M_{\mathrm{halo}} < 10^{11.3} \, \mathrm{M}_\odot$ the virial temperatures are lower than our adopted threshold for hot-mode gas. The hot fraction would have

been much lower without supernova feedback ($f_{\rm hot} < 5$ per cent for $M_{\rm halo} < 10^{10.5}$ M$_\odot$).

4.5   Inflow and outflow

Figures 4.5 and 4.6 show the physical properties of the gas, weighted by the radial mass flux, for all, inflowing, and outflowing gas (black, blue, and red curves, respectively). Except for the last two panels, the curves indicate the medians, i.e. half the mass flux is due to gas above the curves. Similarly, the shaded regions indicate the 16th and 84th percentiles. Note that we do not plot this separately for hot- and cold-mode gas. The differences between the blue and red curves arise purely from the different radial peculiar velocity directions.

We can immediately see that separating gas according to its radial velocity direction yields similar results as when the gas is separated according to its maximum past temperature (compare to Figures 4.3 and 4.4). Like cold-mode gas, inflowing gas has, on average, a higher density, a lower temperature, a lower entropy, and a lower metallicity than outflowing gas.

Comparing Figures 4.3 and 4.5, we notice that the differences in density, temperature, pressure, entropy, and metallicity between in- and outflowing gas tend to be slightly smaller than between cold- and hot-mode gas. This is particularly true outside the haloes (at $R > 3R_{\rm vir}$), where there is a clear upturn in the density and pressure of outflowing gas that is accompanied by a marked decrease in the temperature. These features are due to gas that is flowing towards other haloes and/or large-scale filaments. Although such gas is outflowing from the perspective of the selected halo, it is actually infalling gas and hence more likely to be cold-mode.

Unsurprisingly, the radial peculiar velocities (bottom-left panels) are clearly very different when we separate the gas into in- and outflowing components than when we divide it into cold and hot modes. Low values of the radial velocity are avoided because the plot is weighted by the mass flux. While the radial velocity of cold-mode gas decreases from the virial radius towards the centre, the mass flux-weighted median radial velocity of inflowing gas is roughly constant. Within the haloes, the mass flux-weighted median radial velocity of outflowing gas decreases with radius.

Both the inflow and the outflow mass flux (bottom-middle panel of Figure 4.5) are approximately constant inside $0.7R_{\rm vir}$, which implies that the fraction of the gas that is outflowing is also constant (last panel of Figure 4.5). A mass flux that is independent of radius implies efficient mass transport, as the same amount of mass passes through each shell per unit of time. The inflowing mass flux decreases from $10R_{\rm vir}$ to $\sim R_{\rm vir}$ because the overdensity of the region is increasing and because some of the gas that is infalling at distances $\gg R_{\rm vir}$ is falling towards neighbouring haloes. At $R \gtrsim R_{\rm vir}$ the outflowing mass flux decreases somewhat, indicating that the transportation of outflowing material

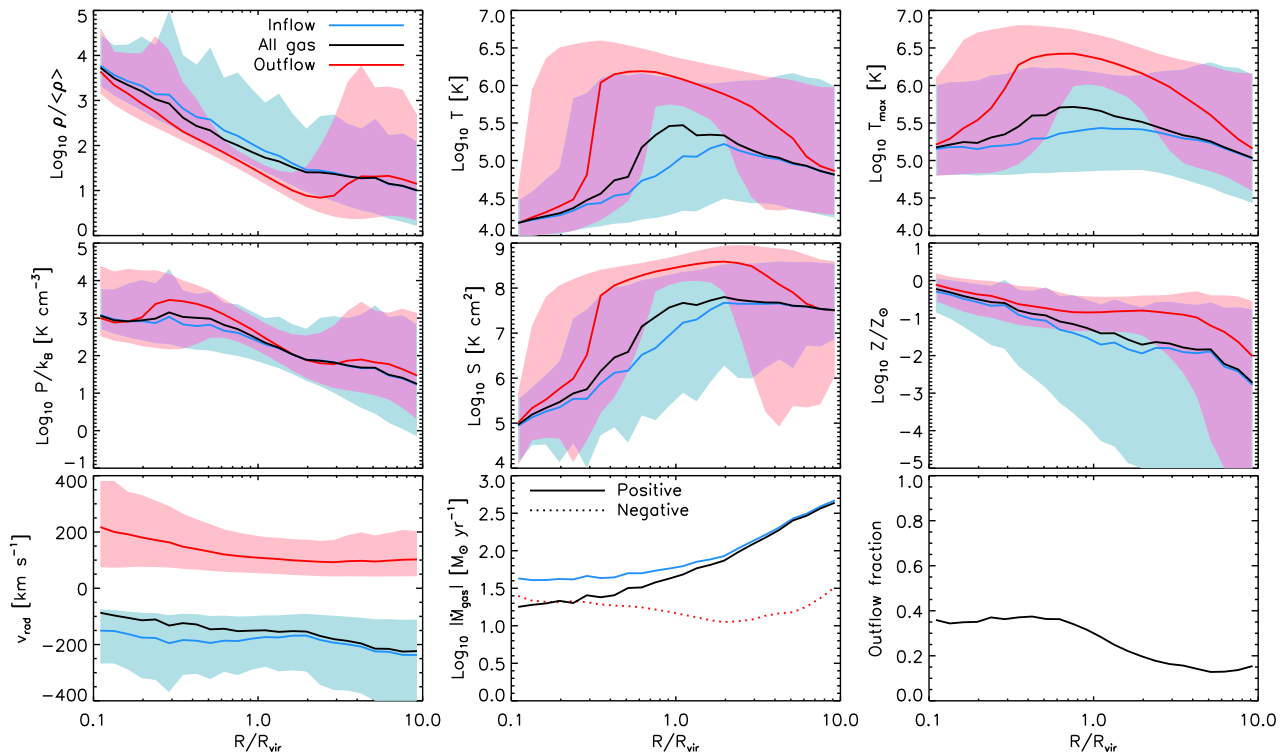**Figure 4.5:** Properties of gas in haloes with $10^{11.5}$ M$_\odot < M_{halo} < 10^{12.5}$ M$_\odot$ at $z = 2$ as a function of radius for all (black curves), outflowing (red curves), and inflowing (blue curves) gas. Results are shown for the simulation *REF_L050N512*. Shaded regions show values within the 16th and 84th percentiles, i.e., the $\pm 1\sigma$ scatter around the median. From the top-left to the bottom-right, the different panels show the mass flux-weighted median gas overdensity, temperature, maximum past temperature, pressure, entropy, metallicity, radial peculiar velocity, the mean accretion rate, and the mean mass fraction of outflowing gas, respectively. Most of the trends with radius for inflowing and outflowing gas are similar to those for cold-mode and hot-mode gas, respectively, as shown in Figure 4.3.
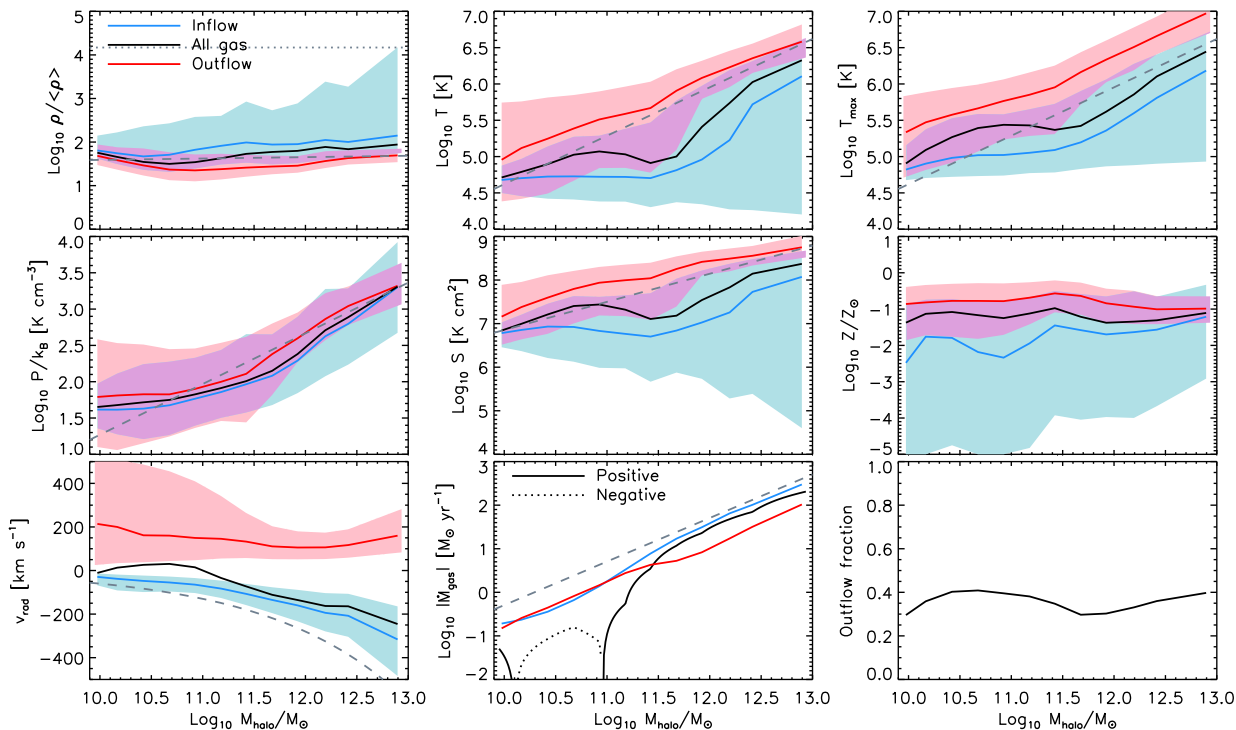
Figure 4.6: Properties of gas at $0.8R_{\rm vir} < R < R_{\rm vir}$ at $z = 2$ as a function of halo mass for all (black curves), outflowing (red curves), and inflowing (blue curves) gas. Results are shown for the simulation *REF_L050N512*. Shaded regions show values within the 16th and 84th percentile, i.e., the $\pm 1\sigma$ scatter around the median. From the top-left to the bottom-right, the different panels show the mass flux-weighted median gas overdensity, temperature, maximum past temperature, pressure, entropy, metallicity, radial peculiar velocity, the mean accretion rate, and the mean mass fraction of outflowing gas, respectively. The horizontal, dotted line in the first panel indicates the threshold for star formation ($n_{\rm H} = 0.1$ cm^{-3}). The dashed, grey curves show analytic estimates from virial arguments. Most of the trends with mass for inflowing and outflowing gas are similar to those for cold-mode and hot-mode gas, respectively, as shown in Figure 4.4.

slows down and that the galactic winds are becoming less efficient. This can also be seen by the drop in outflow fraction around the virial radius in the last panel of Figure 4.5. (The small decrease in outflow fraction below $10^{10.5}$ $M_\odot$ is a resolution effect.) The outflowing mass flux increases again at large radii, because the hot-mode gas is falling towards unrelated haloes.

Comparing Figures 4.4 and 4.6, we see again that, to first order, inflowing and outflowing gas behave similarly as cold-mode and hot-mode gas, respectively. There are, however, some clear differences, although we do need to keep in mind that some are due to the fact that Figure 4.4 is mass-weighted while Figure 4.6 is mass flux-weighted. The mass flux-weighted median temperature of outflowing gas is always close to the virial temperature. For $M_{\text{halo}} \lesssim 10^{11}$ $M_\odot$ this is much lower than the median temperature of hot-mode gas, but that merely reflects the fact that for these haloes the virial temperature is lower than the value of $10^{5.5}$ K that we use to separate the cold and hot modes. The mass flux-weighted maximum past temperature is about 0.5 dex higher than T_{vir}.

Another clear difference is visible at the high-mass end ($M_{\text{halo}} \gtrsim 10^{12.5}$ $M_\odot$). While the cold-mode density increases rapidly with mass, the overdensity of infalling gas remains $\sim 10^2$, and while the cold-mode temperature remains $\sim 10^4$ K, the temperature of infalling gas increases with halo mass. Both of these differences can be explained by noting that, around the virial radius, hot-mode gas accounts for a greater fraction of the infall in higher mass haloes (see the bottom-middle panel of Figure 4.4).

As was the case for the cold-mode gas, the radial peculiar velocity of infalling gas scales like the escape velocity (bottom-middle panel). Interestingly, although the mass flux-weighted median outflowing velocity is almost independent of halo mass, the high-velocity tail is much more prominent for low-mass haloes. Because the potential wells in these haloes are shallow and because the gas pressure is lower, the outflows are not slowed down as much before they reach the virial radius. The flux-weighted outflow velocities are larger than the inflow velocities for $M_{\text{halo}} < 10^{11.5}$ $M_\odot$, whereas the opposite is the case for higher-mass haloes.

Finally, the last panel of Figure 4.6 shows that the fraction of the gas that is outflowing around R_{vir} is relatively stable at about 30–40 per cent. Although the accretion rate is negative for 10^{10} $M_\odot < M_{\text{halo}} < 10^{11}$ $M_\odot$, which indicates net outflow, less than half of the gas is outflowing.

4.6 Effect of metal-line cooling and outflows driven by supernovae and AGN

Figure 4.7 shows images of the same 10^{12} $M_\odot$ halo as Figure 4.2 for five different high-resolution (*L025N512*) simulations at $z = 2$. Each row shows a different property, in the same order as the panels in the previous figures. Different columns show different simulations, with the strength of galactic winds increas-
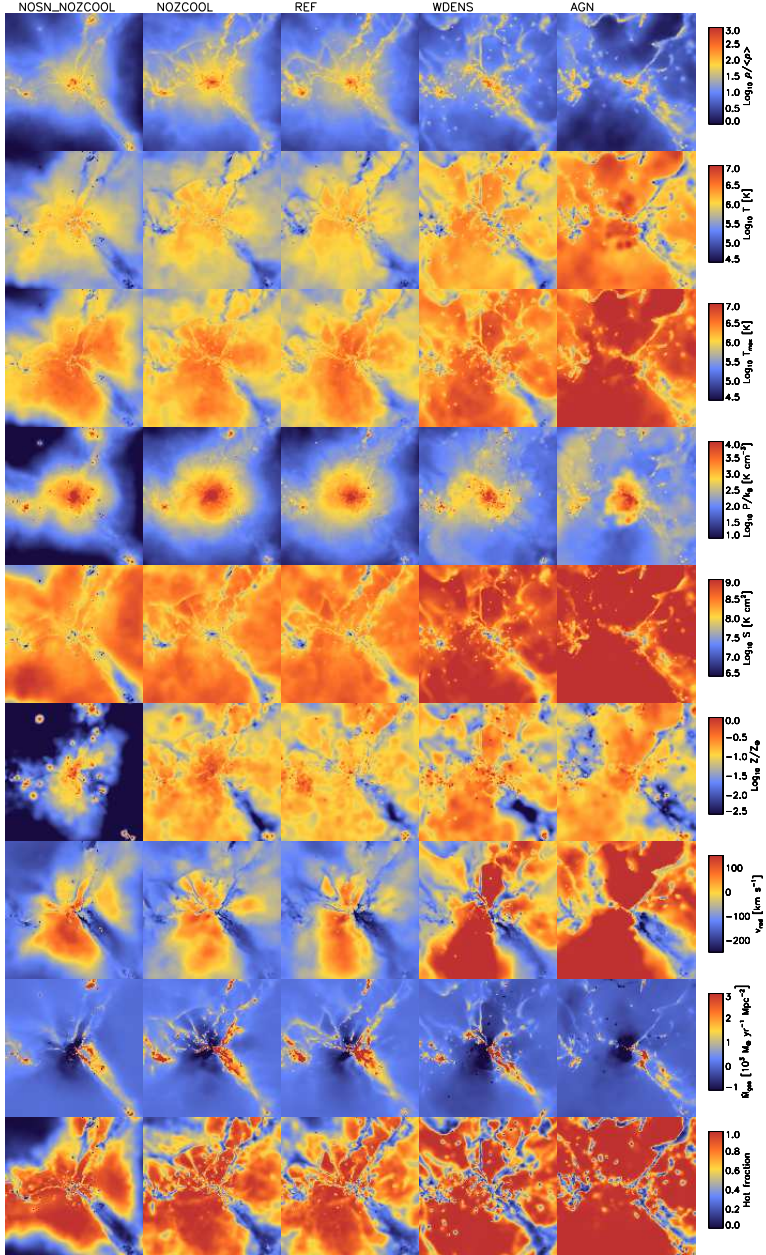
Figure 4.7: As Figure 4.2, but comparing the different simulations listed in Table 4.2. The images show a cubic 1 h^{-1} comoving Mpc region centred on a halo of $M_{\text{halo}} \approx 10^{12}$ M$_\odot$ at $z = 2$ taken from the *L025N512* simulations. From left to right, the different columns show the simulation with neither SN feedback nor metal-line cooling, the simulation without metal-line cooling, the reference simulation (which includes SN feedback and metal-line cooling), the simulation for which the wind speed scales with the effective sound speed of the ISM, and the simulation with AGN feedback. Note that the images shown in the middle column are identical to those shown in Figure 4.2.
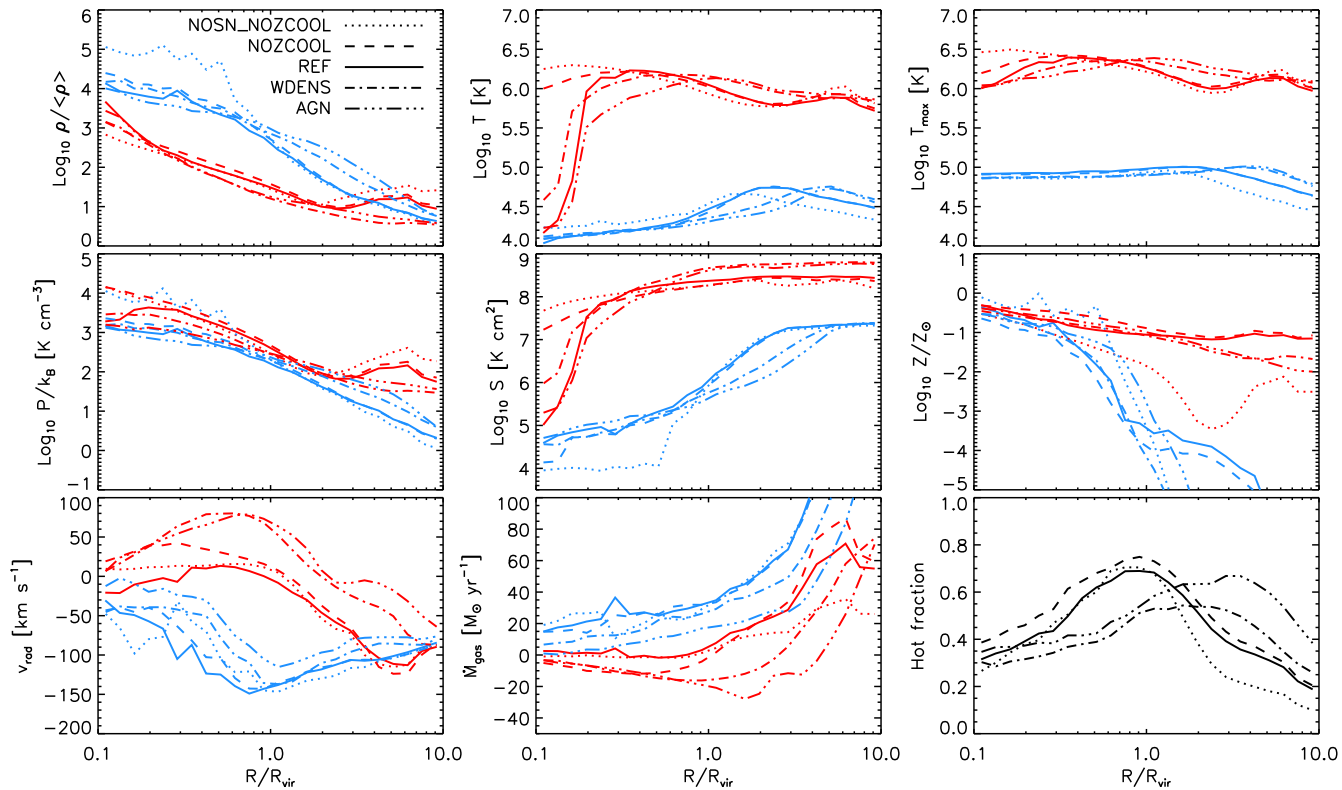
Figure 4.8: Properties of gas in haloes with $10^{11.5}$ M$_\odot$ < $M_{\rm halo}$ < $10^{12.5}$ M$_\odot$ at $z = 2$ as a function of radius for hot-mode (red curves) and cold-mode (blue curves) gas for the five different *L025N112* simulations listed in Table 4.2, as indicated in the legend. From the top-left to the bottom-right, the different panels show the mass-weighted median gas overdensity, temperature, maximum past temperature, pressure, entropy, metallicity, radial peculiar velocity, the mean accretion rate, and the mean mass fraction of hot-mode gas, respectively.

ing from left to right (although the winds are somewhat stronger in *NOZCOOL* than in *REF*). The first column shows the simulation without SN feedback and without metal-line cooling. The second column shows the simulation with SN feedback, but without metal-line cooling. The third column shows our reference simulation, which includes both SN feedback and metal-line cooling. The fourth column shows the simulation with density-dependent SN feedback, which is more effective at creating galactic winds for this halo mass. The last column shows the simulation that includes both SN and AGN feedback.

The images show substantial and systematic differences. More efficient feedback results in lower densities and higher temperatures of diffuse gas and in the case of AGN feedback, even some of the cold filaments are partially destroyed. Although the images reveal some striking differences, Figure 4.8 shows that the trends in the profiles of the gas properties, including the differences between hot and cold modes, are very similar in the different simulations. This is partly because the profiles are mass-weighted, whereas the images are only mass-weighted along the projected dimension. We would have seen larger differences if we had shown volume-weighted profiles, because the low-density, high-temperature regions, which are most affected by the outflows, carry very little mass, but dominate the volume. Although the conclusions of the previous sections are to first order independent of the particular simulation that we use, there are some interesting and clear differences, which we shall discuss below.

We can isolate the effect of turning off SN-driven outflows by comparing models *NOSN_NOZCOOL* and *NOZCOOL*. Without galactic winds, the cold-mode densities and pressures are about an order of magnitude higher within $0.5R_{\mathrm{vir}}$. On the other hand, turning off winds decreases the density of hot-mode gas by nearly the same factor around $0.1R_{\mathrm{vir}}$. Galactic winds thus limit the build up of cold-mode gas in the halo center, which they accomplish in part by converting cold-mode gas into hot-mode gas (i.e. by shock-heating cold-mode gas to temperatures above $10^{5.5}$ K). We can see that this must be the case by noting that the hot-mode accretion rate is negative inside the haloes for model *NOZCOOL*. The absence of SN-driven outflows also has a large effect on the distribution of metals. Without winds, the metallicities of both hot- and cold-mode gas outside the halo are much lower, because there is no mechanism to transport metals to large distances. On the other hand, the metallicity of the cold-mode gas is higher within the halo, because the star formation rates, and thus the rates of metal production, are higher. This suggests that the metals in cold-mode gas are associated with locally formed stars, e.g. infalling companion galaxies.

Increasing the efficiency of the feedback, as in models *WDENS* and particularly *AGN*, the cold-mode median radial velocity becomes less negative and the accretion rate of cold-mode gas inside haloes decreases. At the same time, the radial velocity and the outflow rate of the hot-mode increase. In other words, more efficient feedback hinders the inflow rate of cold-mode gas and boosts the outflows of hot-mode gas. The differences are particularly large outside the

haloes. Whereas the moderate feedback implemented in model *REF* predicts net infall of hot-mode gas, the net accretion rate of hot-mode gas is negative out to about $4R_{\mathrm{vir}}$ when AGN feedback is included. Beyond the virial radius, stronger winds substantially increase the mass fraction of hot-mode gas. This comes at the expense of the hot-mode gas inside the haloes, which decreases if the feedback is more efficient, at least for $0.2R_{\mathrm{vir}} < R < R_{\mathrm{vir}}$.

The effect of metal-line cooling can be isolated by comparing models *NOZ-COOL* and *REF*. Without metal-line cooling, the cooling times are much longer. Consequently, the median temperature of the hot-mode gas remains above 10^6 K (at least for $R > 0.1R_{\mathrm{vir}}$), whereas it suddenly drops to below 10^5 K around $0.2R_{\mathrm{vir}}$ when metal-line cooling is included. Thus, the catastrophic cooling flow of the diffuse, hot component in the inner haloes is due to metals. Indeed, while the median hot-mode radial peculiar velocity within $0.2R_{\mathrm{vir}}$ is positive without metal-line cooling, it becomes negative (i.e. infalling) when metal-line cooling is included.

4.7   Evolution: Milky Way-sized haloes at $z = 0$

Figure 4.9 is identical to Figure 4.3 except that it shows profiles for $z = 0$ rather than $z = 2$. For comparison, the dotted curves in Figure 4.9 show the corresponding $z = 2$ results. As we are again focusing on $10^{11.5}$ M$_\odot$ < M_{halo} < $10^{12.5}$ M$_\odot$, the results are directly relevant for the Milky Way galaxy.

Comparing Figure 4.3 to Figure 4.9 (or comparing solid and dotted curves in Figure 4.9), we see that the picture for $z = 0$ looks much the same as it did for $z = 2$. There are, however, a few notable differences. The overdensity profiles hardly evolve, although the difference between the cold and hot modes is slightly smaller at lower redshift. However, a constant overdensity implies a strongly evolving proper density ($\rho \propto (1+z)^3$) and thus also a strongly evolving cooling rate. The large decrease in the proper density caused by the expansion of the Universe also results in a large drop in the pressure and a large increase in the entropy.

The lower cooling rate shifts the peak of the cold-mode temperature profile from about $2R_{\mathrm{vir}}$ to about R_{vir}. While there is only a small drop in the temperature of the hot-mode gas, consistent with the mild evolution of the virial temperature of a halo of fixed mass ($T_{\mathrm{vir}} \propto (1+z)$; eq. [4.7]), the evolution in the median temperature for all gas is much stronger than for the individual accretion modes. While at $z = 2$ the overall median temperature only tracks the median hot-mode temperature around $0.5R_{\mathrm{vir}} < R < 2R_{\mathrm{vir}}$, at $z = 0$ the two profiles are similar at all radii.

The metallicity profiles do not evolve much, except for a strong increase in the median metallicity of cold-mode gas at $R \gg R_{\mathrm{vir}}$. Both the weak evolution of the metallicity of dense gas and the stronger evolution of the metallicity of the cold, low-density intergalactic gas far away from galaxies are consistent with
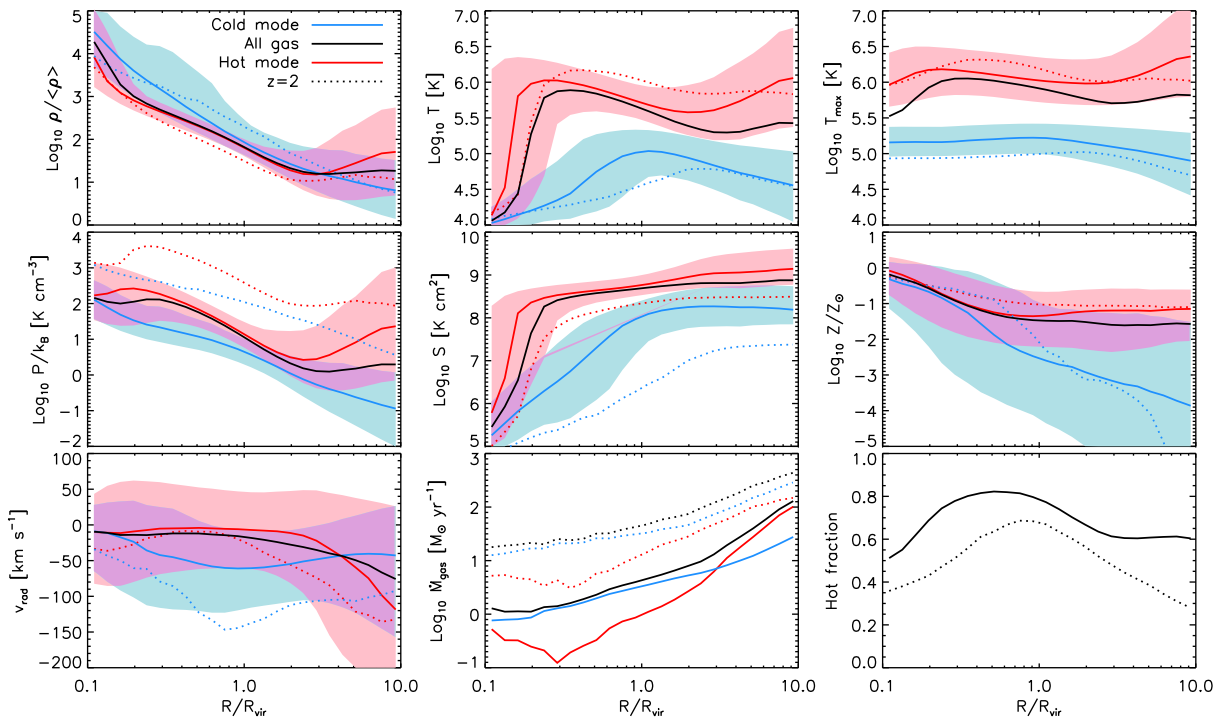
Figure 4.9: Properties of gas in haloes with $10^{11.5}$ M$_\odot$ < $M_{\rm halo}$ < $10^{12.5}$ M$_\odot$ at $z = 0$ as a function of radius for all (black curves), hot-mode (red curves), and cold-mode (blue curves) gas. Results are shown for the simulation *REF_L050N512*. Most $z = 2$ curves from Figure 4.3 have also been included, for comparison, as dotted curves. Shaded regions show values within the 16th and 84th percentiles, i.e., the $\pm 1\sigma$ scatter around the median. From the top-left to the bottom-right, the different panels show the mass-weighted median gas overdensity, temperature, maximum past temperature, pressure, entropy, metallicity, radial peculiar velocity, the mean accretion rate, and the mean mass fraction of hot-mode gas, respectively. The radial profiles at $z = 0$ follow the same trends as at $z = 2$ (compare Figure 4.3), although the pressure, the infall velocity and the accretion rates are lower, the entropy is higher, and the hot mode accounts for a greater mass fraction.

the findings of Wiersma et al. (2011), who found these trends to be robust to changes in the subgrid physics.

The absolute, net radial velocities of both the hot- and cold-mode components are smaller at lower redshift, as expected from the scaling of the characteristic velocity ($v_{esc} \propto (1 + z)^{1/2}$; eq. [4.11]).

While at $z = 2$ the net accretion rate was higher for the cold mode at all radii, at $z = 0$ the hot mode dominates beyond $3R_{vir}$. At low redshift the rates are about an order of magnitude lower than at $z = 2$. For $R < 0.4R_{vir}$ the net accretion rate is of order $1 \, M_{\odot} \, yr^{-1}$, which is dominated by the cold mode, even though most of the mass is in the hot mode. Since a substantial fraction of both the cold- and hot-mode gas inside this radius is outflowing, the actual accretion rates will be a bit higher.

At $z = 0$ the fraction of the mass that has been hotter than $10^{5.5}$ K exceeds 50 per cent at all radii and the profile show a broad peak of around 80 per cent at $0.3 < R < R_{vir}$. Thus, hot-mode gas is more important at $z = 0$ than at $z = 2$, where cold-mode gas accounts for most of the mass for $R \lesssim 0.3R_{vir}$ and $R \gtrsim 2R_{vir}$. This is consistent with van de Voort et al. (2011a), who investigated the evolution of the hot fraction in more detail using the same simulations.

4.8   Conclusions and discussion

We have used cosmological hydrodynamical simulations from the OWLS project to investigate the physical properties of gas in and around haloes. We paid particular attention to the differences in the properties of gas accreted in the cold and hot modes, where we classified gas that has remained colder (has been hotter) than $10^{5.5}$ K while it was extragalactic as cold-mode (hot-mode) gas. Note that our definition allows hot-mode gas to be cold, but that cold-mode gas cannot be hotter than $10^{5.5}$ K. We focused on haloes of $10^{12} \, M_{\odot}$ at $z = 2$ drawn from the OWLS reference model, which includes radiative cooling (also from heavy elements), star formation, and galactic winds driven by SNe. However, we also investigated how the properties of gas near the virial radius change with halo mass, we compared $z = 2$ to $z = 0$, we measured properties separately for inflowing and outflowing gas, and we studied the effects of metal-line cooling and feedback from star formation and AGN. We focused on mass-weighted median gas properties, but noted that volume-weighted properties are similar to the mass-weighted properties of the hot-mode gas, because most of the volume is filled by dilute, hot gas, at least for haloes with $T_{vir} \gtrsim 10^{5.5}$ K (see Figures 4.1 and 4.2).

Let us first consider the properties of gas just inside the virial radius of haloes drawn from the reference model at $z = 2$ (see Figure 4.4). The fraction of the gas accreted in the hot mode increases from 10 per cent for halo masses $M_{halo} \sim 10^{10} \, M_{\odot}$ to 90 per cent for $M_{halo} \sim 10^{13} \, M_{\odot}$. Hence, $10^{12} \, M_{\odot}$ is a particularly interesting mass scale, as it marks the transition between systems dominated by

cold and hot mode gas.

Although the cold streams are in local pressure equilibrium with the surrounding hot gas, cold-mode gas is physically distinct from gas accreted in the hot mode. It is colder ($T < 10^5$ K vs. $T \gtrsim T_{\mathrm{vir}}$) and denser, particularly for high-mass haloes. While hot-mode gas at the virial radius has a density $\sim 10^2 \langle \rho \rangle$ for all halo masses, the median density of cold-mode gas increases steeply with the halo mass.

While the radial peculiar velocity of cold-mode gas is negative (indicating infall) and scales with halo mass like the escape velocity, the median hot-mode velocities are positive (i.e. outflowing) for $M_{\mathrm{halo}} \lesssim 10^{11.5}$ M$_\odot$ and for larger masses they are much less negative than for cold-mode gas. Except for $M_{\mathrm{halo}} \sim 10^{10.5}$ M$_\odot$, the net accretion rate is positive. For $10^{12} < M_{\mathrm{halo}} < 10^{13}$ M$_\odot$ the cold- and hot-mode accretion rates are comparable.

While hot-mode gas has a metallicity $\sim 10^{-1}$ Z$_\odot$, the metallicity of cold-mode gas is typically significantly smaller and displays a much larger spread. The scatter in the local metallicity of cold-mode gas is large because the cold filaments contain low-mass galaxies that have enriched some of the surrounding cold gas. We emphasized that we may have overestimated the median metallicity of cold-mode gas because we find it to decrease with increasing resolution. It is therefore quite possible that most of the cold-mode gas in the outer halo still has a primordial composition.

The radial profiles of the gas properties of haloes with $10^{11.5} < M_{\mathrm{halo}} < 10^{12.5}$ M$_\odot$ revealed that the differences between gas accreted in the cold and hot modes vanishes around $0.1 R_{\mathrm{vir}}$ (see Figure 4.3), although the radius at which this happens decreases slightly with the resolution. The convergence of the properties of the two modes at small radii is due to catastrophic cooling of the hot gas at $R \lesssim 0.2 R_{\mathrm{vir}}$. Interestingly, in the absence of metal-line cooling the hot-mode gas remains hot down to much smaller radii, which suggests that it is very important to model the small-scale chemical enrichment of the circumgalactic gas. While stronger winds do move large amounts of hot-mode gas beyond the virial radius, even AGN feedback is unable to prevent the dramatic drop in the temperature of hot-mode gas inside $0.2 R_{\mathrm{vir}}$, at least at $z = 2$.

While the density and pressure decrease steeply with radius, the mass-weighted median temperature peaks around $0.5 - 1.0 R_{\mathrm{vir}}$. This peak is, however, not due to a change in the temperature of either the cold- or hot-mode gas, but due to the radial dependence of the mass fraction of gas accreted in the hot mode. The hot-mode fraction increases towards the halo, then peaks around $0.5 - 1.0 R_{\mathrm{vir}}$ and decreases moving further towards the centre. Even outside the halo there is a significant amount of hot-mode gas (e.g. ~ 30 per cent at $10 R_{\mathrm{vir}}$).

Beyond the cooling radius, i.e. the radius where the cooling time equals the Hubble time, the temperature of the hot-mode gas decreases slowly outwards, but the temperature of cold-mode gas only peaks around $2 R_{\mathrm{vir}}$ at values just below 10^5 K. The density for which this peak temperature is reached depends on the interplay between cooling (both adiabatic and radiative) and photo-heating.

The metallicity decreases with radius and does so more strongly for cold-mode gas. Near $0.1R_{\rm vir}$ the scatter in the metallicity of cold-mode gas is much reduced, although this could be partly a resolution effect.

The median radial peculiar velocity of cold-mode gas is most negative around $0.5 - 1.0R_{\rm vir}$. For the hot mode, on the other hand, it is close to zero around that same radius. Hence, the infall velocity of the cold streams peaks where the hot-mode gas is nearly static, or outflowing if the feedback is very efficient. We note, however, that the scatter in the peculiar velocities is large. For $R \lesssim R_{\rm vir}$ much of the hot-mode gas is outflowing and the same is true for cold-mode gas at $R \sim 0.1R_{\rm vir}$.

Inside the halo the cold-mode accretion rate increases only slightly with radius ($d\ln\dot{M}/d\ln R \approx 0.4$), indicating that most of the mass is transported to the central galaxy. For the hot-mode, on the other hand, the accretion rate only flattens at $R \lesssim 0.4R_{\rm vir}$. This implies that the hot accretion mode mostly feeds the hot halo. However, hot-mode gas that reaches radii $\sim 0.1R_{\rm vir}$ is efficiently transported to the centre as a result of the strong cooling flow. Nevertheless, cold-mode accretion dominates the accretion rate at all radii.

Dividing the gas into inflowing and outflowing components yields results that are very similar to classifying the gas on the basis of its maximum past temperature. This is because inflowing gas is mostly cold-mode and outflowing gas is mostly hot-mode. The situation is, however, different for high-mass haloes ($M_{\rm halo} \gtrsim 10^{12.5}$ M$_\odot$). Because the two accretion modes bring similar amounts of mass into these haloes, the properties of the infalling gas are intermediate between those of the cold and hot accretion modes.

When expressed in units of the mean density of the universe, the $z = 0$ density profiles (with radius expressed in units of the virial radius) are very similar to the ones at $z = 2$. The same is true for the metallicities and temperatures, although the peak temperatures shift to slightly smaller radii (again normalized to the virial radius) with time. A fixed overdensity does imply that the proper density evolves as $\rho \propto (1+z)^3$, so the pressure (entropy) are much lower (higher) at low redshift. Infall velocities and accretion rates are also significantly lower, while the fraction of gas accreted in the hot mode is higher. The difference in the behaviour of the two accretion modes is, however, very similar at $z = 0$ and $z = 2$.

Although there are some important differences, the overall properties of the two gas modes are very similar between our different simulations, and are therefore insensitive to the inclusion of metal-line cooling and galactic winds. Without SN feedback, the already dense cold-mode gas reaches even higher densities, the metallicity of hot-mode gas in the outer halo is much lower. Without metal-line cooling, the temperature at radii smaller than $0.2R_{\rm vir}$ is much higher. With strong SN feedback or AGN feedback, a larger fraction of the gas is outflowing, the outflows are faster, and the peak in the fraction of the gas that is accreted in the hot mode peaks at a much larger radius (about $3R_{\rm vir}$ instead of $0.5 - 1.0R_{\rm vir}$).

Kereš et al. (2011) have recently shown that some of the hot gas properties

depend on the numerical technique used to solve the hydrodynamics. They did, however, not include metal-line cooling and feedback. They find that the temperatures of hot gas (i.e. $T > 10^5$ K) around 10^{12-13} $M_\odot$ haloes are the same between the two methods, but that the median density and entropy of 10^{12} $M_\odot$ haloes is somewhat different, by less than a factor of two. These differences are comparable to the ones we find when using different feedback models. They also show that the radial velocities are different at small radii. Our results show that including metal-line cooling decreases the radial velocities, whereas including supernova or AGN feedback increases the radial velocities significantly. Even though there are some differences, the main conclusions of this work are unchanged. The uncertainties associated with the subgrid implementation of feedback and the numerical method are therefore unlikely to be important for our main conclusions.

Cold (i.e. $T \ll 10^5$ K) outflows are routinely detected in the form of blueshifted interstellar absorption lines in the rest-frame UV spectra of star-forming galaxies (e.g. Weiner et al., 2009; Steidel et al., 2010; Rubin et al., 2010; Rakic et al., 2011a). This is not in conflict with our results, because we found that the outflowing gas spans a very wide range of temperatures and because the detectable UV absorption lines are biased towards colder, denser gas. Additionally, the results we showed are mass-weighted, but if we had shown volume-weighted quantities, the outflow fractions would have been larger. The inflowing material has smaller cross-sections and is therefore less likely to be detected (e.g. Faucher-Giguère & Kereš, 2011; Stewart et al., 2011a).

How can we identify cold-mode accretion observationally? The two modes only differ clearly in haloes with $T_{\rm vir} \gg 10^5$ K ($M_{\rm halo} \gg 10^{10.5}$ $M_\odot ((1+z)/3)^{-3/2}$), because photo-ionization by the UV background radiation ensures that all accreted gas is heated to temperatures up to $\sim 10^5$ K near the virial radius. Near the central galaxy, $R \lesssim 0.1 R_{\rm vir}$, it is also difficult to distinguish the two modes, because gas accreted in the hot mode is able to cool.

In the outer parts of sufficiently massive haloes the properties of the gas accreted in the two modes do differ strongly. The cold-mode gas is confined to clumpy filaments that are approximately in pressure equilibrium with the diffuse, hot-mode gas. Besides being colder and denser, cold-mode gas typically has a much lower metallicity and is much more likely to be infalling. However, the spread in the properties of the gas is large, even for a given mode and a fixed radius and halo mass, which makes it impossible to make strong statements about individual gas clouds. Nevertheless, it is clear that most of the dense ($\rho \gg 10^2 \langle \rho \rangle$) gas in high-mass haloes ($T_{\rm vir} \gtrsim 10^6$ K) is infalling, has a very low metallicity and was accreted in the cold-mode.

Cold-mode gas could be observed in UV line emission if we are able to detect it in the outer halo of massive galaxies. Diffuse Lyman-α emission has already been detected (e.g. Steidel et al., 2000; Matsuda et al., 2004), but its interpretation is complicated by radiative transfer effects and the detected emission is more likely scattered light from central H II regions (e.g. Furlanetto et al. 2005;

Faucher-Giguère et al. 2010; Steidel et al. 2011; Hayes et al. 2011; Rauch et al. 2011, but see also Dijkstra & Loeb 2009; Rosdahl & Blaizot 2011). Metal-line emission from ions such as C III, C IV, Si III, and Si IV could potentially reveal cold streams, but current facilities do not probe down to the expected surface brightnesses (Bertone et al., 2010b; Bertone & Schaye, 2012).

The typical temperatures ($T \sim 10^4$ K) and densities ($\rho \gtrsim 10^2 \langle \rho \rangle$) correspond to those of strong quasar absorption lines systems. For example, at $z = 2$ the typical H I column density is[3] $N_{\mathrm{H I}} \sim 10^{16}$ cm$^{-2}(\rho/[10^2 \langle \rho \rangle])^{3/2}$ (Schaye, 2001a) with higher column density gas more likely to have been accreted in the cold mode. At low redshift the H I column densities corresponding to a fixed over-density are about 1–2 orders of magnitude lower (Schaye, 2001a).

Indeed, simulations show that Lyman limit systems (i.e. $N_{\mathrm{H I}} > 10^{17.2}$ cm^{-2}) may be used to trace cold flows (Faucher-Giguère & Kereš, 2011; Fumagalli et al., 2011a; van de Voort et al., 2012) and van de Voort et al. (2012) have demonstrated that cold-mode accretion is required to match the observed rate of incidence of strong absorbers at $z = 3$. Many strong QSO absorbers also tend to have low metallicities (e.g. Ribaudo et al., 2011; Giavalisco et al., 2011; Fumagalli et al., 2011b), although it should be noted that metallicity measurements along one dimension may underestimate the mean metallicities of three-dimensional gas clouds due to the expected poor small-scale metal mixing (Schaye et al., 2007). We also note that most Lyman limit systems are predicted to arise in or around haloes with masses that are much lower than required for the presence of stable accretion shocks near the virial radius, so that they will generally not correspond to cold streams penetrating hot, hydrostatic haloes (van de Voort et al., 2012). To study those, it is therefore more efficient to target sight lines to QSOs close to massive foreground galaxies (e.g. Rakic et al., 2011b; Faucher-Giguère & Kereš, 2011; Stewart et al., 2011a; Kimm et al., 2011).

A   Resolution tests

We have checked (but do not show) that the results presented in this work are converged with respect to the size of the simulation volume if we keep the resolution fixed. The only exception is hot-mode gas at $R > 5R_{\mathrm{vir}}$, for which the radial velocities and accretion rate require a box of at least $50h^{-1}$Mpc on a side (which implies that our fiducial simulation is sufficiently large).

Convergence with resolution is, however, more difficult to achieve. In Figures 10 and 11 we show again the radial profiles and mass dependence of the halo properties for the hot- and cold-mode components at $z = 2$. Shown are three different simulations of the reference model, which vary by a factor of 64 (8) in mass (spatial) resolution. All trends with radius and halo mass are very similar in all runs, proving that most of our conclusions are robust to changes

---

[3]For $N_{\mathrm{H I}} \gtrsim 10^{18}$ cm^{-2} the relation is modified by self-shielding, see e.g. Schaye 2001b; Altay et al. 2011.
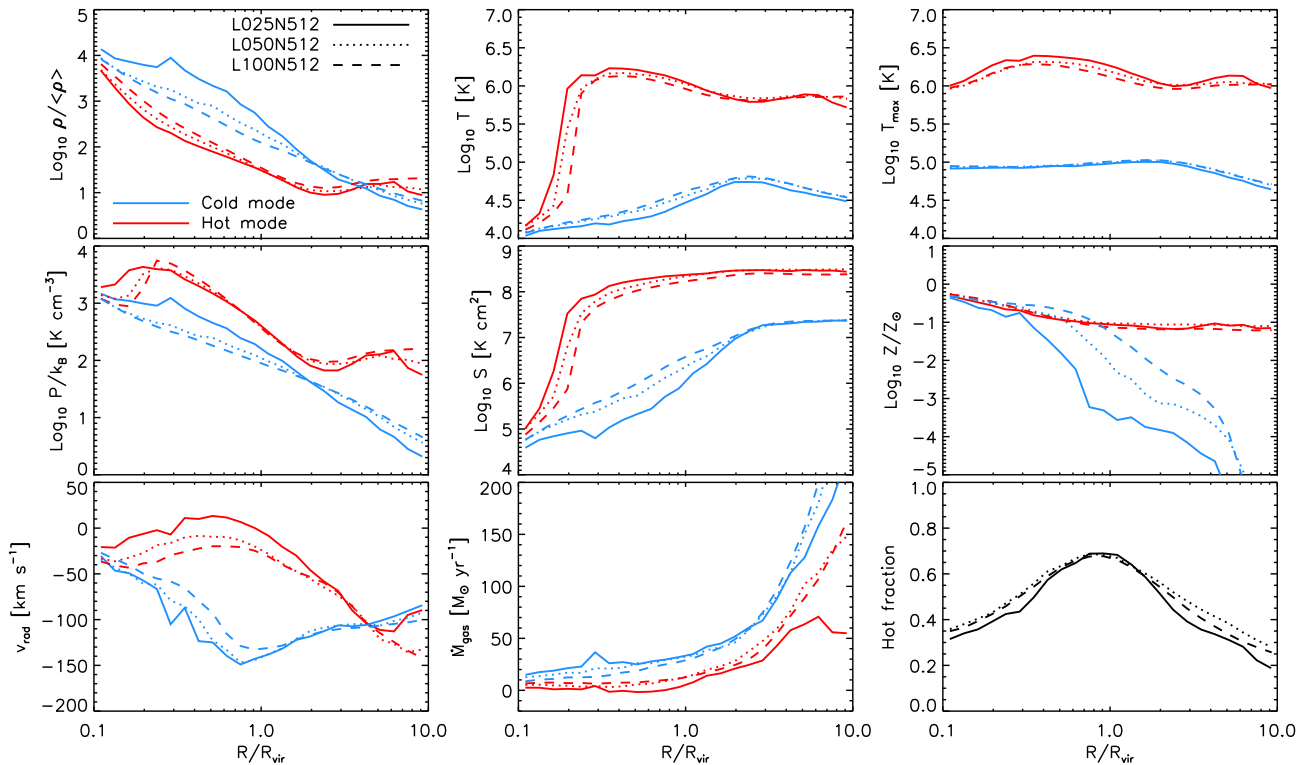
Figure 10: Convergence of gas profiles with resolution. All profiles are for haloes with $10^{11.5}$ M$_\odot$ < M_{halo} < $10^{12.5}$ M$_\odot$ at $z = 2$. Results are shown for simulations *REF_L025N512* (solid), *REF_L050N512* (dotted), and *REF_L050N512* (dashed) and for both the hot (red) and cold (blue) modes. The three simulations vary by a factor of 64 (8) in mass (spatial) resolution. From the top-left to the bottom-right, the different panels show the mass-weighted median gas overdensity, temperature, maximum past temperature, pressure, entropy, metallicity, radial peculiar velocity, the mean accretion rate, and the mean mass fraction of hot-mode gas, respectively.
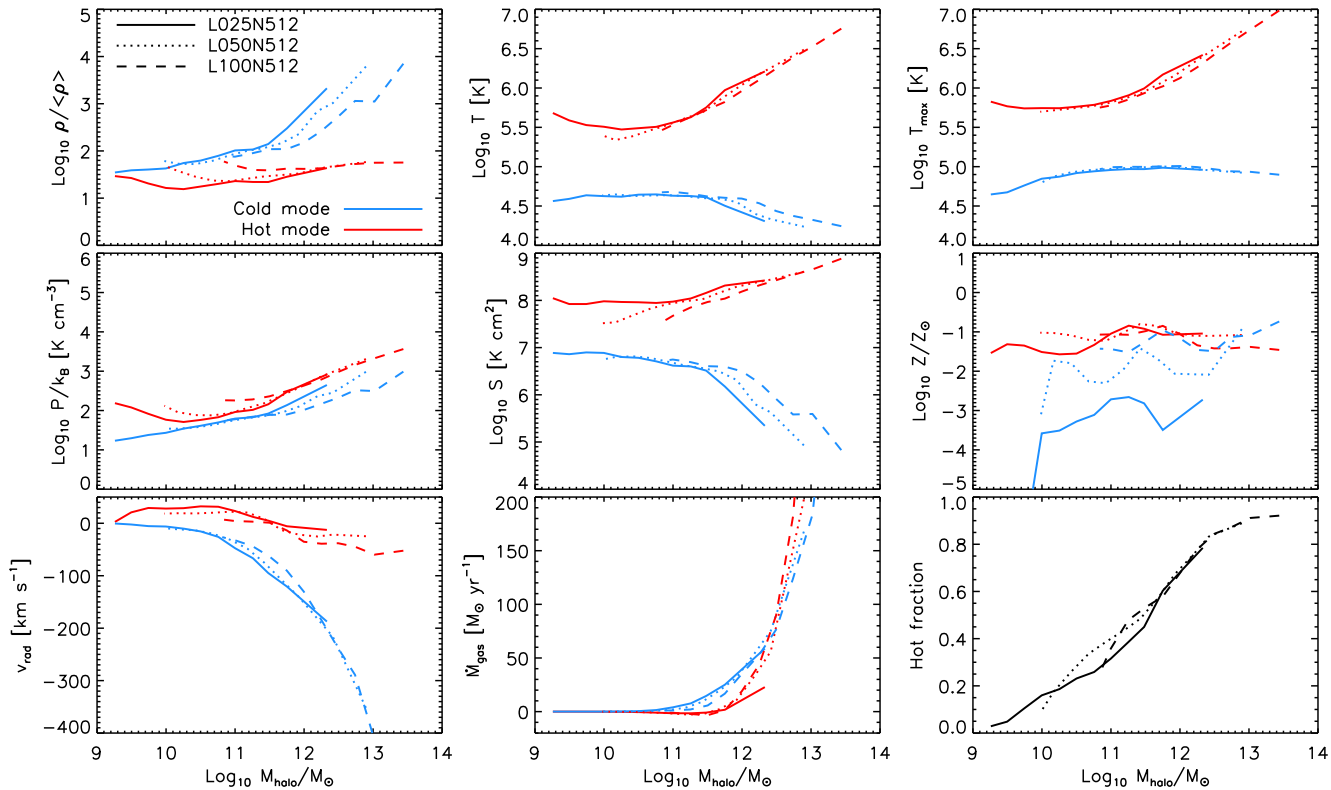
Figure 11: Convergence of the properties of gas at $0.8R_{\text{vir}} < R < 1R_{\text{vir}}$ as a function of halo mass with resolution. Panels and curves as in Figure 10.

in the resolution. Below we will discuss the convergence of hot- and cold-mode gas separately and in more detail.

The convergence is generally excellent for hot mode gas. As the resolution is increased, the density of hot-mode gas decreases slightly and the temperature drop close to the halo centre shifts to slightly smaller radii, which also affects the pressure and entropy. There is a small upturn in the density of hot-mode gas at the virial radius as we approach the halo mass corresponding to the imposed minimum of 100 dark matter particles, showing that we may have to choose a minimum halo mass that is a factor of 5 higher for complete convergence. The radial peculiar velocity increases slightly with resolution, causing the hot-mode accretion rate to decrease.

Convergence is more difficult to achieve for cold-mode gas. The density of cold-mode gas inside haloes, and thereby also the difference between the two modes, increases with the resolution. The pressure of the cold-mode gas also increases somewhat with resolution, which leads to a smaller difference with the pressure of hot-mode gas. The cold-mode radial velocity becomes more negative, increasing the difference between the two modes.

The median metallicity of the cold-mode gas decreases strongly with increasing resolution for $R > 0.3R_{\rm vir}$. The metallicity difference between the two modes therefore increases, although the distributions still overlap (not shown), and the radius at which the metallicities of the two modes converge decreases. In fact, the convergence of the median metallicity of cold-mode gas is so poor that we cannot rule out that it would tend to zero at all radii if we keep increasing the resolution.

If we use particle metallicities rather than SPH smoothed metallicities (see Section 4.3.6), then the median metallicity of both modes is lower and the median cold-mode metallicity plummets to zero around the virial radius (not shown). The decrease in metallicity with increasing resolution is in that case less strong, but still present. The unsmoothed hot-mode metallicities are also not converged and lower than the (converged) smoothed hot-mode metallicities, but they increase with increasing resolution. The difference between the two modes therefore increases with resolution.

With increasing resolution, the radial velocities of cold-mode gas become slightly more negative within the halo. The net accretion rates and hot fractions are converged.

Even though some properties are slightly resolution dependent, or strongly so for the case of the metallicity of cold-mode gas, all our conclusions are robust to increases in the numerical resolution.

Acknowledgements

5

COLD ACCRETION FLOWS AND THE NATURE OF HIGH COLUMN DENSITY H I ABSORPTION AT REDSHIFT 3

Simulations predict that galaxies grow primarily through the accretion of gas that has not gone through an accretion shock near the virial radius and that this cold gas flows towards the central galaxy along dense filaments and streams. There is, however, little observational evidence for the existence of these cold flows. We use a large, cosmological, hydrodynamical simulation that has been post-processed with radiative transfer to study the contribution of cold flows to the observed $z = 3$ column density distribution of neutral hydrogen, which our simulation reproduces. We find that nearly all of the H I absorption arises in gas that has remained colder than $10^{5.5}$ K, at least while it was extragalactic. In addition, the majority of the H I is falling rapidly towards a nearby galaxy, with non-negligible contributions from outflowing and static gas. Above a column density of $N_{\mathrm{H\,I}} = 10^{17}$ cm^{-2}, most of the absorbers reside inside haloes, but the interstellar medium only dominates for $N_{\mathrm{H\,I}} > 10^{21}$ cm^{-2}. Haloes with total mass below 10^{10} M$_{\odot}$ dominate the absorption for $10^{17} < N_{\mathrm{H\,I}} < 10^{21}$ cm^{-2}, but the average halo mass increases sharply for higher column densities. Although very little of the H I in absorbers with $N_{\mathrm{H\,I}} \lesssim 10^{20}$ cm^{-2} resides inside galaxies, systems with $N_{\mathrm{H\,I}} > 10^{17}$ cm^{-2} are closely related to star formation: most of their H I either will become part of the interstellar medium before $z = 2$ or has been ejected from a galaxy at $z > 3$. Cold accretion flows are critical for the success of our simulation in reproducing the observed rate of incidence of damped Lyman-α and particularly that of Lyman limit systems. We therefore conclude that cold accretion flows exist and have already been detected in the form of high column density H I absorbers.

Freeke van de Voort, Joop Schaye, Gabriel Altay, and Tom Theuns

5.1 Introduction

Galaxies grow by accreting gas from their haloes and their haloes grow by accreting gas from the intergalactic medium (IGM). Feedback from star formation and active galactic nuclei returns a significant fraction of the interstellar medium (ISM) to the halo and may even blow it out of the halo into the IGM. This cycle of inflow and outflow makes the circumgalactic medium and the IGM vital ingredients for our understanding of the formation and evolution of galaxies.

Theoretically we expect that gas accreting onto haloes with sufficiently low circular velocities will not shock-heat to the virial temperature of the halo, but will instead flow in cold (i.e. $T \sim 10^4$ K) and relatively unimpeded. This so-called "cold accretion" will happen if the cooling time of virialized gas is too short to maintain a hot, hydrostatic halo (e.g. White & Frenk, 1991; Birnboim & Dekel, 2003; Dekel & Birnboim, 2006). The existence of such a cold accretion mode has been confirmed by simulations, which have furthermore demonstrated that cold-mode accretion can also be important for haloes sufficiently massive to contain hot, hydrostatic gas. Because gas accretes preferentially along the filaments of the cosmic web, the streams of infalling gas have relatively high gas densities and correspondingly low cooling times. This allows the cold streams to penetrate the hot, hydrostatic haloes surrounding massive galaxies, particularly at high redshift (e.g. Kereš et al., 2005; Ocvirk et al., 2008; Dekel et al., 2009a; Kereš et al., 2009a; Brooks et al., 2009; van de Voort et al., 2011a,b; van de Voort & Schaye, 2012; Fumagalli et al., 2011a; Faucher-Giguère et al., 2011).

Although the dilute halo gas that has been shock-heated to the virial temperature is routinely detected in X-ray observations of clusters and groups of galaxies, and has perhaps even been seen around individual galaxies (e.g. Crain et al., 2010a,b; Anderson & Bregman, 2011), there is no clear, direct observational evidence for cold-mode accretion. However, Rauch et al. (2011) have observed cold, filamentary, infalling gas which could be cold-mode accretion. It has been claimed that the diffuse Lyman-α emission detected around some high-redshift galaxies is due to cold accretion (e.g. Dijkstra & Loeb, 2009; Goerdt et al., 2010), but both simulations and observations indicate that the emission is more likely scattered light from central H II regions (e.g. Furlanetto et al., 2005; Faucher-Giguère et al., 2010; Steidel et al., 2010; Hayes et al., 2011; Rauch et al., 2011). Individual H I absorbers have also been suggested to be evidence for cold accretion based on their proximity to a galaxy and their low metallicity (Ribaudo et al., 2011; Giavalisco et al., 2011), but it is difficult to make strong statements for an individual gas cloud, particularly since H I near galaxies does not need to be inflowing, even if it has a low metallicity. Given that outflows are routinely detected in the form of blueshifted interstellar absorption lines in the spectra of star-forming galaxies (e.g. Steidel et al., 2010; Rubin et al., 2010; Rakic et al., 2011a), one may wonder why inflowing gas is not commonly seen in the form of redshifted absorption lines. It is, however, quite possible that the inflowing material has such small cross-sections that the signal is completely swamped by

outflowing material (e.g. Faucher-Giguère & Kereš, 2011; Stewart et al., 2011a).

It is challenging to observe cold gas around distant galaxies in emission, because it typically has densities that are low compared to that of the cold ISM. Absorption line measurements are therefore very important, with the Lyman-α line of neutral hydrogen being the most sensitive probe. Indeed, H I absorption can be detected both within and outside of galaxies and at $z \sim 3$ the column density distribution has been measured over ten orders of magnitude in $N_{\mathrm{H\,I}}$ (e.g. Tytler, 1987; Kim et al., 2002; Péroux et al., 2005; O'Meara et al., 2007; Prochaska & Wolfe, 2009; Noterdaeme et al., 2009; Prochaska et al., 2010). By correlating the H I absorption in the spectra of background quasars with both the transverse and line of sight separations from foreground galaxies, Rakic et al. (2011b) have recently presented strong evidence for infall of cold gas on scales of $\sim 1.4 - 2.0$ proper Mpc at $z \sim 2.4$.

The low column density ($N_{\mathrm{H\,I}} < 10^{17.2}$ cm^{-2}) material is known as the Lyman-α forest and originates mostly in the photo-ionized IGM (e.g. Bi et al., 1992; Cen et al., 1994; Hernquist et al., 1996; Theuns et al., 1998; Schaye, 2001a). Because these systems are optically thin, they are relatively easy to model in simulations. Lyman Limit Systems (LLSs; $10^{17.2} < N_{\mathrm{H\,I}} < 10^{20.3}$ cm^{-2}) and Damped Lyman-α Systems (DLAs; $N_{\mathrm{H\,I}} > 10^{20.3}$ cm^{-2}) are optically thick to Lyman limit photons. Because the gas comprising these strong absorbers is partially shielded from the ambient UV radiation, it will be more neutral, and will also be colder, than if it were optically thin. These high column density systems are harder to model, because in order to know which gas is self-shielded, one needs to perform a radiative transfer calculation. Additionally, at the highest gas densities a fraction of the hydrogen will be converted into molecules, reducing the atomic hydrogen fraction[1] (e.g. Schaye, 2001b; Krumholz et al., 2009).

The difficulty with interpreting absorption-line studies is that they only allow us to study the gas along the line-of-sight direction. It is therefore hard to determine what kind of objects are causing the absorption. Simulations that reproduce the observed absorption-line statistics can be employed to study the three-dimensional distribution of the absorbing gas and to guide the interpretation of the observations.

A lot of progress has been made in understanding and modelling the H I column density distribution function (e.g. Katz et al., 1996; Schaye, 2001a,b; Zheng & Miralda-Escudé, 2002; Altay et al., 2011; McQuinn et al., 2011; Fumagalli et al., 2011a). Building on previous work, we ask what kind of gas is causing the H I absorption. Altay et al. (2011) have post-processed the reference model of the OWLS suite of cosmological simulations (see Section 5.2) with radiative transfer and found that the predicted $z = 3$ H I column density distribution agreed with observations over the full range of observed column densities. We analyse their simulation, selecting different subsets of the gas to see what fraction of the high column density absorption is due to what kind of gas. The selections are based

---

[1] In this work we mean atomic hydrogen when we write "neutral hydrogen" or "H I".

on the maximum past temperature, membership of haloes and the ISM, and the radial velocity towards the nearest galaxy. These properties are all important to determine whether or not the gas is accreting in the cold mode. We find that almost all high column density absorption arises in gas that has never been hotter than $10^{5.5}$ K, at least not while it was extragalactic, and that resides inside of haloes. Most of this gas is strongly linked to star formation because it is either currently in the ISM, has been part of the ISM, or will become part of the ISM before $z = 2$. Inflowing gas provides the largest contribution to the H I column density distribution function, but outflowing and static gas cannot be neglected.

In Section 5.2 we describe the simulation we used. The different gas samples are listed and described in Section 5.3. In Section 5.4 we determine the contribution of the different gas samples to the total amount of gas and H I and to the H I column density distribution function. We discuss our results and conclude in Section 5.5.

5.2   Simulations

We use a modified version of GADGET-3 (last described in Springel, 2005b), a smoothed particle hydrodynamics (SPH) code that uses the entropy formulation of SPH (Springel & Hernquist, 2002), which conserves both energy and entropy where appropriate. This work is part of the OverWhelmingly Large Simulations (OWLS) project (Schaye et al., 2010), which consists of a large number of cosmological simulations with varying (subgrid) physics. Here we make use of the so-called 'reference' model, with the difference that it was run with updated cosmological parameters. We have tested runs with different supernova feedback and with AGN feedback and we found our conclusions to be robust to changes in the model. The model is fully described in Schaye et al. (2010) and we will only summarize its main properties here.

The simulation assumes a ΛCDM cosmology with parameters $\Omega_m = 1 - \Omega_\Lambda = 0.272$, $\Omega_b = 0.0455$, $h = 0.704$, $\sigma_8 = 0.81$, $n = 0.967$. These values are taken from the WMAP year 7 data (Komatsu et al., 2011). In the present work, we use the simulation output at redshifts 3 and 2.

A cubic volume with periodic boundary conditions is defined, within which the mass is distributed over 512^3 dark matter and as many gas particles. The box size (i.e. the length of a side of the simulation volume) of the simulation used in this work is 25 h^{-1} comoving Mpc. The (initial) particle masses for baryons and dark matter are 2.1×10^6 M$_\odot$ and 1.0×10^7 M$_\odot$, respectively. The gravitational softening length is 1.95 h^{-1} comoving kpc, i.e. 1/25 of the mean dark matter particle separation, with a maximum of 0.5 h^{-1} proper kpc.

Star formation is modelled according to the recipe of Schaye & Dalla Vecchia (2008). A polytropic equation of state $P_{tot} \propto \rho_{gas}^{4/3}$ is imposed for densities exceeding $n_H = 0.1$ cm^{-3}, where P_{tot} is the total pressure and ρ_{gas} the density of the gas. Gas particles with proper densities $n_H \geq 0.1$ cm^{-3} and temperatures

$T \leq 10^5$ K are moved onto this equation of state and can be converted into star particles. The star formation rate (SFR) per unit mass depends on the gas pressure and reproduces the observed Kennicutt-Schmidt law (Kennicutt, 1998) by construction.

Feedback from star formation is implemented using the prescription of Dalla Vecchia & Schaye (2008). About 40 per cent of the energy released by type II supernovae is injected locally in kinetic form, while the rest of the energy is assumed to be lost radiatively. The initial wind velocity is 600 km s^{-1} and the initial mass loading is two, meaning that, on average, a newly formed star particle kicks twice its own mass in neighbouring gas particles.

The abundances of eleven elements released by massive stars and intermediate mass stars are followed as described in Wiersma et al. (2009b). We assume the stellar initial mass function (IMF) of Chabrier (2003), ranging from 0.1 to 100 M$_\odot$. As described in Wiersma et al. (2009a), radiative cooling and heating are computed element by element in the presence of the cosmic microwave background radiation and the Haardt & Madau (2001) model for the UV/X-ray background from galaxies and quasars in the optically thin limit.

We apply a self-shielding correction in post-processing by using the radiative transfer calculations described in Altay et al. (2011) and Altay et al. (in preparation). This is an iterative method that uses reverse ray-tracing (i.e. shooting rays starting from the gas element) to compute the optical depth and to calculate a new neutral fraction until the results converge. The method assumes that the radiation field is dominated by the UV background radiation. Altay et al. (2011) have shown that this provides a good match to the observed H I column density distribution function. The temperature of the ISM gas in the simulation is determined by the imposed effective pressure and therefore not realistic, so we set it to 10^4 K, typical of the warm neutral medium. Gas with lower densities ($n_{\rm H} < 0.1$ cm^{-3}) was assumed to be optically thin during the simulation, whereas this may not be the case because of self-shielding. We use the temperatures that were calculated in the presence of the UV background to be self-consistent with the simulation, even though the actual gas temperatures will be lower in the self-shielded case. These choices do not affect the results described here. Hydrogen is converted into molecules with a prescription based on observations by Blitz & Rosolowsky (2006), who provide the molecular fraction as a function of the gas pressure.

Recently Kereš et al. (2011) have shown that the sizes of galaxy discs depend on the computational method used (but see also Hummels & Bryan (2011)). However, Sales et al. (2010) have shown that changes in the feedback model lead to dramatic variations in the morphology of discs, as well as to variations of up to an order of magnitude in disc masses. Indeed, Scannapieco et al. (2011) have shown explicitly that variations in the feedback prescription are much more important than the numerical scheme used to solve the hydrodynamics. To assess the robustness of our conclusions, we have redone our analysis using simulations with different feedback prescriptions, but do not show the results. The simula-

Table 5.1: List of selection criteria for the various gas samples in the same order as in Figures 5.1 and 5.4.

#	name	selection
1.	*all*	all gas
2.	*Tmax<5p5*	gas with $T_{\mathrm{max}} \leq 10^{5.5}$ K
3.	*inhalo*	halo gas (with $M_{\mathrm{halo}} \geq 10^9$ M$_\odot$)
4.	*inmainhalo*	gas in main haloes (with $M_{\mathrm{main\ halo}} \geq 10^9$ M$_\odot$)
5.	*insubhalo*	gas in satellites (with $M_{\mathrm{satellite}} \geq 10^8$ M$_\odot$)
6.	*inhalo9to10*	gas in haloes with $10^9 \leq M_{\mathrm{halo}} < 10^{10}$ M$_\odot$
7.	*inhalo10to11*	gas in haloes with $10^{10} \leq M_{\mathrm{halo}} < 10^{11}$ M$_\odot$
8.	*inhalo11to12*	gas in haloes with $10^{11} \leq M_{\mathrm{halo}} < 10^{12}$ M$_\odot$
9.	*inhalo12to13*	gas in haloes with $10^{12} \leq M_{\mathrm{halo}} < 10^{13}$ M$_\odot$
10.	*inflowing*	gas that is moving towards the nearest (nearest in units of R_{vir}) halo centre with a peculiar velocity greater than a quarter of its circular velocity
11.	*static*	gas that is neither inflowing (#10) nor outflowing (#12)
12.	*outflowing*	gas that is moving away from the nearest (nearest in units of R_{vir}) halo centre with a peculiar velocity greater than a quarter of its circular velocity
13.	*inhalo_inflowing*	halo gas that is moving towards the halo centre with a peculiar velocity greater than a quarter of its circular velocity
14.	*inhalo_static*	halo gas that is neither inflowing (#10) nor outflowing (#12)
15.	*inhalo_outflowing*	halo gas that is moving away from the halo centre with a peculiar velocity greater than a quarter of its circular velocity
16.	*inISM*	gas which is in the ISM at $z = 3$
17.	*pastISM*	gas which is not in the ISM at $z = 3$, but was at some redshift $z > 3$
18.	*futureISM*	gas which is not in the ISM at $z = 3$, but will be before $z = 2$.
19.	*futurefirstISM*	gas which is not in the ISM at $z \geq 3$, but will be before $z = 2$.

tions reproduce the observed H I column density distribution function independent of the feedback scheme (Altay et al. in preparation). Although the relative contributions of the different gas selections to the H I absorption vary somewhat between different simulations, the general conclusions are unchanged. We therefore conclude that the uncertainties associated with the feedback and the numerical method are unlikely to be important for our conclusions.

5.3 Gas samples

We compute the $z = 3$ contribution of gas with different properties to the H I column density distribution function. The gas selections that we consider are listed in Table 5.1. They are based on the maximum past temperature, T_{max}, membership of haloes, the peculiar velocity towards the nearest halo, v_{rad}, and on whether the gas is part of the ISM. These properties are all important to determine whether or not this gas is accreting in the cold mode. Cold-mode gas should have a low temperature at least until it becomes part of the ISM. Gas has only been accreted if it is inside a halo. It is likely to accrete onto a halo or its central galaxy if its radial peculiar velocity towards the halo centre is high, but note that gas orbiting around the central galaxy can also be built up by cold flows and could be viewed as evidence for cold accretion (Stewart et al., 2011b). The gas is certainly accreting onto a galaxy if it enters the ISM of a galaxy and becomes star forming in the near future. Below, we describe the selections in detail.

The maximum past temperature, T_{max}, is the maximum value that the temperature of a gas element has reached over the entire past simulation history. High time resolution is achieved by storing a separate variable during the simulation which is updated every time-step if the gas reaches a higher temperature than the previous value of T_{max}. The artificial temperature that a gas particle has while it is on the imposed equation of state, and thus star forming, is ignored. Because we are interested in the temperature history before the gas accretes onto a galaxy, this is consistent with our aims. Cold-mode gas does not experience a shock at the virial radius and reaches a maximum temperature of $\sim 10^5$ K just before accretion onto a halo due to heating by the UV background (van de Voort et al., 2011a). We therefore select cold-mode gas by using $T_{max} \leq 10^{5.5}$ K (sample *Tmax<5p5* of Table 5.1). While hot-mode gas has by definition been hotter than $10^{5.5}$ K, its *current* temperature can be much lower (e.g. van de Voort & Schaye, 2012).

We note that T_{max} may underestimate the true maximum past temperature. In SPH simulations a shock is smeared out over a few smoothing lengths, leading to in-shock cooling (Hutchings & Thomas, 2000). If the cooling time is of the order of or smaller than the time step, then the maximum temperature will be underestimated. Creasey et al. (2011) have shown that a particle mass of 10^6 $M_\odot$ is sufficient to avoid numerical overcooling of accretion shocks onto

haloes, which is very close to the resolution used in this simulation. Interpolating their results indicates that our mass resolution is indeed sufficient. Even with infinite resolution, the post-shock temperatures may, however, not be well defined. Because they have different masses, electrons and protons will have different temperatures in the post-shock gas and it may take some time before they equilibrate through collisions or plasma effects. We have ignored this complication. Another effect, which was also not included in our simulation, is that shocks may be preceded by the radiation from the shock, which may affect the temperature evolution. Ignoring these issues, van de Voort et al. (2011a) showed that the distribution of $T_{\max}$ is bimodal and that a cut at $T_{\max} = 10^{5.5}$ K naturally divides the gas into filamentary cold- and diffuse hot-mode accretion and that it produces similar results as studies based on adaptive mesh refinement simulations.

Haloes are found by using a Friends-of-Friends (FoF) algorithm. If the separation between two dark matter particles is less than 20 per cent of the average separation (the linking length $b = 0.2$), they are placed in the same group. Assuming a radial density profile $\rho(r) \propto r^{-2}$, corresponding to a flat rotation curve, such a group has an average overdensity of $\langle \rho_{\text{halo}} \rangle / \langle \rho \rangle \approx 180$ (e.g. Lacey & Cole, 1994), which is close to the value for a virialized object predicted by the top-hat spherical collapse model. Baryonic particles are placed in a halo if their nearest dark matter neighbour is part of the halo. Haloes can contain both bound and unbound particles. The selections are made by using haloes with total mass $M_{\text{halo}} \geq 10^9$ M$_\odot$, corresponding to approximately 100 dark matter particles. A gas particle is considered to be in a halo if it is a member of a Friends-of-Friends group (*inhalo*).

We use SUBFIND (Springel et al., 2001; Dolag et al., 2009) on the FoF output to identify gravitationally bound subhaloes. The main halo is the most massive subhalo in a FoF halo and the remaining subhaloes are classified as satellites. Because only bound particles are included in this definition, some unbound particles are not attached to any subhalo, although they are part of the FoF halo. The gas is in a main halo if it is a member of the most massive subhalo, with $M_{\text{main halo}} \geq 10^9$ M$_\odot$ (*inmainhalo*) and the gas is in a satellite if it is a member of a subhalo, with $M_{\text{satellite}} \geq 10^8$ M$_\odot$, that is not a main halo (*insubhalo*).

The halo gas (*inhalo*) is subdivided into four mass bins, $10^9 \leq M_{\text{halo}} < 10^{10}$ M$_\odot$ (*inhalo9to10*), $10^{10} \leq M_{\text{halo}} < 10^{11}$ M$_\odot$ (*inhalo10to11*), $10^{11} \leq M_{\text{halo}} < 10^{12}$ M$_\odot$ (*inhalo11to12*), and $10^{12} \leq M_{\text{halo}} < 10^{13}$ M$_\odot$ (*inhalo12to13*), containing 38 504, 3626, 275, and 17 haloes, respectively.

The radial peculiar velocity of every gas particle is calculated with respect to the nearest halo. The position (and the centre) of the halo is defined as the position of its most bound particle. The virial radius, R_{vir}, is the radius around this centre which encloses an average density that agrees with the prediction from top-hat spherical collapse calculations in a ΛCDM cosmology (Bryan & Norman, 1998). Distances towards a halo, d, are normalized by R_{vir} of that halo. The nearest halo is the one for which d/R_{vir} is minimum. The halo's peculiar

velocity is defined to be the centre of mass velocity of its main subhalo and is subtracted from the gas peculiar velocity to determine the relative radial peculiar velocity. If the gas is located inside a halo, its radial velocity is calculated with respect to the centre of that halo, even if it is also in a satellite. The selections are made by comparing the radial velocity of the gas to a quarter of the circular velocity, $v_{circ} = \sqrt{GM_{vir}/R_{vir}}$, of the nearest halo, where M_{vir} is the total mass inside R_{vir}. The gas is inflowing when $v_{rad} \leq -0.25v_{circ}$ (*inflowing*), static when $-0.25v_{circ} < v_{rad} < 0.25v_{circ}$ (*static*), and outflowing when $v_{rad} \geq 0.25v_{circ}$ (*outflowing*). Note that gas near or inside a small halo embedded in a filament may be classified as outflowing with respect to its nearest halo, whereas it might be inflowing with respect to a much larger halo that is being fed by this filament. It is hard to unambiguously identify this gas, so we just caution the reader that the amount of inflowing gas may be an underestimate. This would only strengthen our conclusions.

The definition of the nearest halo is somewhat arbitrary and the gas may be many virial radii away and unrelated to the nearest halo. This is why we make the same radial velocity cuts for all gas (samples 10–12 of Table 5.1) also for gas that is already inside a (FoF) halo, so that we know it has already been accreted by the halo (samples 13–15 of Table 5.1). Halo gas which is inflowing is in the process of accreting onto the central galaxy (*inhalo_inflowing*).

In our simulation gas becomes star forming when its density exceeds $n_H = 0.1 \text{ cm}^{-3}$ while its temperature $T \leq 10^5$ K. Because of supernova feedback, the gas can leave the ISM and re-enter it (e.g. Oppenheimer et al., 2010). We will call this recycled gas even though it may not have been part of a star before it was ejected from the ISM. We keep track of the time a gas particle last reached or left the ISM. We select all the gas that is star forming at $z = 3$, i.e. the ISM (*inISM*), star forming before but not at $z = 3$, i.e. recycled gas (*pastISM*), star forming before $z = 2$ but not at $z = 3$, i.e. gas that will accrete onto a galaxy before $z = 2$ (*futureISM*), or star forming before $z = 2$ but not at $z \geq 3$, i.e. gas that will accrete onto the galaxy before $z = 2$ for the first time (*futurefirstISM*). The time elapsed between $z = 3$ and $z = 2$ is about 1.2 Gyr, which is similar to the gas consumption time scale implied by the observed Kennicutt-Schmidt star formation law for typical ISM densities and indicates whether the gas will accrete onto a galaxy in the near future.

5.4   Results

5.4.1   Gas and H I fractions

Many of the gas samples listed in Table 5.1 contain a much larger fraction of the total H I mass than of the total gas mass. This is illustrated in Figure 5.1, which shows the fraction of the total amount of gas (left panel) and the fraction of the total amount of neutral hydrogen (right panel) accounted for by the samples
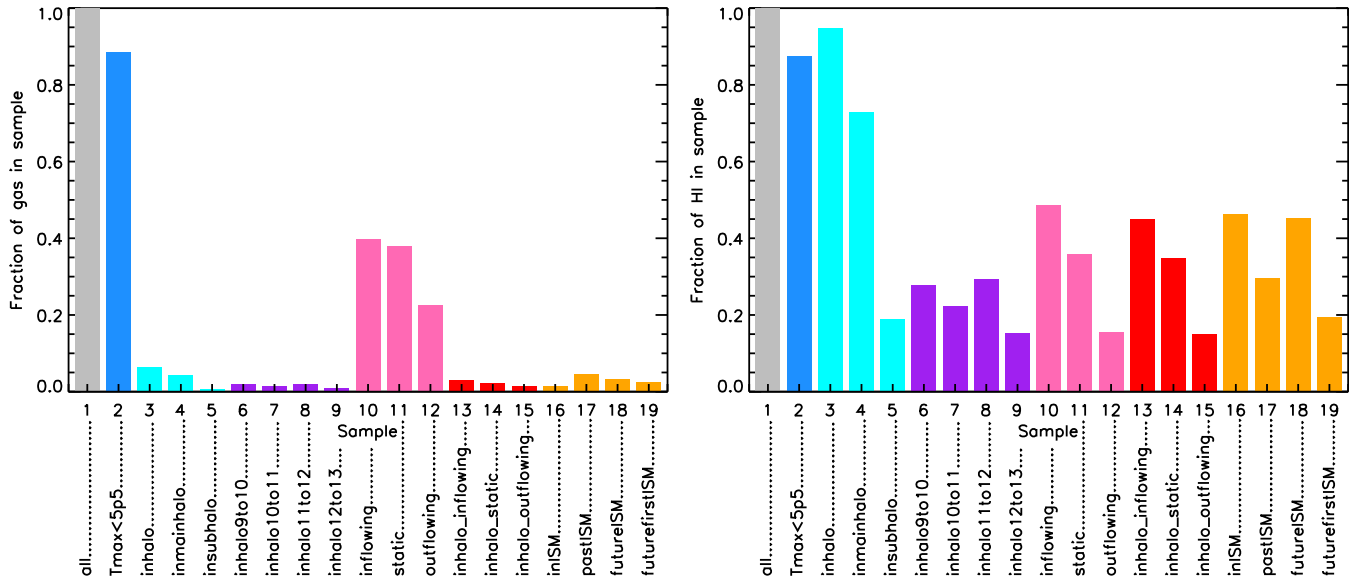
Figure 5.1: Fraction of the total amount of gas (left) and H I (right) at $z = 3$ accounted for by the selections listed in Table 5.1. Many samples (#3–9 and #13–19) contain a much larger fraction of the H I mass than of the total gas mass.

listed in Table 5.1. The density parameter of all the gas $\Omega_{\mathrm{gas}} = 0.15787$ and of neutral hydrogen $\Omega_{\mathrm{H\,I}} = 0.00178$, so at $z = 3$ only about one per cent of the gas mass consists of neural hydrogen. Selections based on halo membership (samples 3–9 and 13–15) and on participation in star formation (samples 16–19) account for little of the gas mass, but a significant part of the H I mass.

The maximum past temperature selection (*Tmax<5p5*) contains almost all gas in the simulation. This is not so surprising, because most of the mass in the Universe is in the IGM and the UV background can only heat this gas to temperatures $\lesssim 10^5$ K. The same selection also contains almost all neutral hydrogen gas. Gas that shocked to $T > 10^{5.5}$ K while it was extragalactic, either through accretion shocks or shocks caused by galactic winds, accounts for only about 10 per cent of both the gas and H I. This already tells us that *most gas and most neutral hydrogen is cold-mode gas*.

Note that this is not a trivial result. While it is true that gas with temperatures above $10^{5.5}$ K will be collisionally ionized and therefore difficult to see in H I absorption, we distinguish cold- and hot-mode gas based on the maximum *past* temperature rather than the *current* temperature. Gas parcels accreted in the hot mode can cool down, reach temperatures similar to those of cold-mode gas, and show up in H I absorption.

Haloes contain less than 10 per cent of the gas, but more than 90 per cent of the neutral hydrogen (*inhalo*). Gas outside haloes contributes little to the H I content, because the neutral fraction increases with density and the highest densities are found inside haloes. Combining this with the finding that sample *Tmax<5p5* accounts for nearly 90 per cent of the neutral hydrogen, proves that most H I absorption arises from gas that has been accreted onto haloes in the cold-mode. All main haloes contain seven times more gas and four times more H I than all satellites (compare *inmainhalo* and *insubhalo*).

Haloes from the entire mass range contain a significant part of the H I mass (samples 6–9). Haloes in the highest mass bin are very rare and their total contribution is the smallest (15 per cent; *inhalo12to13*). Haloes below $M_{\mathrm{halo}} = 10^9$ M$_\odot$, and therefore below our resolution limit, are not expected to contain a large amount of H I, because we already account for the vast majority of H I with higher mass haloes (*inhalo*) and our simulations reproduce the observed H I distribution (Altay et al., 2011).

Approximately 40 per cent of the gas and half of the neutral hydrogen is inflowing faster than a quarter of the circular velocity of the nearest (nearest in units of R_{vir}) halo (*inflowing*). The contribution is even larger for all inflowing gas, without a minimum radial velocity threshold (about 65 per cent; not shown). Outflows always account for less than 25 per cent of the gas and H I mass (*outflowing*). The contribution of outflowing gas and of static gas (i.e. gas moving either in or out at velocities below $0.25v_{\mathrm{circ}}$; *static*) is lower for H I than for all gas, whereas the contribution of inflowing gas is higher.

Within haloes, the importance of inflows (*inhalo_inflowing*), with respect to outflows (*inhalo_outflowing*) and static gas (*inhalo_static*), increases slightly. This

is not visible in Figure 5.1, because the bars are too small. The H I inside haloes is distributed over the inflowing, static, and outflowing components in the same way as all H I (i.e. both inside and outside of haloes), because haloes account for nearly all the H I. Thus, about half of the H I can be accounted for by gas inside the virial radius that is falling towards the halo centre with a velocity greater than 25 per cent of the halo's circular velocity.

Very little gas is contained in the ISM of galaxies, but almost half of the H I mass is (*inISM*). The amount of gas that has been ejected from galaxies at $z > 3$ (*pastISM*) is greater than the amount that is in the ISM at $z = 3$ (*inISM*), but the situation is reversed for H I. Similarly, more gas has been ejected from galaxies at $z > 3$ (*pastISM*) than will accrete onto galaxies at $2 \leq z < 3$ (*futureISM*), but it is the other way around for neutral hydrogen. Taken together, gas that is currently in the ISM and gas that will enter the ISM within 1.2 Gyr (*inISM + futureISM*) account for most of the H I in the Universe. Gas/H I that will accrete onto a galaxy at $2 \leq z < 3$ *for the first time* (*futurefirstISM*) accounts for most/less than half of the total amount of gas/H I that will accrete at $2 \leq z < 3$ (*futureISM*).

5.4.2   Spatial distribution: A visual impression

To gain insight into the spatial distribution of the neutral hydrogen, Figure 5.2 shows the H I column densities at $z = 3$ in a 2 by 2 comoving h^{-1} Mpc region centred on a $10^{12.4}$ M$_\odot$ halo, one of the most massive objects in the simulation. The Figure is meant to illustrate the spatial distribution of the H I corresponding to some of the samples listed in Table 5.1. Some gas samples trace only a subset of the high column density sightlines, while others trace the full morphology of the H I.

In the top row, the column densities are shown when including all gas (left), only gas with $T_{max} \leq 10^{5.5}$ K (middle), and only gas inside haloes (right). The vast majority of neutral gas inside and outside haloes satisfies $T_{max} \leq 10^{5.5}$ K, so even for the $10^{12.4}$ M$_\odot$ halo with $T_{vir} = 10^{6.2}$ K, most of the H I is contributed by gas that has $T_{max} \leq 10^{5.5}$ and that has thus not gone through an accretion shock near the virial radius. When we exclude gas outside haloes (top right panel), we lose the filamentary material connecting different haloes, as well as most of the $N_{H I} < 10^{17}$ cm^{-2} sightlines.

The middle row shows the column density when including only gas that is inflowing towards the nearest (nearest in units of R_{vir}) halo faster than a quarter of the circular velocity of that halo (left), only gas outflowing faster than a quarter of the circular velocity (right), and the remaining and hence "static" gas (middle). The morphologies of the H I gas are very different. The inflowing gas traces most of the extended and filamentary structure of the total H I distribution, while the static and outflowing gas are concentrated in the centres of the haloes.

The images shown in the bottom row include only gas that is not part of the ISM at $z = 3$. Additionally, the panels include only gas that was part of the ISM
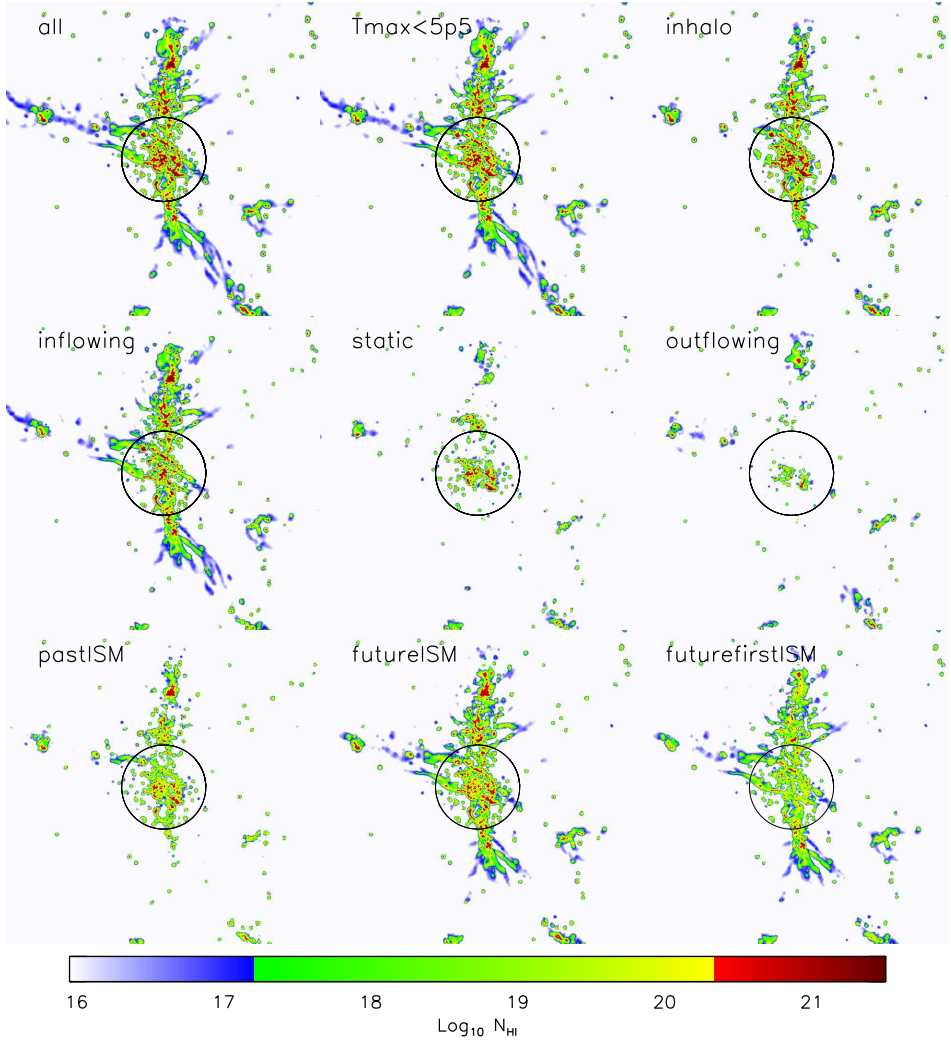
Figure 5.2: H I column density images for a cubic region of 2 comoving h^{-1} Mpc on a side centred on a $10^{12.4}$ M$_\odot$ halo at $z = 3$, one of the most massive haloes in this simulation. For reference, the virial radius of this halo is 268 comoving h^{-1} kpc and indicated with black circles. For all but the first panel, the H I column densities were computed including only gas selected to be part of the samples indicated in each panel and listed in Table 5.1. Some gas samples trace the full H I morphology, whereas others only trace a subset of the high column density sightlines.

for some redshift $z > 3$ (i.e. ejected gas; left panel), only gas that becomes part of the ISM at $2 \leq z < 3$ (middle), and only gas that joins the ISM at $2 \leq z < 3$ for the first time (right). The ejected gas that is not currently part of the ISM (bottom left panel) is located relatively close to the centres of haloes, where star formation is taking place, but it is more spread out than the actual ISM (not shown). Comparing it to the middle row, with inflowing (left), static (centre), and outflowing (right) gas, we immediately see that some of the ejected gas is already inflowing and thus recycling. Note that it may have been ejected from a different halo than the one it is in now. Most of the lower column density filamentary gas, especially the gas outside the halo, is missing. Even though ejected gas contributes significantly to $N_{\mathrm{H\,I}} \gtrsim 10^{18}$ cm^{-2} gas, it is unimportant for lower column densities.

If we include all the gas that will reach the ISM between $2 \leq z < 3$, i.e. within 1.2 Gyr from the redshift at which we are studying the H I column densities (bottom middle panel), we leave the morphology of the $N_{\mathrm{H\,I}} > 10^{16}$ cm^{-2} sightlines intact, including the filaments in between haloes, although they become somewhat weaker. Most, but not all, H I gas in filaments close to a halo will accrete onto a galaxy before $z = 2$.

The last panel shows a subset of the gas in the previous panel, because it only includes gas that reaches the ISM between $2 \leq z < 3$ for the first time. The general morphology of H I is the same, apart from some extra holes in the central region of the halo, which are dominated by ejected gas. The column densities above 10^{18} cm^{-2} are lower for a given pixel.

We conclude that the large-scale H I filaments that feed massive haloes consist mostly of gas that has never gone through a virial shock, that is inflowing and that will join the ISM, and hence participate in star formation, in the near future. This gas typically has H I column densities similar to those of LLSs or higher for embedded clumps. Within haloes, the infalling cold-mode gas has higher H I column densities and tends to have a more clumpy morphology than the H I in filaments outside haloes.

5.4.3   The column density distribution function

The H I column density distribution function is defined as the number of absorption lines $\mathcal{N}$, per unit column density $dN_{\mathrm{H\,I}}$, per unit absorption distance dX.

$$f(N_{\mathrm{H\,I}}, z) \equiv \frac{d^2\mathcal{N}}{dN_{\mathrm{H\,I}} dX} \equiv \frac{d^2\mathcal{N}}{dN_{\mathrm{H\,I}} dz} \frac{dz}{dX} \tag{5.1}$$

Absorbers with a fixed proper size and a constant comoving number density are distributed uniformly, in a statistical sense, per unit absorption distance along a line-of-sight (Bahcall & Peebles, 1969). The absorption distance is related to the redshift path dz as $dX/dz = H_0(1+z)^2/H(z)$, where $H(z)$ is the Hubble parameter.
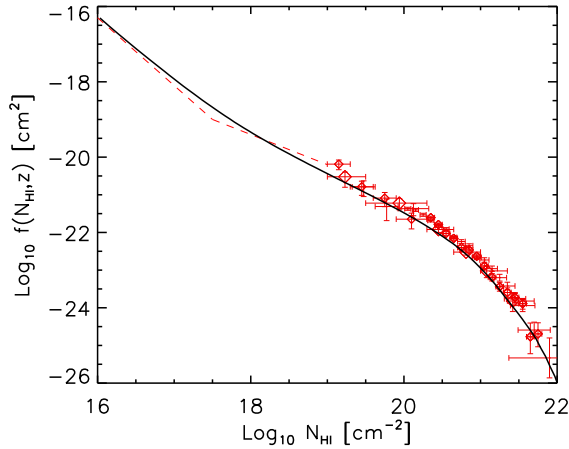
Figure 5.3: Predicted H I column density distribution function at $z = 3$ (black curve) and a compilation of observations around the same redshift (data points: Péroux et al., 2005; O'Meara et al., 2007; Noterdaeme et al., 2009; Prochaska et al., 2010) and power-law constraints (dashed curve: Prochaska & Wolfe, 2009). The black curve is obtained by collapsing the full three-dimensional H I distribution onto a plane. The observations are matched well (see also Altay et al., 2011).

The predicted H I column density distribution function is shown in Figure 5.3 as the black curve. It was calculated by projecting the full three-dimensional gas distribution onto a two-dimensional grid with $16\,384^2$ pixels, which is sufficient to achieve convergence. Observationally determined power-law slopes at $N_{\mathrm{H\,I}} < 10^{19}\,\mathrm{cm}^{-2}$ (Prochaska & Wolfe, 2009) and data points at $N_{\mathrm{H\,I}} > 10^{19}\,\mathrm{cm}^{-2}$ (Péroux et al., 2005; O'Meara et al., 2007; Noterdaeme et al., 2009; Prochaska et al., 2010) have been converted to the cosmology assumed in our simulation and are shown as red, dashed lines and red data points, respectively. The observations of the H I column density distribution function are matched well, also at column densities lower than shown here (Altay et al., 2011). The match would have been even better if we had corrected the gas temperatures for the effect of self-shielding (see Altay et al., 2011). Including the radiation from local sources might worsen the agreement, although Nagamine et al. (2010) have shown this effect to be unimportant.

For $N_{\mathrm{H\,I}} \gtrsim 10^{17}\,\mathrm{cm}^{-2}$ nearly all sightlines are dominated by a single absorption system, because they are very rare (Prochaska et al., 2010; Altay et al., 2011). For column densities $\lesssim 10^{16}\,\mathrm{cm}^{-2}$ our method of projecting the entire 25 comoving $h^{-1}\,\mathrm{Mpc}$ simulation box does not recover the true column density distribution due to the projection of unrelated lower column density absorbers. Altay et al. (2011) therefore determine the column density distribution in this regime by decomposing H I absorption spectra into Voigt profiles. Above $N_{\mathrm{H\,I}} \sim 10^{18}\,\mathrm{cm}^{-2}$ the column density distribution function flattens, because self-

shielding becomes important (Katz et al., 1996; Zheng & Miralda-Escudé, 2002; Altay et al., 2011). It steepens again at $N_{\mathrm{H\,I}} \gtrsim 10^{20.3}$ cm^{-2}, because the neutral hydrogen fraction saturates (Altay et al., 2011), and at $N_{\mathrm{H\,I}} \gtrsim 10^{21.5}$ m^{-2} due to the formation of molecules (Schaye, 2001b; Zwaan & Prochaska, 2006; Krumholz et al., 2009; Noterdaeme et al., 2009).

We can quantify the contribution of different gas samples by calculating the mean fraction of the H I column density that is due to each gas selection as a function of the total H I column density. This is shown in Figure 5.4 for all the samples listed in Table 5.1. Note that the mean fraction would be 0.5 for a column density $N'_{\mathrm{H\,I}}$ if the selection includes all $N'_{\mathrm{H\,I}}$ absorbers, but only half of their H I. However, a mean fraction of 0.5 would also be obtained if the selection includes half of the absorbers with column density $N'_{\mathrm{H\,I}}$, but all the H I of the selected absorbers. Samples based on cuts in halo mass are best described by the second case, but most other samples combine the two types of possibilities.

Figure 5.4 shows that most of the H I absorption is due to cold-mode gas that is flowing towards the centre of the nearest halo. Above $N_{\mathrm{H\,I}} = 10^{17}$ cm^{-2} this gas is primarily inside haloes. Most of the H I gas at these column densities is currently in the ISM or will become part of the ISM within the next 1.2 Gyr. We discuss this in more detail below.

For absorbers with $N_{\mathrm{H\,I}} < 10^{21}$ cm^{-2} more than 90 per cent of the H I column density is due to gas that has never gone through a virial shock, i.e. cold-mode gas (top left panel). For higher column densities, which arise mostly in the ISM of galaxies residing in haloes with $M_{\mathrm{halo}} > 10^{11}$ M$_\odot$, this cold-mode fraction drops to 70 per cent. We do not know what caused the remaining gas to be heated above $10^{5.5}$ K (note that the same gas had a much smaller neutral fraction at the time when it was this hot). It could have been a virial shock, an accretion shock at a smaller radius, or a shock associated with a galactic wind. Note that the gas that has $T_{\mathrm{max}} > 10^{5.5}$ K because it has been shocked in an outflow, may have been accreted in the cold mode.

Most high column density gas resides in haloes, but the halo fraction drops below 50 per cent for $N_{\mathrm{H\,I}} < 10^{17}$ cm^{-2} (top middle panel). Combining this with the fact that most gas has $T_{\mathrm{max}} < 10^{5.5}$ K, we conclude that most LLSs and most DLAs arise from gas inside haloes that has been accreted in the cold mode. Most of the H I absorption occurs in main haloes. Satellites contribute less than 20 per cent for all column densities, but their contribution increases slightly with the H I column density.

Very low-mass haloes ($10^9 < M_{\mathrm{halo}} < 10^{10}$ M$_\odot$) are most abundant and therefore contain the largest amount of H I below $N_{\mathrm{H\,I}} = 10^{21}$ cm^{-2}, accounting for about 40 per cent of the total absorption (top right panel). For $N_{\mathrm{H\,I}} > 10^{21}$ cm^{-2}, a single very low-mass halo is simply not large enough to provide a significant cross section. The contribution from haloes with $M_{\mathrm{halo}} > 10^{11}$ M$_\odot$ is dominant and steeply increasing at $N_{\mathrm{H\,I}} > 10^{21}$ cm^{-2}. The fact that low-(high-) mass haloes dominate low (high) column density DLAs agrees qualitatively with Pontzen et al. (2008), although they found that haloes more mas-
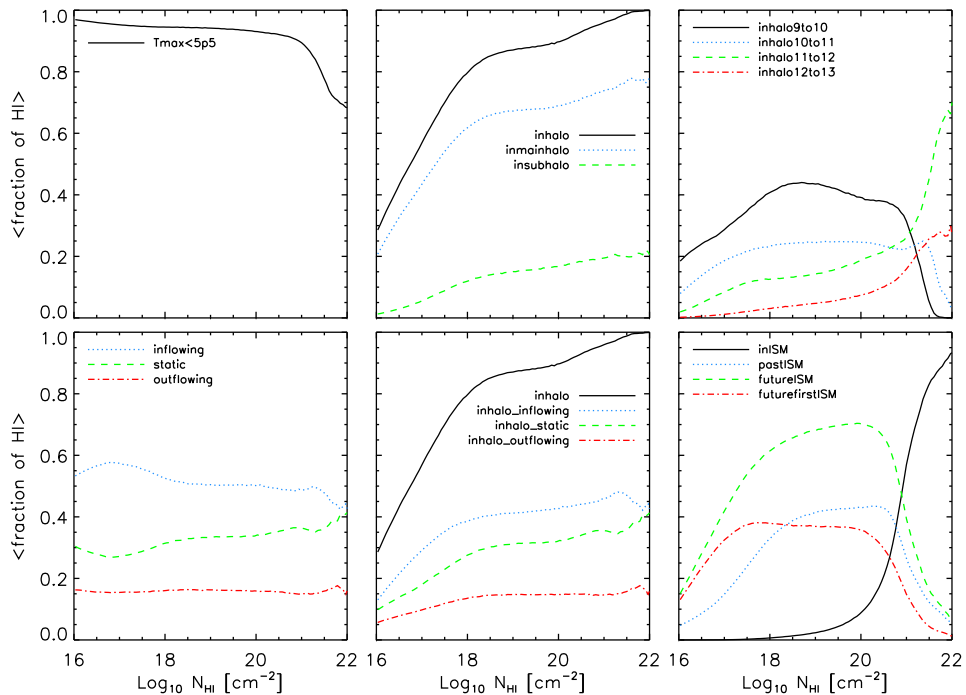
Figure 5.4: Mean fraction of the H I column density at $z = 3$ contributed by the gas which fulfils the selection criteria listed in Table 5.1 as a function of the total H I column density. Almost all of the contributing gas has $T_{\mathrm{max}} < 10^{5.5}$ K although hot-mode gas becomes significant, accounting for up to 30 per cent of the absorption, above 10^{21} cm^{-2}. More than 80 per cent of $N_{\mathrm{H\,I}} > 10^{18}$ cm^{-2} gas is located inside (main) haloes. About 55 per cent of the H I is inflowing, but the contributions from static and outflowing gas are about 30 and 15 per cent, respectively, and therefore not negligible. The contribution from gas accreting onto galaxies, i.e. gas that will join the ISM in the near future, is dominant for $10^{17} - 10^{21}$ cm^{-2}, accounting for up to 70 per cent. Strong DLAs ($N_{\mathrm{H\,I}} > 10^{21}$ cm^{-2}) are dominated by ISM gas (contributing more than 60 per cent to the absorption) and the Lyman-α forest by gas that will remain intergalactic down to at least $z = 2$ (contributing more than 60 per cent to the absorption).

sive than $10^{10.5}$ M$_\odot$ only dominate for $N_{\mathrm{H\,I}} > 10^{21.5}$ cm^{-2}. Unresolved haloes ($M_{\mathrm{halo}} < 10^9$ M$_\odot$) cannot dominate the absorption for $N_{\mathrm{H\,I}} > 10^{17}$ cm^{-2}, because most of it is already accounted for by resolved haloes.

We also split the gas into several SFR bins, but do not show the result. We found that for $N_{\mathrm{H\,I}} < 10^{21}$ cm^{-2}, the largest contribution (about 30 per cent), comes from haloes with $0.01 < \mathrm{SFR} < 0.1$ M$_\odot$/yr. For higher column densities objects with SFR > 10 M$_\odot$/yr are most important, accounting for 30–65 per cent of the H I absorption, depending on the H I column density.

At all column densities, most H I gas is inflowing, but there are important and roughly equal contributions from static and outflowing gas (bottom left panel). The contributions from inflowing, static, and outflowing gas are nearly constant (about 55, 30, and 15 per cent, respectively) up to $N_{\mathrm{H\,I}} = 10^{21}$ cm^{-2}, at which point the contribution of static gas increases relative to those of both in- and outflows. If we separate the gas into inflowing or outflowing without any minimum radial velocity threshold (not shown), then the ratio of inflowing to outflowing remains approximately the same, with 65 per cent (35 per cent) of the H I absorption due to inflowing (outflowing) gas.

Above $N_{\mathrm{H\,I}} = 10^{18}$ cm^{-2}, the contribution to H I absorption from gas that is *in haloes* and inflowing, static, or outflowing (bottom middle panel) is almost equally large as that from *all* gas that is inflowing, static, or outflowing (bottom left panel). Below $N_{\mathrm{H\,I}} = 10^{18}$ cm^{-2}, their contribution is lower, because many absorbers reside outside of haloes.

The fraction of H I absorption due to gas inside galaxies, i.e. the ISM, is only significant for DLAs and dominates at $N_{\mathrm{H\,I}} \gtrsim 10^{21}$ cm^{-2} (bottom right panel). Two-thirds of the $10^{17.5} < N_{\mathrm{H\,I}} < 10^{21}$ cm^{-2} material is not participating in star formation yet, but will do so within the next 1.2 Gyr. About half of this gas will accrete onto a galaxy for the first time. Gas previously ejected from galaxies contributes a comparable amount of absorption as gas accreting onto galaxies for the first time.

5.5   Discussion and conclusions

After post-processing with radiative transfer, the OWLS reference simulation matches the observed $z = 3$ H I column density distribution over ten orders of magnitude in $N_{\mathrm{H\,I}}$ (Altay et al., 2011). This success gives us confidence that we can use this simulation to study the relation between cold accretion and high column density H I absorbers.

Like other simulations, our simulation also shows cold streams and filaments inside and outside of haloes (van de Voort et al., 2011a). Gas in many of these streams does not go through an accretion shock near the virial radius and, because it is able to accrete onto a galaxy much more efficiently than the hot, diffuse gas, it is vital for fuelling star formation (e.g. Kereš et al., 2005; Ocvirk et al., 2008; Kereš et al., 2009a; van de Voort et al., 2011a,b; van de Voort & Schaye,

2012; Faucher-Giguère et al., 2011). Here, we demonstrated that our simulation would not have matched the observed H I column density distribution without cold accretion. This fact alone provides evidence that cold accretion has already been observed.

Motivated by the theoretical framework of cold, filamentary accretion, we have investigated the importance of gas that satisfies certain selection criteria for column densities above $N_{\mathrm{H\,I}} = 10^{16}$ cm^{-2} at $z = 3$. It is difficult to check the morphology of all the H I in the simulation, but from images (see also Figure 5.2) we do know that a lot of the accreting cold-mode gas is filamentary. However, the highest column density gas tends to be clumpy. Even though much of this gas is infalling and has never gone through a virial shock, it would not all be classified as streams based on its morphology.

We will first discuss the results separately for three column density regimes: i) the Lyman-α forest; ii) LLSs and low column density DLAs, and iii) high column density DLAs. We will then discuss our results in the context of the cold-mode accretion paradigm, compare them to recent theoretical results from Fumagalli et al. (2011a), and conclude.

1. Nearly all H I absorbing gas in the denser part of the Lyman-α forest ($N_{\mathrm{H\,I}} = 10^{16-17}$ cm^{-2}) has never gone through a virial shock ($T_{\max} < 10^{5.5}$ K) and most of it is outside of haloes (the same is true for the low column density forest, but we did not show this here). Even though 60 per cent is flowing towards the nearest halo (nearest in units of R_{vir}) with velocities greater than a quarter of its circular velocity, only 15–40 per cent will participate in star formation before $z = 2$, i.e. within 1.2 Gyr. Most of the Lyman-α forest gas that will accrete onto a galaxy before $z = 2$ will do so for the first time.

2. Nearly all H I absorbing gas in LLSs ($10^{17} < N_{\mathrm{H\,I}} < 10^{20.3}$ cm^{-2}) and in low column density DLAs ($10^{20.3} < N_{\mathrm{H\,I}} < 10^{21}$ cm^{-2}) has never gone through a virial shock. About 60–95 per cent of the H I in LLSs is inside haloes with larger contributions from lower-mass haloes: 30–40 per cent from 10^{9-10} M$_\odot$, 20 per cent from 10^{10-11} M$_\odot$, 10–25 per cent from 10^{11-12} M$_\odot$, and less than 15 per cent from 10^{12-13} M$_\odot$ haloes. Even inside haloes, almost half of the neutral gas is inflowing with velocities greater than 25 per cent of the circular velocity. For LLSs, more than 90 per cent of the H I is currently outside of galaxies, but 40–70 per cent will accrete onto a galaxy within 1.2 Gyr and just over 30 per cent will do so for the first time. The gas reservoir that is feeding galaxies is thus, at least in part, associated with LLSs. A significant fraction of the gas in LLSs and low column density DLAs has previously already been inside a galaxy. This agrees with the finding that the re-accretion of gas that has been ejected is important for the build-up of galaxies (Oppenheimer et al., 2010).

3. About 10–30 per cent of H I absorbing gas in high column density DLAs

($N_{\rm H\,I} > 10^{21}$ cm^{-2}) was heated above $10^{5.5}$ K in the past. This gas has either been accreted in the hot mode or it has been shock-heated by a galactic wind. Depending on the column density, 55–95 per cent of the high-$N_{\rm H\,I}$ DLA gas is contained in the ISM of galaxies and 50–70 per cent of the H I is inside haloes more massive than 10^{11} M$_\odot$. Outflowing gas contributes about 15 per cent of the H I. Inflowing gas provides the largest contribution to the H I of high column density DLAs, but the static gas component approaches the importance of the inflowing gas at the highest column densities.

The simplest way of defining cold-mode accretion is purely based on its maximum past temperature. Gas with temperatures below $10^{5.5}$ K is able to cool efficiently, because the cooling function peaks at $T \approx 10^{5-5.5}$ K (e.g. Wiersma et al., 2009a). Above this temperature, cooling times become longer. We define cold-mode gas as having $T_{\rm max} < 10^{5.5}$ K. Using this definition, practically all H I absorption is due to cold-mode gas. This is not so surprising for the Lyman-α forest, which is comprised mostly of gas outside of haloes and would therefore not be expected to have been shock-heated to high temperatures. LLSs are dominated by low-mass haloes with $M_{\rm halo} < 10^{11}$ M$_\odot$ and $T_{\rm vir} < 10^{5.4}$ K. Even if this gas were heated to the virial temperature, we would still classify it as cold-mode accretion. However, most neutral gas in haloes more massive than 10^{11} M$_\odot$ cannot have been heated to the virial temperature, or we would have found that the fraction of the H I with $T_{\rm max} > 10^{5.5}$ K exceeds the fraction of the H I contributed by haloes with mass $> 10^{11}$ M$_\odot$, which increases from about 20 to more than 95 per cent from $N_{\rm H\,I} = 10^{18}$ to 10^{22} cm^{-2}. However, we find that the actual fraction of H I contributed by gas with $T_{\rm max} > 10^{5.5}$ K is only 5–30 per cent for this column density range. Thus, it is clear that even for high column density absorbers, the H I content is dominated by gas that has never gone through an accretion shock near the virial radius.

We can also think of cold-mode accretion as gas that has already accreted onto haloes, but not yet onto galaxies, without having reached temperatures above $10^{5.5}$ K, flowing in with relatively high velocities, and that will accrete onto a galaxy in the near future. About 30 per cent of all $10^{18} < N_{\rm H\,I} < 10^{20.5}$ cm^{-2} systems satisfy all these criteria. Therefore, even this set of highly restrictive criteria leads to the conclusion that cold-mode accretion has already been observed in the form of high column density H I absorption systems.

However, if we think of cold-mode accretion as accreting onto galaxies for the first time, in addition to having low $T_{\rm max}$, being inside haloes, and rapidly inflowing, the fraction of LLSs satisfying this requirement is about a factor of two lower, but still around 15 per cent. Cold streams also contain galaxies, so the gas that is being recycled could still be accreting along these streams. If we include previously ejected gas in our definition of cold-mode accretion, the metallicity of cold-mode gas would not necessarily be low.

Fumagalli et al. (2011a) already pointed out that cold streams have likely

been detected as LLSs. They used high-resolution simulations of seven galaxies with $10^{10.7} < M_{\mathrm{halo}} < 10^{11.5}$ M$_\odot$ at $z \approx 3$ by resimulating a cosmological simulation. They included ionizing radiation from local stellar sources, which we did not. Nagamine et al. (2010) have shown that local stellar sources change the column density distribution function by less than 0.1 dex, although Fumagalli et al. (2011a) find a somewhat larger effect (0–0.5 dex). Fumagalli et al. (2011a) investigated H I absorption from "central galaxies", which they defined as all gas within $0.2R_{\mathrm{vir}}$, and from "streams", defined as all gas at radii $0.2R_{\mathrm{vir}} < R < 2R_{\mathrm{vir}}$, and found that "cold streams" mostly have $10^{17} < N_{\mathrm{H\,I}} < 10^{19}$ cm^{-2}. However, their definition of "cold streams" was all gas at $0.2R_{\mathrm{vir}} < R < 2R_{\mathrm{vir}}$, which excludes neither gas that has been shock-heated to the virial temperature, i.e. hot accretion, nor gas that is outflowing.

The halo sample of Fumagalli et al. (2011a) underproduces $N_{\mathrm{H\,I}} < 10^{17}$ cm^{-2} systems, which they argue is because many of these absorbers live outside of haloes. This is in agreement with our finding that the contribution of halo gas is strongly declining with decreasing $N_{\mathrm{H\,I}}$, although we find that up to 30 per cent still stems from low-mass haloes not covered by their simulations. We find that for $10^{16} < N_{\mathrm{H\,I}} < 10^{20}$ cm^{-2}, haloes with $10^9 < M_{\mathrm{halo}} < 10^{10}$ M$_\odot$ account for about as much H I absorption as all higher-mass haloes combined. The fact that $10^{18} < N_{\mathrm{H\,I}} < 10^{20}$ cm^{-2} systems are also underproduced in their sample is therefore consistent with our finding that very low-mass haloes dominate the H I column density distribution function. Fumagalli et al. (2011a) conclude that haloes in the mass range $10^{10} < M_{\mathrm{halo}} < 10^{12}$ M$_\odot$ already account for 20–30 per cent of the LLSs and DLAs. We have found this fraction to be even larger: 30–40 per cent for LLSs and 40–70 per cent for DLAs. This difference could be due to their inclusion of ionizing radiation from local sources.

Our results lead to the somewhat stronger conclusion that for $10^{18} < N_{\mathrm{H\,I}} < 10^{21}$ cm^{-2} more than 80 per cent of the H I absorption is caused by cold-mode halo gas. Only about 5 per cent is caused by hot-mode gas. The remainder may arise from the high-density part of the IGM or from haloes with $M_{\mathrm{halo}} < 10^9$ M$_\odot$. At lower column densities ($N_{\mathrm{H\,I}} < 10^{18}$ cm^{-2}), the contribution of halo gas declines, though more than 95 per cent of the absorbing gas is still cold mode. For higher column densities ($N_{\mathrm{H\,I}} > 10^{21}$ cm^{-2}), the absorption is dominated by the ISM of galaxies in haloes with $M_{\mathrm{halo}} > 10^{11}$ M$_\odot$ and, depending on the column density, the mean cold-mode contribution is between 70 and 90 per cent. At all column densities, inflowing gas accounts for most of the H I column density, but there are significant contributions from static and outflowing gas.

We conclude that cold streams are real. They have already been observed in the form of high column density absorbers, mainly in systems with $10^{17} < N_{\mathrm{H\,I}} < 10^{21}$ cm^{-2}. Cold flows are critical for the success of our simulation in reproducing the observed $z = 3$ column density distribution of damped Lyman-α and particularly that of Lyman limit systems.

Acknowledgements

6

SOFT X-RAY AND ULTRA-VIOLET METAL-LINE EMISSION FROM THE GAS AROUND GALAXIES

The gas around galaxies is diffuse and much fainter than the galaxies themselves. A large fraction of the gas has temperatures between $10^{4.5}$ and 10^7 K. If the gas has metallicities above $0.1\,Z_\odot$, it will cool primarily through metal-line emission. With current and upcoming instruments we may be able to detect the halo gas in emission, either directly or statistically. We stack the galaxies in several large cosmological, hydrodynamical simulations and calculate the expected metal-line surface brightness as a function of radius from the centre. We then compare it to the capabilities of current and future facilities. At low redshift, proposed X-ray telescopes can detect O VIII emission out to the virial radius of groups and clusters (assuming a detection limit of 10^{-1} photon $s^{-1}\,cm^{-2}\,sr^{-1}$). C VI, N VII, O VII, and Ne x can also be detected to smaller radii, $0.1-0.5R_{vir}$. At high redshift it will be possible to observe rest-frame UV lines, C III, C IV, O VI, Si III, and Si IV, out to $10-20$ per cent of the virial radius in haloes larger than $10^{11}\,M_\odot$ with upcoming instruments (assuming a detection limit of 10^{-20} erg $s^{-1}\,cm^{-2}\,arcsec^{-2}$). Most of these lines have surface brightnesses a factor of a few higher at low redshift and could therefore easily be detected with the next generation UV space telescope. The metal-line emission is, in general, biased towards regions of high density and high metallicity and also towards the temperature where the emissivity peaks. This bias varies with radius, halo mass, redshift and between different emission lines. We can quantify the clumpiness of the emitting gas with respect to the underlying density using the clumping factor. The clumping factor is highest in the most massive haloes, because for these haloes the mass-weighted temperature is much higher than the peak emissivity temperature and the emission is thus dominated by cold, dense clumps. The X-ray-flux-weighted properties are similar for all metal lines considered, whereas the UV-flux-weighted properties vary strongly between metal lines.

6.1 Introduction

Haloes grow by accreting gas from their surroundings, the intergalactic medium (IGM), which is the main reservoir of baryons. Galaxies grow by accreting gas from their haloes, from which they can form stars. Some of the gas is returned to the circumgalactic medium (CGM) in galactic winds driven by supernovae or active galactic nuclei. Metals produced in stars are also blown out of the galaxy and enrich the CGM. To understand the evolution of galaxies, one needs to study the evolution of the halo gas.

UV and X-ray absorption line studies have revealed cold, neutral gas and the warm-hot intergalactic medium around galaxies. Unfortunately, this type of observation can only provide information along the line of sight, so there is no information about the transverse extent of the absorbing gas cloud. Another limitation is that we can only probe gas in case there is a bright background object. Therefore, absorption line studies are excellent for the regions of moderate overdensity in the IGM, but because galaxies are rare, the statistics are poor for relatively dense halo gas.

The gas emissivity scales with the square of the density. The signal is thus dominated by high-density regions and more sensitive to the CGM than to the general IGM. In this way, emission line studies complement absorption line studies. They have the added advantage of providing a two-dimensional image, in addition to the third dimension provided by the redshift of the emission line, allowing us to study the three-dimensional spatial distribution.

H I Lyman-α (Lyα) emission originates from regions with $T \approx 10^4$ K. It therefore provides an excellent route to studying cold gas in the CGM. Diffuse Lyα emission has been (statistically) detected around high-redshift galaxies at $z \sim 3$ (e.g. Steidel et al., 2000; Matsuda et al., 2004; Bower et al., 2004; Steidel et al., 2011). A large fraction of the halo gas is expected to heat to temperatures above $10^{4.5}$ K, either through photo-ionization, accretion shocks, or through shocks caused by galactic winds. UV metal-line emission enables us to probe gas with $T = 10^{4.5-5.5}$ K, which is more diffuse than colder Lyα emitting gas and a better probe of the average gas properties around galaxies. X-ray metal-line emission traces even hotter gas $T = 10^{6-7}$ K, which is the relevant temperature of the halo gas around high-mass galaxies and in galaxy groups. At $T \sim 10^{4.5-7}$ K the emission is dominated by metal lines for $Z \gtrsim 0.1 \, Z_\odot$ (e.g Wiersma et al., 2009a) and not by hydrogen lines or continuum emission as is the case at lower and higher temperatures.

Dilute halo gas that has been shock-heated to the virial temperature is routinely detected in X-ray observations of the centres of clusters and groups of galaxies, and it may even have been seen around individual galaxies (e.g. Crain et al., 2010a,b; Anderson & Bregman, 2011; Li & Wang, 2012). Most of the detections are made in X-ray continuum emission and Fe lines, see Böhringer & Werner (2010) for a recent review. In the last year, a lot of progress has been made on observing X-ray emission close to the virial radii of clusters (Simionescu

et al., 2011; Akamatsu et al., 2011; Miller et al., 2011; Urban et al., 2011), but see also Eckert et al. (2011). Additionally, there are claims of detections of metal lines (e.g. Kaastra et al., 2003; Takei et al., 2007), whereas other observations set upper limits at lower values than these claimed detections (e.g. Mitsuishi et al., 2011, and references therein).

Observing metal-line emission from diffuse halo gas would yield a lot of information about the physical state of the gas, the distribution of metals, and thus the cycle of gas between haloes and galaxies. In general, however, emission from gas outside of galaxies is faint and thus difficult to detect. Many missions have been proposed to study the diffuse halo gas in emission. With the next generation of spectrographs we should be able to detect certain metal lines. Motivated by future instrumentation and recent proposals, recent studies have quantified the expected emission using cosmological, hydrodynamical simulations (Furlanetto et al., 2004; Bertone et al., 2010a,b; Takei et al., 2011; Frank et al., 2011; Bertone & Schaye, 2012). These studies are focussed mostly on quantifying the emission expected from the warm-hot intergalactic medium in a large section of the Universe or in mock datacubes.

It is possible to increase the signal-to-noise by stacking many observations, centred on a galaxy. In this way we cannot study the halo gas around a single object, but we can characterize the general properties of gas around a certain type of galaxy. In this work we will quantify the expected surface brightness (SB) for the brightest metal lines for a range of halo masses, both in UV at high and low redshift and in soft X-ray at low redshift. Our study complements previous work by predicting mean surface brightness profiles for different halo masses.

In Section 6.2 we describe the simulations we used, how we identify haloes, and how we calculate the emission signal. The results obtained for soft X-ray lines at $z = 0.125$ and UV lines at $z = 0.125$ and $z = 3$ and their detectability are described in Section 6.3. This Section also contains the prediction for H I Balmer-α (Hα). Finally, we conclude in Section 6.4.

In all our calculations we assume the same cosmological parameters as during our simulation (see Section 6.2.1). Most notably $\Omega_m = 1 - \Omega_\Lambda = 0.238$ and $h = 0.73$.

6.2 Method

6.2.1 Simulations

We use a modified version of GADGET-3 (last described in Springel, 2005b), a smoothed particle hydrodynamics (SPH) code that uses the entropy formulation of SPH (Springel & Hernquist, 2002), which conserves both energy and entropy where appropriate. This work is part of the OverWhelmingly Large Simulations (OWLS) project (Schaye et al., 2010), which consists of a large number of cos-

mological simulations with varying (subgrid) physics. Here we make use of the so-called 'reference' model. The model is fully described in Schaye et al. (2010) and we will only summarize its main properties here.

The simulations assume a ΛCDM cosmology with parameters $\Omega_m = 1 - \Omega_\Lambda = 0.238$, $\Omega_b = 0.0418$, $h = 0.73$, $\sigma_8 = 0.74$, $n = 0.951$. These values are consistent[1] with the WMAP year 7 data (Komatsu et al., 2011). In the present work, we use the simulation output at redshifts 3 and 0.125.

A cubic volume with periodic boundary conditions is defined, within which the mass is distributed over 512^3 dark matter and as many gas particles. The box size (i.e. the length of a side of the simulation volume) of the simulations used in this work are 25, 50, and 100 h^{-1} comoving Mpc. The (initial) particle masses for baryons and dark matter are $2.1 \times 10^6 (\frac{L_{box}}{25\ h^{-1}\text{Mpc}})^3$ M$_\odot$ and $1.0 \times 10^7 (\frac{L_{box}}{25\ h^{-1}\text{Mpc}})^3$ M$_\odot$, respectively. The gravitational softening length is 1.95 $(\frac{L_{box}}{25\ h^{-1}\text{Mpc}})$ h^{-1} comoving kpc, i.e. 1/25 of the mean dark matter particle separation, with a maximum of 0.5 $(\frac{L_{box}}{25\ h^{-1}\text{Mpc}})$ h^{-1} proper kpc, which is reached at $z = 2.91$.

Star formation is modelled according to the recipe of Schaye & Dalla Vecchia (2008). A polytropic equation of state $P_{tot} \propto \rho_{gas}^{4/3}$ is imposed for densities exceeding $n_H = 0.1$ cm^{-3}, where P_{tot} is the total pressure and ρ_{gas} the density of the gas. Gas particles with proper densities $n_H \geq 0.1$ cm^{-3} and temperatures $T \leq 10^5$ K are moved onto this equation of state and can be converted into star particles. The star formation rate (SFR) per unit mass depends on the gas pressure and reproduces the observed Kennicutt-Schmidt law (Kennicutt, 1998) by construction.

Feedback from star formation is implemented using the prescription of Dalla Vecchia & Schaye (2008). About 40 per cent of the energy released by type II supernovae is injected locally in kinetic form, while the rest of the energy is assumed to be lost radiatively. The initial wind velocity is 600 km s^{-1} and the initial mass loading is two, meaning that, on average, a newly formed star particle kicks twice its own mass in neighbouring gas particles.

The abundances of eleven elements released by massive stars and intermediate mass stars are followed as described in Wiersma et al. (2009b). We assume the stellar initial mass function (IMF) of Chabrier (2003), ranging from 0.1 to 100 M$_\odot$. As described in Wiersma et al. (2009a), radiative cooling and heating are computed element by element in the presence of the cosmic microwave background radiation and the Haardt & Madau (2001) model for the UV/X-ray background from galaxies and quasars assuming the gas to be optically thin and in (photo-)ionization equilibrium.

Using the suite of simulations from OWLS, Wiersma et al. (2011) have shown that galactic winds driven by supernovae are essential for the enrichment of the

---

[1]The only significant discrepancy is in σ_8, which is 8 per cent, or 2.3σ, lower than the value favoured by the WMAP 7-year data.

IGM. Close to the centre of a halo, most gas has been enriched to $Z > 0.1 \, Z_\odot$, but at the virial radius the scatter is very large (van de Voort & Schaye, 2012).

6.2.2   Identifying haloes

The first step towards finding gravitationally bound structures is to identify dark matter haloes. These can be found using a Friends-of-Friends (FoF) algorithm. If the separation between two dark matter particles is less than 20 per cent of the average separation (the linking length $b = 0.2$), they are placed in the same group. Baryonic particles are linked to a FoF halo if their nearest dark matter neighbour is in that halo. We then use SUBFIND (Dolag et al., 2009) to find the most bound particle of a FoF halo, which serves as the halo centre and also corresponds to the location of the central galaxy. We compute the virial radius, R_{vir}, within which the average density agrees with that predicted by the top-hat spherical collapse model in a ΛCDM cosmology (Bryan & Norman, 1998). The halo mass is the mass contained inside R_{vir}.

Table 6.1 lists which simulation and halo mass bins are used for various lines and redshifts. It also lists the median halo mass, median stellar mass, median star formation rate, and the number of haloes in the different mass bins.

6.2.3   Emission

We calculate the emissivities of the gas following Bertone et al. (2010a). We only summarize the method here and refer the reader to Bertone et al. (2010a) for details on the procedure. The names and wavelengths of the lines considered in this work are given in Table 6.2 for soft X-rays, which also includes the energy of the lines, and in Table 6.4 for UV and Hα.

We created emissivity tables as a function of temperature, density, and redshift with the photo-ionization package CLOUDY, which was last described in Ferland et al. (1998). The gas is assumed to be optically thin and in ionization equilibrium in the presence of the cosmic microwave background and the Haardt & Madau (2001) UV background. These assumptions were also made when calculating cooling rates during the simulation (Wiersma et al., 2009a) and are thus fully consistent with the simulation. We further assumed solar abundances when creating the tables, but the results are scaled to the abundances derived from the simulation. The tables are created for temperatures 10^2 K$< T < 10^{8.5}$ K with $\Delta \mathrm{Log}_{10} T = 0.05$ bins and densities 10^{-8} cm^{-3} $< n_H <$ 10 cm^{-3} with $\Delta \mathrm{Log}_{10} n_H = 0.2$ bins.

We calculate the emission only for gas with $n_H < 0.1$ cm^{-3}, which is therefore not star forming. Our simulations do not resolve the multiphase interstellar medium at $n_H \geq 0.1$ cm^{-3}. As we are interested in determining the emission from diffuse gas in haloes, this is consistent with our aims.

The emissivity, ϵ, for an emission line is derived from the tables as a function of $\mathrm{Log}_{10} T$ and $\mathrm{Log}_{10} n_H$ through interpolation. A gas particle's luminosity is

Table 6.1: List of the simulation box sizes and halo mass ranges used for different emission lines at different redshifts. Included are also the median halo mass, median stellar mass, median star formation rate, and the number of haloes in each halo mass bin.

redshift	band	simulation	$Log_{10}M_{halo}$ range	$Log_{10}M_{halo}$	$Log_{10}M_{star}$		SFR	# haloes
0.125	X-ray	100 h^{-1}Mpc	12-13 [M$_\odot$]	12.3 [M$_\odot$]	10.8 [M$_\odot$]	8.9	M$_\odot$ yr^{-1}	2771
			13-14 [M$_\odot$]	13.2 [M$_\odot$]	11.8 [M$_\odot$]	46	M$_\odot$ yr^{-1}	301
			14-15 [M$_\odot$]	14.2 [M$_\odot$]	12.6 [M$_\odot$]	144	M$_\odot$ yr^{-1}	18
0.125	UV & Hα	50 h^{-1}Mpc	11-12 [M$_\odot$]	11.3 [M$_\odot$]	9.3 [M$_\odot$]	0.05	M$_\odot$ yr^{-1}	2723
			12-13 [M$_\odot$]	12.3 [M$_\odot$]	10.9 [M$_\odot$]	9.3	M$_\odot$ yr^{-1}	374
			13-14 [M$_\odot$]	13.2 [M$_\odot$]	11.7 [M$_\odot$]	39	M$_\odot$ yr^{-1}	46
3.0	UV	25 h^{-1}Mpc	10-11 [M$_\odot$]	10.3 [M$_\odot$]	8.2 [M$_\odot$]	0.11	M$_\odot$ yr^{-1}	1857
			11-12 [M$_\odot$]	11.3 [M$_\odot$]	9.5 [M$_\odot$]	4.2	M$_\odot$yr^{-1}	117
			12-13 [M$_\odot$]	12.2 [M$_\odot$]	11.0 [M$_\odot$]	111	M$_\odot$ yr^{-1}	5

then

$$L = \epsilon(z, T, n_{\mathrm{H}}) \frac{m_{\mathrm{gas}}}{\rho} \frac{X_y}{X_y^{\odot}} \tag{6.1}$$

in $\mathrm{erg\,s^{-1}}$, where m_{gas} is its mass, ρ is its density, X_y is the 'SPH-smoothed' mass fraction of the element corresponding to the emission line, and $X_y^{\odot}$ is the solar mass fraction of the same element. We use smoothed abundances as described by Wiersma et al. (2009b). This is consistent with the simulation, because these smoothed abundances were also used in the simulation to compute the cooling rates. The flux is

$$F = \frac{L}{4\pi d_{\mathrm{L}}^2} \tag{6.2}$$

in $\mathrm{erg\,s^{-1}\,cm^{-2}}$, or

$$F = \frac{L}{4\pi d_{\mathrm{L}}^2} \frac{\lambda}{h_{\mathrm{p}} c} (1 + z) \tag{6.3}$$

in $\mathrm{photon\,s^{-1}\,cm^{-2}}$, with d_{L} the luminosity distance, h_{p} the Planck constant, c the speed of light, and λ the rest-frame wavelength of the emission line.

To calculate the emission profiles, we project the flux using a flux-conserving SPH interpolation scheme onto a two-dimensional grid, centred on the halo centre. The surface brightness is calculated by dividing the flux by the solid angle subtended by a pixel either in arcsec^2 or in sr,

$$S_{\mathrm{B}} = F/\Omega. \tag{6.4}$$

In this paper, we investigate the detectability of the emission lines listed in Tables 6.2 and 6.4, originating from circumgalactic gas. We quantify the expected surface brightness as a function of radius for a range of halo masses. Our predictions made should be considered with care. We did not take into account the velocities of the gas and thus the width of the lines, nor the effect of the atmosphere. A robust study of detectability should produce datacubes, including noise, and analyze them using the same pipeline as the observations. This is beyond the scope of the present work in which we show and discuss the theoretically expected surface brightnesses.

O VII is a line triplet at 0.574, 0.568, and 0.561 keV. The first line is a resonance line, the second one an intercombination line and the last one a forbidden line. Resonance photons have large cross-sections and will be scattered in random directions, giving rise to lower observed fluxes or even absorption. The intercombination line is significantly weaker ($0.5 - 0.6$ dex) than the other two. The resonance line is only slightly stronger than the forbidden line (by about 0.1 dex) without taking into account attenuation. The actual 0.574 keV surface brightness may be much lower due to resonant scattering. We therefore only show the surface brightness of the forbidden line at 0.561 keV, but note that if the emission at all three wavelengths is added together, the signal could be more than twice as strong.

Table 6.2: List of ion, rest-frame wavelength, and energy for the X-ray emission lines used in this work.

ion	λ (Å)	E (keV)
C VI	33.74	0.367
N VII	24.78	0.500
O VII	22.10	0.561
O VIII	18.97	0.654
Ne x	12.14	1.021

The UV doublets, C IV, O VI, and Si IV, have flux ratios of 2:1. We consider only the strongest line in this paper, but the results for the weaker lines thus follow directly.

6.3 Results

6.3.1 Soft X-ray

Current X-ray telescopes, i.e. *Chandra* and *XMM-Newton*, have not detected metal-line emission from diffuse, intergalactic gas, which is consistent with the predictions (Yoshikawa et al., 2003, 2004; Fang et al., 2005). To map the halo gas with future instruments, a combination of high angular and spectral resolution and a large field of view are preferred (Bertone et al., 2010a). As the emission is dominated by bright, compact regions, high angular resolution is necessary prevent smearing out the emission, in which case it would be harder to detect as well as impossible to correctly identify its origin. *ASTRO-H*[2] will be launched in a few years, but its field of view is rather small and its spatial resolution is coarse (e.g. Soong et al., 2011). Therefore, it is not an ideal instrument for studying halo X-ray profiles. A number of X-ray missions have been proposed in the past years, such as *IXO/ATHENA*[3] and *ORIGIN* (den Herder et al., 2011). Their proposed specifications are listed in Table 6.3, as are those for existing and future UV instruments, which are discussed in Sections 6.3.2 and 6.3.3.

The instrumental background is 2×10^{-2} photon $s^{-1}cm^{-2}keV^{-1}$, which corresponds to 1.3×10^3 photon $s^{-1}sr^{-1}keV^{-1}$ for CRIS on *ORIGIN* (with a pixel size of 300 μm and 24 arcsec). In the narrow field mode, the energy resolution is 2.5 eV, so this corresponds to 3 photon $s^{-1}sr^{-1}$. For an effective area of 10^3 cm^2, the surface brightness of the instrumental background equals 3×10^{-3} photon $s^{-1}cm^{-2}sr^{-1}$. (It would be twice as much in the wide field mode.)

For XMS on *IXO/ATHENA* the instrumental background is also 2×10^{-2} photon $s^{-1}cm^{-2}keV^{-1}$, which corresponds to 8.5×10^4 photon $s^{-1}sr^{-1}keV^{-1}$ (with

---

[2]http://astro-h.isas.jaxa.jp/
[3]http://ixo.gsfc.nasa.gov/, http://sci.esa.int/ixo

Table 6.3: Summary of technical specifications for instruments discussed in the main text.

Telescope (instrument)	Field of view (arcmin^2)	Angular resolution (arcsec)	Spectral resolution
ORIGIN (CRIS)	10×10 (30 × 30)	30	2.5 (5) eV
IXO/ATHENA (XMS)	2×2 (5 × 5)	5	2.5 (10) eV
ASTRO-H (SXS)	3 × 3	78	5 eV
FIREBALL	2.67 × 2.67	10	0.4 Å
Hale (CWI)	1 × 0.67	2.5 × 1	0.12 Å
Keck (KCWI)	0.33 × (0.14 − 0.57)	0.35 − 1.4	0.03-0.6 Å
VLT (MUSE)	1 × 1	0.2	0.4 Å

a pixel size of 300 μm and 3 arcsec). For an energy resolution of 2.5 eV, which is appropriate for the narrow field mode, this corresponds to 2×10^2 photon $s^{-1}sr^{-1}$. For an effective area of 3×10^4 cm^2, the surface brightness of the instrumental background equals 7×10^{-3} photon $s^{-1}cm^{-2}sr^{-1}$. (It would be four times as much in the wide field mode.)

Hickox & Markevitch (2006) determined that the unresolved cosmic X-ray background is about 14 ± 1 photon $s^{-1}cm^{-2}sr^{-1}keV^{-1}$ in the energy range we are interested in ($0.5 - 1$ keV). This unresolved signal is dominated by diffuse Galactic emission and local thermal-like emission. Part of this unresolved background could be resolved in deeper observations (Hickox & Markevitch, 2007). We will use the limit of 14 ± 1 photon $s^{-1}cm^{-2}sr^{-1}keV^{-1}$ as it is an upper limit on the unresolved background for future observations. For the energy resolution of CRIS on *ORIGIN* and XMS on *IXO/ATHENA* (i.e. 2.5 eV) this corresponds to about 3×10^{-2} photon $s^{-1}cm^{-2}sr^{-1}$. The instrumental background is therefore lower than the unresolved X-ray background. Observations should be able to probe down to 10^{-1} photon $s^{-1}cm^{-2}sr^{-1}$ without being strongly affected by the background. For this surface brightness a 1 Msec exposure would result in about 2 detected photons per resolution element for a 1 arcmin^2 feature with *ORIGIN* at 30 arcsec resolution and *IXO/ATHENA* at 5 arcsec resolution.

Figure 6.1 shows images of the mean surface brightness in the O VIII (0.654 keV) line at $z = 0.125$, which is the brightest soft X-ray line we consider. We use three halo mass bins, corresponding to (the haloes of) galaxies, groups, and clusters, with masses of $M_{halo} = 10^{12-13}$ M$_\odot$, 10^{13-14} M$_\odot$, and 10^{14-15} M$_\odot$ with $R_{vir} \approx 0.25$, 0.51, and 1.1 h^{-1} comoving Mpc, respectively. The images are 3 h^{-1} comoving Mpc on a side, which corresponds to 28 arcmin at $z = 0.125$, and the white circles indicate the median virial radii of the haloes. Haloes with $M_{halo} > 10^{13}$ M$_\odot$ have O VIII emission that is stronger than 10^{-1} photon $s^{-1}cm^{-2}sr^{-1}$ out to $0.7R_{vir}$, whereas for $M_{halo} = 10^{12-13}$ M$_\odot$ this is only the case at $R \lesssim 0.4R_{vir}$.

To make emission profiles for all the metal lines listed in Table 6.2, we calculate the average of the surface brightness azimuthally. In Figure 6.2 we show the mean (median) X-ray line surface brightness profiles for haloes at $z = 0.125$ as solid (dotted) curves. We show the same three halo mass bins as in Figure 6.1 out to twice the median virial radius.

The strongest observable soft X-ray line is O VIII (0.654 keV). It is followed by C VI (0.367 keV) and OVII (0.561 keV) for galaxies. In groups, Ne X (1.021 keV) is the second strongest line in the centre of the halo, but it is much weaker than C VI and O VII in the halo outskirts. As mentioned in Section 6.2.3, O VII is a triplet and the emission will be stronger when adding the contributions of the three lines. For both galaxies and groups, the Ne X profile is steeper than that of all the other lines shown. In clusters C VI and Ne X are of comparable brightness at all radii and about 0.6 dex below O VIII. N VII (0.500 keV) is similar to O VII at all radii for cluster haloes and about an order of magnitude fainter than O VIII. Ne X has the lowest surface brightness for $M_{halo} = 10^{12-13}$ M$_\odot$, but it is as strong as C VI for clusters. We also computed the emissivities of C V (0.308 keV), N VI

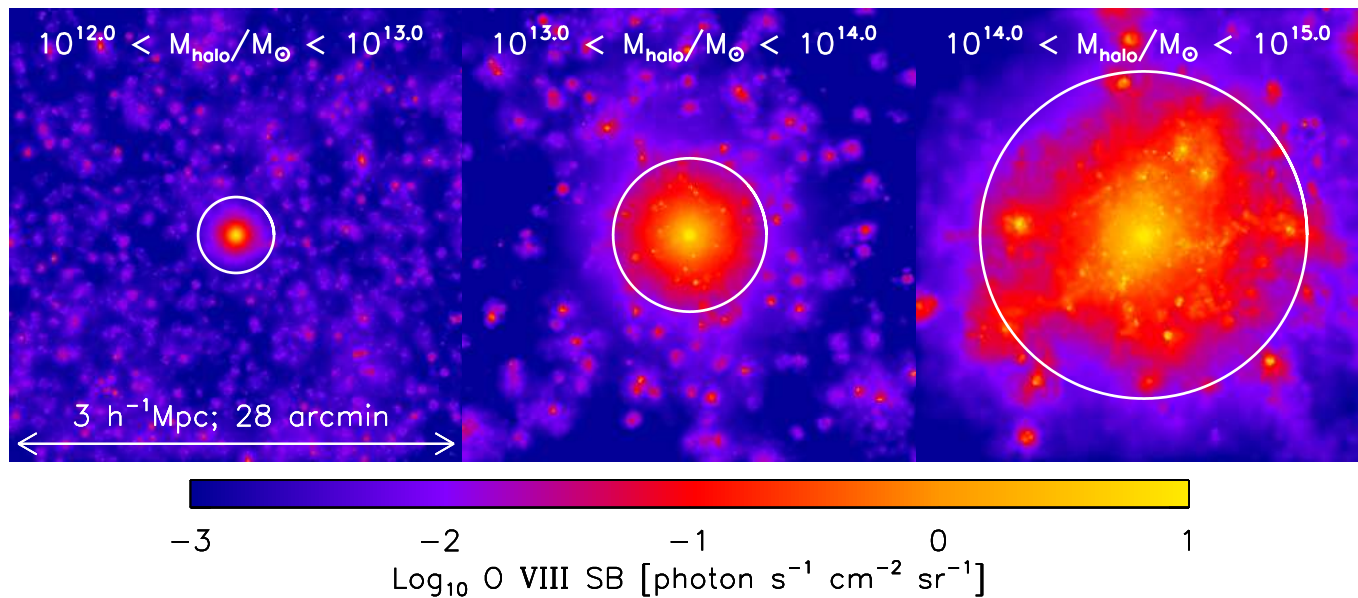**Figure 6.1:** Mean O VIII emission maps for haloes with $M_{\text{halo}} = 10^{12-13} \text{ M}_\odot$, $10^{13-14} \text{ M}_\odot$, and $10^{14-15} \text{ M}_\odot$, from left to right, at $z = 0.125$. The images are $3\ h^{-1}$ comoving Mpc on a side, span 28 arcmin on the sky, and have a pixel size of 5 arcsec. The white circles indicate the median virial radius.
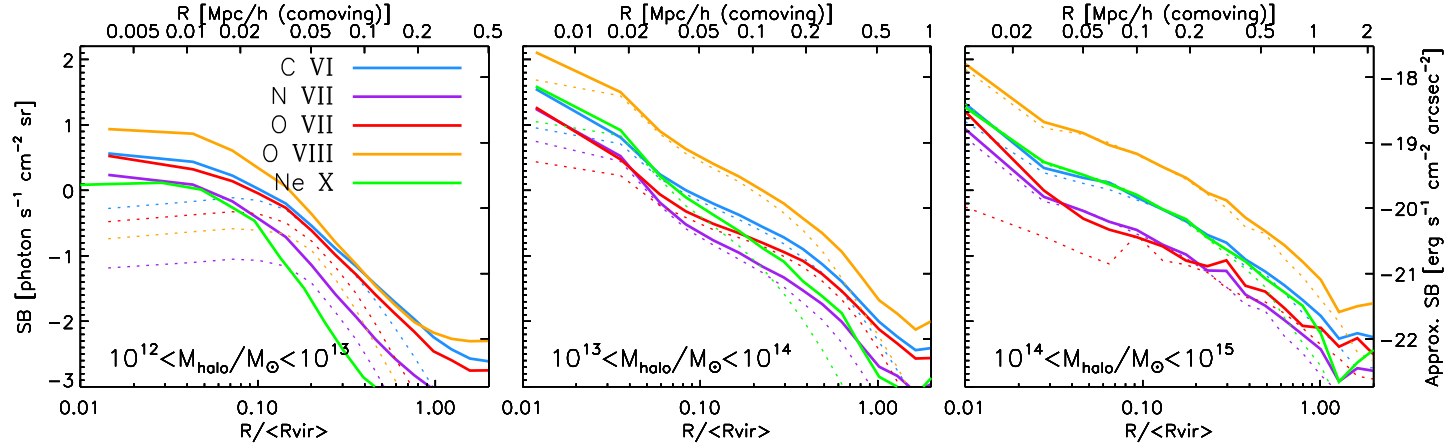
Figure 6.2: Mean surface brightness (solid curves) as a function of radius at $z = 0.125$ for the same haloes as in Figure 6.1 for the X-ray lines indicated in the legend. Dotted curves the median profile. The radius is normalized by dividing by the median virial radius in each mass bin. The surface brightness in photon $s^{-1}cm^{-2}sr^{-1}$ indicated by the left y-axis is exact. For the right y-axis it has been converted to erg $s^{-1}cm^{-2}arcsec^{-2}$ using $\langle\lambda\rangle = 22.2$ Åfor the right axis. The pixel size was 5 arcsec before binning it and the thickness of the region is 5 h^{-1} comoving Mpc. O VIII is the brightest line at all halo masses, followed by C VI. The relative strengths of the lines vary with halo mass. For galaxy-sized haloes, the profiles flatten at $R \lesssim 10\ h^{-1}$kpc, because this region is dominated by the ISM, which we excluded from our analysis.

(0.420 keV), Ne IX (0.922 keV), Mg XII (1.472 keV), Si XIII (1.865 keV), Si XV (2.460 keV), Fe XVII (0.727 keV), which were generally all weaker than the lines shown (see also Bertone et al., 2010a). The emissivities of Ne IX and Fe XVII are as high as those of N X in galaxies and Fe XVII is as high as O VII for $R < 0.2R_{\text{vir}}$ in groups. Both lines are fainter in cluster centres, but possibly still detectable.

At a limiting surface brightness of 10^{-1} photon s^{-1}cm^{-2}sr^{-1}, we would be able to detect O VIII emission out to the 80 per cent of the virial radius of cluster with $M_{\text{halo}} = 10^{14-15}$ M$_\odot$, C VI out to 40 per cent, and O VII and N VII out to 20 per cent. For lower-mass haloes, $M_{\text{halo}} = 10^{13-14}$ M$_\odot$, O VII can be observed out to the same physical scale, 200 h^{-1} comoving kpc, which corresponds to a larger fraction of the virial radius, $0.4R_{\text{vir}}$. In this case, O VIII is observable out to $0.7R_{\text{vir}}$ and C VI out to $0.5R_{\text{vir}}$. For $M_{\text{halo}} = 10^{12-13}$ M$_\odot$, O VIII, O VII, and C VI can be observed out to the same radius of $0.3R_{\text{vir}}$.

The instrumental background for SXS on *ASTRO-H* is even lower, but its angular resolution is much worse and the effective area is very small. It should be able to detect O VIII emission in the centres of groups, but it will not be able to see detailed structure, because the emission would be contained in a single pixel.

Figure 6.3 shows the X-ray flux-weighted median overdensity, clumping factor, temperature, and metallicity. The solid lines and crosses show the result for the gas at $0.1R_{\text{vir}} - 0.5R_{\text{vir}}$, while the dashed lines and triangles show $0.5R_{\text{vir}} - R_{\text{vir}}$. The flux-weighted overdensities of the gas responsible for the different lines are very similar and close to the 84th percentile of the mass-weighted overdensity and this is $\sim 0.2 - 0.7$ dex above the median density. The reason for this is that the emissivity scales as ρ^2, which biases the emission towards high densities. The flux-weighted densities increase by $\sim 0.7 - 0.9$ dex over two orders of magnitude in halo mass, but the mass-weighted median density increases by only 0.4 dex over the same range of halo masses, indicating that the clumpiness of the gas probed by the lines increases with halo mass.

Because the line flux scales with ρ^2 and the mass with ρ, we can quantify the clumpiness of the emitting gas with respect to the underlying density using the clumping factor. In this case the clumping factor is calculated as

$$C = \left(\langle\rho\rangle_{\text{Flux}} / \langle\rho\rangle_{\text{Mass}}\right)^2 \tag{6.5}$$

where $\langle\rho\rangle_{\text{Flux}}$ is the flux-weighted density and $\langle\rho\rangle_{\text{Mass}}$ the mass-weighted density. If the clumping factor is known, it is possible to derive the underlying density profile from metal-line observations. The assumption $C = 1$ is clearly not applicable.

For galaxies and groups, $C \lesssim 3$ and it is lower in the halo outskirts than in the halo core. For clusters, the story is very different. The clumping factor is around 10, with a spread of 0.4 dex for the different lines, so in this case the emission gives a more biased view. The clumping factor is higher in the cluster outskirts than in the centre, possibly indicating that a larger part of the emission originates from satellites.
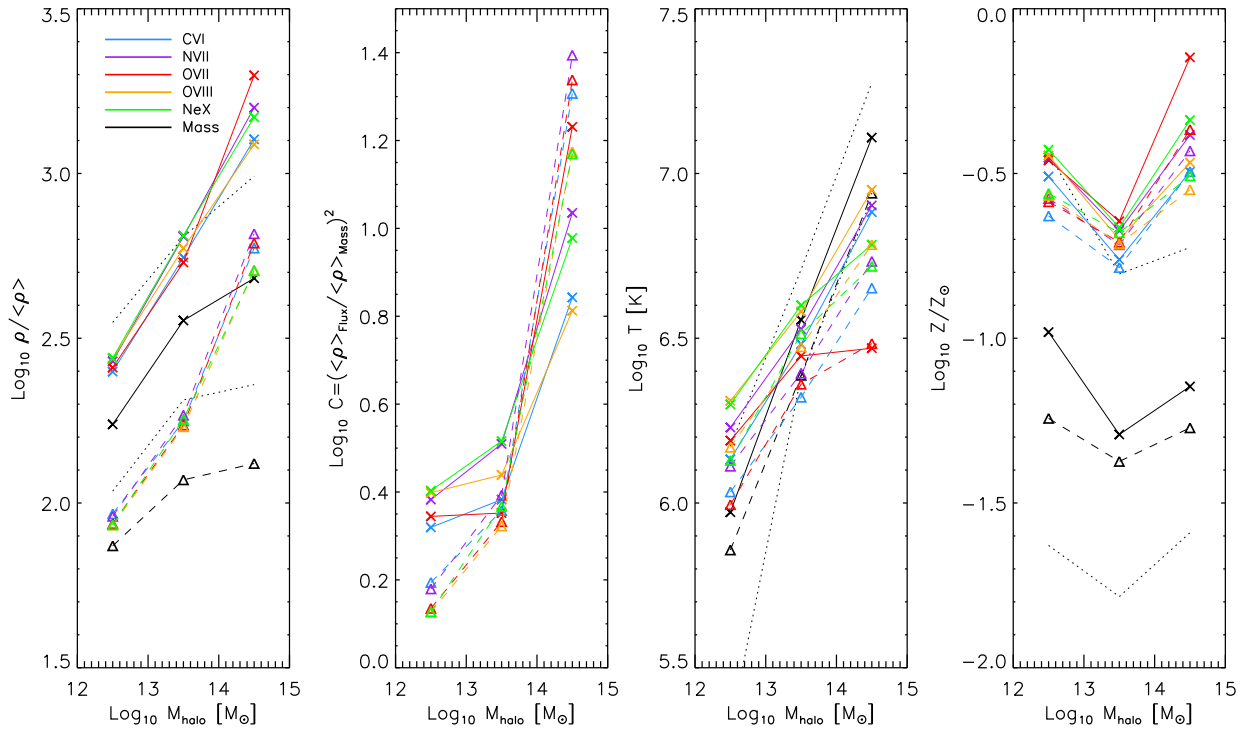
Figure 6.3: Mass-weighted (black curves) and X-ray flux-weighted (colours for different lines as in Figure 6.2) median overdensity, clumping factor, temperature, and metallicity at $z = 0.125$ averaged over haloes with $M_{\mathrm{halo}} = 10^{12-13}$ $M_\odot$, $M_{\mathrm{halo}} = 10^{13-14}$ $M_\odot$, and $M_{\mathrm{halo}} = 10^{14-15}$ $M_\odot$, from left to right. The solid curves and crosses show the result for the gas at $0.1R_{\mathrm{vir}} - 0.5R_{\mathrm{vir}}$, while the dashed curves and triangles show $0.5R_{\mathrm{vir}} - R_{\mathrm{vir}}$. The dotted, black curves show the mass-weighted 16th and 84th percentiles for the inner halo. The flux-weighted properties are biased towards high density and metallicity. The flux-weighted temperature is biased towards the temperature at which the line reaches its peak emissivity. The clumping factor is large in clusters.

Table 6.4: List of ion and rest-frame wavelengths for the Hα and UV metal-line emission lines used in this work.

ion	λ (Å)	λ_2 (Å)
H I (Hα)	6563	-
C III	977	-
C IV	1548	1551
O VI	1032	1038
Si III	1207	-
Si IV	1394	1403

The temperature at which the emissivity peaks is highest for Ne x, at $\sim 10^{6.8}$ K, and O VIII, around $10^{6.5}$ K, and it decreases slowly towards higher temperatures (Bertone et al., 2010a). This is the reason why, for galaxies and groups, these lines have the highest flux-weighted temperatures. For clusters, the Ne x-weighted temperature is lower than that of O VIII. The flux-weighted median temperatures increase less steeply with halo mass than the mass-weighted median temperature, although the former still increase by ~ 0.7 dex for an increase of 2 dex in halo mass. For the lowest (highest) mass bin the flux-weighted temperatures are higher (lower) than the mass-weighted temperature. The O VII flux-weighted temperature stays roughly constant with halo mass. This is due to the fact that the emissivity curve of O VII is more strongly peaked in temperature than the emissivity of the other lines (see Figure 1 of Bertone et al., 2010a). It peaks at $10^{6.3}$ K and drops quickly for higher and lower temperatures.

In the halo outskirts, the temperatures probed are somewhat lower, by $0.2 - 0.3$ dex, than in the inner parts. The densities are lower by $0.5 - 0.7$ dex. This is true for flux-weighted as well as mass-weighted median temperatures and densities, so they follow the same trend.

The median mass-weighted metallicity is 0.04-0.1$Z_\odot$, but the flux-weighted metallicities are 0.5-1.0 dex higher. The median flux-weighted metallicities are similar to the 84th percentile of the mass-weighted metallicity, for galaxies and groups. The flux-weighted metallicities for clusters are significantly above the 84th percentile, especially for O VII, which also has the highest overdensity and lowest temperature. Thus, perhaps not surprisingly, X-ray metal-line emission is biased towards high-metallicity gas. As metal lines dominate the emission in the soft X-ray band (0.5-1.0 keV), the same will be true for broad band emission (e.g. Crain et al., 2010a).

6.3.2 Low-redshift UV

For detecting UV metal-line emission as a tracer of halo gas, instruments should ideally have a large field of view and a high spatial and angular resolution, as is also the case for X-ray emission. The emission will be dominated by relatively

high-density material. With high spatial resolution, it will be possible to verify its clumpiness.

A surface brightness limit of order 10^{-18} erg s^{-1}cm^{-2}arcsec^{-2}, as is the case for the *FIREBALL*[4] balloon experiment (Tuttle et al., 2008, 2010), will only be sufficient to detect metal-line emission in the centres of massive haloes. The wavelength range of *FIREBALL* (2000–2200 Å) is such that it will only probe the UV metal lines at a somehat higher redshift than shown here ($z \approx 0.35$ for C IV) where the surface brightness is a bit lower. A detection limit of order 10^{-21} erg s^{-1}cm^{-2}arcsec^{-2} is envisioned for the next generation UV mission *ATLAST* (Postman, 2009).

Figure 6.4 shows images of C III (977 Å) line emission at $z = 0.125$. We use three halo mass bins of $M_{\rm halo} = 10^{11-12}$ M$_\odot$, 10^{12-13} M$_\odot$, and 10^{13-14} M$_\odot$ with $R_{\rm vir} \approx 0.11$, 0.25, and 0.50 h^{-1}Mpc, respectively. The images are 1 h^{-1} comoving Mpc on a side, which corresponds to 9 arcmin at $z = 0.125$. The surface brightness in the haloes with mass below 10^{13} M$_\odot$ looks relatively smooth, because it has been averaged over many haloes (see Table 6.1 . There are only 46 haloes in the last bin and the image looks very patchy. We will discuss the clumpiness of the gas responsible for the emission below.

As in the previous section, we calculate the average of the surface brightness azimuthally for the UV metal lines listed in Table 6.4. We include also Hα from the same haloes and discuss it in Section 6.3.4. Figure 6.5 shows the mean (median) surface brightness profiles for different UV lines for stacked haloes at $z = 0.125$ as the solid (dotted) curves. We use the same three halo mass bins as in Figure 6.4.

C III (977 Å) is the brightest line, followed by Si III (1207 Å). The emission profile for all lines peaks in the halo core, where it may, however, be outshone by the galaxy. O VI (1032 Å) gives the most extended profile, in the sense that the ratio between emission in the halo core and outskirts is largest. This is caused by the fact that O VI traces warmer and more diffuse gas than the other lines. C IV (1548 Å) and Si IV (1294 Å) are weaker than C III and Si III, but because they have frequencies redward of Lyα, they are less easily absorbed. We also computed the emissivities of He II (1640 Å) and N V (1239 Å), which were weaker and therefore not shown.

A surface brightness limit of 10^{-18} erg s^{-1}cm^{-2}arcsec^{-2} should enable us to observe metal-line emission from the centres of fairly massive galaxies ($M_{\rm halo} > 10^{12}$ M$_\odot$. However, it is possible that the galaxy will outshine the halo in these regions.

By stacking haloes, *FIREBALL* could in principle probe down to a surface brightness limit of 10^{-19} erg s^{-1}cm^{-2}arcsec^{-2}. Its wavelenth rage is such that it can only detect C III and Si III at $z \approx 1$. As the surface brightness is lower at $z = 1$ as compared to $z = 0.125$ by ~ 0.5 (not shown), it may see emission out to $\sim 0.1 R_{\rm vir}$ for $M_{\rm halo} > 10^{12}$ M$_\odot$. A complicating factor is that C III and Si III have

---

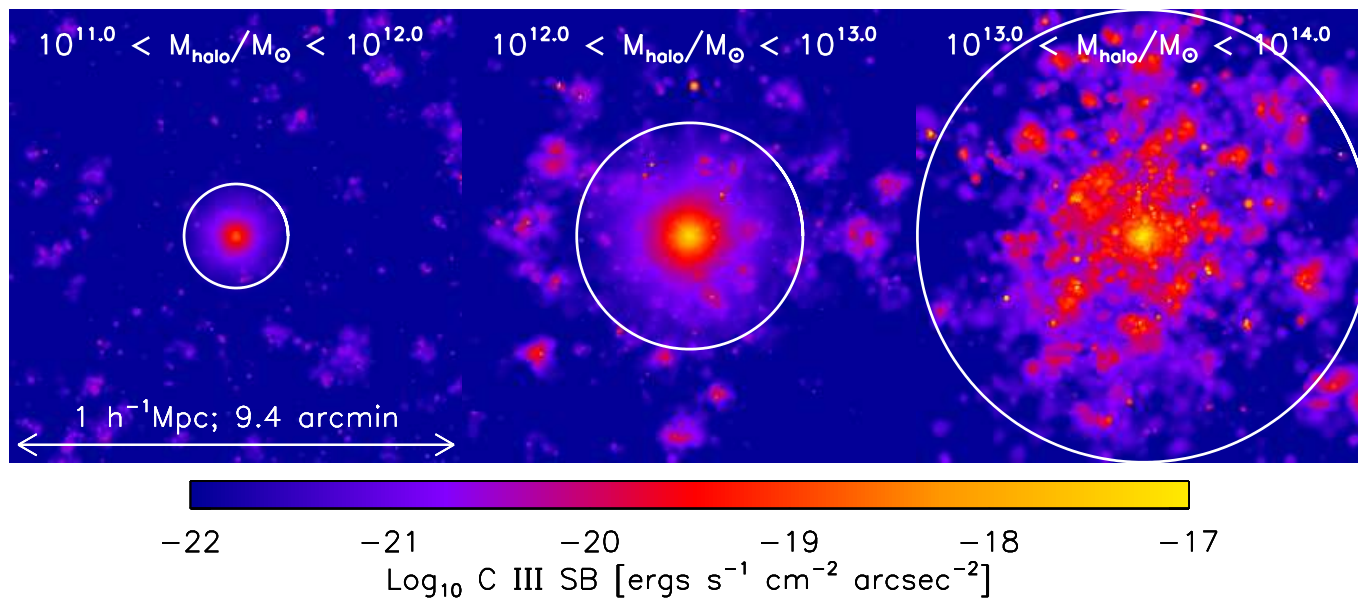[4]http://www.srl.caltech.edu/sal/fireball.html

Figure 6.4: Mean C III emission maps for haloes with $M_{\rm halo} = 10^{11-12}$ M$_\odot$, $M_{\rm halo} = 10^{12-13}$ M$_\odot$, and $M_{\rm halo} = 10^{13-14}$ M$_\odot$, from left to right, at $z = 0.125$. The images are $1\ h^{-1}$ comoving Mpc on a side, span 9.4 arcmin on the sky, and have a pixel size of 2 arcsec. The white circles indicate the median virial radius.
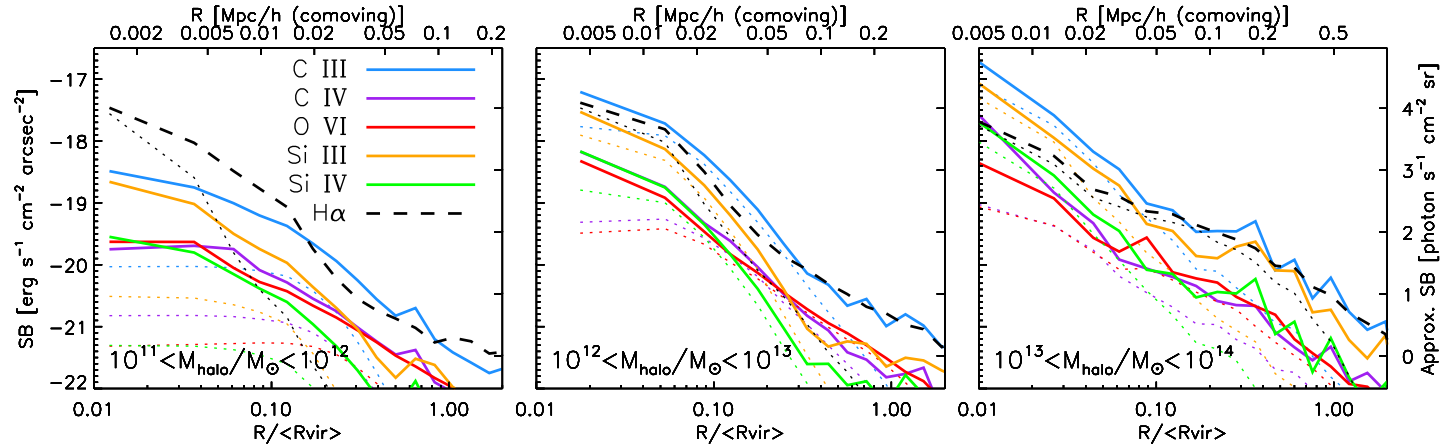
Figure 6.5: Mean UV (solid curves) and Hα (dashed curve) surface brightness as a function of radius at $z = 0.125$ for the same haloes as in Figure 6.4. The emission lines are indicated in the legend. Dotted curves show the median profile. The radius is normalized by dividing by the median virial radius in each mass bin. The surface brightness in erg s^{-1}cm^{-2}arcsec^{-2} on the left y-axis is exact. It has been converted to photon s^{-1}cm^{-2}sr^{-1} using $\langle \lambda \rangle = 1232$ Å. The pixel size was 2 arcsec before it was binned and the thickness of the region is 2.2 h^{-1} comoving Mpc. C III is the brightest line, followed by Si III.

frequencies blueward of Lyα and could therefore be absorbed by intervening hydrogen, an effect that is much worse for C III than Si III.

With a detection limit of order 10^{-21} erg s^{-1}cm^{-2}arcsec^{-2} we would be able to detect C III out to the virial radius and several other metal lines out to 50 per cent of R_{vir}. Such a low surface brightness limit may be attainable for the next generation UV mission *ATLAST* (Postman, 2009). As Lyα emission is even brighter (e.g. Furlanetto et al., 2003), one can even probe the gas in emission outside galactic haloes, in the filaments of the cosmic web.

In Figure 6.6 the UV flux-weighted overdensity, clumping factor, temperature, and metallicity are shown for several metal lines at $z = 0.125$ for the same three halo mass bins as in Figure 6.4. The solid lines and crosses show the result for the gas at $0.1R_{vir} - 0.5R_{vir}$, while the dashed lines and triangles show $0.5R_{vir} - R_{vir}$. The different metal lines probe very different densities, all higher than the mass-weighted overdensity. O VI results in the lowest flux-weighted overdensity. The flux-weighted density increases via C IV to C III to Si IV and is the highest for Si III. For all halo masses, the silicon lines have higher flux-weighted densities than the 84th percentile of the mass-weighted density. In group-sized haloes all lines are dominated by gas denser than the mass-weighted 84th percentile. The difference between the O VI and Si III flux-weighted overdensities is ~ 1 dex. The flux-weighted overdensities increase somewhat more steeply with halo mass than the mass-weighted overdensity, by about 1.5 dex for an increase of 2 dex in halo mass.

Because the median flux-weighted densities vary a lot between different UV metal-lines, the clumping factor, defined in Equation 6.5, does so as well. The clumpiness is lowest for O VI emission and highest for Si III, with a difference in clumping factor of around 1.5 dex for a fixed halo mass. The clumping difference between centre and outskirts is relatively minor, $\Delta Log_{10}C \lesssim 0.2$ dex. For O VI in galaxy haloes ($M_{halo} < 10^{13}$ M$_\odot$), the clumping factor is close to one and hence a good tracer of the density (although it is still biased towards high metallicities). For the metal lines and halo mass range probed, the clumping factor varies between $\sim 1 - 10^3$. This means that the UV metal-line emission is quite clumpy. This is in agreement with Bertone et al. (2010b) and Frank et al. (2011) who find that most of the UV flux comes from discrete, compact sources.

The flux-weighted temperature depends on the specific metal line, decreasing as the corresponding overdensity increases. They are insensitive to the mass-weighted temperature of the halo, because the emissivities are strongly peaked at specific temperatures (Bertone et al., 2010b). The difference between Si III and O VI is just over an order of magnitude. All UV metal-lines probe gas with temperatures $10^{4.5-5}$ K with the exception of O VI, which is dominated by $10^{5.5}$ K gas.

The mass-weighted temperature is up to 0.2 dex lower in the outskirts of the halo than in to the core, but the flux-weighted temperatures differ by at most 0.1 dex. The overdensity is consistently lower by $0.3 - 0.6$ dex in the halo outskirts for both flux-weighted and mass-weighted densities.
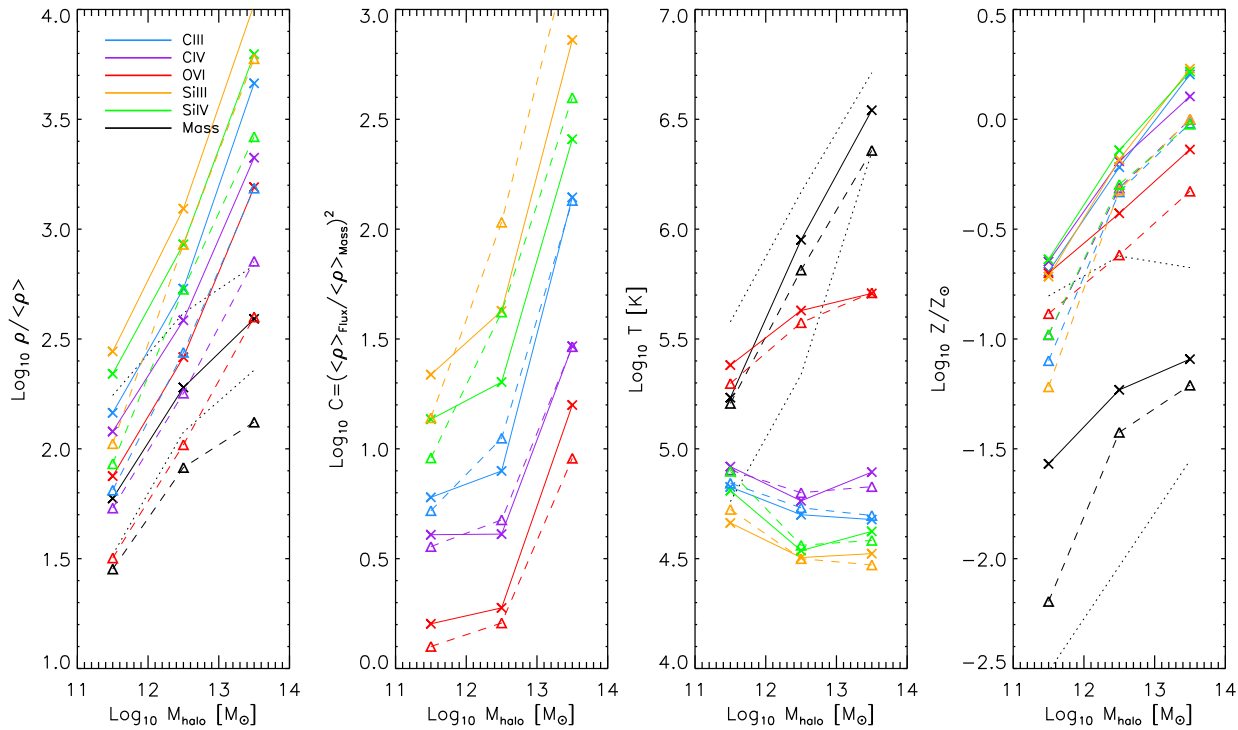
Figure 6.6: Mass-weighted (black curves) and UV flux-weighted (colours for different lines as in Figure 6.5 and indicated in the legend) median overdensity, clumping factor, temperature, and metallicity at $z = 0.125$ averaged over haloes with $M_{\rm halo} = 10^{11-12}$ $M_\odot$, 10^{12-13} $M_\odot$, and 10^{13-14} $M_\odot$, from left to right. The solid curves and crosses show the result for the gas at $0.1R_{\rm vir} - 0.5R_{\rm vir}$, while the dashed curves and triangles show $0.5R_{\rm vir} - R_{\rm vir}$. The dotted, black curves show the mass-weighted 16th and 84th percentiles for the inner halo.

The flux-weighted median metallicity is about an order of magnitude higher than the mass-weighted median metallicity and it is also higher than the mass-weighted 84th percentile. For high-mass haloes with $M_{halo} > 10^{12}$ M$_\odot$, O VI probes gas with ~ 0.3 dex lower metallicities than the other lines. In the centres of groups the emission is dominated by gas with supersolar metallicities, even though on average the gas is enriched to $Z \approx 0.1$ Z$_\odot$. All computed metallicities increase with halo mass. Low-mass haloes with $M_{halo} = 10^{11-12}$ M$_\odot$ have 0.6 dex lower mass-weighted metallicities in their outskirts as compared to their cores. This difference is somewhat smaller for flux-weighted metallicities and for higher mass haloes.

6.3.3   High-redshift UV

It is possible to detect rest-frame UV emitted at high redshift from the ground, in the optical. In the near future, several integral field unit spectrographs will become operational, such as the Multi-Unit Spectroscopic Explorer[5] (MUSE) on the *Very Large Telescope* (Bacon et al., 2010) and the Keck Cosmic Web Imager[6] (KCWI) on *Keck* (Martin et al., 2010). The Cosmic Web Imager[7] (CWI) is already installed on the 200-inch *Hale* telescope (Rahman et al., 2006; Matuszewski et al., 2010).

With narrow band observations it has already been demonstrated that diffuse Lyα emission can be detected down to $\sim 10^{-18}$ erg s^{-1}cm^{-2}arcsec^{-2} in individual objects (e.g. Steidel et al., 2000; Matsuda et al., 2004) and down to $\sim 10^{-19}$ erg s^{-1}cm^{-2}arcsec^{-2} in stacks (Steidel et al., 2011). New instrumentation, such as MUSE and KCWI[8], will allow us to go one order of magnitude deeper. This is essential for the detection of metal lines (Bertone & Schaye, 2012).

Figure 6.7 shows images of C III line emission at $z = 3$. We use halo mass bins of $M_{halo} = 10^{10-11}$ M$_\odot$, 10^{11-12} M$_\odot$, and 10^{12-13} M$_\odot$ with $R_{vir} \approx 0.06, 0.14$, and $0.29\ h^{-1}$ comoving Mpc, respectively. The images are $0.5\ h^{-1}$ comoving Mpc on a side, which corresponds to 22 arcsec on the sky at $z = 3$. The surface brightness is smoother than at $z = 0.125$ even though there are less haloes per bin, so the flux is coming from less clumpy material.

As before, we calculate the average of the surface brightness azimuthally for the metal-lines listed in Table 6.4. Figure 6.8 shows the mean (median) UV line surface brightness profiles at $z = 3$ as the solid (dotted) curves for the same three halo mass bins as in Figure 6.8. The surface brightness is about one order of magnitude lower at $z = 3$ than at $z = 0.125$ at a fixed fraction of R_{vir}. Additionally, the profile shows a strong flattening inside 10 per cent of the virial radius. This is because we are probing down to smaller physical scales, where the emission is dominated by star-forming gas, which we have excluded from
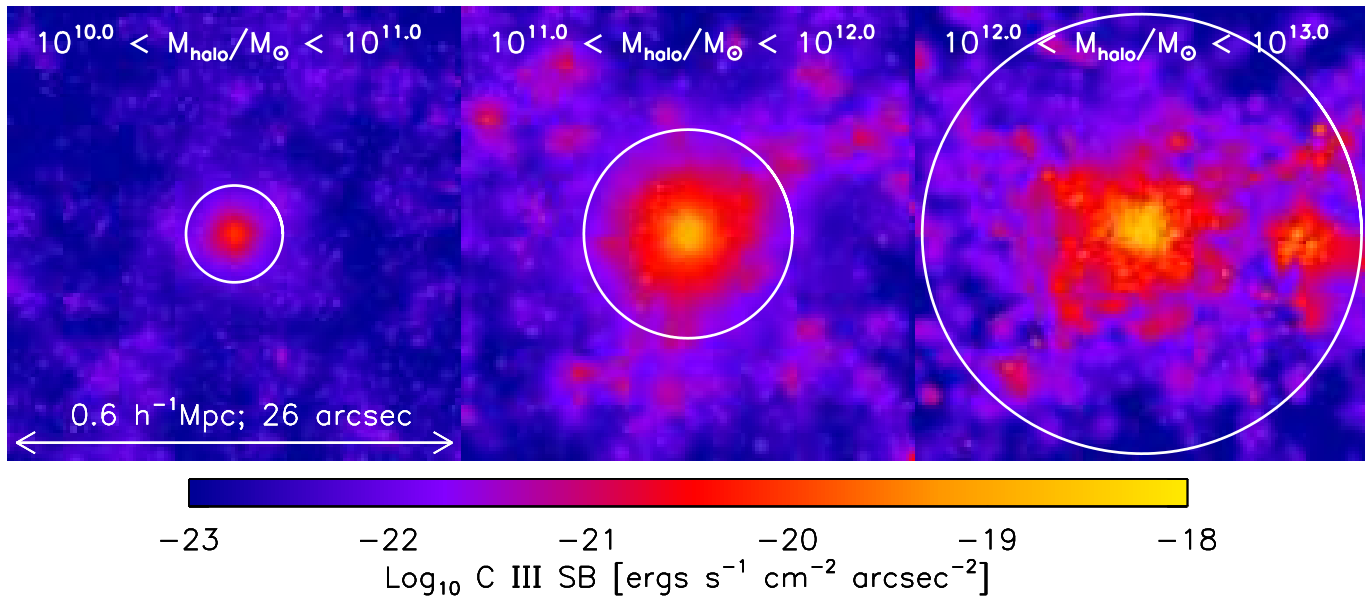
---

[5]http://muse.univ-lyon1.fr/
[6]http://www.srl.caltech.edu/sal/keck-cosmic-web-imager.html
[7]http://http://www.srl.caltech.edu/sal/cosmic-web-imager.html
[8]http://www.srl.caltech.edu/sal/keck-cosmic-web-imager.html

Figure 6.7: Mean CIII emission maps for haloes with $M_{halo} = 10^{10-11}$ M$_\odot$, 10^{11-12} M$_\odot$, and 10^{12-13} M$_\odot$, from left to right, at $z = 3$. The images are $0.6\ h^{-1}$ comoving Mpc on a side, span 26 arcsec on the sky, and have a pixel size of 0.2 arcsec. The white circles indicate the median virial radius.
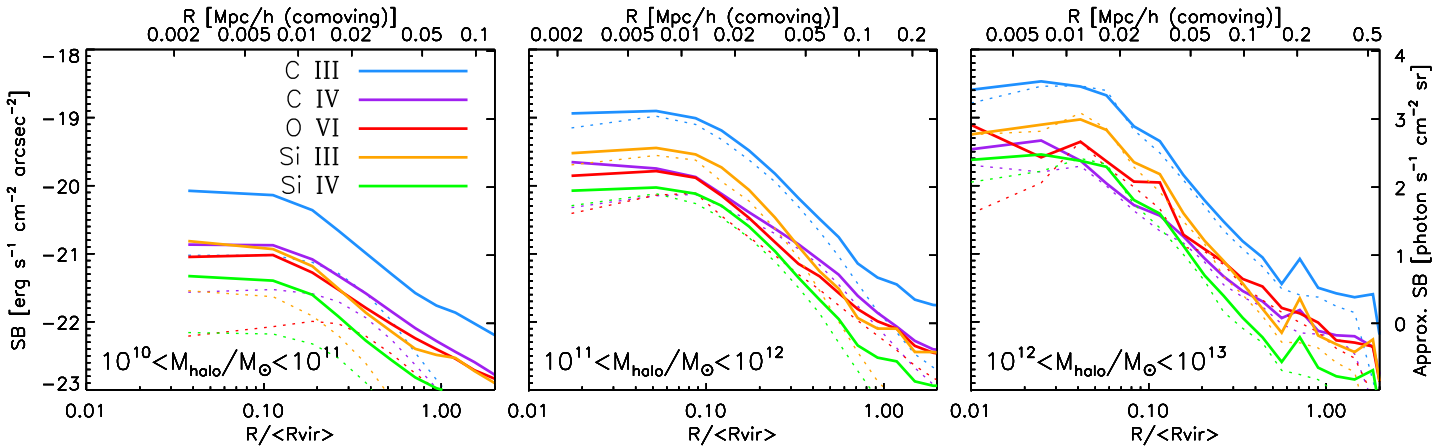
Figure 6.8: Mean UV surface brightness (solid curves) as a function of radius at $z = 3$ for the same haloes as in Figure 6.7. Dotted curves the median profile. The emission lines are indicated in the legend. The radius is normalized by dividing by the median virial radius in each mass bin. The surface brightness in erg s^{-1}cm^{-2}arcsec^{-2} on the left y-axis is exact. For the right y-axis, it has been converted to photon s^{-1}cm^{-2}sr^{-1} using $\langle\lambda\rangle = 1232$ Å. The pixel size was 0.2 arcsec before it was binned and the thickness of the region is 1.2 h^{-1} comoving Mpc. C III is the brightest line. C IV, Si III, and Si IV are of similar strength. The surface brightnesses are lower than at $z = 0.125$ and the flattening at small radii is more pronounced.

our calculations.

Comparing our metal-line results to the Lyα profile observed by Steidel et al. (2011) for $M_{halo} \sim 10^{12}$ and $\langle z \rangle = 2.65$, we predict that the C III surface brightness is about 1–2 dex lower than the Lyα brightness. The other metal lines that are shown are about 0.5–1 dex fainter than C III. Because C III has a much shorter wavelength than Lyα, it is strongly absorbed by the intervening medium. It is therefore possible that the other metal lines are in fact stronger than C III. We calculated, but do not show, the Lyα surface brightness profile from our simulations in the optically thin limit and without a contribution from star formation. The observed profile is ~ 0.7 dex higher than the predicted profile, which is not surprising considering that the Lyα emission is thought to be originating from H II regions in the ISM.

With a detection limit of 10^{-20} erg s^{-1}cm^{-2}arcsec^{-2}, C III can be seen out to $0.3R_{vir}$ for $M_{halo} = 10^{11-12}$ M$_\odot$ and out to $0.2R_{vir}$ for 10^{12-13} M$_\odot$ at $z = 3$. Other metal lines are weaker, but can still be probed to 10 per cent of R$_{vir}$ for $M_{halo} > 10^{11}$ M$_\odot$. Nothe, however, that the emission may in reality be brighter at these small radii, because we excluded emission from gas with $N_H > 0.1$ cm^{-3}. We predict that the surface brightness for lower-mass haloes is below this limit.

In Figure 6.9 the UV flux-weighted overdensity, clumping factor, temperature, and metallicity are shown at $z = 3$ for the same metal lines as in Figure 6.6. The solid lines and crosses show the result for the gas at $0.1R_{vir} - 0.5R_{vir}$, while the dashed lines and triangles show $0.5R_{vir} - R_{vir}$. The general picture is unchanged at high redshift, although the density differences between different lines is somewhat reduced. The flux-weighted overdensities are lower, but the physical densities are higher at high redshift.

At $z = 3$ and for $M_{halo} < 10^{12}$ M$_\odot$, O VI and C IV have clumping factors (see Equation 6.5) below unity, which means that the emission is biased towards lower-density regions. For the same haloes, $C \approx 1$ for C III emission and the clumping factor is 1–3 for the silicon lines. At higher halo masses, the clumping facor is $1 - 1.5$ dex higher and for most lines $C \approx 10 - 100$. Because the average temperature of the gas in these haloes is much higher than the temperature at which the emissivity of the UV metal lines peaks, the emission is originating from cold, dense clumps in the much hotter halo. For O VI the temperature difference and hence the clumping factor is smallest.

At $z = 3$ the scatter in density is larger than at $z = 0.125$: the difference between the 16th and 84th percentile is more than an order of magnitude as opposed to 0.4 dex. As a result, none of the lines are dominated by overdensities above the 84th percentile at this redshift. O VI and C IV are tracing densities below the median mass-weighted density for low-mass haloes ($M_{halo} < 10^{12}$ M$_\odot$). The flux-weighted densities increase with halo mass, even if the mass-weighted density does not. The median density in the outskirts is lower than in the centre, for both flux- and mass-weighted quantities, by up to ~ 0.6 dex.

The flux-weighted temperatures are insensitive to halo mass. They trace temperatures near or above the median mass-weighted temperature for low-mass
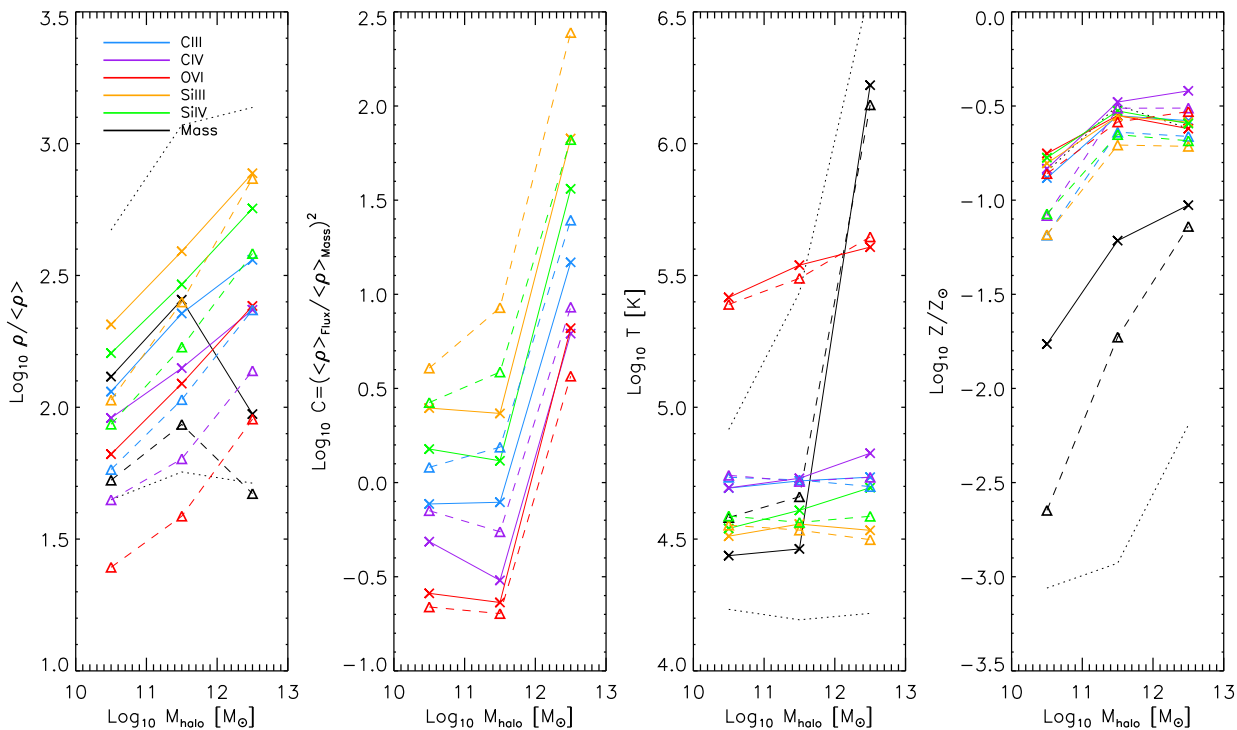
Figure 6.9: Mass-weighted (black curves) and UV flux-weighted (colours for different lines as in Figure 6.8 and indicated in the legend) median overdensity, clumping factor, temperature, and metallicity at $z = 3$ averaged over haloes with $M_{halo} = 10^{10-11}$ $M_\odot$, $M_{halo} = 10^{11-12}$ $M_\odot$, and $M_{halo} = 10^{12-13}$ $M_\odot$, from left to right. The solid curves and crosses show the result for the gas at $0.1R_{vir} - 0.5R_{vir}$, while the dashed lines and triangles show $0.5R_{vir} - R_{vir}$. The dotted, black curves show the mass-weighted 16th and 84th percentiles for the inner halo.

haloes ($M_{\text{halo}} < 10^{12}$ M$_\odot$), but the opposite is true for higher-mass haloes. The scatter in temperature increases with halo mass and becomes very large, with the mass-weighted 84th percentile 2.2 dex above the 16th percentile. This reflects the bimodal nature of halo gas in massive high-redshift galaxies, where the gas either has a temperature close to the virial temperature and or has $T < 10^5$ K (e.g. van de Voort & Schaye, 2012). O vi traces gas about an order of magnitude warmer than the other metal lines shown, because its emissivity peaks around $10^{5.5}$ K.

As we found before, the flux-weighted properties are biased towards high metallicities. All lines trace metallicities of about 0.1–0.4 Z$_\odot$ in the inner halo and $0.1 - 0.4$ dex lower in the outer halo. Because the spread in metallicity is much larger at $z = 3$ than at $z = 0.125$, the flux-weighted metallicities trace the mass-weighted 84th percentile at $z = 3$ as opposed to being significantly higher at $z = 0.125$.

6.3.4 Low-redshift Hα

Hα (6563 Å) emission at low redshift is observable with the same instruments as high redshift rest-frame UV emission. The predicted emission from gas around galaxies is shown in Figure 6.5 as a dashed, black curve. Interestingly, the Hα emission is comparable to C iii emission at $R > 50$ kpc for all haloes with $M_{\text{halo}} = 10^{11-14}$ M$_\odot$. However, for $R < 50$ kpc, Hα is much brighter than C iii for the lowest halo mass bin ($M_{\text{halo}} = 10^{11-12}$ M$_\odot$) and up to an order of magnitude fainter for the highest halo mass bin ($M_{\text{halo}} = 10^{13-14}$ M$_\odot$). We stress again that we ignored emission from gas with $n_{\text{H}} > 0.1$ cm^{-3}.

Assuming a limiting surface brightness of 10^{-20} erg s^{-1}cm^{-2}arcsec^{-2}, Hα emission from halo gas can be detected out to $0.5R_{\text{vir}}$ for haloes with $M_{\text{halo}} = 10^{11-12}$ M$_\odot$, $0.25R_{\text{vir}}$ for haloes with $M_{\text{halo}} = 10^{12-13}$ M$_\odot$, and out to $0.4R_{\text{vir}}$ for group-sized haloes. This is feasible when stacking deep observations with MUSE or KCWI centred on galaxies.

6.4 Discussion and conclusions

A large fraction of the gas in galaxy haloes, groups, and clusters has temperatures $T = 10^{4.5-7}$ K (van de Voort & Schaye, 2012). At these temperatures, the cooling is dominated by metal-line emission for metallicities $Z \gtrsim 0.1$ Z$_\odot$ (e.g. Wiersma et al., 2009a). Observing these lines therefore constitutes an excellent route to studying the diffuse, warm-hot gas around galaxies, both at low and at high redshift. Additionally, metal-line emission may also provide us with clues as to how the circumgalactic gas was enriched and thus about the feedback process responsible for this enrichment.

We used cosmological, hydrodynamical simulations to quantify the surface brightness profiles of diffuse, circumgalactic gas, for both soft X-ray and rest-

frame UV metal lines. The lines we considered are C VI (0.367 keV), N VII (0.500 keV), O VII (0.561 keV), O VIII (0.654 keV), and Ne X (1.021 keV) in the X-ray band and C III (977 Å), C IV (1548 Å), Si III (1207 Å), Si IV (1294 Å), and O VI (1032 Å) in the rest-frame UV band. We discussed their detectability with current and future instruments and computed the flux-weighted physical properties of the gas in the halo core and outskirts.

The strongest soft X-ray line at redshift $z = 0.125$ is O VIII. It traces gas that is denser than the mass-weighted density, but the clumping factor is only a few for haloes with $M_{halo} < 10^{14}$ M)$\odot$ and of order 10 for clusters. The temperature probed is within a factor of three from $10^{6.5}$ K, the temperature at which the emissivity peaks. It increases with halo mass, but less steeply than the mass-weighted temperature. The emission originates from regions with metallicities of about 0.3 $Z_{\odot}$, whereas the mass-weighted metallitcity is a factor of three lower. The difference between the inner and outer halo is largest for the flux-weighted density, about a factor of three. The other X-ray lines are biased towards the same densities, temperatures, and metallicity, but are at least a factor of three weaker.

The strongest UV metal-line, both at $z = 0.125$ and $z = 3$, is C III. The temperature of the gas the emission originates from is very close to $10^{4.7}$ K, the temperature at which the emissivity peaks, and does not vary with halo mass. At low redshift, the line is severely biased towards high metallicities. The flux-weighted metallicity is about an order of magnitude higher than the mass-weighted metallicity. At high redshift, the bias is smaller and the difference is a factor of a few. The clumping factor varies with halo mass from 10 to 100 at $z = 0.125$ and from 1 to 10 at $z = 3$. The flux-weighted overdensity increases from O VI to C IV to C III to Si IV to Si III by a facor of $\sim 3 - 10$. The Si III clumping factor reaches 10^3 in massive haloes. The temperature of the gas probed is about the same for all lines, except for O VI, whose emissivity peaks around $10^{5.5}$ K.

Proposed X-ray missions with detection limits of 10^{-1} photon $s^{-1}\,cm^{-2}\,sr^{-1}$ will be able to easily detect metal-line emission in galaxy haloes, groups, and clusters at $z = 0.125$. O VIII emission can be detected out to 80 per cent of the virial radius of groups and clusters and out to $0.4R_{vir}$ for $M_{halo} = 10^{12-13}$ M$_\odot$. C VI, N VII, O VII, and Ne X can also be detected out to smaller radii, $0.1 - 0.5R_{vir}$.

Assuming a detection threshold of 10^{-20} erg $s^{-1}\,cm^{-2}\,arcsec^{-2}$, future optical instruments should be able to detect several rest-frame UV metal lines, C IV, O VI, Si III, and Si IV, out to $0.1R_{vir}$ at $z = 3$ for haloes more massive than 10^{11} M$_\odot$. C III can be observed out to twice that distance. The same instruments can also observe Hα at low redshift, which provides a good probe of the cold (10^4 K) halo gas. Assuming the same detection threshold, Hα can be detected out to 0.2, 0.3, and 0.5 R_{vir} for $M_{halo} = 10^{11-12}$, 10^{12-13}, and 10^{13-14} M$_\odot$, respectively. Because C III has a frequency blueward of Lyα, it may be strongly absorbed, especially when it is emitted at high redshift. The other UV metal lines may therefore be stronger.

If we assume the same detection limit of 10^{-20} erg s^{-1} cm^{-2} arcsec^{-2} for UV metal lines at $z = 0.125$, C III can be detected out to $0.3R_{\mathrm{vir}}$ for 10^{11-13} M$_\odot$ haloes and out to $0.5R_{\mathrm{vir}}$ for 10^{13-14} M$_\odot$ haloes. C IV, O VI, Si III, and Si IV can be detected out to $0.1-0.2$ R$_{\mathrm{vir}}$ for all haloes, and Si III can even be seen out to the same radius as C III for 10^{13-14} M$_\odot$ haloes.

Galaxies form inside (intersections of) filaments and we therefore expect that neighbouring galaxies are connected by these filaments. Stacking haloes randomly will not show filamentary emission, because the filaments will be oriented randomly. However, before stacking the galaxies, we can first rotate them towards their nearest neighbour of similar mass. This should enhance the emission of the gas in one direction. The signal at large radii is hard to detect, so the brightest emission lines should be chosen for this. We tested this using our simulations, but found that the enhancement is only about 0.2 dex (not shown).

Apart from stacking all images, one can stack only pixels with a detection in the brightest emission line and then look for emission from other lines. Because the emission is highest in the densest regions, the emission from different lines will be correlated. This also leads to an enhancement of the signal. Using pixels with a detection in Lyα would be well suited for detecting C III, C IV, Si III, and Si IV as these probe cold ($10^{4.5}$ K) gas.

In the near future, before we submit this paper to a journal, we will recompute the surface brightness profiles for simulations that include AGN feedback, because this feedback has been shown to be important (e.g. McCarthy et al., 2010; Bertone et al., 2010a). Additionally, we will test the dependence of our results on the resolution, pixel size, bin size of the surface brightness profile, and on the thickness of the region for which the emission is added.

Acknowledgements

De groei van sterrenstelsels en hun gasrijke halo's

Wanneer je omhoog kijkt op een donkere plek op Aarde op een maanloze nacht, kun je een lichte band van sterren zien. Dit komt doordat het merendeel van de sterren in ons eigen sterrenstelsel verdeeld zit in een schijf, die we de Melkweg noemen. De Melkweg bevat ongeveer 100 miljard sterren en er wordt elk jaar ongeveer één nieuwe geboren. Deze sterren worden gemaakt in grote, koude gaswolken. Daarbinnen trekken verdichtingen zich steeds verder samen onder invloed van de zwaartekracht, totdat de dichtheid groot genoeg wordt om kernfusie te laten plaatsvinden, waarbij zodoende een ster ontstaat.

Sterren in sterrenstelsels vormen maar een klein deel van de totale materie in het heelal. Omdat ze zo helder zijn, zijn ze relatief eenvoudig waar te nemen. Om te bestuderen hoe sterrenstelsels groeien wordt daarom vaak gekeken naar hoe snel ze sterren vormen. Wat moeilijker te bepalen is via waarnemingen is waar het materiaal waaruit sterren vormen vandaan komt, omdat dit gas erg weinig licht uitstraalt. Daarom gebruiken we bovendien kosmologische simulaties om de vorming van sterrenstelsels te bestuderen. Hierbij wordt de ontwikkeling van een representatief deel van het heelal gesimuleerd, van vlak na de oerknal tot nu, waarbij alle relevante natuurwetten worden meegenomen. Met kosmologische simulaties is het juist makkelijk om uit te zoeken waar de materie zich bevindt. Bovendien zien we in observaties altijd een stilstaand beeld, terwijl we met simulaties de ontwikkeling in de tijd kunnen volgen. Een ander voordeel van simulaties is dat we precies weten welke ingredienten we in ons 'heelal' stoppen. Willen we vervolgens weten wat het effect van een enkel proces is, dan kunnen we een tweede simulatie doen waarbij we dit proces uitschakelen en deze beide simulaties vergelijken.

In het jonge heelal was alle materie vrijwel homogeen verspreid. Kleine verschillen in dichtheid trokken vervolgens samen onder de invloed van zwaartekracht. Hierbij ontstond een 'kosmisch web' van filamenten. Tussen deze filamenten bevinden zich grote leegtes, maar in deze filamenten vormen zich gebonden objecten, die we halo's noemen. Deze halo's bestaan voor het grootste gedeelte uit donkere materie, maar ook uit baryonische materie[9]. Donkere materie kan zijn kinetische energie heel moeilijk verliezen, maar gas kan licht uitstralen en zodoende energie kwijtraken. Hierdoor kan het gas nog verder samentrekken dan de donkere materie en op deze manier ontstaan sterrenstelsels in de centra van halo's.

---

[9]Dit is de materie die we het beste kennen, waar alles op aarde uit gemaakt is en waar ook sterren uit bestaan.

De inhoud van dit proefschrift

Hieronder volgt een vereenvoudigde samenvatting van dit proefschrift. Voor meer informatie verwijs ik graag naar het desbetreffende hoofdstuk.

Hoofdstuk 2: Het invallen van gas op sterrenstelsels en halo's

Het invallen van gas op halo's gebeurt ongeveer even efficiënt als het invallen van donkere materie. Dit komt doordat in dit geval de zwaartekracht allesbepalend is. Hoe snel dit gas vervolgens deel wordt van het sterrenstelsel, hangt af van hoe snel het kan koelen. Dit hangt op zijn beurt weer af van de temperatuur van het gas, dat weer afhangt van de massa van de halo. Bovendien koelt het gas efficiënter als het veel zware metalen heeft, omdat deze ook licht uitstralen.

Wanneer er in de simulaties niets gedaan wordt om het instromen van gas tegen te gaan, vindt er te veel stervorming plaats en komen de simulaties niet overeen met de werkelijkheid. Daarom bevatten veel simulaties modellen om de feedback van sterren en zwarte gaten te beschrijven. Een deel van de energie die vrijkomt bij het ontploffen van sterren, zogenaamde supernova explosies, en bij het groeien van zwarte gaten koppelt terug naar het gas eromheen. Op deze manier een gedeelte van het gas uit het sterrenstelsel geblazen. Hierbij botst het ook tegen invallend gas aan, waardoor het invallen vertraagd wordt.

In dit hoofdstuk laten we zien dat feedback vooral een groot effect heeft, tot wel een orde van grootte, op de inval van gas op sterrenstelsels en in mindere mate op de inval op halo's. De halomassa waarbij sterrenstelsels het snelst groeien verschuift met een factor honderd omhoog door de toevoeging van feedback processen.

Het gas stroomt halo's binnen met een hoge snelheid en dus met een hoge kinetische energie. Om deel te worden van de halo moet het deze kinetische energie kwijtraken. Als het gas supersonisch beweegt, kan het bij inval een schok ondergaan en daarbij zijn kinetische energie omzetten in thermische energie. Het bereikt daarbij de karakteristieke temperatuur van de halo. Als het gas heter wordt dan ongeveer 300.000 graden Celsius, wordt afkoelen door het uitstralen van licht steeds inefficiënter. Het kan ook zijn dat er geen schok plaatsvindt wanneer het gas de halo binnenkomt. Daardoor zal het gas met dezelfde snelheid blijven bewegen, richting het centrale sterrenstelsel, en pas later afremmen bij veel hogere dichtheid. Omdat de emissie sterk toeneemt met de dichtheid kan het gas snel zijn energie wegstralen en zal het altijd een relatief lage temperatuur behouden.

Welke van deze twee routes het gas volgt, hangt af van de massa van de halo en van de dichtheid van het gas bij invallen. Als de halomassa laag is valt al het gas 'koud' in. Als de halomassa hoog is en de dichtheid laag, vindt er een schok plaats en valt het gas 'heet' in. Stel nu echter dat de halomassa hoog is, maar dat de dichtheid van het invallende gas tegelijkertijd ook hoog is, dan vindt er ook geen schok plaats en blijft het gas dus 'koud'. De grens tussen de 'hete' en de 'koude' modus definiëren we als een maximum temperatuur die bereikt is van

ongeveer 300.000 graden.

In dit hoofdstuk beschrijven we bovendien dat de 'hete' modus belangrijker is naarmate de halomassa toeneemt en naarmate het heelal ouder wordt. De 'koude' modus is het belangrijkst voor de voeding van sterrenstelsels in het centrum van halo's, zelfs als die halo voornamelijk gevoed wordt door 'hete' inval. Feedback en veranderingen in de koeling (door wel of geen zware elementen mee te nemen in de berekening) hebben weinig effect op de verhouding van 'heet' en 'koud' invallend gas voor halo's, maar wel of geen feedback geeft wel enig verschil voor sterrenstelsels.

Hoofdstuk 3: De val van de kosmische stervormingssnelheid

Vanuit waarnemingen weten we dat, als we alle stervorming in het heelal bij elkaar optellen op verschillende tijdstippen, de stervormingssnelheid per volume-eenheid eerst toeneemt, tot het universum ongeveer 3 miljard jaar oud was, en daarna sterk afneemt tot nu toe[10]. Omdat de structuur van het heelal blijft groeien onder invloed van de zwaartekracht, is dit niet een logisch gevolg van structuurvorming. In dit hoofdstuk beschrijven we een aantal belangrijke ingrediënten voor het begrijpen van de evolutie van de kosmische stervormingssnelheid.

Allereerst volgt de globale stervormingssnelheid de globale inval van 'koud' gas, maar niet de globale inval van 'heet' gas of van de totale inval. Hierdoor kunnen we direct concluderen dat de totale hoeveelheid stervorming in het heelal wordt bepaald door de hoeveelheid 'koude' inval van gas. Feedback van zwarte gaten speelt hierbij een cruciale rol doordat het voorkomt dat 'heet' gas in massieve halo's de centrale sterrenstelsels bereikt. Zonder deze zwarte gaten zou de 'hete' modus in het huidige heelal de overhand hebben bij het veroorzaken van stervorming. In dat geval zou de kosmische stervormingssnelheid veel hoger zijn dan nu wordt waargenomen en de val van de kosmische stervormingssnelheid veel minder groot.

Hoofdstuk 4: De eigenschappen van gas in en rond galactische halo's

Zoals al eerder gezegd is de dichtheid van belang bij het bepalen van de maximale temperatuur van gas in halo's. In dit hoofdstuk beschrijven we nog veel meer eigenschappen van het gas als functie van straal en halomassa. In de buitendelen van halo's zijn de eigenschappen van de 'hete' en 'koude' modus goed te onderscheiden. Het gas dat altijd 'koud' is gebleven, bevind zich voornamelijk in de filamenten van het kosmische web. Zodoende heeft de structuur van het heelal een belangrijke invloed op de modus van gasinval en op de voeding van sterrenstelsels. Naast het feit dat gas in deze modus kouder en dichter is, heeft het gemiddeld genomen ook minder zware elementen en valt het sneller naar het centrum van de halo. De spreiding rond het gemiddelde is echter groot.

Sterkere feedback zorgt voor hogere snelheden van het gas dat de halo uitstroomt. 'Heet' gas wordt naar grotere afstanden geduwd. Het verschil tussen

---

[10]Het universum is ongeveer 13,7 miljard jaar oud.

'heet' en 'koud' gas lijkt op het verschil tussen instromend en uitstromend gas, alleen zijn de verschillen bij die laatste kleiner.

Hoofdstuk 5: Kanalen van koud gas in absorptie

Koud gas in de halo's van sterrenstelsels absorbeert licht van heldere achtergrondbronnen. Deze bronnen zijn heel heldere, ver weg gelegen sterrenstelsels, die licht uitzenden over een groot golflengtegebied. Het neutrale waterstof in het gas binnen en buiten sterrenstelsels absorbeert licht met een golflengte van precies 121,6 nm (oftewel licht van één bepaalde kleur). Dit is te zien als absorptielijn in het spectrum van de achtergrondbron. Met heel veel waarnemingen van achtergrondbronnen kan er berekend worden hoeveel absorptiesystemen er per volume-eenheid te vinden zijn in het heelal. We weten dan alleen nog niet wat dit voor objecten zijn, behalve dan dat het gaswolken zijn met een redelijke hoeveelheid koud (10.000 graden) gas. Daarvoor kunnen we kosmologische simulaties gebruiken. Als we daarmee de waarnemingen kunnen reproduceren, kunnen we de simulaties vertrouwen en kijken wat de eigenschappen van deze absorptiesystemen zijn.

In dit hoofdstuk kijken we naar in hoeverre de absorptiesystemen overeenkomen met de 'koude' modus, waarbij we specifiek kijken naar de maximum temperatuur van het gas, diens lidmaatschap van halo's, diens snelheid in de richting van het centrale sterrenstelsel en diens connectie met stervorming. We hebben ontdekt dat bijna alle 121,6 nm absorptie plaatsvindt in gas dat in de hele geschiedenis van het heelal (de tijd vlak na de oerknal niet meegerekend) kouder dan 300.000 graden is gebleven. Daarnaast valt het meeste gas met hoge snelheid richting het dichtstbijzijnde sterrenstelsel. Sterke absoptiesystemen bevinden zich bijna allemaal binnen de halo's van sterrenstelsels, maar alleen de allersterkste zitten binnen de sterrenstelsels zelf. De absorptie wordt gedomineerd door de kleinste halo's, omdat er daar veel meer van zijn. De meeste sterke 121,6 nm absorptiesystemen bestaan uit gas dat in de nabije toekomst stervormend wordt.

Het bestaan van inval van 'koude' modus gas in de simulaties, beschreven in de vorige hoofdstukken van dit proefschrift, is essentieel voor het reproduceren van de waarnemingen. We concluderen daarom dat deze vorm van inval bestaat en zelfs al gezien is als sterke 121,6 nm absorptiesystemen.

Hoofdstuk 6: Emissie van gas rond sterrenstelsels

Gas in het heelal straalt licht uit, waarbij het energie verliest. Dit gebeurt wanneer een elektron een ion tegenkomt, dus dit proces schaalt met het kwadraat van de dichtheid. Het atoom kan vervolgens recombineren, wat betekent dat het vrije electron in een gebonden toestand rond de atoomkern terechtkomt. Hierbij wordt licht uitgezonden van een specifieke golflengte (oftwel een specifieke kleur). Met simulaties kunnen we berekenen hoeveel licht van een bepaalde golflengte we verwachten rondom een sterrenstelsel. In dit hoofdstuk wordt beschreven hoeveel licht op een aantal golflengtes (zowel röntgen als ultravio-

let) corresponderend met diverse zware elementen, wordt uitgezonden door gas in halo's rond verschillende sterrenstelsels. Het licht uitgezonden door gas om sterrenstelsels heen is veel zwakker dan het licht van de sterrenselsels zelf. Met de emissielijnen die in dit hoofdstuk besproken worden, kunnen we het gas bestuderen dat niet heel koud en niet heel heet is, maar temperaturen heeft tussen de 30.000 en 10 miljoen graden. De sterkte van de emissielijnen wordt berekend, zowel in dichtbijgelegen als ver weg gelegen halo's. Vervolgens worden voorspellingen gemaakt voor wat in de toekomst waarneembaar is met nieuwe instrumenten en telescopen. De röntgenstraling zal zichtbaar zijn tot de rand van halo's en de ultraviolette straling tot 20 procent van deze straal. Dit is dus een uitstekende manier om halogas te bestuderen. Deze emissielijnen zijn afkomstig van gas met relatief hoge dichtheid en veel zware elementen. De emissie is klonteriger dan de onderliggende gasdistributie. De temperatuur van het gas dat op deze manier onderzocht kan worden, hangt sterk af van welke emissielijn waargenomen wordt. Röntgenstraling ontstaat in heter gas dan ultraviolette straling. Hoe sterk de lijnen zijn hangt af van de massa van de halo en van de leeftijd van het heelal.

De toekomst

Het proefschrift eindigt hier, maar het onderzoek gaat altijd door. Nieuwe vragen ontstaan als oude beantwoord zijn en er is dus nog genoeg te doen. Bovendien gaan de ontwikkelingen in dit vakgebied snel en in de nabije toekomst zullen we betere simulaties en betere observaties hebben. De voorspellingen die we in dit proefschrift maken, zullen zo ook getest kunnen worden in de toekomst. Hoewel de simulaties die we hier gebruikt hebben, op verscheidene fronten lijken op het waarneembare heelal, verschillen ze weer op andere punten. Als we begrijpen waarom dat zo is, kunnen we betere modellen maken voor de relevante processen, zodat we steeds een stapje dichter bij de werkelijkheid komen en steeds meer leren over hoe sterrenstelsels vormen.

References

Agertz O., Moore B., Stadel J., et al., 2007, MNRAS, 380, 963

Agertz O., Teyssier R., Moore B., 2009, MNRAS, 397, L64

Akamatsu H., Hoshino A., Ishisaki Y., Ohashi T., Sato K., Takei Y., Ota N., 2011, PASJ, 63, 1019

Altay G., Theuns T., Schaye J., Crighton N. H. M., Dalla Vecchia C., 2011, ApJL, 737, L37

Anderson M. E., Bregman J. N., 2011, ApJ, 737, 22

Angulo R. E., White S. D. M., 2010, MNRAS, 401, 1796

Bacon R., Accardo M., Adjali L., et al. 2010, in Society of Photo-Optical Instrumentation Engineers (SPIE) Conference Series Vol. 7735 of Society of Photo-Optical Instrumentation Engineers (SPIE) Conference Series, The MUSE second-generation VLT instrument

Bahcall J. N., Peebles P. J. E., 1969, ApJL, 156, L7+

Baldry I. K., Glazebrook K., Brinkmann J., Ivezić Ž., Lupton R. H., Nichol R. C., Szalay A. S., 2004, ApJ, 600, 681

Barkana R., Loeb A., 2001, Physics Reports, 349, 125

Bate M. R., Burkert A., 1997, MNRAS, 288, 1060

Bauer A. E., Drory N., Hill G. J., Feulner G., 2005, ApJL, 621, L89

Bauermeister A., Blitz L., Ma C., 2010, ApJ, 717, 323

Benson A. J., Bower R., 2010, MNRAS, pp 1615–+

Bertone S., Schaye J., 2012, MNRAS, 419, 780

Bertone S., Schaye J., Booth C. M., Dalla Vecchia C., Theuns T., Wiersma R. P. C., 2010b, MNRAS, 408, 1120

Bertone S., Schaye J., Dalla Vecchia C., Booth C. M., Theuns T., Wiersma R. P. C., 2010a, MNRAS, 407, 544

Bi H. G., Boerner G., Chu Y., 1992, A&A, 266, 1

Binney J., 1977, ApJ, 215, 492

Birnboim Y., Dekel A., 2003, MNRAS, 345, 349

Blitz L., Rosolowsky E., 2006, ApJ, 650, 933

Böhringer H., Werner N., 2010, Astronomy and Astrophysics Review, 18, 127

Bondi H., Hoyle F., 1944, MNRAS, 104, 273

Booth C. M., Schaye J., 2009, MNRAS, 398, 53

Booth C. M., Schaye J., 2010, MNRAS, in press, arXiv:1005.0844

Bouché N., Dekel A., Genzel R., Genel S., Cresci G., Förster Schreiber N. M., Shapiro K. L., Davies R. I., Tacconi L., 2010, ApJ, 718, 1001

Bower R. G., Benson A. J., Malbon R., Helly J. C., Frenk C. S., Baugh C. M., Cole S., Lacey C. G., 2006, MNRAS, 370, 645

Bower R. G., Morris S. L., Bacon R., Wilman R. J., Sullivan M., Chapman S., Davies R. L., de Zeeuw P. T., Emsellem E., 2004, MNRAS, 351, 63

Brinchmann J., Charlot S., White S. D. M., Tremonti C., Kauffmann G., Heckman T., Brinkmann J., 2004, MNRAS, 351, 1151

Brooks A. M., Governato F., Quinn T., Brook C. B., Wadsley J., 2009, ApJ, 694, 396

Bryan G. L., Norman M. L., 1998, ApJ, 495, 80

Cattaneo A., Dekel A., Faber S. M., Guiderdoni B., 2008, MNRAS, 389, 567

Cecil G., Bland-Hawthorn J., Veilleux S., Filippenko A. V., 2001, ApJ, 555, 338

Cen R., Miralda-Escudé J., Ostriker J. P., Rauch M., 1994, ApJL, 437, L9

Ceverino D., Dekel A., Bournaud F., 2010, MNRAS, 404, 2151

Chabrier G., 2003, PASP, 115, 763

Chen Y.-M., Wild V., Kauffmann G., Blaizot J., Davis M., Noeske K., Wang J.-M., Willmer C., 2009, MNRAS, 393, 406

Crain R. A., McCarthy I. G., Frenk C. S., Theuns T., Schaye J., 2010a, MNRAS, 407, 1403

Crain R. A., McCarthy I. G., Schaye J., Frenk C. S., Theuns T., 2010b, arXiv:1011.1906

Creasey P., Theuns T., Bower R. G., Lacey C. G., 2011, MNRAS, 415, 3706

Croton D. J., Farrar G. R., 2008, MNRAS, 386, 2285

Croton D. J., Springel V., White S. D. M., et al., 2006, MNRAS, 365, 11

Dabringhausen J., Kroupa P., Baumgardt H., 2009, MNRAS, 394, 1529

Dalla Vecchia C., Schaye J., 2008, MNRAS, 387, 1431

Davé R., Cen R., Ostriker J. P., Bryan G. L., Hernquist L., Katz N., Weinberg D. H., Norman M. L., O'Shea B., 2001, ApJ, 552, 473

Dekel A., Birnboim Y., 2006, MNRAS, 368, 2

Dekel A., Birnboim Y., Engel G., et al., 2009a, Nature, 457, 451

Dekel A., Sari R., Ceverino D., 2009b, ApJ, 703, 785

den Herder J.-W., Piro L., Ohashi T., et al. 2011, Experimental Astronomy, p. 30

Dijkstra M., Loeb A., 2009, MNRAS, 400, 1109

Dolag K., Borgani S., Murante G., Springel V., 2009, MNRAS, 399, 497

Duffy A. R., Schaye J., Kay S. T., Dalla Vecchia C., 2008, MNRAS, 390, L64

Eckert D., Molendi S., Gastaldello F., Rossetti M., 2011, A&A, 529, A133

Fakhouri O., Ma C., 2010, MNRAS, 401, 2245

Fall S. M., Efstathiou G., 1980, MNRAS, 193, 189

Fang T., Croft R. A. C., Sanders W. T., Houck J., Davé R., Katz N., Weinberg D. H., Hernquist L., 2005, ApJ, 623, 612

Fardal M. A., Katz N., Gardner J. P., Hernquist L., Weinberg D. H., Davé R., 2001, ApJ, 562, 605

Faucher-Giguère C.-A., Kereš D., 2011, MNRAS, 412, L118

Faucher-Giguère C.-A., Kereš D., Dijkstra M., Hernquist L., Zaldarriaga M., 2010, ApJ, 725, 633

Faucher-Giguère C.-A., Kereš D., Ma C.-P., 2011, MNRAS, pp 1399–+

Ferland G. J., Korista K. T., Verner D. A., Ferguson J. W., Kingdon J. B., Verner E. M., 1998, PASP, 110, 761

Ferrarese L., Merritt D., 2000, ApJL, 539, L9

Feulner G., Gabasch A., Salvato M., Drory N., Hopp U., Bender R., 2005, ApJL, 633, L9

Frank S., Rasera Y., Vibert D., et al. 2011, ArXiv e-prints, 1111.3028

Frenk C. S., White S. D. M., Davis M., Efstathiou G., 1988, ApJ, 327, 507

Fumagalli M., O'Meara J. M., Prochaska J. X., 2011b, ArXiv e-prints

Fumagalli M., Prochaska J. X., Kasen D., Dekel A., Ceverino D., Primack J. R., 2011a, ArXiv e-prints, 1103.2130

Furlanetto S. R., Schaye J., Springel V., Hernquist L., 2003, ApJL, 599, L1

Furlanetto S. R., Schaye J., Springel V., Hernquist L., 2004, ApJ, 606, 221

Furlanetto S. R., Schaye J., Springel V., Hernquist L., 2005, ApJ, 622, 7

Genel S., Bouché N., Naab T., Sternberg A., Genzel R., 2010, ApJ, 719, 229

Giavalisco M., Vanzella E., Salimbeni S., et al., 2011, ArXiv e-prints, 1106.1205

Goerdt T., Dekel A., Sternberg A., Ceverino D., Teyssier R., Primack J. R., 2010, MNRAS, 407, 613

Haardt F., Madau P., 2001, in Neumann D. M., Tran J. T. V., eds, Clusters of Galaxies and the High Redshift Universe Observed in X-rays Modelling the UV/X-ray cosmic background with CUBA

Hayes M., Scarlata C., Siana B., 2011, Nature, 476, 304

Hernquist L., Katz N., Weinberg D. H., Miralda-Escudé J., 1996, ApJL, 457, L51+

Hickox R. C., Markevitch M., 2006, ApJ, 645, 95

Hickox R. C., Markevitch M., 2007, ApJ, 671, 1523

Hopkins A. M., Beacom J. F., 2006, ApJ, 651, 142

Hui L., Gnedin N. Y., 1997, MNRAS, 292, 27

Hummels C., Bryan G., 2011, ArXiv e-prints, 1112.0009

Hutchings R. M., Thomas P. A., 2000, MNRAS, 319, 721

Kaastra J. S., Lieu R., Tamura T., Paerels F. B. S., den Herder J. W., 2003, A&A, 397, 445

Katz N., Gunn J. E., 1991, ApJ, 377, 365

Katz N., Keres D., Dave R., Weinberg D. H., 2003, in J. L. Rosenberg & M. E. Putman ed., The IGM/Galaxy Connection. The Distribution of Baryons at z=0 Vol. 281 of Astrophysics and Space Science Library, How Do Galaxies Get Their Gas?. pp 185–+

Katz N., Weinberg D. H., Hernquist L., Miralda-Escude J., 1996, ApJL, 457, L57+

Kauffmann G., Heckman T. M., White S. D. M., et al., 2003, MNRAS, 341, 54

Kay S. T., Pearce F. R., Jenkins A., Frenk C. S., White S. D. M., Thomas P. A., Couchman H. M. P., 2000, MNRAS, 316, 374

Kennicutt Jr. R. C., 1998, ApJ, 498, 541

Kereš D., Hernquist L., 2009, ApJL, 700, L1

Kereš D., Katz N., Davé R., Fardal M., Weinberg D. H., 2009b, MNRAS, 396, 2332

Kereš D., Katz N., Fardal M., Davé R., Weinberg D. H., 2009a, MNRAS, 395, 160

Kereš D., Katz N., Weinberg D. H., Davé R., 2005, MNRAS, 363, 2

Kereš D., Vogelsberger M., Sijacki D., Springel V., Hernquist L., 2011, ArXiv e-prints, 1109.4638

Khalatyan A., Cattaneo A., Schramm M., Gottlöber S., Steinmetz M., Wisotzki

L., 2008, MNRAS, 387, 13

Kim T.-S., Carswell R. F., Cristiani S., D'Odorico S., Giallongo E., 2002, MNRAS, 335, 555

Kimm T., Slyz A., Devriendt J., Pichon C., 2011, MNRAS, 413, L51

Klessen R. S., Spaans M., Jappsen A., 2007, MNRAS, 374, L29

Komatsu E., Smith K. M., Dunkley J., et al., 2011, ApJS, 192, 18

Kormendy J., Richstone D., 1995, ARA&A, 33, 581

Krumholz M. R., Ellison S. L., Prochaska J. X., Tumlinson J., 2009, ApJL, 701, L12

Lacey C., Cole S., 1994, MNRAS, 271, 676

Lagos C. D. P., Cora S. A., Padilla N. D., 2008, MNRAS, 388, 587

Lehnert M. D., Heckman T. M., Weaver K. A., 1999, ApJ, 523, 575

Leitner S. N., Kravtsov A. V., 2010, ArXiv e-prints, 1011.1252

Li J.-T., Wang Q. D., 2012, ArXiv e-prints, 1201.0551

Mac Low M.-M., Ferrara A., 1999, ApJ, 513, 142

Martin C., Moore A., Morrissey P., Matuszewski M., Rahman S., Adkins S., Epps H., 2010, in Society of Photo-Optical Instrumentation Engineers (SPIE) Conference Series Vol. 7735 of Society of Photo-Optical Instrumentation Engineers (SPIE) Conference Series, The Keck Cosmic Web Imager

Matsuda Y., Yamada T., Hayashino T., Tamura H., Yamauchi R., Ajiki M., Fujita S. S., Murayama T., Nagao T., Ohta K., Okamura S., Ouchi M., Shimasaku K., Shioya Y., Taniguchi Y., 2004, AJ, 128, 569

Matuszewski M., Chang D., Crabill R. M., Martin D. C., Moore A. M., Morrissey P., Rahman S., 2010, in Society of Photo-Optical Instrumentation Engineers (SPIE) Conference Series Vol. 7735 of Society of Photo-Optical Instrumentation Engineers (SPIE) Conference Series, The Cosmic Web Imager: an integral field spectrograph for the Hale Telescope at Palomar Observatory: instrument design and first results

McCarthy I. G., Schaye J., Bower R. G., et al., 2011, MNRAS, in press, arXiv:1008.4799

McCarthy I. G., Schaye J., Ponman T. J., et al., 2010, MNRAS, 406, 822

McQuinn M., Oh S. P., Faucher-Giguere C.-A., 2011, ArXiv e-prints, 1101.1964

Miller E. D., Bautz M., George J., Mushotzky R., Davis D., Henry J. P., 2011, ArXiv e-prints, 1112.0034

Mitsuishi I., Gupta A., Yamasaki N. Y., Takei Y., Ohashi T., Sato K., Galeazzi M., Henry J. P., Kelley R. L., 2011, ArXiv e-prints, 1109.4647

Nagamine K., Choi J.-H., Yajima H., 2010, ApJL, 725, L219

Navarro J. F., Frenk C. S., White S. D. M., 1996, ApJ, 462, 563

Neistein E., van den Bosch F. C., Dekel A., 2006, MNRAS, 372, 933

Noterdaeme P., Petitjean P., Ledoux C., Srianand R., 2009, A&A, 505, 1087

Ocvirk P., Pichon C., Teyssier R., 2008, MNRAS, 390, 1326

O'Meara J. M., Prochaska J. X., Burles S., Prochter G., Bernstein R. A., Burgess K. M., 2007, ApJ, 656, 666

Oppenheimer B. D., Davé R., Kereš D., Fardal M., Katz N., Kollmeier J. A.,

Weinberg D. H., 2010, MNRAS, 406, 2325

Padmanabhan T., 2002, Theoretical Astrophysics, Volume III: Galaxies and Cosmology. Theoretical Astrophysics, by T. Padmanabhan, pp. 638. ISBN 0521562422. Cambridge, UK: Cambridge University Press, October 2002.

Padoan P., Nordlund A., Jones B. J. T., 1997, MNRAS, 288, 145

Péroux C., Dessauges-Zavadsky M., D'Odorico S., Sun Kim T., McMahon R. G., 2005, MNRAS, 363, 479

Pontzen A., Governato F., Pettini M., et al., 2008, MNRAS, 390, 1349

Postman M., 2009, ArXiv e-prints, 0904.0941

Powell L. C., Slyz A., Devriendt J., 2011, MNRAS, 414, 3671

Prochaska J. X., O'Meara J. M., Worseck G., 2010, ApJ, 718, 392

Prochaska J. X., Wolfe A. M., 2009, ApJ, 696, 1543

Rahman S., Martin C., McLean R., Matuszewski M., Chang D., 2006, in Society of Photo-Optical Instrumentation Engineers (SPIE) Conference Series Vol. 6269 of Society of Photo-Optical Instrumentation Engineers (SPIE) Conference Series, Cosmic web imager

Rakic O., Schaye J., Steidel C. C., Rudie G. C., 2011a, MNRAS, 414, 3265

Rakic O., Schaye J., Steidel C. C., Rudie G. C., 2011b, ArXiv e-prints, 1109.4944

Rauch M., Becker G. D., Haehnelt M. G., Gauthier J.-R., Ravindranath S., Sargent W. L. W., 2011, MNRAS, 418, 1115

Rees M. J., Ostriker J. P., 1977, MNRAS, 179, 541

Ribaudo J., Lehner N., Howk J. C., Werk J. K., Tripp T. M., Prochaska J. X., Meiring J. D., Tumlinson J., 2011, ArXiv e-prints, 1105.5381

Rosdahl J., Blaizot J., 2011, ArXiv e-prints, 1112.4408

Rubin K. H. R., Weiner B. J., Koo D. C., Martin C. L., Prochaska J. X., Coil A. L., Newman J. A., 2010, ApJ, 719, 1503

Sales L. V., Navarro J. F., Schaye J., Vecchia C. D., Springel V., Booth C. M., 2010, MNRAS, pp 1326–+

Salpeter E. E., 1964, ApJ, 140, 796

Scannapieco C., Wadepuhl M., Parry O. H., et al. 2011, ArXiv e-prints, 1112.0315

Schaye J., 2001b, ApJL, 562, L95

Schaye J., 2001a, ApJ, 559, 507

Schaye J., Carswell R. F., Kim T.-S., 2007, MNRAS, 379, 1169

Schaye J., Dalla Vecchia C., 2008, MNRAS, 383, 1210

Schaye J., Dalla Vecchia C., Booth C. M., et al., 2010, MNRAS, 402, 1536

Semboloni E., Hoekstra H., Schaye J., van Daalen M. P., McCarthy I. G., 2011, MNRAS, 417, 2020

Shapley A. E., Steidel C. C., Pettini M., Adelberger K. L., 2003, ApJ, 588, 65

Sheth R. K., Tormen G., 1999, MNRAS, 308, 119

Shull J. M., Smith B. D., Danforth C. W., 2011, ArXiv e-prints

Silk J., 1977, ApJ, 211, 638

Simionescu A., Allen S. W., Mantz A., et al. 2011, Science, 331, 1576

Sommer-Larsen J., 2006, ApJL, 644, L1

Soong Y., Serlemitsos P. J., Okajima T., Hahne D., 2011, in Society of Photo-

Optical Instrumentation Engineers (SPIE) Conference Series Vol. 8147 of Society of Photo-Optical Instrumentation Engineers (SPIE) Conference Series, ASTRO-H Soft X-ray Telescope (SXT)

Spergel D. N., Bean R., Doré O., et al., 2007, ApJS, 170, 377

Spergel D. N., Verde L., Peiris H. V., et al., 2003, ApJS, 148, 175

Springel V., 2005b, MNRAS, 364, 1105

Springel V., Di Matteo T., Hernquist L., 2005, MNRAS, 361, 776

Springel V., Hernquist L., 2002, MNRAS, 333, 649

Springel V., White S. D. M., Jenkins A., et al. 2005a, Nature, 435, 629

Springel V., White S. D. M., Tormen G., Kauffmann G., 2001, MNRAS, 328, 726

Steidel C. C., Adelberger K. L., Shapley A. E., Pettini M., Dickinson M., Giavalisco M., 2000, ApJ, 532, 170

Steidel C. C., Bogosavljević M., Shapley A. E., Kollmeier J. A., Reddy N. A., Erb D. K., Pettini M., 2011, ApJ, 736, 160

Steidel C. C., Erb D. K., Shapley A. E., Pettini M., Reddy N., Bogosavljević M., Rudie G. C., Rakic O., 2010, ApJ, 717, 289

Stewart K. R., Kaufmann T., Bullock J. S., Barton E. J., Maller A. H., Diemand J., Wadsley J., 2011a, ApJL, 735, L1+

Stewart K. R., Kaufmann T., Bullock J. S., Barton E. J., Maller A. H., Diemand J., Wadsley J., 2011b, ApJ, 738, 39

Takei Y., Henry J. P., Finoguenov A., Mitsuda K., Tamura T., Fujimoto R., Briel U. G., 2007, ApJ, 655, 831

Takei Y., Ursino E., Branchini E., et al. 2011, ApJ, 734, 91

Theuns T., Leonard A., Efstathiou G., Pearce F. R., Thomas P. A., 1998, MNRAS, 301, 478

Theuns T., Viel M., Kay S., Schaye J., Carswell R. F., Tzanavaris P., 2002, ApJL, 578, L5

Tuttle S. E., Schiminovich D., Grange R., Rahman S., Matuszewski M., Milliard B., Deharveng J.-M., Martin D. C., 2010, in Society of Photo-Optical Instrumentation Engineers (SPIE) Conference Series Vol. 7732 of Society of Photo-Optical Instrumentation Engineers (SPIE) Conference Series, FIREBALL: the first ultraviolet fiber fed spectrograph

Tuttle S. E., Schiminovich D., Milliard B., et al. 2008, in Society of Photo-Optical Instrumentation Engineers (SPIE) Conference Series Vol. 7014 of Society of Photo-Optical Instrumentation Engineers (SPIE) Conference Series, The FIRE-Ball fiber-fed UV spectrograph

Tytler D., 1987, ApJ, 321, 49

Urban O., Werner N., Simionescu A., Allen S. W., Böhringer H., 2011, MNRAS, 414, 2101

van Daalen M. P., Schaye J., Booth C. M., Dalla Vecchia C., 2011, MNRAS, 415, 3649

van de Voort F., Schaye J., 2012, ArXiv e-prints, 1111.5039

van de Voort F., Schaye J., Altay G., Theuns T., 2012, ArXiv e-prints, 1109.5700

van de Voort F., Schaye J., Booth C. M., Dalla Vecchia C., 2011b, MNRAS, 415,

2782

van de Voort F., Schaye J., Booth C. M., Haas M. R., Dalla Vecchia C., 2011a, MNRAS, 414, 2458

Veilleux S., Cecil G., Bland-Hawthorn J., 2005, ARA&A, 43, 769

Wang J., Navarro J. F., Frenk C. S., et al., 2011, MNRAS, 413, 1373

Weaver R., McCray R., Castor J., Shapiro P., Moore R., 1977, ApJ, 218, 377

Weinberg D. H., Davé R., Katz N., Hernquist L., 2004, ApJ, 601, 1

Weiner B. J., Coil A. L., Prochaska J. X., Newman J. A., Cooper M. C., Bundy K., Conselice C. J., Dutton A. A., Faber S. M., Koo D. C., Lotz J. M., Rieke G. H., Rubin K. H. R., 2009, ApJ, 692, 187

White S. D. M., Frenk C. S., 1991, ApJ, 379, 52

White S. D. M., Rees M. J., 1978, MNRAS, 183, 341

Wiersma R. P. C., Schaye J., Smith B. D., 2009a, MNRAS, 393, 99

Wiersma R. P. C., Schaye J., Theuns T., 2011, MNRAS, 415, 353

Wiersma R. P. C., Schaye J., Theuns T., Dalla Vecchia C., Tornatore L., 2009b, MNRAS, 399, 574

Yoshikawa K., Dolag K., Suto Y., et al. 2004, PASJ, 56, 939

Yoshikawa K., Yamasaki N. Y., Suto Y., Ohashi T., Mitsuda K., Tawara Y., Furuzawa A., 2003, PASJ, 55, 879

Zheng Z., Miralda-Escudé J., 2002, ApJL, 568, L71

Zwaan M. A., Prochaska J. X., 2006, ApJ, 643, 675

Publications

1. *Properties of gas in and around galaxy haloes*
   Freeke van de Voort & Joop Schaye
   2012, MNRAS, submitted, *arXiv:1111.5039*

2. *Cold accretion flows and the nature of high column density HI absorption at redshift 3*
   Freeke van de Voort, Joop Schaye, Gabriel Altay, Tom Theuns
   2012, MNRAS, in press, *arXiv:1109.5700*

3. *ORIGIN: Metal Creation and Evolution from the Cosmic Dawn*
   Jan-Willem den Herder et al.
   2011, Experimental Astronomy, 30

4. *The drop in the cosmic star formation rate below redshift 2 is caused by a change in the mode of gas accretion and by active galactic nucleus feedback*
   Freeke van de Voort, Joop Schaye, C. M. Booth, Claudio Dalla Vecchia
   2011, MNRAS, 415, 2782

5. *The rates and modes of gas accretion on to galaxies and their gaseous haloes*
   Freeke van de Voort, Joop Schaye, C. M. Booth, Marcel R. Haas, Claudio Dalla Vecchia
   2011, MNRAS, 414, 2458

6. *The physics driving the cosmic star formation history*
   Joop Schaye, Claudio Dalla Vecchia, C.M. Booth, Robert P.C. Wiersma, Tom Theuns, Marcel R. Haas, Serena Bertone, Alan R. Duffy, I.G. McCarthy, Freeke van de Voort
   2010, MNRAS, 402, 1536

Curriculum Vitae

I was born on 16 September 1983 in Eindhoven. I grew up in Hulsel and Bladel, both in the South-East of the Dutch province North-Brabant. After my primary school years at 'De Sleutelaar' I went to the 'gymnasium', i.e. taking ancient languages as well as other courses, at 'Pius-X college'. I was always interested in far too many subjects and, besides Dutch, English, mathematics, physics, chemistry, and biology, I also took French, Latin, music, and history. I graduated in 2001 cum laude.

The reason I became interested in astronomy is that I joined my friend in taking a master class in astronomy aimed at high-school students. I actually wanted to go to chemistry, but she thought astronomy would be more fun. This eventually led to my decision to study astronomy in Leiden. I assumed that finding a job in a different part of society would be easy enough and that the most important thing was to study something I enjoyed. I certainly did not expect to stay at Leiden University for this long.

Because I was also intrigued by the physics I was taught, I started a bachelor in physics as well and received two bachelor degrees after four years. Realizing that I was fascinated most by astronomy, I continued with the master's degree in astronomy. I went to the *Space Telescope Science Institute* in Baltimore for half a year to do one of my research projects. Back in The Netherlands, I did my final project with Joop Schaye and graduated cum laude in 2008. I liked my research project so much that I decided to stay for my PhD.

During my PhD, I enjoyed working with Joop Schaye and his research group. I spent three months working in Saint-Genis-Laval, France, at the *Centre de Recherche Astrophysique de Lyon*, *Observatoire de Lyon* and six months in Garching-bei-München, Germany, at the *Max-Planck Institut für Astrophysik*.

Over the years I gave approximately forty presentations about my research, some of those were addressed at the general audience or high-school students, but most of them were aimed at colleagues. I participated in international conferences in The Netherlands, Germany, France, Great-Britain, and Switzerland and also in a summer school in the United States. During my PhD I was a teaching assistant for the course 'radiative processes' twice and for 'introductory astrophysics' once. Furthermore, I was a member of the board of the amateur astronomy association *Leidse Weer- en Sterrekundige Kring* and spent many years answering astronomy-related questions as a member of the outreach committee.

In April I will move to Córdoba in Argentina for half a year with an *Early Stage Researcher* fellowship granted by the *CosmoComp* programme of the European Union. In October I will start as a post-doctoral researcher at the *University of California* in Berkeley, United States, in collaboration with the *Academia Sinica Institute of Astronomy and Astrophysics* in Taipei, Taiwan.

Acknowledgements

Four years is a long time, but now, quite suddenly, the end is near. I would like to thank everyone at the Sterrewacht, including the people who have already moved on and left me behind, for their excellent company and for making this such a wonderful place to work. A special mention has to be made of the support staff, who keep the institute together.

Being a (long-term) member of my research group has been awesome. Claudio, Andreas, Rob, you made sure the atmosphere in the group was excellent when I arrived and it has never been the same since the three of you left. Luckily, we ran into each other on various occasions. I hope we will continue to do so. Marcel, thanks for all your help at the start, your friendship, your directness, and for always being your down to earth self. Olivera, thank you for educating me about the dangers I am facing, from eating grapefruits to bungee jumping, and for your never waning faith in me. I have the same faith in you. Ali, thanks to you I was, finally, no longer the new one in the group. Thanks so much for your interest in my work, for proof reading my papers, and for making our meetings more lively. Ben, you are incredible. Please continue to amaze me and others. Milan, Monica, Marco, Alex, Rob, I am very happy that all of you joined our group. You are the future. Please keep the group as fun as it is now, because I intend to come back to visit you. Marcel, it was great having you around in Munich to keep the Leiden spirit (and gossip) going. You are a worthy office mate replacement and a great help with the thesis formatting. Without you, there would not be any unicorns. Craigy, thanks for your interesting contributions to our group meetings, for giving me all the advice and help I needed all these years, and for being my bestest friend. No-one calls me Freaky like you do. Making fun of you and being made fun of by you, mostly by recycling our ten favourite jokes, were highlights of my day.

Lensing, i.e. Edo, Malin, Stefania, and Elisabetta, Sterrewacht life certainly improved after we merged our tea breaks. Isa, I am so happy we suddenly became good friends after many years. I value your good advice, your honest opinions about everything, and I like that you are as loud as I am. Ann-Marie, all the places where we end up together (Leiden, Dwingeloo, Princeton, and Chicago, thus far) are always better with you there. I am excited about us both going to Berkeley. Thank you for recruiting me. I will enjoy sharing a cubicle with you. Edith, all of your cakes are as wonderful as you are. Shannon, you are the best. Thank you for motivating me, as well as for distracting me, and for keeping me alive during the thesis writing months.

Inge, Hilde, and Karolina, we changed and our lives changed since high school, but we will be friends forever. I enjoy every minute we spend together, especially when there are not enough of those minutes. Carola, having you around all the time made Herengracht 14 in The Hague the best place to live. I do not want it to end. Papa, mama, Tom, and Anne, I cannot think of a better family to have. We are different and we are the same, which I find very inspiring.

Thank you for always supporting me in my decisions. Evelyn and Eveline, we arrived in Leiden together more than a decade ago and, although you were no longer at the Sterrewacht with me during my PhD, you suffered through all my stories without any complaints. You were there at the beginning and I am extremely happy and grateful that both of you will be by my side at the end.

My time in France and Germany would not have been as fantastic without the amazing people I met there, both at work and outside of work. I would also like to warmly thank the Leiden student scuba diver club *LSD* and The Hague student orchestra *Valerius* for making the past four years about more than just astronomy. Finally, to all my friends who are not mentioned here, thank you for being who you are.